The evolution of star-forming galaxies : analysis of infrared observations by AKARI

Thesis

The evolution of star-forming galaxies: analysis of infrared observations by *AKARI*

Chris Sedgwick BBS BA FCA BSc

School of Physical Sciences

The Open University

A thesis submitted for the degree of

Doctor of Philosophy

March 2015

Abstract

This thesis presents the results of several projects on the analysis of infrared observations of star-forming galaxies, all of which included observations by the *AKARI Space Telescope*.

Spectroscopic redshifts have been measured for over 400 galaxies using the fibre spectrograph AAOmega in the *AKARI* Deep Field South, the first significant spectroscopic campaign in a relatively new, cirrus-free deep field. A local luminosity function of galaxies in this field is also presented, using far-infrared data from *AKARI*. Various properties are deduced from the atomic emission lines detected, and star-forming spectral energy distribution templates are fitted to these sources using the multi-wavelength data available. The majority of these galaxies are dominated by emission from star formation, and local sources show relatively low dust extinction.

AKARI's own near-infrared spectroscopic facility was used to observe well-known submillimetre targets in other well-studied deep fields. The most interesting result was the detection of high redshift ($z > 3.5$) Hα emission lines in two radio galaxies and two submillimetre galaxies shown to be associated with one of them, the highest-redshift Hα detections so far discovered in star-forming galaxies. Both radio galaxies are shown to be quasars, and one is part of a binary quasar. The result from stacking all the Hα targets is also presented.

Two Graphic User Interfaces (GUIs) were written to help with these projects and are described in this thesis.

Finally, the early results of an ongoing experiment to detect gravitational lenses by identifying quasars with enhanced far-infrared luminosity are presented, with about twenty quasars identified in the *AKARI* all-sky far-infrared survey. Several sources at high redshift appear to show enhanced luminosity, and follow-up optical spectroscopy of seven of these sources shows that three are high-redshift quasars.

I would like to dedicate this thesis to
Brigit, Helen (returning the compliment!), Stephen and Ally

Contents

List of Figures

List of Tables

Chapter 1

Introduction to infrared astronomy

The understanding of the evolution of star-forming galaxies has been transformed by the development of infrared astronomy. Star-forming regions in galaxies are typically surrounded by the remains of the dense gas and dust clouds from which the stars have formed, and to which they contribute via supernovae; we now know that these clouds absorb much of the optical/ultraviolet radiation from the newly-formed stars and re-emit it in the infrared region of the spectrum. Infrared astronomy is essential to identify such galaxies and to fully understand the history of star-forming galaxies.

This region of the spectrum has been opened up for observation in recent decades by space telescopes. The work in this thesis is based on data from one of these space missions, the AKARI Space Telescope. This first chapter outlines recent developments and discoveries in infrared astronomy as a background for the work described in later chapters, and provides a brief overview of this work.

1.1 Introduction

This chapter gives some details of the background and context for the work presented in this thesis. Section 1.2 will outline the main infrared space telescopes and submillimetre facilities, including their objectives and main extragalactic results, from the first infrared satellite telescope to future planned missions. The remaining sections of this chapter will then briefly describe the main discoveries (and surprises) of infrared astronomy so far in relation to the evolution of star forming galaxies: the discoveries of the cosmic infrared background (Section 1.3), of luminous infrared galaxies (Section 1.4), of PAHs (Section 1.5) and of the submillimetre galaxy population (Section 1.6). The chapter ends with an overview of the work presented in this thesis (Section 1.7).

1.2 Infrared space telescopes and submillimetre facilities

Infrared astronomy[1] became a significant area for research with the launch of the InfraRed Astronomical Satellite (IRAS) in 1983 which began to cover parts of the spectrum now known to be critical in understanding star formation. Prior to the launch of IRAS, even the extent of radiant energy in this region of the spectrum was not known. Data collected by IRAS and other early infrared telescopes, the COsmic Background Explorer (COBE, launched 1989) and the Infrared Space Observatory (ISO, launched 1995) and ground-based measurements in the submillimetre windows by the Submillimetre Common User Bolometer Array (SCUBA) instrument on the James Clerk Maxwell Telescope (from ∼1998), started a revolution in our understanding of how and when star formation occurred.

Brief details of the infrared space telescopes and ground-based facilities which have made these results possible are given in this section. In particular, there is some background on the instruments and surveys which are used or referred to in the science chapters that follow. All the space instruments are cryogenically cooled down to a few Kelvin in order to observe in the infrared, to overcome thermal noise in the infrared (in particular, that from the detector itself) in order to make sensitive measurements. The cryogen has a limited lifetime; in some cases, 'warm phase' observations are made after the cryogen runs out and the instruments begin to warm up. Details of the infrared space telescopes and their spectroscopic facilities are listed in Tables 1.1 and 1.2, and the wavelength coverage for photometry and for spectroscopy are shown in Figures 1.1 and 1.2.

The Infrared Astronomical Satellite (IRAS)

The InfraRed Astronomical Satellite (IRAS; Neugebauer et al. [1984]) was launched on 25 January 1983. A survey satellite to map the whole sky in the infrared had been proposed as early as 1971 and had proved controversial. The

[1]The infrared region can be broadly defined as the region with wavelengths from ~ 1 μm to 1000 μm. Within this region, ~ 25 μm to 500 μm is referred to as the far-infrared and 500 μm to 1000 μm is often called the submillimetre region, particularly for observations made by ground-based instruments.

primary goal for IRAS was to perform the first infrared all-sky survey in four wavelength bands centred on 12 μm, 25 μm, 60 μm and 100 μm. Half of the sky was covered by more than 12 scans; about 96% of the sky by at least four scans over the ten months of the mission. The average 10σ sensitivity at 60 μm was 0.85 Jy. Early results for extragalactic sources were reviewed in Soifer et al. [1987a].

The two main published catalogues of all sources from IRAS observations are (a) the Point Source Catalogue (PSC) which reached a depth of 0.6 Jy at 60 μm and contained 245,889 sources, together with a PSC rejects file (PSCR) of 372,753 objects; and (b) the Faint Source Catalogue (FSC; Moshir et al. [1992]) which used stacking[2] to reach a depth of 0.2 Jy at 60 μm and held 173,044 sources, with a FSC Rejects (FSCR) catalogue of 593,516 sources. The FSC avoided a band in the galactic plane $|b| < 10^\circ$, and 100 μm sources were only included if also detected at other wavebands. The FSC sources have a signal-to-noise ratio SNR > 5; the rejects catalogue includes sources with SNR > 3. Of the FSC sources, 42% are also PSC sources and 58% are new sources. Not all PSC sources for $|b| \geq 10^\circ$ are in the FSC. The main catalogues were designed to catalogue fixed sources, so moving objects, such as those in the solar system, will appear in the reject catalogues.

A catalogue of spectroscopic redshifts for 15,411 infrared galaxies from the IRAS Point Source Catalogue (PSCz; Saunders et al. [2000]) was later published. These are all local sources, with a median redshift of $z = 0.028$, and a maximum redshift of $z \sim 0.1$. This catalogue is complete to within a few percent at high latitudes (and within 10% at low latitudes) down to its $S_{60} > 0.6$ Jy flux limit. It was used, together with the colour-temperature relation found in the SCUBA Local Universe Galaxy Survey and colour-colour relations, to predict local luminosity functions and source counts for a range of wavelengths from 70 μm to 850 μm (Serjeant and Harrison [2005]).

A catalogue of 60,303 redshifts (56% spectroscopic) for the FSC was published as the Imperial IRAS-FSC Redshift Catalogue (IIFSCz), later revised to include multi-wavelength data as the Revised IRAS-FSC Redshift Catalogue (RIFSCz; Wang et al. [2014a]). The 90% completeness limit is $S_{60} > 0.36$ Jy.

[2]Stacking is discussed in Section 6.3.2.

1.2 Infrared space telescopes

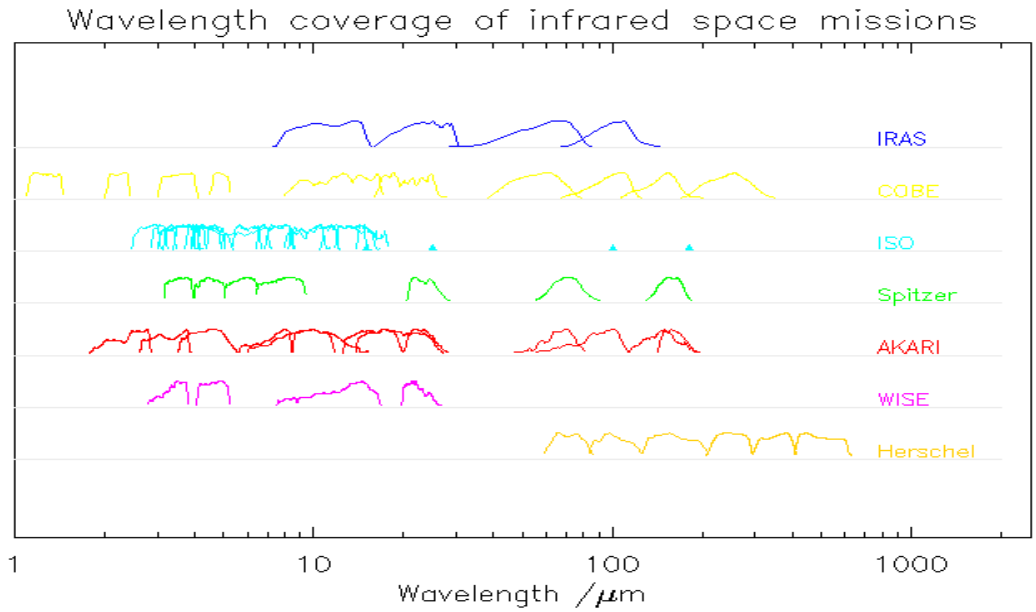

Figure 1.1: Spectral response curves of infrared space telescopes/instruments/filters. Note: for ISO, response curves are shown for ISOCAM, but peaks only for ISOPHOT.

IRAS remains one of the cornerstones of infrared astronomy. The only other all-sky survey which includes mid- and far-infrared wavelengths was made some 23 years later by the *AKARI Space Telescope* (see below). The continuing importance of the IRAS catalogue is shown by the fact that papers continue to be published using its data: for example, Rowan-Robinson and Wang [2010] identified 179 Hyper-Luminous InfraRed Galaxies (HyLIRGs, $L_{\rm FIR} > 10^{13} L_{\odot}$) in the IIFSCz catalogue.

Cosmic Background Explorer (COBE)

The COsmic Background Explorer (COBE; Boggess et al. [1992]) was launched in 1989 and observed in both the infrared and microwave regions of the spectrum. In fact, the primary goal of COBE was to measure the cosmic microwave background (CMB), and it succeeded in showing that this is a near perfect blackbody spectrum at 2.73 K. It also measured the tiny anisotropies in the CMB over a 4-year period. A later satellite, the Wilkinson Microwave Anisotropy Probe (WMAP), launched in 2001 and observing at microwave frequencies 23 -

94 GHz, mapped the CMB with greater sensitivity and higher resolution (Hinshaw et al. [2013]). More recently, the Planck satellite (Planck-Collaboration [2014]), launched in 2009 and observing mostly at microwave frequencies (350 μm - 10,000 μm, so it covers part of the infrared region also), has obtained the most detailed map to date of the CMB.

A second major achievement of COBE, more directly relevant to the topics of this thesis, was the first measurement of the cosmic infrared background (CIB) radiation by its Diffuse Infrared Background Experiment (DIRBE; Hauser et al. [1998]). This was a significant discovery, and is discussed in Section 1.3 below.

Among other results, observations by COBE showed that the star formation rate at $z \sim 1.5$ must exceed that inferred from UV/optical measurements by a factor of two, demonstrating the key role played by dust obscuration in observing star-forming galaxies. This result used observations of the far-infrared extragalactic background light by DIRBE and by the Far InfraRed Absolute Spectrophotometer (FIRAS; Fixsen et al. [1994]) to show that the CIB must be generated mainly by dust-shrouded massive stars, which also accounted for the observed metal enrichment of the intra-cluster medium (Dwek et al. [1998]). This implies that the dominant source of energy contributing to the CIB was from nuclear fusion (i.e. from star formation), with only 10% - 20% contributed by Active Galactic Nuclei (AGNs; see review in Hauser and Dwek [2001]), a conclusion confirmed in many later studies. This topic recurs throughout this thesis, and is discussed in detail in Section 3.2.2. The total CIB energy density is comparable to the UV/optical/NIR background, implying that half of the star formation in the universe is shrouded in dust (see Section 1.3).

An important result for Galactic astronomy from the FIRAS instrument was the mapping of fine structure emission lines in the far infrared for [CII] λ157.7 μm and (for the first time) [NII] λ205.3 μm (Wright et al. [1991]; Fixsen et al. [1999]), key to understanding the heating and cooling occurring between various phases of the interstellar medium. It was inferred that the [CII] arises from the cold neutral medium whereas the [NII] arises from the warm ionised medium (Bennett et al. [1994]). It also enabled an estimate of the total ionising photon rate in the Galaxy independent of the obscuration affecting UV/optical measurements.

The Infrared Space Observatory (ISO)

Following on from the all-sky survey results and discoveries by IRAS and the discovery of the CIB by COBE, the first infrared space observatory, ESA's Infrared Space Observatory (ISO; Kessler et al. [1996]) was launched in 1995 to make detailed studies of individual objects and regions with instruments of greater sensitivity and covering more infrared wavelength bands. Two spectrometers were included as well as the imaging polarimeter (ISOPHOT) and camera (ISOCAM) shown in Table 1.1. The mission lasted for about two and a half years (several months longer than planned). ISO extragalactic observations were focussed on the role of star formation and the evolution of galaxies. A summary of the extragalactic results from ISO is given in Genzel and Cesarsky [2000]. The importance of PAH[3] emission in the mid-infrared was demonstrated. A key result of ISO spectroscopy was distinguishing between AGNs and starbursts in local galaxies (discussed in Section 3.2.2).

The European Large Area ISO Survey (ELAIS; Oliver et al. [2000]) was the largest open-time project of ISO, and covered 12 deg^2 at 15 μm with ISOCAM and at 90 μm with ISOPHOT. The results included evidence for strong evolution of star-forming galaxies (Efstathiou et al. [2000a]; Serjeant et al. [2000]). This survey also included a 90 μm luminosity function (Serjeant et al. [2004])[4].

Spitzer Space Telescope

NASA's *Spitzer Space Telescope* (Werner et al. [2004]), launched in 2003, has produced observations at fluxes up to three orders of magnitude lower than previous space telescopes. The Infrared Array Camera (IRAC; Fazio et al. [2004]) observed simultaneously at four wavelengths (3.6 μm, 4.5 μm, 5.8 μm and 8 μm). The Multiband Imaging Photometer for Spitzer (MIPS; Rieke et al. [2004]) observed at 24 μm, 70 μm and 160 μm. The cryogenic lifetime of *Spitzer* was nearly six years, and parts of IRAC continued observing in a subsequent 'warm phase'.

The most extensive extragalactic data from *Spitzer* was at 24 μm, and many

[3]The discovery of emission bands from Polycyclic Aromatic Hydrocarbons (PAHs) is discussed in Section 1.5.

[4]In Chapter 4, I have compared and combined the ELAIS luminosity function with my *AKARI* 90 μm luminosity function.

papers have based their work on data at this wavelength (see, for example, Section 4.2.4). Although this is far below the infrared peak from re-emission by cold molecular clouds surrounding star forming galaxies (which peaks at $\sim$ 50 μm - 200 μm), it is near the peaks in the mid-infrared given by PAH features from molecular clouds (at least up to $z \sim 2$) although it may potentially be dominated by infrared radiation from Active Galactic Nuclei (AGNs). Observations at 24 μm also uncovered large numbers of dust obscured galaxies (DOGs; Dey et al. [2008]) at $1.5 < z < 2.5$.

The 70 μm data from *Spitzer* have been used to construct luminosity functions in the far infrared (see Section 4.2.4). Using the higher observed wavelength enables luminosity functions to be prepared which are not affected by PAH and silicate features and are less affected by AGNs, and also allows more accurate estimates to be made of total infrared luminosity (see Section 2.7).

The *Spitzer* Wide-area InfraRed Extragalactic legacy survey (SWIRE; Lonsdale et al. [2003]) was the largest legacy survey made by *Spitzer* and covered 49 deg^2 across six deep fields[5], using all seven *Spitzer* wavelength bands. *Spitzer* observations were also made in the ADF-S field at 24 μm and 70 μm (these are used in Chapter 5). *Spitzer* 70 μm sources were used for some of the targets for near-infrared spectroscopy in Chapter 6.

AKARI Space Telescope

The *AKARI Space Telescope* (Murakami et al. [2007]), developed by the Japan Aerospace Exploration Agency (JAXA) in cooperation with institutes in Europe and Korea, was launched in February 2006 and was a cryogenically-cooled mid/far-infrared 68.5 cm telescope in a low Earth, Sun-synchronous orbit. It performed an all-sky survey at six infrared wavelengths and a series of deep pointed surveys in two newly selected deep fields called the *AKARI* Deep Field South (ADF-S) and the North Ecliptic Pole field (*AKARI*-NEP) (Matsuhara et al. [2006]). The instruments on *AKARI* were the Far Infrared Surveyor (FIS; Kawada et al. [2007]) which observed in four bands centred on 65 μm, 90 μm, 140 μm and 160 μm, and the InfraRed Camera (IRC; Onaka et al. [2007]) which

[5]Extragalactic deep fields are discussed in Section 2.3 and the main ones listed in Table 2.1.

covered a range of near- to mid-infrared wavelengths from 3.2 μm - 24 μm.

The primary objective of *AKARI* was to make the all-sky survey, which included observations at longer wavelengths and at greater sensitivity than those by IRAS some 23 years earlier. Improvements in cryogenic techniques meant that the cold phase lasted for nearly 16 months, compared to 10 months for IRAS. The first versions of these catalogues, covering 98% of the sky in multiple scans, were published in March 2010 and were called the *AKARI*-FIS Bright Source Catalogue (BSC) with 427,071 sources (at 65 μm, 90 μm, 140 μm and 160 μm), and the *AKARI*-IRC Point Source Catalogue (PSC) with 870,973 sources (at 9 μm and 18 μm). Revised versions of the catalogues (together with a faint source catalogue) are expected over the coming five years.

In the *AKARI*-NEP deep field, a study of data from observed wavelengths of 2 μm - 24 μm analysed data out to $z \sim 2.2$ and found strong evidence for evolution of galaxy luminosities towards higher redshift (Goto et al. [2010]); also, the first galaxy source counts at 18 μm were calculated (Pearson et al. [2014]).

Preliminary versions of *AKARI* FIS and IRC pointed survey catalogues were used to select most of the targets for the AAOmega spectroscopy in the ADF-S described in Chapters 3 and 4. After the cryogen ran out in August 2007, a warm-phase of observations took place, and the work in Chapters 6 and 7 was based on a program which took place in this phase using the IRC-NIR spectrograph. The *AKARI*-BSC was used for the work on far-infrared(FIR)-luminous quasars in Chapter 8.

Wide-field Infrared Survey Explorer (WISE)

The Wide-field Infrared Survey Explorer (WISE; Wright et al. [2010]) is a NASA telescope which was launched in 2009 and over 10 months performed an all-sky survey in the mid-infrared with much higher sensitivity than previous missions. It had four bands centred on 3.4 μm, 4.6 μm, 12 μm and 22 μm.

In March 2012 an atlas and catalogue of the entire sky was published, containing 563,921,584 sources at SNR > 5 in at least one band. There is also a reject catalogue of 283,887,651 detections at SNR < 5 in all bands which may contain spurious detections. Many solar system objects, including tens of thousands of

asteroids and several nearby brown dwarfs, were discovered by WISE. Active galaxies, particularly luminous AGNs and HyLIRGs, were discovered by WISE and are being studied at other wavelengths. Fluxes from the WISE catalogue were included in the multi-wavelength data matched to the spectroscopic-redshift sources in Chapter 5.

Herschel Space Observatory

The *Herschel Space Observatory* (Pilbratt [2003]; Pilbratt et al. [2010]) was launched in May 2009 and produced wide-ranging and significant results in the far-infrared and submillimetre. Orbiting at the L2 point[6] in the Sun/Earth system about 1.5 million km from the Earth, with cryogenically cooled instruments, it had a much improved observing location, a larger telescope (3.5 m diameter) and wider far-infrared coverage (with bands centred on 70 μm up to 500 μm) than those of previous infrared space missions. The instruments included the Spectral and Photometric Imaging REceiver (SPIRE; Griffin et al. [2010]) which made observations at 250 μm, 350 μm and 500 μm, and the Photodetector Array Camera and Spectrometer (PACS; Poglitsch et al. [2010]) which observed at 70 μm, 100 μm and 160 μm.

The instrument design which became SPIRE was tested in 2006 before the launch of *Herschel* on the Balloon-borne Large Aperture Submillimetre Telescope (BLAST; Pascale et al. [2008]). BLAST operated at an altitude of 35 km, above most of the atmospheric water vapour that absorbs infrared radiation. Some of the targets for the spectroscopy in Chapter 3 were chosen from early versions of the BLAST catalogues.

[6]The Lagrangian point L2 is the orbit outside the Earth's orbit where the combined gravitational pull of the Sun and the Earth on the satellite equals the pull of the Sun on the Earth, so an orbit can be maintained which matches that of the Earth, so the Earth substantially shields the satellite from the Sun, enabling lower temperatures to be maintained for infrared observations. Also, an L2 orbit has fewer restrictions on observations, unlike a Sun-synchronous orbit in which disruptions are caused by Earth occultation and the South Atlantic Anomaly.

Table 1.1: Infrared space telescopes. Note that spectroscopic instruments are shown in Table 1.2. †COBE also carried microwave instruments. ††EUCLID's coverage will include the red end of the visible spectrum. *FIRSPEX is now named INSPIRE (see text). Note that the Hubble Space Telescope (not shown) had instruments covering the near-infrared. Orbital types: G=geocentric; H=heliocentric; SS=Sun-synchronous. The sensitivities shown are typical 5σ point source survey limits.

Name	Reference	Year of launch	Telescope diameter (m)	Orbit type	Average distance (km)	Orbital period	Instrument	Wavelengths (μm)	—Instrument details at indicative wavelength— Field of view (FOV) (arcmin^2)	Resolution FWHM PSF (arcsec)	Typical 5σ sensitivity (Jy)	at λ (μm)
IRAS	Neugebauer et al. [1984]	1983	0.57	G	900	100 mins		12, 25, 60, 100	7	216	4.3×10^{-1}	60
COBE†	Boggess et al. [1992]	1989	0.19	G	900	103 mins	DIRBE	1.25 to 240	1,800			
ISO	Kessler et al. [1996]	1995	0.60	G	35,000	24 hours	ISOCAM	2.5 to 17	7	1.5	10^{-4}	15
							ISOPHOT	2.5 to 240	7	34	10^{-2}	100
Spitzer	Werner et al. [2004]	2003	0.85	H		1 year	IRAC	3.6, 4.5, 5.8, 8	27	2	10^{-5}	8
							MIPS	24, 70, 160	29	6	10^{-4}	24
AKARI	Murakami et al. [2007]	2006	0.68	G (SS)	695	96.6 mins	IRC	2.4 to 24	91	3.4	10^{-4}	9
							FIS	65, 90, 140, 160	9.6 - 30.1	39	5.5×10^{-1}	90
WISE	Wright et al. [2010]	2009	0.40	G	525	95 mins		3.4, 4.6, 12, 22	2,209	6	10^{-3}	12
Herschel	Pilbratt [2003] Pilbratt et al. [2010]	2009	3.50	H (L2)	1.5×10^6	1 year	SPIRE	250, 350, 500	32	18	2×10^{-3}	250
							PACS	70, 100, 160	6.1	5	10^{-3}	100
Next planned missions:												
JWST	Gardner et al. [2006]	2018	6.5	H (L2)	1.5×10^6	1 year	NIRCam	0.6 to 5	4.8	0.05	10^{-8}	2
							MIRI	5 to 28	2.4	1	10^{-7}	10
EUCLID††	Laureijs et al. [2011]	2020	1.2	H (L2)	1.5×10^6	1 year		Y, J, H				
FIRSPEX*	Rigopoulou et al. [2015]	2029	0.85	G (SS)	600	1 year		63, 119, 158, 179, 205				
SPICA	Swinyard et al. [2009]	2029	2.5	H (L2)	1.5×10^6	1 year		17 to 210				

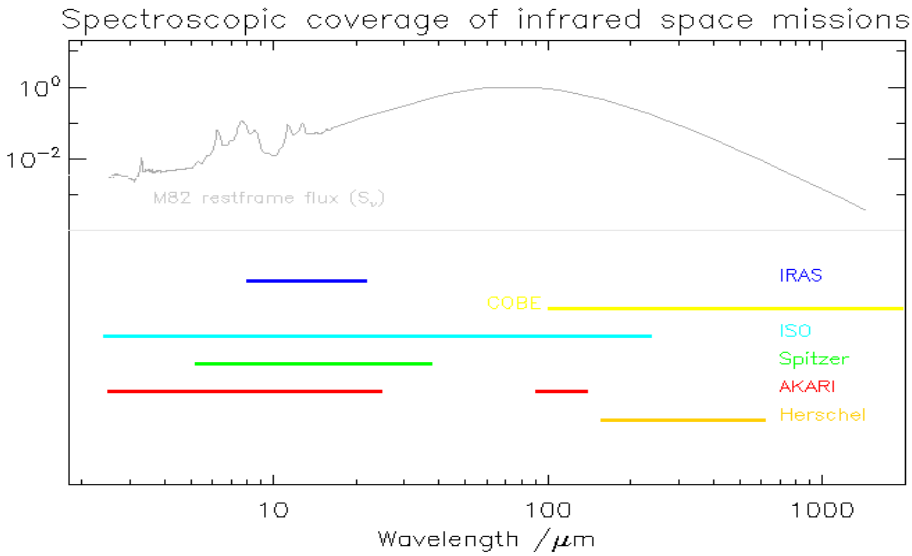

Figure 1.2: Spectroscopic coverage of infrared space missions in relation to the spectral energy distribution (SED) of a typical star forming galaxy (M82, restframe).

The extragalactic science objectives of *Herschel* included the investigation of galaxy evolution back to high redshifts, star formation and molecular chemistry. *Herschel* observations included four large extragalactic legacy projects. The largest open-time project was the Astrophysical Terahertz Large Area Survey (H-ATLAS; Eales et al. [2009]) covering 510 deg^2 in five photometric bands. Secondly, the *Herschel* Multi-tiered Extragalactic Survey (HerMES; Oliver et al. [2012]) is a legacy programme covering 41 well-studied deep fields (most recent data release DR2: Wang et al. [2014b]). Thirdly, the PACS Evolutionary Probe (PEP; Lutz et al. [2011]) undertook deeper extragalactic surveys in several well-established deep fields (see Table 2.1) at 70 μm, 100 μm and 160 μm. Fourthly, the GOODS-*Herschel* programme (Elbaz et al. [2011]) obtained deep PACS and SPIRE coverage of the two GOODS deep fields.

One important result from *Herschel* has been the discovery of a new, efficient method for identifying gravitational lenses using sources with bright 500 μm fluxes (Negrello et al. [2010]), and an extension of this method to select fainter lensed galaxies (HALOS; Gonzalez-Nuevo et al. [2012]). Methods of identifying gravitational lenses are discussed in Section 8.3.

Table 1.2: Spectroscopic instruments on the infrared space telescopes listed in Table 1.1. *FIRSPEX is now named INSPIRE (see text). The sensitivities shown are typical 5σ point source survey limits.

					——— Instrument details at indicative wavelength ———			
Name	Year of launch	Telescope diameter (m)	Spectroscopic instrument	Wavelengths (μm)	Type / FOV	Spectral resolution (R=$\lambda/\Delta\lambda$)	Typical 5σ sensitivity (Jy)	at λ (μm)
IRAS	1983	0.57	LRS	8 - 22	Slitless	14 to 35	0.43	60
COBE	1989	0.19	FIRAS	100 to 10,000	7° diameter	300		
ISO	1995	0.60	SWS LWS	2.4 to 45 43 to 196.8	0.08 - 0.19 arcmin^2 $\sim$40 arcsec radius	1000 to 2000 150 to 9700	10^{-3}	5
Spitzer	2003	0.85	IRS	5.2 to 38	11.3 - 168 arcsec (slit length)	64 to 600	10^{-3}	20
AKARI	2006	0.68	IRC FIS FTS	2.5 to 26 90 to 140	95 arcmin^2	10 to 500 200 to 450	2×10^{-3}	5
Herschel	2009	3.50	HIFI	157 to 625	10 - 40 arcsec (half power beam width)	10^6	2.5	300
			PACS SPIRE	55 to 210 194 to 671	0.6 arcmin^2 2 arcmin diameter	1000 to 5000 20 to 1000		
Next planned missions:								
JWST	2018	6.5	NIRSpec MIRI	0.6 to 5 5 to 29	12 arcmin^2	1000 to 2700 3000	10^{-8}	3
EUCLID	2020	1.2	NISP	1.1 to 2	Slitless	250		
FIRSPEX*	2021	1.0		63, 119, 158, 179, 205		10^6		
SPICA	2029	2.5	SAFARI SMI	35 to 200 12 to 37	100 arcmin^2			

Planck

The *Planck* space telescope (Planck-Collaboration [2011]) was primarily designed to measure the spatial and polarization anisotropies in the CMB to obtain accurate measurements of cosmological parameters. It observed in nine bands in the wavelength range 350 μm to 10000 μm. Many maps and catalogues have now been released (the most recent releases are summarised in Planck-Collaboration [2015]).

Future infrared space missions

The *James Webb Space Telescope* (JWST; Gardner et al. [2006]), due to launch in 2018, is a NASA / ESA mission which will orbit at L2, will have a large 6.5 m diameter mirror and will cover the wavelength range from 0.6 μm to 28.5 μm. It will have resolution and sensitivity unprecedented in previous space telescopes. It has many science goals not achievable with existing facilities, observing the first (Population III) stars in the epoch of reionization, high-redshift Balmer lines in the earliest galaxies, high-redshift PAHs, as well as observing protoplanetary systems and the atmospheres of exoplanets.

Euclid (Laureijs et al. [2011]) is led by ESA, and is due for launch in 2020. It primary objective will be to measure the dark energy equation of state using measurements of baryon acoustic oscillations, redshift-space distortions and weak gravitational lensing ellipticity distortion. It will also orbit at L2 and cover optical to near infrared wavelengths (currently planned to be from 5500 Å to 2 μm). Its spectrometry is planned to cover the wavelength range 1.1 μm - 2 μm.

The *SPace Infrared telescope for Cosmology and Astrophysics* (SPICA; Swinyard et al. [2009]) is a mission currently under consideration for the fifth medium-class mission (M5) in Cosmic Visions, also led by ESA (previously led by JAXA) with a prospective launch date of 2029 (not yet confirmed). It will also orbit at the L2 point and will have a mirror of 2.5 m diameter. Its wavelength range will be further into the far infrared than JWST, and is planned to cover 17 μm to 210 μm. Its imaging spectrometer SAFARI will be provided by ESA.

The Far-Infrared Spectroscopic Explorer (FIRSPEX; Rigopoulou et al. [2015]) was a proposed ESA / Chinese Academy of Sciences (CAS) small mission to

make an all-sky spectroscopic survey in five far-infrared bands. It is now under consideration for M5 under the new name INSPIRE.

Ground-based facilities: near-infrared

Radiation in the near-infrared can be detected at a few wavebands from the ground, and many optical telescopes can be used for observations in these bands. A key all-sky survey in the J (1.25 μm), H (1.65 μm) and K_S (2.17 μm) bands was the Two Micron All Sky Survey (2MASS; Skrutskie et al. [2006]) which was published in its final form in 2003. This survey used observations at the Mt. Hopkins, Arizona observatory for the northern hemisphere, and at the Cerro Tololo Inter-American Observatory (CTIO) in Chile for the southern hemisphere. The point source catalogue contains ∼300 million stars and other objects, and the extended source catalogue contains positions and magnitudes for over 1 million galaxies and other nebulae. The Hawaii-based United Kingdom Infrared Telescope (UKIRT) Infrared Deep Sky Survey (UKIDSS; Lawrence et al. [2007]) covered the Y (1.03 μm), J, H and K (2.20 μm) bands for 7500 deg^2 in the northern hemisphere; its extragalactic component covered about 35 deg^2. The Visible and Infrared Survey Telescope for Astronomy (VISTA) Hemisphere Survey (VHS) covered the southern sky in the $YJHK_S$ bands, with deeper surveys over smaller areas. Data from VISTA were used in Chapter 5.

Ground-based facilities: far-infrared and submillimetre

Radiation at certain bands in the far infrared can also penetrate the atmosphere, in particular at around 450 μm and 850 μm. When observed from the ground, these regions are usually referred to as submillimetre wavelengths. The Submillimetre Common-User Bolometer Array (SCUBA; Holland et al. [1998]) on the James Clerk Maxwell Telescope (JCMT) in Hawaii has played a key role in investigating star formation, including the discovery of a previously unsuspected population of submillimetre galaxies (see Section 1.6 below). The SCUBA HAlf Degree Extragalactic Survey (SHADES; Mortier et al. [2005]) surveyed high-redshift submillimetre sources, clusters and AGN in the SXDF and Lockman Hole East deep fields. The SCUBA Local Universe Galaxy Survey (SLUGS; Dunne

et al. [2000]) surveyed the submillimetre properties of the local Universe.

SCUBA-2 (Holland et al. [2013]) has now replaced the previous SCUBA instrument and started observing in 2011. With a 10,000 pixel bolometer camera, compared to only 128 pixels on SCUBA, it has a significantly faster mapping speed. This, together with other technological improvements, means that SCUBA-2 can undertake wide-field surveys to unprecedented depths. The SCUBA-2 All-Sky Survey (SASSy) has recently completed a map of part of the northern sky at 850 μm. Other submillimetre instruments include AzTEC (Wilson et al. [2008]) (used on more than one telescope; sources from observations on ASTE were used in Chapter 3), LABOCA (Siringo et al. [2009]) on APEX, SHARC-2 and MAMBO on Institut de Radioastronomie Millimétrique (IRAM) radio telescope in the Spanish Sierra Nevada (see Table 1.3). The targets for my work in Chapters 6 and 7 were mostly chosen from submillimetre sources.

The Atacama Large Millimetre/submillimetre Array (ALMA) is an interferometer of 66 radio telescopes and a wavelength range which potentially extends down to 350 μm. Situated at an altitude of 5000 metres, it was completed in 2014 and has recently started observations. ALMA has a much higher resolution, and greater sensitivity, than previous interferometers. The South Pole Telescope (SPT) is a 10 m diameter telescope which can operate down to 220 μm. It has recently detected lensed dusty galaxies at high redshifts in a survey covering an area of 1300 deg^2 (Vieira et al. [2013]). The next generation of ground-based telescopes with infrared coverage will include the Cerro Chajnantor Atacama Telescope (CCAT), a 25 m telescope for observing from 350 μm to 2100 μm (due to start construction shortly). The Large Millimeter Telescope (LMT) in Mexico is the world's largest steerable single-dish millimetre telescope, covering the wavelength range 850 μm to 4 mm, and has just started observations.

Airborne infrared observatory

The Stratospheric Observatory For Infrared Astronomy (SOFIA; Young et al. [2012]) is an airborne observatory in a modified Boeing with a 2.7 m telescope. It flies at an altitude of 13.7 km, which is above 99.8% of the atmospheric water vapour. It can observe in the wavelength range 0.3 μm to 1800 μm. Although

Table 1.3: The main ground-based submillimetre facilities which have been used to study star-forming galaxies.

Instrument	Telescope	Dates	Wavelengths (μm)	Beam size (arcsec)	Field of view (arcmin^2)	Pixels (no.)	Reference
UKT14	UKIRT JCMT	1986-88 1988-96	350 - 2000	19 - 27	0.1	1	Duncan et al. [1990]
SCUBA	JCMT	1997-2005	450, 850	7, 15	5	91, 37	Holland et al. [1998]
MAMBO	IRAM	1998-2011	1200	11	4	117	Kreysa et al. [1999]
SHARC-II	CSO	2002-13	350	9	2.3	384	Dowell et al. [2003]
BOLOCAM	CSO	2002-13	1100	30	8	151	Laurent et al. [2005]
AzTEC	JCMT ASTE LMT	2005-6 2007-8 2011-	1100	19 29 9	20	144	Wilson et al. [2008]
LABOCA	APEX	2006-	870	19	100	313	Siringo et al. [2009]
SCUBA-2	JCMT	2011-	450, 850	7, 14	43	10240	Holland et al. [2013]

first launched in 2010, its official operational phase began in 2014. Its lifetime is estimated at 20 years.

1.3 Discovery of the cosmic infrared background

The existence of the cosmic infrared background (CIB) was discovered by COBE (Puget et al. [1996]; Hauser et al. [1998]) which found significant and isotropic radiation at all infrared wavelengths observed after removing emission expected from models of sources such as interplanetary and interstellar dust. In a review of infrared astronomy shortly after its discovery, Hauser and Dwek [2001] said that although the total CIB was still very uncertain, it was already clear that the dominant energy source was from thermonuclear fusion reactions - i.e. the energy was generated by star-formation rather than by the release of gravitational potential energy via accretion onto black holes in galaxies with Active Galactic Nuclei (AGNs). Their conclusion was based on observational studies of the relation between AGNs, hard X-ray, and submillimetre sources, by theoretical models for the infrared contributions from the sources of the hard cosmic X-ray background, and from a global energetic argument based on the abundance of black holes.

Data from later surveys, in particular from *Spitzer* (launched 2003, see Section

1.2), led to a detailed estimate of the extent of this energy (Dole et al. [2006]): by integrating the extragalactic background spectral energy distribution (SED), they showed that the CIB has the same brightness as the Cosmic Optical Background (COB), implying that approximately half the energy emitted since the big bang by all the objects in the Universe has been absorbed by dust and then re-radiated between 8 μm and 1000 μm (see Figure 1.3).

In the local universe, the infrared output of galaxies is only about one-third their output at optical wavelengths (e.g. Soifer and Neugebauer [1991]) which means that the infrared output of galaxies was much higher in the past. As redshift increases, the observed peak for high redshift galaxies will extend toward the submillimetre (and galaxies discovered in the submillimetre have been shown to be at high redshifts, as discussed in Section 1.6 below). A recent study by Schmidt et al. [2015] found that the CIB peaked at $z \sim 1.2$. With *Spitzer*-MIPS 24 μm-selected sources, Pascale et al. [2009] used stacking analysis[7] on both SWIRE 70 μm and BLAST submillimetre maps to show that most of the 70 μm background is generated by sources at redshifts $z < 1.1$, whereas most of the 500 μm background is from sources at $z > 1.1$. They also confirmed that the star formation rate estimated from the far infrared (i.e. from energy re-radiated by dust) is about three times higher than the star formation rate estimated from (non-dust-obscured) optical-UV radiation in the redshift range $0.1 < z < 1.0$. By stacking UV/optical-selected sources onto maps from *Spitzer*, *Herschel* and AzTEC at wavelengths ranging from 24 μm to 1100 μm, a recent HerMES study by Viero et al. [2013] found that at wavelengths below $\sim$200 μm, the CIB is mostly from galaxies at $z \lesssim 1$ while at wavelengths above $\sim$200 μm, most of the CIB comes from galaxies at $1 \lesssim z \lesssim 2$.

1.4 Discovery of luminous infrared galaxies

A number of infrared-luminous galaxies had been discovered prior to IRAS, using ground-based telescopes and observing in the wavelength range 2.5 μm - 25 μm (e.g. Kleinmann and Low [1970]; Rieke and Low [1972]). Early studies suggested that the shape of the infrared continuum of these sources was best explained as

[7]Stacking is discussed in Section 6.3.2.

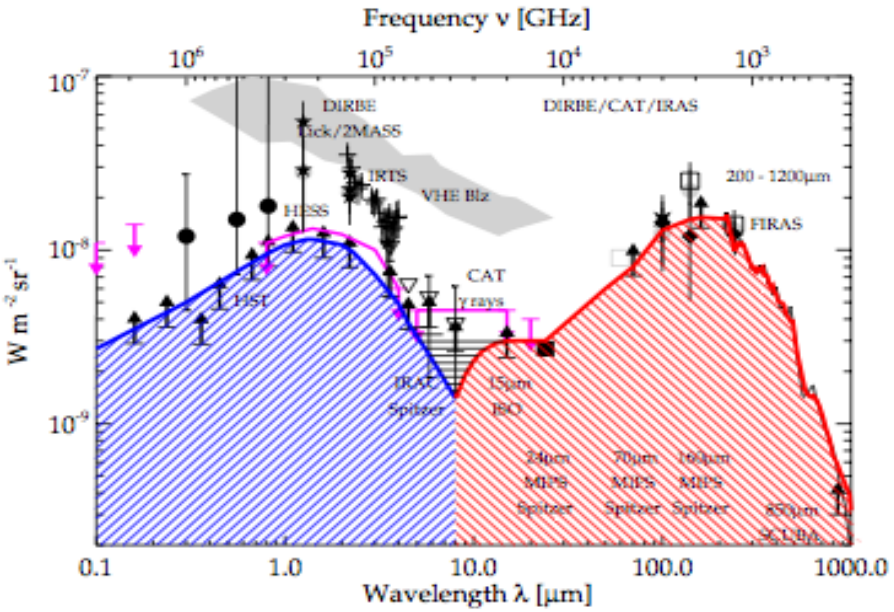

Figure 1.3: Extragalactic background radiation in optical to sub-millimetre regions of the spectrum. An iconic figure taken from Dole et al. [2006].

thermal emission from dust, rather than synchrotron radiation (e.g. Neugebauer et al. [1976]).

However, most infrared radiation is absorbed by water vapour and carbon dioxide in the atmosphere, and the atmosphere itself radiates strongly in the infrared, peaking at around 10 μm. It was the results from IRAS that established Luminous Infrared Galaxies (LIRGs; $L_{IR} > 10^{11} L_{\odot}$, with the wavelength range 8 μm$< \lambda <$1000 μm) as an important new class of object, whose energy output was primarily in the infrared region of the spectrum and could rival that of quasars, until then the only highly energetic objects known. Brighter infrared galaxies, Ultra-Luminous Infrared Galaxies (ULIRGs; $L_{IR} > 10^{12} L_{\odot}$ were also found by IRAS, and even some Hyper-luminous Infrared Galaxies (HyLIRGs; $L_{IR} > 10^{13} L_{\odot}$), defined in Rowan-Robinson [2000], at which time only 39 were known. Most of the emission from these galaxies is caused by highly luminous bursts of star formation[8] (e.g. Helou [1986]; see review in Sanders and Mirabel

[8]The methods by which star formation can be distinguished from AGNs are discussed in Section 3.2.2.

[1996]). This energy, mostly from young massive stars, is absorbed by the gas and dust surrounding these starbursts and re-emitted in the infrared. The star formation rates can be several hundred (sometimes over a thousand) solar masses per year (in contrast, the Milky Way forms only 1−2 solar masses per year). These objects often also have active accretion onto their central black holes, and the relative contributions of star formation and AGN accretion to the energy outputs of these galaxies are discussed below in Section 2.5 and are also covered in the science chapters below.

In the local universe ($z \lesssim 0.2$), ULIRGs are relatively rare: less than 4% of the galaxies in the IRAS Revised Bright Galaxy Sample (RBGS; Sanders et al. [2003]) are ULIRGs, and many of these objects are the result of major mergers (see Section 2.4 below). Efstathiou et al. [2014], using *Herschel* data with SED fitting of a radiative transfer model, found that the AGN of our closest HyLIRG (IRAS 08572+3915, at $z = 0.06$) contributed ∼90% of its total luminosity. On the other hand, using *Herschel* observations of the far-infrared fine-structure lines of 25 ULIRGs at $z < 0.27$, Farrah et al. [2013] found that these lines arise from gas heated predominantly by starlight and not by AGNs. Elbaz et al. [2011] in a large sample of star-forming galaxies in the GOODS-*Herschel* program confirmed that local ($z < 0.25$) LIRGs and ULIRGs are generally in starburst mode, lying above the galaxy main sequence and with suppressed PAH emission features.

ULIRGs are much more common at higher redshifts ($z > 0.5$) where they are apparently not the result of mergers but the result of more normal (secular) star-forming processes (e.g. Elbaz et al. [2011]). Rigopoulou et al. [2014] in a *Herschel*-SPIRE study of [CII] emission lines, found that ULIRGs at $z \sim 0.5$ were similar to local normal galaxies in their $L_{[CII]}/L_{IR}$ ratio. Caputi et al. [2007] found that ∼90% of the total infrared luminosity density associated with star formation at $z \sim 2$ came from LIRGs and ULIRGs.

When dust obscuration is extreme, galaxies which are observed in the infrared are sometimes termed Dust-Obscured Galaxies (DOGs[9]), the definition often used being a ratio between mid-infrared 24 μm flux and R-band flux: $S_{24}/S_{0.65} > 1000$ (Dey et al. [2008]).

[9]Many other acronyms which are used for star-forming galaxies (e.g. DSFG for dusty star-forming galaxies) are listed in Casey et al. [2014].

In this thesis, over 20 ULIRGs and HyLIRGs were found in the ADF-S in high-redshift sources ($z \gtrsim 0.4$) in Chapter 3 (see Table 3.5), and 8 were found by SED fitting in Chapter 5 (Table 5.5). The two radio galaxies and one of the submillimetre galaxies investigated in Chapter 7 at $z > 3.5$ were HyLIRGs and one of the submillimetre galaxies was a ULIRG.

1.5 Discovery of PAHs

Another unexpected result from infrared astronomy has been the discovery of a series of emission bands in the mid-infrared, which occur together in many galaxies, including galaxies showing strong evidence of star formation. The first discoveries of these bands were made before infrared space telescopes (Gillett et al. [1973]; Russell et al. [1975]). The ISO and *Spitzer* confirmed the original discoveries and greatly expanded the number of emission bands and features observed in this wavelength region (e.g. Genzel and Cesarsky [2000]). It was realised that a species of benzene-ring carbonaceous molecules referred to as polycyclic aromatic hydrocarbons (PAHs) could be sufficiently long-lived to account for these emission bands. PAHs are known from deposits of fossil fuels on earth, and it now appears that they also formed in the early universe.

The previously unexpected emission bands now attributed to PAHs are at 3.3 μm, 6.2 μm, 7.7 μm, 8.6 μm, 11.3 μm and 12.7 μm, in addition to a large number of weaker bands (see Figures 1.4 and 3.8). Their identification as PAHs was by Duley and Williams [1981], Leger and Puget [1984] and Allamandola et al. [1985]. They are now thought to play a significant role in the energy budget of the interstellar medium (ISM). They are excited by UV emission from young stars, absorbing UV photons and then emitting in the infrared via relaxation in their vibrational modes. The emission bands (of which the 7.7 μm emission line is the strongest) can dominate luminosity in this region of the spectrum. Since they are usually destroyed by strong emission from AGNs, they can provide an important diagnostic in distinguishing between AGNs and star-forming galaxies (discussed in Section 3.2.2). Murata et al. [2014] using a sample of 1868 galaxies (excluding those with dominant AGNs) in the *AKARI*-NEP deep survey showed

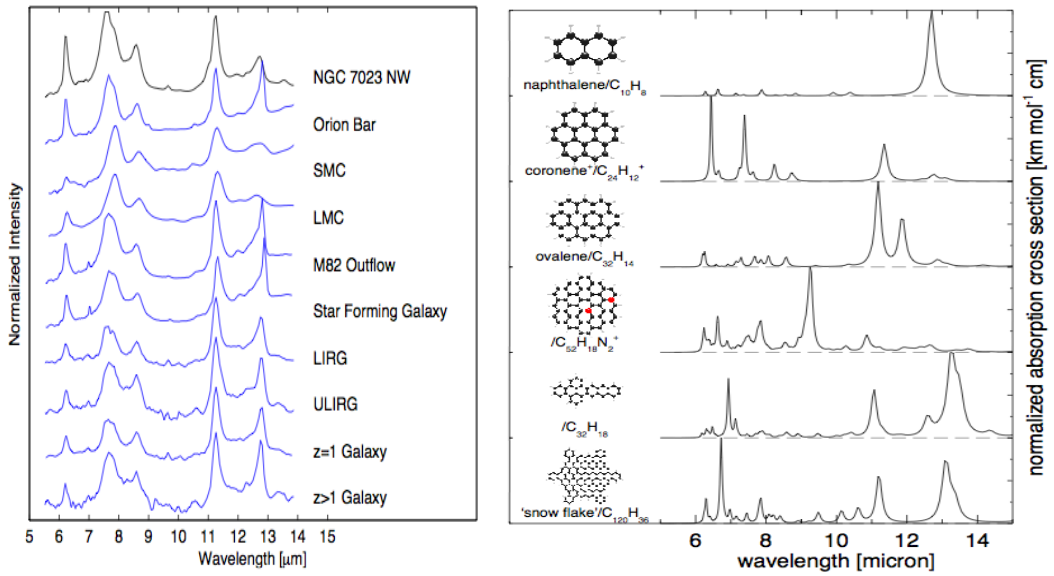

Figure 1.4: PAH emission lines in the mid-infrared: (left) observed spectra from a range of galaxy types and (right) computed vibrational lines for a selection of PAHs. Both figures from Rosenberg et al. [2014].

that starburst galaxies have less PAH emission than main-sequence[10] star-forming galaxies, suggesting that intense radiation from starbursts (like that of AGNs) can also destroy PAHs.

Surprisingly, although the existence of PAHs in space is now generally accepted, no single PAH has yet been successfully identified. A recent study by Rosenberg et al. [2014] suggests a large number of individual PAH types contribute to the observed emission bands (see Figure 1.4), which may be why individual molecules have not yet been identified. To date, fullerenes (mainly C_{60}) are the only large aromatic chemicals unambiguously identified in space (Bernard-Salas et al. [2013]). The use of PAH bands as star formation indicators is discussed in Sections 2.7 and 3.2.2.

[10]The main sequence for galaxies is discussed in Section 2.6.

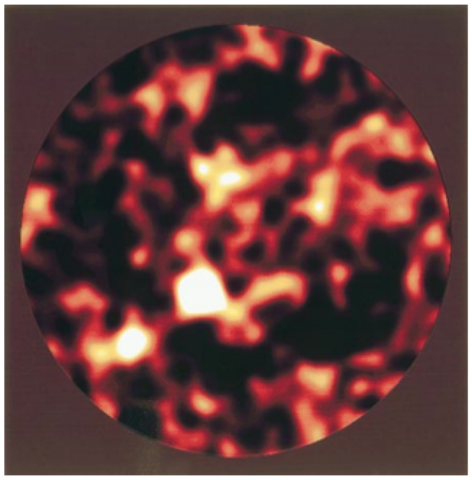

Figure 1.5: One of the original discoveries of the submillimetre population at 850 μm with SCUBA in the HDF. The image radius is 100″. The five most significant sources are shown in white, including the strongest source (HDF850.1). The figure is taken from Hughes et al. [1998].

1.6 Discovery of the submillimetre population

Two submillimetre wavelength windows which can be observed from the ground are bands around 450 μm and 850 μm. Hughes et al. [1998] identified five galaxies with SCUBA on the James Clerk Maxwell Telescope (JCMT) in the Hubble Deep Field (see Figure 1.5), and also showed statistically that the confusion limited background contained further discrete sources. Smail et al. [1997] used two large lensing clusters to amplify fluxes from sources at 450 μm and 850 μm, also using SCUBA, and concluded that the majority of such sources lies at high redshift, $z > 1$. Barger et al. [1998], using SCUBA data in the Lockman Hole and SSA13 fields, identified two submillimetre galaxies at 850 μm.

The discovery of this population of submillimetre sources was not widely expected; prior to the discovery of downsizing[11] in the mid-1990s, galaxy evolution models had not predicted such sources. Part of the explanation is an effect that

[11]Downsizing is discussed in Section 2.4.

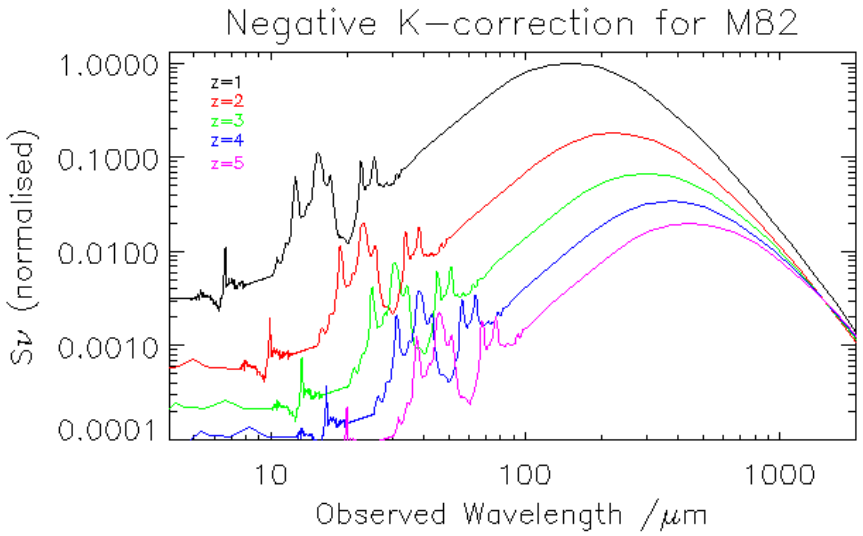

Figure 1.6: Example of the M82 spectral energy distribution (SED) at various redshifts showing that the 'negative K-correction' - the wavelength shift of the Rayleigh-Jeans tail of the SED - more-or-less offsets the flux decrease due to distance at higher redshifts in the submillimetre region.

had been predicted by Blain and Longair [1993]: at sufficiently high redshifts, the peak radiation (and Rayleigh-Jeans tail) of the thermal distribution from starburst activity is shifted from the far infrared into the submillimetre region (or as it is usually put, a strong negative K-correction offsets the diminution with distance). In fact, this effect gives an almost constant flux density across redshifts $z > 1$ for observations at submillimetre wavelengths (see Figure 1.6).

Chapman et al. [2005] took a sample of 73 submillimetre galaxies at 850 μm and found a median redshift of $z \sim 2.2$ and an inter-quartile range of $z = 1.7-2.8$. This paper found similar results for both AGNs and starburst galaxies (SBGs). The median redshift of $z = 2.2$ equates to a median rest-frame wavelength around 250 μm, somewhat above the expected peak for emission by dust heated by star-forming galaxies. Other studies have shown that $\sim 80\%$ of submillimetre galaxies are SBGs, and that the radiation in the other 20% with AGNs also have significant starburst activity (Coppin et al. [2011] and references therein).

These high-luminosity submillimetre galaxies are not only undergoing massive starbursts at high redshifts, but many are probably also quasars (I have found

evidence of this in some of the sources studied in Chapter 7). Some may be progenitors of present-day massive ellipticals, but their evolutionary links are still not proven. To date, we have not been able to identify optical counterparts for most submillimetre sources because of the low angular resolution of most submillimetre facilities, and even identification by radio interferometry[12] has proved difficult. However, the strongest HDF source (HDF850.1; Figure 1.5) has recently been identified at 5.8 μm and 8 μm with reanalysed *Spitzer* data (Serjeant and Marchetti [2014]), and it has been found to be at $z \approx 5.2$ (Walter et al. [2012]) from two CO lines observed in the 3 mm band by IRAM. A submillimetre galaxy at $z = 4$ was recently found to have PAH and near-infrared continuum emission using the *Spitzer* spectrograph (Riechers et al. [2014]).

The first results from ALMA (a radio interferometer with 66 antennae spread over 18.5 km at an altitude of 5 km) are beginning to improve radio identification of submillimetre sources. In a sample of 99 submillimetre sources, Swinbank et al. [2014] used ALMA to find precise coordinates to identify submillimetre galaxies in *Herschel*-SPIRE, giving redshifts of $2.1 < z < 4.0$, star formation rates of 300 ± 30 $M_\odot$ yr^{-1}, and a characteristic dust temperature of 32 ± 1 K. Wiklind et al. [2014] have made secure identifications of ten submillimetre sources using high angular resolution observations at 870 μm with ALMA, enabling multi-wavelength identifications and finding a redshift range of $1.65 < z < 4.76$ with extremely high star formation rates. Three were mergers; seven (unlike local ULIRGs) were isolated sources and contained a surprisingly old population of stars with high metallicities. Another ALMA study, by Hodge et al. [2013], of 126 submillimetre sources from the LABOCA ECDFS Submillimetre Survey (LESS) found that at least 35%, and possibly up to 50%, of these sources could be resolved into multiple submillimetre galaxies. Simpson et al. [2015] found that ALMA imaging of 52 submillimetre SCUBA-2-selected galaxies showed that starbursts were occurring in regions about four times smaller than the restframe optical sizes of the galaxies. Compact starbursts at $z \gtrsim 3$ were also found by Ikarashi et al. [2015]. Chen et al. [2015] found the morphology of most of a

[12]By using an array of telescopes acting together, radio interferometry can achieve significant improvement in angular resolution, which is inversely proportional to the effective diameter of the telescope (array): θ=1.22λ/D.

sample of 48 submillimetre galaxies at $z = 2 - 3$ suggested they were major mergers.

A few of the targets in Chapters 3 and 4, and most of the targets in Chapters 6 and 7 were selected from submillimetre galaxy catalogues.

1.7 An overview of the thesis

This thesis presents the results of a number of studies to determine the spectroscopic redshifts and investigate the physical properties causing the infrared luminosity of extragalactic sources selected from mid- and far-infrared and submillimetre observations, such as star formation rates, the interaction between AGNs and star formation, dust extinction and cosmological evolution. As explained earlier in this chapter, this means that the sources have been detected through the re-emission of their UV/optical radiation by dust clouds surrounding them, and they will generally be star-forming galaxies. The next chapter (Chapter 2) will outline the current state of our knowledge of the evolution of star-forming galaxies. It will focus on the many outstanding questions in this field, which form the background to the original work presented in the following six chapters.

AKARI Deep Field South (ADF-S)

AKARI's newly-selected deep field ADF-S provides an opportunity to investigate the evolution of star-forming galaxies and their interaction with AGNs in a relatively cirrus-free area of the sky, with initial observations provided by the *AKARI* far-infrared observations. As a step in the multi-wavelength exploitation of this field, spectroscopic observations were taken over four nights with AAOmega (the fibre-optic spectrograph at the Anglo Australian Telescope) for sources selected mainly from *AKARI's* observations. Chapter 3 presents the results of this optical spectroscopic campaign. Redshifts were identified for over 400 galaxies. I have used these redshifts to examine properties of these galaxies from the spectroscopic data, finding that most sources are (as expected) star-forming galaxies and show relatively low dust extinction. The proportion of these sources

whose infrared emission is found to be dominated by AGNs is consistent with that found in earlier studies.

In Chapter 4, a subset of these spectroscopic-redshift galaxies is used to prepare a new 90 μm luminosity function for sources at $z < 0.25$. This contributes to a previously fairly light amount of work near this wavelength, which is close to the SED peak for star-forming galaxies, and provides a relatively local benchmark for further studies. The result has confirmed an earlier ISO result in a different field, and is shown to be consistent with a recent backward-evolution model (Gruppioni et al. [2011])[13]. Luminosity functions provide key observational data in the development of theoretical models.

Fitting theoretical SEDs to multi-wavelength photometric flux measurements is another technique which can be used to explore the properties of galaxies. In Chapter 5, I have cross-matched the 400 spectroscopic-redshift sources to the multi-wavelength data now available in the ADF-S, and have fitted the resulting photometric points to a suite of star-forming model templates. I found good fits for ~ 150 sources with these starburst templates, of which 88 were good fits across the whole range of data available. Various properties could then be identified, which broadly confirmed the results found from the spectroscopic analysis.

The *AKARI*-FUHYU project

The objective of the *AKARI*-FUHYU project was to provide photometric and spectroscopic infrared observations of well-known extragalactic sources, most of which had not previously been observed in this region of the spectrum; most were submillimetre galaxies. I worked on the spectroscopic phase of this project, which involved near-infrared (2.5 μm to 5.0 μm) observations using *AKARI*'s own spectrograph which took place in the final (warm) phase of the mission.

Chapter 6 outlines the project and general results, which were disappointing; of the 72 sources targeted, reliable emission line identifications were achieved in only about half a dozen cases. The main reasons were the poor quality of the spectra obtained by the (warm-phase) observations and dust obscuration of the high-redshift sources. Six tentative Hα emission line detections were obtained

[13]Theoretical models of galaxy evolution, such as backward-evolution models, are discussed in Section 2.8.

Table 1.4: Data sources for the six science chapters.

Chapter	Sources selected	New data analysed	Matched catalogues
Chapter 3	*AKARI* FIS, IRC; various submm	AAOmega spectroscopy	-
Chapter 4	*AKARI* FIS	AAOmega spectroscopy	-
Chapter 5	*AKARI* FIS, IRC; BLAST; AzTEC	AAOmega spectroscopy	Various multi-wavelength catalogues
Chapter 6	Various submm; *Spitzer* 70 μm	*AKARI*-IRC spectroscopy	-
Chapter 7	Various submm	*AKARI*-IRC spectroscopy	-
Chapter 8	Various QSO catalogues	WHT-ISIS spectroscopy	*AKARI* BSC

from the 43 submillimetre galaxies observed; when these are stacked, the resulting emission line has a signal-to-noise ratio of 6.5. I also made tentative detections of Pa-α lines for one submillimetre source and one 70 μm -selected source.

The most significant result from this project is described in Chapter 7. Two radio galaxies at known redshifts of $z > 3.5$ (see Figure 7.1) and associated star-forming galaxies were identified from their Hα emission lines - the highest-redshift star-forming galaxies yet identified in this manner. The radio galaxies are shown to be quasars, and both these and the two associated submillimetre galaxies are forming stars at $> 10^3$ $M_\odot$ per year. The detection of Hα emission lines from two of the nearby submillimetre galaxies confirmed their association with the quasar by providing a first identification of their redshifts. The location showed that one of the radio galaxies was one of a binary quasar pair, providing support to the recent evidence (Kayo and Oguri [2012]) that models under-predict binary AGN/quasars at high redshift. The results also demonstrated that the significant decrease in dust obscuration of Hα in ULIRGs continues out to $z > 3.5$.

The *AKARI* all-sky catalogue: quasars with excess FIR luminosity

Finding and observing gravitational lenses has become a key area for research recently (Negrello et al. [2010]; Gonzalez-Nuevo et al. [2012]; Ishigaki et al. [2015]), enabling more distant sources to be seen in more detail, and providing information about the dark matter halos of the lensing object. Possible new ways of finding lenses are therefore of considerable interest.

Chapter 8 describes an ongoing project to identify gravitationally lensed quasars at high redshift using their excess far-infrared (FIR) luminosity. A cor-

relation between optical and far-infrared luminosity for quasars, which flattens at high luminosity, was confirmed by the work in this chapter. About 20 known quasars were identified in the *AKARI* all-sky far-infrared bright source catalogue, with those at $z > 1$ all showing far-infrared luminosity above that predicted by the correlation, suggesting magnification bias caused by a gravitational lens. Initial follow-up spectroscopy with the ISIS spectrograph on the William Herschel Telescope of seven of these high-redshift sources confirmed that three of these sources were high-redshift quasars.

Chapter 2

Introduction to star-forming galaxies

This chapter outlines our present knowledge of the evolution of star formation in galaxies, and covers a number of key topics which are areas of active research and form the background to the work in this thesis.

2.1 Introduction

Most galaxies, apart from ellipticals[14], are undergoing star formation to a certain extent. A typical spiral galaxy (such as the Milky Way) may be forming stars (mostly in its spiral arms) at a rate as low as one or two solar masses per year, although rates of tens to hundreds $M_\odot$ yr^{-1} are common. In extreme cases, where the star formation rate (SFR) can exceed 1000 $M_\odot$ yr^{-1}, they are called starburst galaxies, although this term is sometimes used more loosely to refer to any galaxy with significant star formation. Chapter 3 has sources with star formation rates from 0.1 $M_\odot yr^{-1}$ to 100 $M_\odot$ yr^{-1} for local galaxies, and over 1000 $M_\odot$ yr^{-1} for several galaxies at redshift $z > 1$. Chapter 7 investigates sources with star formation rates of up to $\sim$ 4000 $M_\odot$ yr^{-1} in high-redshift galaxies. A recent study using SCUBA-2 data found galaxies with SFRs as high as $\sim$ 6000 $M_\odot$ yr^{-1}, but detected a downturn in the SFR distribution function above 2000 $M_\odot$ yr^{-1} (Barger et al. [2014]). The most extreme starbursts are thought to be triggered by mergers between gas-rich galaxies.

To study star-forming galaxies, far-infrared sources are often selected, since this is where the re-emission by dust and gas of the radiation from star formation peaks. This is what has been done in Chapters 3, 4, 5 and 8. For very high redshift sources, selection is made further into the submillimetre region (as in Chapters 6 and 7). Selection in the optical region is sometimes made using

[14]A minority of elliptical galaxies has a low level of star formation.

emission lines such as Hα or using formulae based on relative UV or optical fluxes (e.g. a formula using the B, z and K photometric bands, so-called BzK galaxies). One of the great advantages of studying star formation in the far infrared is that extinction is far lower than it is in UV/optical astronomy, for which the estimation of SFRs needs to be adjusted by estimated extinction. Some star-forming galaxies detected in the far-infrared and submillimetre are not detected at all at UV/optical wavelengths due to extinction.

In this chapter, I will first describe some representative star-forming galaxies (Section 2.2) the SEDs of which are often used (and are used in this thesis) in calculating K-corrections and in extrapolating from measurements of luminosity at individual wavelengths to total luminosity. I will then outline the use of deep fields in extragalactic observations (Section 2.3). Our current understanding of the history of star formation is described in some detail in Section 2.4 and the observational evidence for the interaction between star formation and AGNs, still poorly understood, is described in Section 2.5. The recently developed idea of a galaxy main sequence is discussed in Section 2.6. A description of some of the observed correlations found from studies of distant star formation is given in Section 2.7. A very brief overview of current theoretical models describing star formation is given in Section 2.8, and finally a list of the cosmological assumptions used in this thesis is in Section 2.9.

2.2 Representative star-forming galaxies

Several galaxies have been taken to be typical star-forming galaxies, and their normalised spectral energy distributions (SEDs) are often used in K-corrections[15] and to predict properties of other star-forming galaxies such as total FIR luminosity from measurements of luminosities at individual wavelengths (see Section 2.7).

A nearby galaxy which is often used is M82 (see Figure 2.1, left), which is about 3.5 Mpc from the Milky Way. M82 is about five times more luminous than the Milky Way and is forming stars at a rate of $\sim$10 $M_\odot$ per year (e.g. Rieke

[15]When the flux of a source is measured at one wavelength, and we need to estimate the source's flux at a different wavelength (e.g. to bring a selection of sources to a common wavelength for analysis, or to find the source's flux at its restframe wavelength) the resulting correction is called a K-correction.

Figure 2.1: Images of the star-forming galaxies whose SEDs have been used as standards in calibations in this thesis. From left: M82 (source: HST, NASA); Arp 220 (NICMOS, HST); and the 'Cosmic Eyelash' MACSJ2135-0102 (HST image; white contours are 870 μm emission from LABOCA; red lines denote the lensed galaxy at $z = 2.326$ from a best-fit lens model (source: Swinbank et al. [2010])). Approximate diameters are 11, 1.5 and 3 kpc respectively.

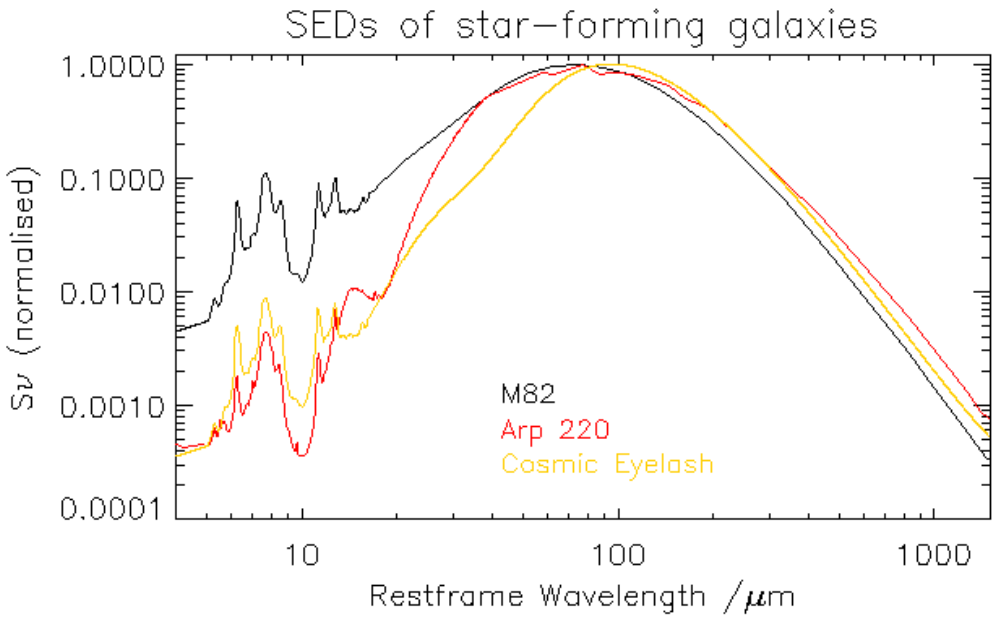

Figure 2.2: Comparative infrared SEDs of M82 (black), Arp 220 (red) and the Cosmic Eyelash SMMJ2135-0102 (orange).

et al. [1980]; Rieke et al. [1993]; Mayya et al. [2006]). The M82 SED is used in the estimation of total infrared luminosities and thereby star formation rates in Chapter 3 and for K-corrections in Chapter 4.

Arp 220 (Soifer et al. [1984]) (Figure 2.1, centre) is a starburst galaxy with a much higher star formation rate, $\sim$400 $M_\odot$ per year, and is our closest ULIRG (at about 77 Mpc). It is believed to be in the late stages of a merger between two large galaxies[16] and has been extensively studied (e.g. Solomon et al. [1990]; Scoville et al. [1998]; Spoon et al. [2004]; Wilson et al. [2006]).

A more distant, lensed, star forming galaxy is SMMJ2135-0102 (the 'Cosmic Eyelash'; Figure 2.1, right) at $z = 2.326$ (Swinbank et al. [2010]). The star formation rate is estimated to be $\sim$210 $M_\odot$ per year. The SED of this galaxy was used in estimating far-infrared luminosity in Chapters 6 and 7, since it was considered more likely to be similar to the objects found at high redshifts in those chapters. Figure 2.2 compares the SEDs for these three galaxies.

Other examples of starburst galaxies which are often used include the interacting NGC4038/NGC4039 (the 'Antennae' galaxies, currently merging and undergoing starbursts), NGC 253 (the 'Sculptor' galaxy, currently undergoing a starburst), NGC 4631 (the 'Whale' galaxy, an edge-on spiral with a central starburst), NGC 4666, NGC 3256, NGC 1808, the Circinus galaxy (one of the closest star-forming galaxies to the Milky Way), Centaurus A (a starburst galaxy which is one of the closest radio galaxies to the Milky Way), M77 and UGC 1505.

Very high rates of star formation (hundreds of solar masses per year) cannot be sustained for long (there is not enough gas and dust) - certainly for a much shorter period than the lifetime of a galaxy[17] - so a starburst must be a phase in the life of a galaxy.

[16] Section 2.4 discusses the role of mergers in star formation.

[17] The mass of molecular gas can reach 5×10^{10} $M_\odot$ in the most massive galaxies (Young and Scoville [1991]). At a star formation rate in starbursts of say 5×10^{2} $M_\odot$ p.a., this gives a maximum duration for a starburst of $\sim10^{8}$ years. Also, simulations suggest that the most massive starbursts last for a few 10^{8} years (di Matteo et al. [2008]).

2.3 Deep fields

The depth (and therefore the lookback time) of cosmology has been much extended by the use of deep fields. The observation of deep fields (long integration times to discover distant sources) became central to extragalactic astronomy with the 10-day Director's Discretionary program on the *Hubble Space Telescope* (HST) in December 1995 (Williams et al. [1996]). Focussing on an apparently blank field in its continuous viewing zone, *Hubble* took images for ten consecutive days. Instead of reaching its confusion limit[18] as many expected, many hundreds of very distant, previously unobserved galaxies were discovered. Thousands of galaxies are now known in the *Hubble* Deep Field (HDF). The brightest submillimetre source (HDF850.1) was discussed in Section 1.6 (see Figure 1.5). This initial *Hubble* Deep Field in the northern hemisphere (HDF-N) was later expanded to 0.124 deg^2 and when follow-up multi-wavelength observations were made with other NASA space telescopes was re-titled The Great Observatories Origins Deep Survey North (GOODS-N).

Hubble followed this with a deep field in the southern hemisphere (HDF-S). However, the premier deep field in the southern hemisphere has become the Chandra Deep Field South (CDF-S; an extended area is called ECDF-S), which was re-christened GOODS-S, and comprises 0.25 deg^2. Another *Hubble* field which extended further in depth (to magnitude $m_{\rm AB} \sim 29$ for point sources) was the *Hubble* Ultra Deep Field (HUDF; Beckwith et al. [2006]) and many other deep fields have since been explored. The main deep fields used in extragalactic cosmology, with their central coordinates and sizes, and some of the main surveys carried out to date in each field, are listed in Table 2.1.

There is of course a trade off between the depth and area of a field when using

[18]The confusion limit is the flux below which sources cannot be detected individually because of random fluctuations of the background sky brightness (from sources or other structures below the detection flux limit). It is determined by the angular resolution of the telescope (its diameter in relation to the observed wavelength) and it also varies by position on the sky (e.g. it will be affected by foreground cirrus). It is the point beyond which the sensitivity of an instrument cannot be improved by increasing the observation time because the fluctuations in the image become dominated by the the fixed pattern noise from astronomical sources instead of by random noise from the instrument and the sky. A discussion of confusion is given in Condon [1974].

2.3 Deep fields

Table 2.1: Well-studied extragalactic deep fields (in order of declination). Chapters 3 to 5 deal with the ADF-S; Chapter 6 covers sources selected from several of these deep fields.

Deep Field	Centre (J2000) RA (h m s)	Dec (d m s)	Size deg^2	Selection of Key Deep Surveys
AKARI-NEP	17 55 24	+66 37 32	0.5	AKARI, WSRT, CFHT, Herschel-NEP, Subaru
HDF-N (GOODS-N, CDF-N)	12 36 49	+62 12 58	0.04-0.124	HDF, SCUBA, Chandra, XMM-Newton, FIDEL, HerMES , PEP, CANDELS, GOODS-Herschel
Spitzer FLS	17 18 00	+59 30 00	4.0	xFLS, HerMES
Lockman Hole: ISO Deep Field	10 52 43	+57 28 48	1.2	SWIRE, SHADES, ISOPHOT, PEP, HST/WFPC2, XMM-Newton, VLA, DXS, HerMES, ROSAT
ELAIS N1	16 08 44	+56 26 30	2.74	ELAIS, SWIRE, DXS, HerMES
Extended Groth Strip	14 17 52	+52 29 46	1.0	FIDEL, CUDSS, AEGIS, HerMES, CFHTLS-D3, CANDELS, SCUBA2
CFRS-14	14 17 49	+52 30 23		(bisects the Groth Strip)
SSA 13	13 12 17	+42 38 05	0. 3	VLA, Subaru/Subprime-Cam, ISOCAM
ELAIS N2	16 39 44	+41 15 43	2.98	ELAIS, SWIRE, HerMES
Boötes / ELAIS N3	14 32 06	+34 16 48	9.3	XBoötes, ELAIS, NDWFS, Spitzer 24 HerMES, SCUBA2
NGP	13 18 00	+29 00 00	150	H-ATLAS, GAMA
Subaru Deep Field	13 24 39	+27 29 26	0 26	Subaru, UKIRT, GALEX
COSMOS	10 00 29	+02 12 21	2.0	COSMOS, COSBO, VLA, VLT, Spitzer, CFHTLS-D2, Subaru, XMM-Newton, HerMES, UltraVISTA, PEP, CANDELS
GAMA A	09 00 00	00 00 00	36	GAMA, H-ATLAS, GALEX
GAMA B	12 00 00	00 00 00	36	GAMA, H-ATLAS, GALEX
GAMA C	14 30 00	00 00 00	36	GAMA, H-ATLAS, GALEX
WHDF	00 22 30	+00 21 00	0.014	WHDF
VIMOS 4 / SSA 22	22 17 00	+00 20 00	8.75	VVDS, DXS
VVDS	02 26 00	-04 30 00	2.0	VVDS, VVDS Radio, SWIRE, DXS, CFHTLS-D1, HerMES
Cetus	02 10 00	-04 30 00	9.2	NDWFS
XMM-LSS-SXDF / UDS	02 18 00	-07 00 00	1.3	SWIRE, SXDS, VLA, SHADES, DXS, UDS, HerMES, CANDELS
NTT	12 05 20	-07 44 20	0.0015	NTT-SUSI
CFHTLS-D4	22 15 31	-17 43 56	0.74	CFHTLS, XMM-Newton
HUDF	03 32 39	-27 47 00	0.003	HUDF, UDF09, UDF12, CANDELS, XDF
CDF-S (GOODS-S, ECDFS)	03 32 28	-27 48 30	0.11 - 0.25	CDFS, SWIRE, BLAST, LABOCA, FIDEL, GEMS, LABOCA, HerMES, PEP, SCUBA2, CANDELS, GOODS-Herschel
FORS Deep Field (FDF)	01 06 04	-25 45 46	0.01	VLT-FORS
SGP B	23 15 36	-32 54 00	66	H-ATLAS, GAMA
SGP A	02 26 48	-33 00 00	66	H-ATLAS, GAMA
ELAIS S1	00 38 24	-43 32 02	4.15	ELAIS, SWIRE, HerMES
ADF-S	04 44 00	-53 20 00	12	AKARI, BLAST, Spitzer, AzTEC, ATCA, HerMES, Herschel-PACS
SSDF	23 30 00	-55 00 00	94	Spitzer, SPT, Herschel-SPIRE, XMM, VISTA, ATCA
Marano	03 15 09	-55 13 57	1	Studies with ISOCAM, VLT, ATCA etc
HDF-S	22 32 56	-60 33 03	0.001	HDF-S

a telescope's time. Whilst wide fields are essential for understanding large scale structure and anisotropies in the universe, deep fields are essential for studies extending back to high redshifts. There is also a trade-off between fields with low foreground contamination (e.g. away from the galactic plane), and easy accessibility by ground-based instruments (available to a wider range of instruments nearer the equator). Foreground contamination may include emission from the Solar System (e.g. zodiacal thermal emission from dust and asteroids), from the Galaxy (from Galactic cirrus and from local stars, although at least a few foreground stars are needed for accurate calibration) and from known extragalactic sources. Absence of very bright optical sources (e.g. local bright stars or clusters of galaxies) is a factor in selecting which part of the sky is observed. Some deep surveys have selected several non-contiguous regions of the sky (e.g. ELAIS which comprised six regions across both hemispheres, and HerMES which included almost all of the well-known deep fields).

The *Hubble Space Telescope* Frontier Fields project (another Director's Discretionary observing time project) has recently started a 3-year program to make deep observations in six fields centred on strongly lensing galaxy clusters at $0.3 < z < 0.55$. The aim is to make use of the magnification caused by gravitational lensing[19] to detect the earliest galaxies back to $z \sim 10$ (age of Universe < 0.5 Gyr)(Richard et al. [2014]). The first data was released in July 2014 (Coe et al. [2015]; Ishigaki et al. [2015]); observations are scheduled to run to July 2015.

The work in Chapters 3, 4 and 5 is based on ADF-S, one of two deep fields chosen by *AKARI* (Matsuhara et al. [2006]), the other being near the north ecliptic pole, *AKARI*-NEP. The two *AKARI* fields were chosen as particularly low cirrus regions. The work in Chapters 6 and 7 is based on a selection of sources in various well-known deep fields.

[19]Gravitational lensing is discussed in Section 8.3.

2.4 Star formation rate density evolution

The Madau diagram

A famous constraint on the comoving-volume-averaged star formation rate history which was made before some of the recent discoveries of infrared astronomy was the Madau diagram or Madau-Lilly diagram (Madau et al. [1996]; Lilly et al. [1996]; Madau et al. [1998]), which suggested that star formation peaked at $z \sim 1$ (see Figure 2.3, left) based on semi-analytic hierarchical models[20] and optical/UV observations corrected for dust extinction. However, the discovery of the extent of extragalactic infrared radiation means that we now know that the Madau diagram underestimates star formation at earlier epochs. The latest consensus view (see recent review of cosmic star formation in Madau and Dickenson [2014]) is that the peak of the star formation rate density occurred at $z \sim 2$ (when the universe was about 3 billion years old), and that most of the stellar mass in the present-day Universe was formed between $z \sim 3$ and $z \sim 1$. A recent Madau diagram from Bouwens et al. [2011] is also shown in Figure 2.3 (right). The decline in star formation rate since then occurs at all masses (Sobral et al. [2014]). A star formation rate function prepared recently using UV luminosity for $4 < z < 7$ galaxies found that a Schechter function[21] can fit the data well (Smit et al. [2012]).

Downsizing

The concept of "downsizing"- that the most massive galaxies formed earlier than less massive galaxies - was introduced by Cowie et al. [1996] in a study of 393 galaxies at $0.2 < z < 1.7$. This pattern was supported by results from Brinchmann and Ellis [2000] whose study of a sample of 321 galaxies at $0 < z < 1$ suggested that the most massive galaxies had formed their stars by $z \sim 1$. This picture was confirmed by Juneau et al. [2005], whose sample of 207 galaxies extended back to $z \sim 2$. This paper also makes the point that the downsizing of stellar mass assembly is the opposite of the accepted picture for dark matter assembly which is thought to proceed from small mass to large mass units. Dye

[20] Theoretical models of galaxy evolution are discussed in Section 2.8.
[21] Schechter functions are described in Section 4.2.3.

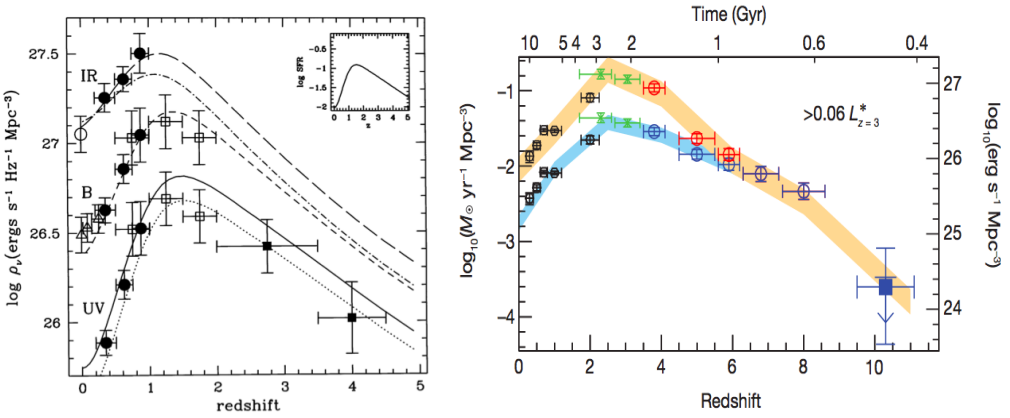

Figure 2.3: Evolution of luminosity density: the Madau diagram. **Left:** The original Madau diagram from Madau et al. [1998] which used data from optically-selected galaxy studies and assumed a Salpeter IMF and dust extinction of E(B-V)=0.1. **Right:** A recent Madau diagram from Bouwens et al. [2011] with recent candidate discoveries at $z \sim 6$, 7 and 10. The inferred star formation rate density is in red/orange and on the left axis; the observed rest-frame UV luminosity density is in blue and on the right axis. A Salpeter IMF was assumed and the conversion from luminosity density to SFR uses a dust extinction correction based on the estimated UV continuum slope.

et al. [2010] investigated the star formation histories of 92 BLAST sources and also found that high mass sources evolved more strongly and peaked at earlier times than low mass sources, which form a much higher fraction of their stellar mass at later times. Downsizing has also been confirmed by luminosity function studies (see Section 4.2.4).

The earliest galaxies, $z \gtrsim 5$ (age of universe $\lesssim 1$ Gyr)

The timescale of cosmic reionization is still unknown, but is thought to have been completed by about $z \sim 6-7$ (e.g. Zahn et al. [2012] and references therein). Since the installation of the Wide Field Camera 3 (WFC3) on the HST in May 2009, candidate galaxies at redshifts up to $z \sim 10$ have been reported regularly. These are usually found by either by the Lyman Break method[22] (e.g. Oesch et al. [2014]; Bouwens et al. [2011]), or by fitting an SED using multi-wavelength broad-band photometry, and calculating the probability of a high-redshift fit. These

[22]The Lyman limit (912 Å) is redshifted into optical bands at $z > 3$ and galaxies identified by this method, the so-called Lyman Break Galaxies (LBGs), are currently the largest population of star-forming galaxies identified at very high redshift.

candidates are mostly too faint for confirmation with detailed emission-line spectroscopy. Finkelstein et al. [2013] recently reported identifying a Lyα emission line in a Lyman Break galaxy at $z = 7.51$. No candidate at $z > 7.6$ has yet been spectroscopically confirmed. Several major surveys are now underway to improve this situation. The *Hubble Space Telescope* Frontier Fields project was discussed in Section 2.3. Another deep survey is the Brightest of Reionizing Galaxies survey (BoRG; Trenti et al. [2011]). Another is the eXtreme Deep Field (XDF) in the Hubble Ultra-Deep Field, combining deep observations already taken with many previous surveys (Illingworth et al. [2013]).

Table 2.2 shows look-back time, the age of the universe, and the estimated peak of infrared flux from starburst galaxies for various redshifts, using the current concordance cosmological assumptions (see Section 2.9).

Galaxies at $5 \gtrsim z \gtrsim 3$ (age of universe ~ 1 to ~ 2 Gyr)

Most galaxies at this distance have been identified with the Lyman Break technique, as with higher-redshift sources. This tends to miss less-luminous sources: a search for Lyα emission in a field with LBGs found several times the number of sources at $z \sim 3$ (Steidel et al. [2000]). Most galaxies observed at high redshift are forming stars at a high rate, often hundreds of $M_\odot$ per year, which contrasts with galaxies in the local universe where such high SFRs are rare (this was also found in the work in Chapter 3). A recent HerMES study found that star formation at $z > 4$ is significantly higher than predicted by models, finding 38 candidate galaxies above this redshift in 21 deg^2 using SPIRE data at 250 μm, 350 μm and 500 μm (Dowell et al. [2014]). A study of Lyman Break Galaxies[23] with SCUBA-2 (Coppin et al. [2015]) suggests SFRs of 40 - 200 $M_\odot$ per year at $5 > z > 3$.

Perhaps surprisingly, many relatively quiescent galaxies already exist at this early period, as shown in a recent major study of 14,200 galaxies in the COSMOS field at redshifts up to $z \sim 3$ (Man et al. [2014]). Another recent paper which selected galaxies by fitting SEDs (using line breaks and bumps rather than emission

[23]Newly discovered populations of galaxies are usually called after the wavelength range of discovery, such as radio galaxies, Ultra Luminous Infrared Galaxies (ULIRGs), Lyman Break Galaxies and submillimetre galaxies, and it is often some time before the connection between these newly discovered populations and other known populations becomes clear.

Table 2.2: Lookback time and the age of the universe and the estimated far-infrared SED peak (assuming 100 μm peak at $z = 0$) by redshift. Assumptions: $H_o = 72$ km s^{-1}Mpc^{-1}, $\Omega_M = 0.3$, $\Omega_\Lambda = 0.7$.

Redshift	0	0.2	0.4	0.6	0.8	1.0	2	3	4	5	10
Lookback time / Gyr	0	2.4	4.2	5.6	6.6	7.5	10.0	11.0	11.6	12.0	12.6
Age of universe / Gyr	13.1	10.7	8.9	7.5	6.5	5.6	3.1	2.1	1.5	1.1	0.5
Est. FIR peak /μm	100	120	140	160	180	200	300	400	500	600	1100

lines) found a quiescent population (57 sources) of dusty galaxies at this redshift (Spitler et al. [2014]). A population of massive, quiescent galaxies at $z > 4$ has recently been reported in Straatman et al. [2014]. These results suggest an earlier obscured phase of rapid star formation.

Chapter 7 presents the detection of submillimetre-selected galaxies at $z > 3.5$ identified by their Hα emission lines. These comprise two radio galaxies and two submillimetre galaxies associated with one of them.

The role of galaxy mergers in star formation

Galaxy mergers are relatively common. Major mergers were once thought to be a significant cause of star formation, but recent work suggests that though they may well trigger starbursts, they do not make a dominant contribution to the total star formation rate density (e.g. Rodighiero et al. [2011]; Kaviraj et al. [2013]). Cold gas accretion and minor mergers, rather than major mergers, are now thought to be the main processes driving the evolution of star-formation.

A major new study (Schreiber et al. [2015]) from the GOODS-*Herschel* program combined with the CANDELS-*Herschel* program across both PACS and SPIRE wavelengths, using data selected primarily from *Hubble's* ultra-deep H-band catalogues, found 10,497 sources (and, with stacking, 62,361 sources) in the *Herschel* data. They showed that most star formation is secular, i.e. at a relatively low, steady rate, corresponding to main-sequence mode (see Section 2.6), and that major mergers have had relatively little impact in triggering starbursts since $z = 4$. The *Herschel* data reached ~ 10 mJy at 250 μm. A study of a typical star-forming galaxy at $z = 2.3$ (Bouché et al. [2013]) found that the gas accretion rate was comparable to the star formation rate ($\sim 33^{+40}_{-11}$ M$_\odot$ yr^{-1}), supporting

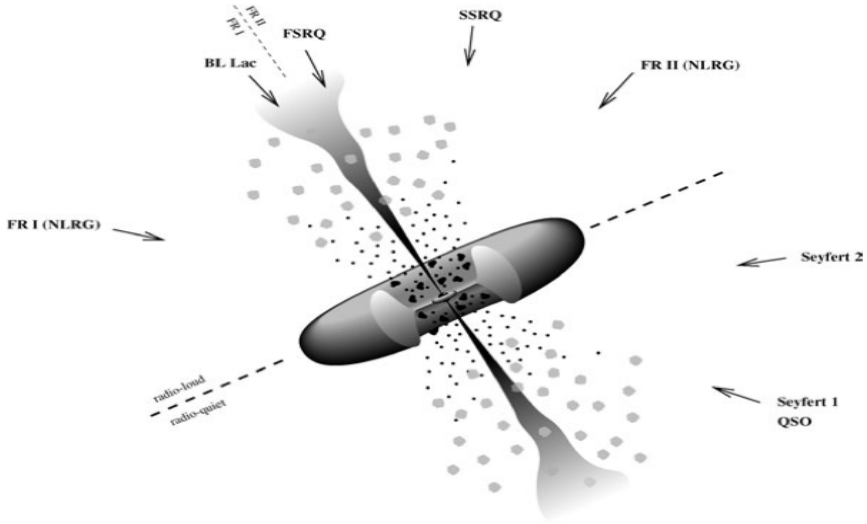

Figure 2.4: The AGN unification model. Viewed along the jet axis, we observe blazers; perpendicular to the jet axis, we observe a morphology typical of radio galaxies. At an orientation of $\sim 30^{o}$ we see Seyfert 1s and quasars; at larger angles, Seyfert 2s as the Broad Line Region is obscured by the torus. Figure from Torres and Anchordoqui [2004].

the idea that continuous accretion of gas plays the major role in galaxy growth.

2.5 Star formation and active galactic nuclei

The broad picture which has emerged from observations in the last thirty years is that the extragalactic flux which we receive (apart from the CMB radiation) comes from two main types of source. Firstly, we receive radiation from the energy released by nuclear fusion in stars[24], which peaks in the UV/optical region of the spectrum. We now know, however, that much of the radiation emitted during star formation does not reach us directly, but is absorbed by the dust and gas in the giant molecular clouds within which the stars are forming. This energy is then re-emitted as thermal radiation which reaches us in the infrared region of the spectrum, peaking between 50 μm and 200 μm restframe wavelength. Sec-

[24]The flux which reaches us is dominated by hot, massive stars and we need to assume an initial mass function (IMF) in order to account for the flux from less massive stars in our models. The IMFs of stars are discussed in Section 5.2.3.

ondly, we receive radiation from Active Galactic Nuclei (AGNs). Supermassive black holes (SMBHs) are thought to reside in the centres of essentially all galaxies, and matter accretes onto them via an accretion disc which forms around the black hole. As mass falls on to the accretion disc, gravitational potential energy is released in a highly efficient conversion process. SMBHs which are actively accreting material are called AGNs, and the most luminous of these ($L \gtrsim 10^{13} L_{\odot}$) are called quasars. Most models predict that radiation from AGN dust tori peaks in the mid-infrared (e.g. Efstathiou and Rowan-Robinson [1995]). Figure 2.4 shows the standard unification model (Antonucci [1993]; Urry and Padovani [1995]) in which the AGN classification depends on the orientation at which the source is observed. The AGN-related gas velocity dispersion tends to exceed that of the surrounding host galaxy.

One of the surprises of recent observations has been that there appears to be a close relationship between the SMBH activity in galaxies and the star formation of the host galaxies, a result which has yet to be fully understood. The next few subsections describe the evidence for this relationship.

M_{BH} - $M_{stellar\ bulge}$ (Magorrian relation)

Based on dynamical models and using a sample of 36 local galaxies observed with the HST, Magorrian et al. [1998] found a correlation between the black hole mass and the stellar bulge mass in the galaxies (it is interesting that even as recently as 1998 the authors were reluctant to identify the central 'massive dark objects' in the galaxies as black holes). This is referred to as the 'Magorrian relation'. Häring and Rix [2004], with a sample of 30 local galaxies and using improved M_{BH} values, confirmed the Magorrian relation with a tighter correlation.

M_{BH}-sigma relation

A couple of years after the Magorrian paper, Ferrarese and Merritt [2000] and Gebhardt et al. [2000] using samples of 12 and 26 local galaxies respectively, found a much stronger correlation between the black hole mass and the stellar velocity dispersion in the spheroid of galaxies (i.e. in the bulge for spiral galaxies, the whole galaxy for ellipticals), referred to as the M_{BH}-σ relation. Although the original studies used quiescent galaxies, recent work has found the same relationship for galaxies with AGNs (Kang et al. [2013]; Woo et al. [2013]). This relation is now

so well established that it is often used to estimate M_{BH}. Marconi and Hunt [2003] found a similarly tight correlation between black hole masses and near-infrared bulge luminosities. Although these results are based on local galaxies, the closeness of the correlation proves a close connection between the black hole in a galaxy and its stellar mass evolution. In a recent review, Kormendy and Ho [2013] showed that while black hole masses correlated tightly with bulges and ellipticals, the correlation was much weaker for dark matter halos, and did not exist at all with wider disk properties.

Further evidence of connection

To explore the connection more deeply, we need ideally to compare AGN accretion rates and star formation rates. This has proved less clearcut, and different results have been claimed, with low-luminosity AGNs showing little such correlation; it is also bound up with the question of whether the emission from AGNs quenches star formation (negative feedback), which is discussed in the next subsection.

The conflicting results may be caused by the different timescales, with SMBH accretion rates varying by orders of magnitude on a time scale much shorter (as short as months or less; e.g. Peterson et al. [1999]; Hopkins and Hernquist [2009]; Keel et al. [2012]; Ivezic et al. [2014]) than the time scale of typical starbursts ($\gtrsim$ 100 Myr; Wong [2009]; Hickox et al. [2012]). A study matching the **average** black hole accretion rates with star formation rates has shown a far tighter correlation: Chen et al. [2013] used 1,767 *Herschel* sources selected at 250 μm to cross-match with detected (121 AGNS) and stacked (the remainder) sources in *Chandra* X-ray and *Spitzer* 24 μm data and found a strong linear relationship between star formation rate (based on the *Herschel* data) and average black hole accretion rate (based on the *Chandra* and *Spitzer* data, averaged in SFR bins) in the redshift range $0.25 < z < 0.8$.

Boyle and Terlevich [1998] found a close similarity in published studies of the evolution of the quasar luminosity density and the evolution of the star formation rates of field galaxies to support their model of quasar luminosity being caused by nuclear starbursts. Chapman et al. [2005] in their study of submillimetre galaxies with radio identifications found a similar redshift distribution for AGNs

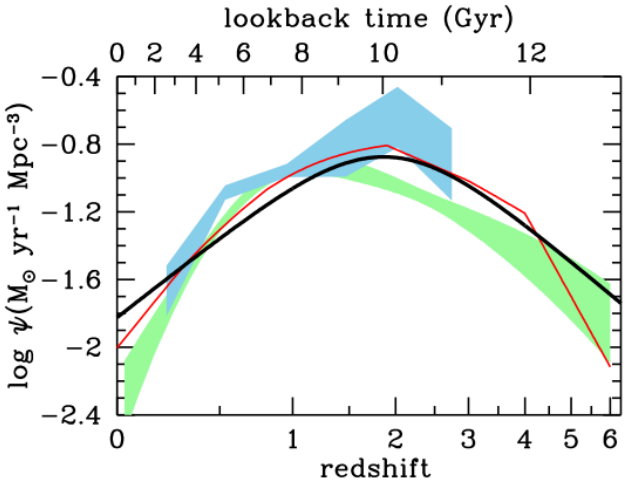

Figure 2.5: Star formation vs. black hole growth over cosmic time. Best-fit star formation history is the solid black line. Black hole accretion history from X-ray data is shown as a red line and green curve, and from infrared data as a blue curve, scaled up by factor of 3300 to aid visual comparison. Figure from Madau and Dickenson [2014]: see source for references on these curves.

and starbursts in their sample. Franceschini et al. [1999] found a close match between the evolution rates of star formation and AGN emissivity in both high-luminosity and low-luminosity galaxies. Delvecchio et al. [2014] found that AGN activity peaked at $z \sim 2$ in a *Herschel*-PEP study using SED fitting in the GOODS-S and COSMOS fields with a sample of 4,343 galaxies selected at 160 μm. This is similar to the peak for star-forming galaxies.

A further indication of the close AGN/SFR connection is shown by the downsizing[25] of AGNs, in which the most massive AGNs develop earlier (e.g. Hasinger et al. [2005]). Figure 2.5 shows a recent comparison of star formation rate history against black hole accretion history.

The investigation of the relationship between star-forming galaxies and galaxies dominated by AGNs relies on an ability to separate the relative contributions in our observations. Techniques to do this are discussed in Section 3.2.2.

Mid-infrared spectroscopy has contributed to our knowledge of the relative contributions of star formation and AGNs in active galaxies. ISO spectroscopic

[25]Downsizing in relation to the history of star formation was discussed in Section 2.4.

studies showed that ULIRGs are predominantly powered by starbursts (Genzel et al. [1998]; Lutz et al. [1998]), but that the AGN contribution increases for higher-luminosity ULIRGs. Later work using ISO and *Spitzer* mid-infrared data showed that most ULIRGs have simultaneous AGN and starburst activity in their nuclei (Spoon et al. [2007]). The Great Observatories All-Sky LIRG Survey (GOALS; Armus et al. [2009]) showed that the energy output from LIRGs is also dominated by starbursts (Petric et al. [2011]; Inami et al. [2013]). This mid-infrared work is discussed further in Section 3.2.2.

Feedback between AGN accretion and star formation

The interaction(s) between AGN outflows (either jets or winds) and star formation, both in initiating and (possibly) quenching star formation, is a key area of research at present. Other phenomena, in particular supernovae, may quench star formation, but are not sufficient to explain quenching in the most massive galaxies. Quenching by AGNs may be either through kinetic energy, driving out gas, or by thermal energy, heating up gas so that stars cannot form.

Simulations of galaxy mergers have incorporated the growth of black holes and star formation, showing AGN feedback as a mechanism to regulate SFR (e.g. Springel et al. [2005]; di Matteo et al. [2005]) and finding that negative feedback from AGNs to quench star formation can prevent excessively massive galaxies forming (and can account for the existence of the population of old, passive galaxies). Semi-analytic source count models[26] can also best reproduce massive galaxy number densities when incorporating AGN feedback in the co-evolution of galaxies and their central black holes (e.g. Croton et al. [2006]; Bower et al. [2006]). However, a recent high-resolution simulation found that although AGN-driven outflows can remove massive amounts of gas in the longer term, the impact on star formation may be marginal (Roos et al. [2015]).

Observational evidence seems to show that negative feedback is not significant. Support for AGN quenching was originally provided by Page et al. [2012] using quasars selected from the X-ray catalogue of CDF-N and stacking observations at 250 μm from *Herschel*-SPIRE (there were only 11 observed matches). However, this finding was not confirmed when the analysis was extended to the COSMOS

[26]Semi-analytic models of galaxy evolution are discussed in Section 2.8.

and CDF-S fields, which showed no clear downturn of star formation rate with increasing AGN luminosity (Harrison et al. [2012]). Studies using a combination of submillimetre and X-ray observations at $z \sim 2$ have confirmed the positive association of AGNs and intense star formation (Alexander et al. [2005]). Other studies have also suggested that there is no clear evidence of quenching of star formation by powerful AGN. A paper cited earlier, Chen et al. [2013] found evidence of a linear relationship between star formation and black hole accretion rate in a large sample, i.e, showing no evidence that strong accretion quenches star formation. Using a very large sample (∼230,000) of star-forming galaxies (SFGs), Torres-Papaqui et al. [2013] found no evidence of quenching of star formation by the SMBH (whether AGN or not). A recent study by Yesuf et al. [2014] of post-starburst galaxies found a time delay between starburst quenching and AGN activity, suggesting that AGNs are not primarily responsible for quenching starbursts. On the other hand, Bluck et al. [2014] did find a correlation between black hole mass and the fraction of passive galaxies in a large sample of SDSS central galaxies.

Bongiorno et al. [2012], using SED fitting of multi-wavelength data for ~ 1700 AGNs in the COSMOS field, found that although AGN activity and star formation appear to have a common triggering mechanism, there was no conclusive evidence showing that AGNs influenced the star formation rates of SFGs. Rosario et al. [2013] in a recent *Herschel*/PEP study of a large sample of quasars out to $z \sim 2$ found that the SFRs of quasars lie in the main sequence, and do not show evidence of starbursting. Maiolino et al. [2012] found evidence for massive AGN outflows (>3000 $M_\odot$ yr^{-1}) at high redshift ($z = 6.4$). Karman et al. [2014] also found evidence for high-velocity outflows from AGNs in massive galaxies at $z \sim 3$. However, the recent simulation (cited earlier) by Roos et al. [2015] suggests that even strong AGN radiation may cause very little quenching in star formation.

As mentioned above, relative timescales may be critical in understanding the relation: Hickox et al. [2014] shows that a simple model of galaxies with a tight correlation between AGN activity and SFR over galaxy evolution timescales, may reproduce only a weak correlation where AGN timescales range from hours to Myr (and the evidence for this variability is discussed in that paper) while star formation events take ≥ 100 Myr. Episodes which are intense but short-lived

may fail to appear in average properties observed.

To the extent that it does happen, quenching may result from the role of jets in radio-loud (though not X-ray luminous) galaxies (Zinn et al. [2013]). Nesvadba et al. [2010] found low star formation in a radio galaxy with a gas surface density of a starburst galaxy, suggesting radio jets deposit mechanical energy in the ISM leading to the quenching of star formation. Further confirmation that this may be the case is given in a recent study by Karouzos et al. [2014]. Using a sample of 321 radio sources detected in the near-infrared in the *AKARI*-NEP field, they fitted SEDs to the multi-wavelength data available and found a significant AGN component in the sample and (a) a positive correlation between AGN luminosity and star formation and also (b) within narrow redshift and AGN luminosity ranges, a negative correlation between radio luminosity and the specific star formation rate. The loudest radio sources were found to be on the main sequence (steady star formation).

Haines et al. [2013] found that the specific star formation rates (SSFRs; $\dot{M}_*/M_*$) of star-forming cluster galaxies (in a sample of 30) were $\sim 28\%$ lower that those of their counterparts in the field at fixed stellar mass and redshift, consistent with these cluster galaxies being slowly quenched as they join the cluster, suggesting either ram-pressure stripping or dust starvation. Alberts et al. [2014] also found evidence that star formation in clusters evolves more quickly than in field galaxies, with blue cluster galaxies having systematically lower SSFRs than blue field galaxies (except in the outskirts of the cluster, which showed enhanced star formation). This again suggests the action of either ram pressure stripping or dust strangulation to quench star formation within clusters.

Sell et al. [2014] studied 12 massive galaxies at $z \sim 0.6$ with high-velocity gas outflows, concluding that these were driven largely by feedback from star formation rather than from AGNs: that is, quenching being caused by compact starbursts. Two-thirds of the sample showed morphological evidence of undergoing mergers. Rodighiero et al. [2015] found that the relation between star formation rates and black hole accretion was different in the cases of quiescent, main-sequence and starburst galaxies.

Another, even simpler explanation may be that both AGN accretion and star formation are driven by the inflow and availability of cold gas; perhaps no further

interaction is required to explain the correlations (Rosario and Lutz [2013]). A supply of cold gas drives both star formation and black hole growth; the energy released by the AGN may trigger new star formation; it may also deplete the supply of cold gas, but on a timescale which has only a marginal impact on starburst events.

To summarise: most star formation, and most black hole accretion, appear to take place via secular, smooth, main-sequence, processes. Major mergers play a minor role, although they are seen in some dramatic cases. Star formation and black hole accretion co-evolve, but the extent and direction of feedback between each is still controversial; the earlier view of AGNs quenching star formation seems unlikely to be a dominant process, and perhaps the inflow and availability of cool gas flows, which power both processes, accounts for the similarity in their evolution. However, the existence of large numbers of quiescent galaxies by $z \sim 3$ (Man et al. [2014]) still remains to be explained successfully.

2.6 The galaxy main sequence and starbursts

In recent years, in analogy with the 'main sequence' of stars (the Hertzsprung-Russell diagram), a main sequence for galaxies (the 'star-forming main sequence') has been proposed, showing that the star formation rate (SFR) of normal galaxies (i.e. not quasars or starbursts) is correlated with stellar mass (Noeske et al. [2007]; Elbaz et al. [2007]; Daddi et al. [2007]; see Figure 2.6):

$$\mathrm{SFR} \propto M_*^{\alpha} \tag{2.1}$$

with $\alpha \sim 0.9$ for a sample of galaxies at $z \sim 2$ in Daddi et al. [2007].

Outliers above the main sequence are thought to be starburst galaxies (i.e. with enhanced SFRs, up to $\sim 10^3$ $\mathrm{M}_\odot$ yr^{-1} or higher). As shown in Figure 2.6, the correlation is fairly broad, and the line above which starbursts are defined is somewhat arbitrary. The galaxy main sequence varies with redshift. Unlike the Hertzsprung-Russell diagram for stars, variations in the galaxy main sequence for different samples of galaxies cannot be used to find an evolutionary path for galaxies.

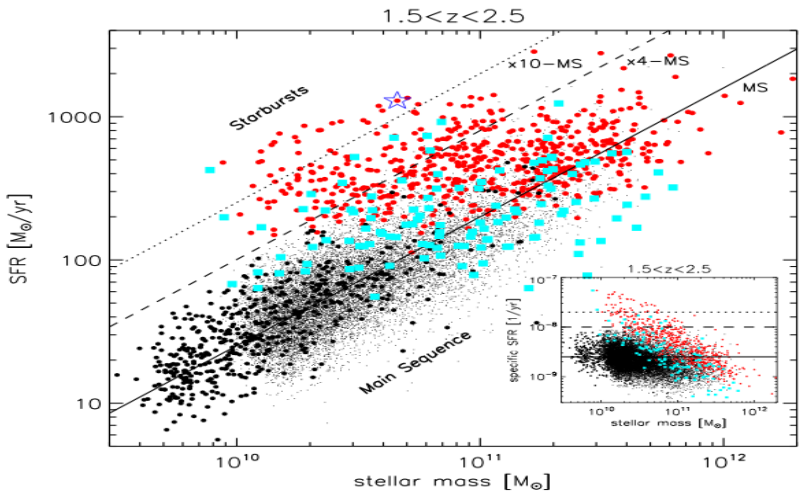

Figure 2.6: The galaxy main sequence: the stellar mass - SFR relation at $1.5 < z < 2.5$ (figure from Rodighiero et al. [2011]). The different coloured symbols show four different surveys: red circles = shallow PACS-COSMOS; cyan squares = deeper PACS-GOODS-S; black circles = deep BzK-GOODS-S; black dots = BzK-COSMOS. The solid black line shows the main sequence for star-forming galaxies defined by Daddi et al. [2007]. The bottom-right region is not well sampled. Inset is the SSFR-M_* relation.

The stellar mass of a galaxy reflects past star formation, and current star formation comes from cold gas and dust, so the 'main sequence' relation implies a correlation between stellar mass and the mass of cold gas and dust, which is difficult to measure directly. In effect, the galaxy main sequence is a reformulation of the Kennicutt-Schmidt law which relates the star formation rate density to the surface density of gas (Schmidt [1959]; Kennicutt [1998a]).

This relationship of the SFR with stellar mass is sometimes normalised by the stellar mass (referred to as the specific SFR: SSFR= $\dot{M}_*/M_*$) which was defined in Brinchmann et al. [2004] who suggested that the correlation between stellar mass and SFR normalised by mass may make relationships with other physical parameters of galaxies clearer. Star formation has two modes: a "normal" star formation mode (or main-sequence mode), which has a typical SSFR at each redshift, and an accelerated (starburst) mode, probably caused by a merger of two galaxies, with a higher SSFR.

Rodighiero et al. [2011] used four samples of star-forming galaxies in the

COSMOS and GOODS-S fields at $1.5 < z < 2.5$ to study the SFR - M_* relation. Two of the samples were from PACS observations as part of Herschel-PEP (with fairly high SFRs), and two were star-forming galaxy (SFG) samples selected using UV and BzK selections from existing data, in order to probe to lower SFRs (it reached down to a few $M_\odot$ yr^{-1}, not quite reaching down to the star formation level of the Milky Way). The result (see Figure 2.6) is different for each sample, but broadly confirms a general correlation. Starbursts are suggested above lines at either 4× or 10× main sequence level. Rodighiero et al. [2014] found that galaxies selected from far-infrared *Herschel*-PACS data did not conform to the previously found slope for SFR-M_* but stacking BzK-selected galaxies on the PACS maps did find overall agreement with previous results. They concluded that far-infrared-selected galaxies were outliers from the main sequence.

Whitaker et al. [2012] analysed a sample of 22,816 star-forming galaxies in the range $0 < z < 2.5$. They found that star-forming galaxies could be classified into three groups: dusty blue galaxies with high SFRs; actively star-forming galaxies on the main sequence and red star-forming galaxies with low SFR (possibly on their way to quiescence). Excluding the red star-forming galaxies gave a linear main-sequence relation, whereas including all galaxies did not. Whitaker et al. [2014] extended this with a study of 39,106 low-mass star-forming galaxies at $0.5 < z < 2.5$, finding the slope of the SFR-stellar mass relation is steeper for low mass ($\alpha \sim 1$) than for high-mass galaxies. Leja et al. [2015] found this variation in the slope made possible a reconciliation with observed stellar mass functions, which was not possible for a single $\alpha \sim 0.9$ slope.

Speagle et al. [2014] combined 25 studies to investigate the evolution of the main sequence for a redshift range out to $z \sim 6$, finding a clear consensus among observations. They found the width of the scatter was ∼0.2 dex throughout this period, with an evolution in the slope of the main sequence. BzK-selected galaxies were well below galaxies selected by other methods. Steinhardt et al. [2014] found the main sequence relation extended out to $z \sim 6$ in a study of 3,398 star forming galaxies. Bauer et al. [2013] found that an analysis of the GAMA survey for ∼73,000 low-mass galaxies at $0.05 < z < 0.32$ showed a surprisingly high SSFR. Atek et al. [2014] found that starbursts may be more common than thought, from a study of dwarf galaxies at high redshift ($1 \geq z \geq 2$). Pannella et al. [2015] in a

Herschel-GOODS-N study found a slope of $\alpha = 0.8$ to be identical at all redshifts up to $z = 1.5$. With a large sample of star-forming galaxies in the COSMOS field, Lee et al. [2015] found that a broken power-law gave the best fit to the main sequence data.

A recent *Herschel* data paper (Hung et al. [2013]) found that while the proportion of galaxies showing signs of merging increases systematically with deviation from the galaxy main sequence, as expected, it was also the case that $\gtrsim 18\%$ of massive, infrared-luminous main sequence galaxies are interacting systems.

2.7 Star formation: empirical relations

Many correlations between observed quantities, some of them surprising, have been found which have proved useful in analysing observations and in providing constraints on theoretical models explaining star formation. Some will be discussed in later chapters (for example, the relation between emission line ratios and AGN fractions and dust obscuration in Sections 3.2.1 and 3.2.2). This section outlines others which have been used in this thesis.

Estimating star formation rates from L_{FIR} and from $L_{H\alpha}$

Several luminosity - star formation rate relationships for star forming galaxies are reviewed in Kennicutt [1998b]. The ones which have been used in this thesis (which assume a Salpeter IMF, as in the Kennicutt paper) estimate star formation from the total FIR luminosity and Hα luminosity respectively:

$$\mathrm{SFR}/(\mathrm{M}_\odot \mathrm{yr}^{-1}) = 4.5 \times 10^{-37} \mathrm{L}_{\mathrm{FIR}}/\mathrm{W} \tag{2.2}$$

$$\mathrm{SFR}/(\mathrm{M}_\odot \mathrm{yr}^{-1}) = 7.9 \times 10^{-35} \mathrm{L}_{\mathrm{H}\alpha}/\mathrm{W} \tag{2.3}$$

Comparing the results in each case can be informative. In the case of highly luminous radio galaxies in Chapter 7, it was found that using Hα under-estimated the SFR by a factor of about 10, agreeing with earlier studies of active galaxies. In Chapter 3, on the other hand, little diminution was found, suggesting that the (relatively local) galaxies observed were not enclosed in extensive dust clouds,

Table 2.3: Estimating far-infrared luminosity from single wavelength luminosity for star-forming galaxies. Note that metallicity may affect the ratios. Estimated accuracy varies between authors. References: Bav=Bavouzet et al. [2008]; Boq=Boquien et al. [2010]; Elb=Elbaz et al. [2011]; Got=Goto et al. [2011a]; Rie=Rieke et al. [2009].

Restframe	Dominant emission at this wavelength	Evidence provided by ratio $L_{FIR}/\ \lambda L_{\lambda}$	Estimated accuracy	References
8 μm	PAHs	High ratio implies AGN (or strong starburst)	∼40%	Bav; Boq; Got; Elb
24 μm	AGNs	High ratio implies low AGN emission	∼50%	Bav; Boq; Got; Rie
60 μm (or 70 μm)	Star formation	Best for estimate of SFR	∼16%	Bav; Boq
160 μm	Cold gas & dust		∼31%	Bav; Boq

unlike more active galaxies, and confirming the relatively cirrus-free nature of the *AKARI* Deep Field South (ADF-S).

Estimating L_{FIR} from single wavelength luminosity

Insofar as the SEDs of specific types of galaxies have a similar shape, it is not surprising that correlations are found between fluxes at different wavelengths, and this enables an estimate of total FIR flux to be obtained from a single measurement, provided our judgment of the galaxy type is correct. Recent studies examining these correlations have been Bavouzet et al. [2008], Boquien et al. [2010] (both using *Spitzer* data), and Goto et al. [2011a] (using *AKARI* and IRAS data). The correlations most often used are described below and summarised briefly in Table 2.3.

$\mathbf{L_{8\mu m(restframe)} \propto L_{FIR}}$: In a GOODS-*Herschel* study, Elbaz et al. [2011] found that the distribution of this relation (sometimes called IR8=$L_{FIR}/L_{8\mu m}$) for star-forming galaxies was a Gaussian with mean=4 and σ=1.6, but with a high value tail of outliers (i.e. with relatively low 8 μm luminosity) which were starbursts. The 8 μm luminosity will be dominated by emission from PAHs, which may be triggered by star formation but may be partly suppressed by strong starburst activity. IR8 is correlated closely with infrared surface brightness[27], and therefore

[27]The Schmidt-Kennicutt law relates the star formation rate density to the surface density of gas: $\Sigma_{SFR} = A(\Sigma_{gas})^n$ (Schmidt [1959]; Kennicutt [1998a]).

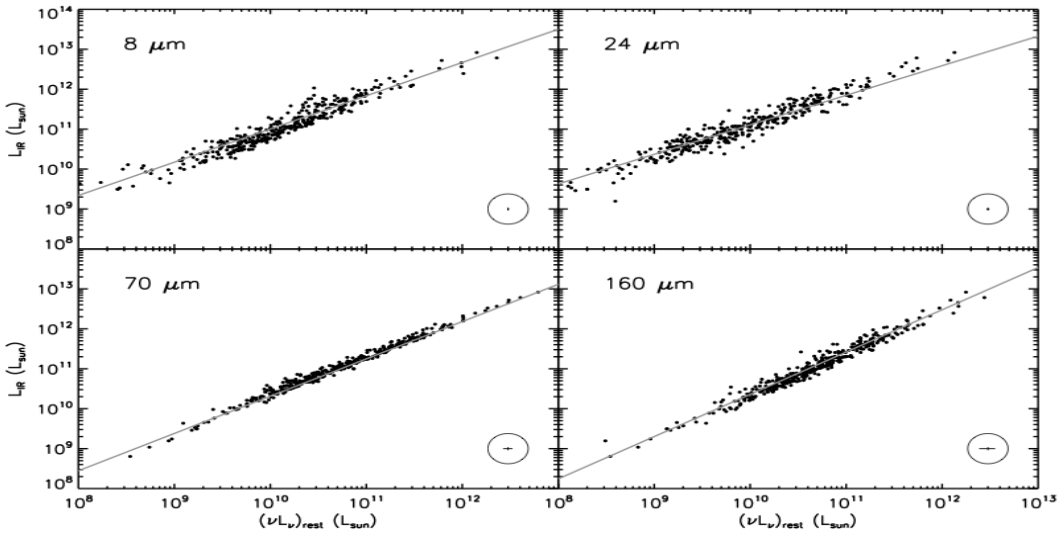

Figure 2.7: Estimating far-infrared luminosity from single wavelength luminosity, using 372 star-forming galaxies from *Spitzer* (figure from Bavouzet et al. [2008]). Note the closest correlation is at 70 μm (the uncertainty in the estimate is $\pm$16%). Typical error bars are shown in circles in the bottom right-hand corners. I have used luminosity from a nearby wavelength, 60 μm, to estimate far-infrared luminosity in Chapters 3 and 7.

with star formation rate density. IR8 will be even higher for AGNs, the radiation from which will normally destroy PAHs. Section 3.2.2 will discuss the use of PAH bands in separating AGNs from star-forming galaxies.

$\mathbf{L}_{24\mu\mathrm{m(restframe)}} \propto \mathbf{L}_{\mathrm{FIR}}$ (z dependent): The deep *Spitzer* 24 μm catalogues mean that many galaxies have well-established 24 μm fluxes. At this wavelength, the flux from galaxies is likely to be dominated by AGN emission, so it is not ideal to use in estimates of star formation. Nevertheless, there is a correlation for star-forming galaxies up to $z \sim 1.5$ with a dispersion of $\sim$40% (Elbaz et al. [2010]).

$\mathbf{L}_{60\mu\mathrm{m(restframe)}} \propto \mathbf{L}_{\mathrm{FIR}}$: This relation is often used to estimate $\mathrm{L_{FIR}}$ and thence star formation rates in star forming galaxies. This is the closest correlation for star-forming galaxies, with an uncertainty of only $\sim$16% (see Figure 2.7). I have used this correlation to estimate far-infrared luminosity with the M82 SED for the relatively local galaxies in the ADF-S in Chapter 3, and with the 'Cosmic Eyelash' galaxy SED for high-redshift active galaxies in Chapter 7.

The L_{FIR} - L_{radio} correlation

An extraordinarily tight, linear correlation exists between far-infrared luminosity and radio luminosity for star-forming and quiescent galaxies. Results from IRAS showed a correlation within a factor of ∼2 over more than three orders of magnitude between the far-infrared flux and the flux density at 1.4 GHz for star-forming galaxies (Helou et al. [1985]; Soifer et al. [1987a]). The correlation is usually defined in terms of the log ratio q_{FIR}:

$$q_{FIR} = \log_{10}[L_{FIR}/(3.75 \times 10^{12}W)] - \log_{10}[L_{1.4GHz}/WHz^{-1}] \tag{2.4}$$

where far-infrared is usually taken from 8 μm - 1000 μm, although the original IRAS work took 40 μm - 400 μm.

It is thought that the radio luminosity is non-thermal and caused mainly by electron synchrotron radiation (van der Kruit [1971]; Condon [1992]). Star formation controls the far infrared luminosity and given this close correlation, star formation must therefore also be responsible for this radio luminosity. The most favoured explanation at present is that both arise from massive stars and their deaths, with the cosmic ray electrons resulting from supernovae losing their energy at radio wavelengths via synchrotron emission. Sopp and Alexander [1991] found that radio-quiet quasars and Seyfert galaxies lie on the same correlation as the star-forming galaxies and ULIRGs, suggesting that star formation is also responsible for the radio emission in these types of galaxies. They found that radio-loud quasars showed a different correlation, suggesting a different physical origin for the radio emission. A full theoretical explanation is still unclear.

Far-infrared luminosity is more effective in tracing the star formation of more luminous galaxies than that of faint galaxies. The L_{FIR} - L_{radio} correlation remains linear for faint galaxies, so the radio flux from low-luminosity galaxies must also be suppressed (Bell [2003]). A study with *Herschel* data found tentative evidence for a break in the ratio at $L_{1.4GHz} \sim 10^{22.7}WHz^{-1}$ where radio-loud AGNs start to dominate the radio power density (Ivison et al. [2010]; see also Figure 2.8). A GOODS-*Herschel* study has found that the L_{FIR} - L_{radio} correlation does not evolve up to $z \simeq 4$ (Pannella et al. [2015]). A H-ATLAS study also found no redshift evolution, but did find a temperature dependence (Smith et al. [2014]).

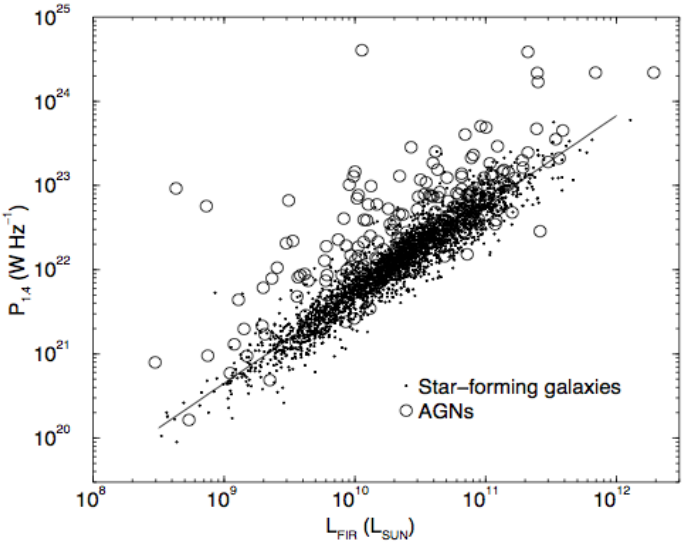

Figure 2.8: The radio - far-infrared correlation for 2690 star-forming galaxies (dots) showing also that the relation does not apply to 208 radio-loud AGNs (open circles) in a 6dFGS/NVSS/IRAS-FSC sample (Mauch and Sadler [2007]; figure from that paper). I found a similar relationship for star-forming galaxies in the ADF-S (Figure 5.5).

A recent study by Magnelli et al. [2015] found a small but statistically significant redshift evolution, with the ratio (q_{FIR}) falling from 2.4 locally to ~ 2.1 at $z = 2$. Carilli and Yun [1999] have used the correlation to find the distance of high-redshift galaxies. In this thesis, the L_{FIR} - L_{radio} correlation was observed for ADF-S sources for which radio fluxes were available in Chapter 5 (see Figure 5.5).

Flux vs. number density: source counts

A technique which does not require redshifts is based on a simple count of sources above a range of given fluxes. The number of galaxies observed varies as the cube of the distance in a Euclidean universe (due to the projection of three dimensions onto two) whereas the flux of galaxies varies as the inverse square of the distance, so the graph plotting integral number count density against flux should show a gradient of -1.5. Source counts (also called number counts) are usually shown normalised to this Euclidean slope so that deviation from a flat line shows evolution. Number counts are usually one of the first results from a new survey, before significant numbers of redshifts are available.

Source counts over a wide range of wavelengths have shown that the universe did evolve (e.g. Pearson [2001]; Héraudeau et al. [2004]; Scott et al. [2012]); in the infrared, strongly from $z = 2$ to the present. The evolution shown by radio source counts were one of the earliest lines of evidence in favour of the big bang cosmology in the 1960s. More recent results include those of Papovich et al. [2004], who used 24 μm *Spitzer* data to show that number counts exceed predictions by non-evolving models by an order of magnitude at $S_{24\mu m} = 0.1$ mJy. Berta et al. [2011], using *Herschel* data, presented number counts at 70 μm, 100 μm and 160 μm which agreed with more recent models, but with differences to the model redshift distributions.

2.8 A brief outline of theoretical models

The evolution of star forming galaxies involves a wide variety of physical processes, many of which are non-linear, and a full ab initio analytic or numeric model is a long way from our current capabilities. Three approaches to the subject have been taken in recent years: detailed simulations, simplified analytic models with tuneable free parameters (usually referred to as semi-analytic models), and a phenomenological approach called backwards evolution.

The first approach, N-body simulation, attempts to solve (in most cases numerically) the equations of gravitation, gas hydrodynamics, radiative cooling and transfer, magnetic fields, feedback from supernovae, interaction with black holes etc. for a large number of points (a recent model by Springel et al. [2005] uses 10^{10} particles). Simulations quickly become massively expensive (or prohibitive) in computer time. Insights gained from simulations are often used to constrain semi-analytic models (and vice versa).

Semi-analytic models have been developed in recent years (e.g. White and Frenk [1991]; Kauffmann et al. [1993]; Cole et al. [1994]), treating the evolution on galaxy scales by using approximations for the physics that underlies galaxy formation. They start with primordial density fluctuations and various physical assumptions about the parameters which determine star formation efficiency and feedback, and work forward to predict the present day situation. By taking galaxies as objects, rather than individual dust grains and photons, the computer

time is much reduced and the work simplified. For realistic modelling, the model must also include dust radiative transfer.

The third approach is a more empirically-driven method often referred to as backward-evolution (Lonsdale [1996]). Backward-evolution models start from observed $z = 0$ luminosity functions and evolve them back to earlier redshifts assuming various evolution parameters. This approach requires fewer parameters, but yields less physical insight than semi-analytic models since the underlying physics does not form the starting point. However, it can provide strong constraints to galaxy SEDs and evolving luminosity functions. The evolution of different types of galaxies will be modelled separately (e.g. Pearson and Rowan-Robinson [1996]). In preparing the ADF-S luminosity function in Chapter 4, I used the backward-evolution model of Lagache et al. [2004] in estimating the completeness of the sample used (Section 4.4), and compared the observed luminosity function at $z \leq 0.25$ with that predicted by the backward-evolution model of Gruppioni et al. [2011] (Section 4.6). Semi-analytic models involve a large degree of approximation and have the problem of a large number of free or unknown parameters, but are based on more fundamental physical and chemical conditions than back-evolution models.

Models may be used to investigate specific aspects of star formation and galaxy evolution. In particular, they may be used to forecast galaxy SEDs, and in Chapter 5, where I fit multi-wavelength observations of sources in the ADF-S to model SEDs, I discuss this in more detail (Section 5.2.1). Our knowledge of the evolution of star formation is likely to continue to be driven by observations. However, as observations improve the precision of constraints, theories are adapting and improving their ability to provide testable predictions.

2.9 Cosmological assumptions in this work

The work in this thesis has been done within the currently widely accepted ΛCDM model, assuming $H_o = 72.0$ km s^{-1} Mpc^{-1}, $\Omega_M = 0.3$ and $\Omega_\Lambda = 0.7$. Where results are compared with earlier results, the earlier results have been adjusted to conform with these values. Astrometry is given in J2000 coordinates throughout this thesis, and magnitudes are in AB units unless specified. For SFR calculations,

the Salpeter IMF has been assumed.

Recent results from the *Planck* mission suggest a lower value (67.8 $\pm$0.9 km $s^{-1}Mpc^{-1}$) for the Hubble constant and a higher value for matter density ($\Omega_M = 0.308 \pm 0.012$) (Planck-Collaboration [2015]). A recent study using WMAP, Planck and BAO data gives a value for the Hubble constant of 69.6 $\pm$0.7 km $s^{-1}Mpc^{-1}$ and $\Omega_M = 0.286 \pm 0.008$ (Bennett et al. [2014]).

Compared to the values I have used (and assuming similar errors), the Planck value for H_o is about 2.3σ below the value I used, and the WMAP/Planck/BAO value is 1.7σ below. The values for Ω_M in these recent studies are within 1σ of the value used. These revised estimates have not yet started to be used generally, and will not significantly affect the results in this thesis.

Chapter 3

AKARI Deep Field South: spectroscopic observations of infrared sources

The AKARI Deep Field South (ADF-S) is a low-cirrus field near the South Ecliptic Pole. Following its choice by AKARI as one of two deep fields for surveys, it has become the subject of extensive multi-wavelength follow-up observations. This chapter presents the first significant spectroscopic redshift survey in the field, covering the central 3.14 deg^2 using observations with the AAOmega fibre spectrograph. Targets were chosen mainly from AKARI catalogues (with the addition of a number of submillimetre sources) for which optical identifications could be obtained, and a total of 404 spectroscopic redshifts have been identified. The sources with identified redshifts include 316 with Hα detections at $z \leq 0.345$ and 15 sources at $z > 1$ which included either MgII or Lyα emission lines. The emission lines have been flux-calibrated with available photometric data and are used, together with line widths, to investigate various properties of these galaxies in this chapter. About 13% of the $z \leq 0.345$ sources are dominated by active galactic nuclei (AGN) emission, although many show emission from both star formation and AGNs. Star formation rates for these relatively local galaxies were typically $\leq 20 M_{\odot}\mathrm{yr}^{-1}$, and the median Balmer decrement was $\sim$5.9. For the higher-redshift sources, star formation rates were over $\sim 10^3 M_{\odot}\mathrm{yr}^{-1}$, and 12 ULIRGs and 11 HyLIRGs were found.

3.1 Introduction: The *AKARI* Deep Field South

The *AKARI* Deep Field South (ADF-S) is located close to the South Ecliptic Pole and has the major advantage of very low cirrus and zodiacal dust, which makes it an ideal field for extragalactic observations. The original field was observed by the

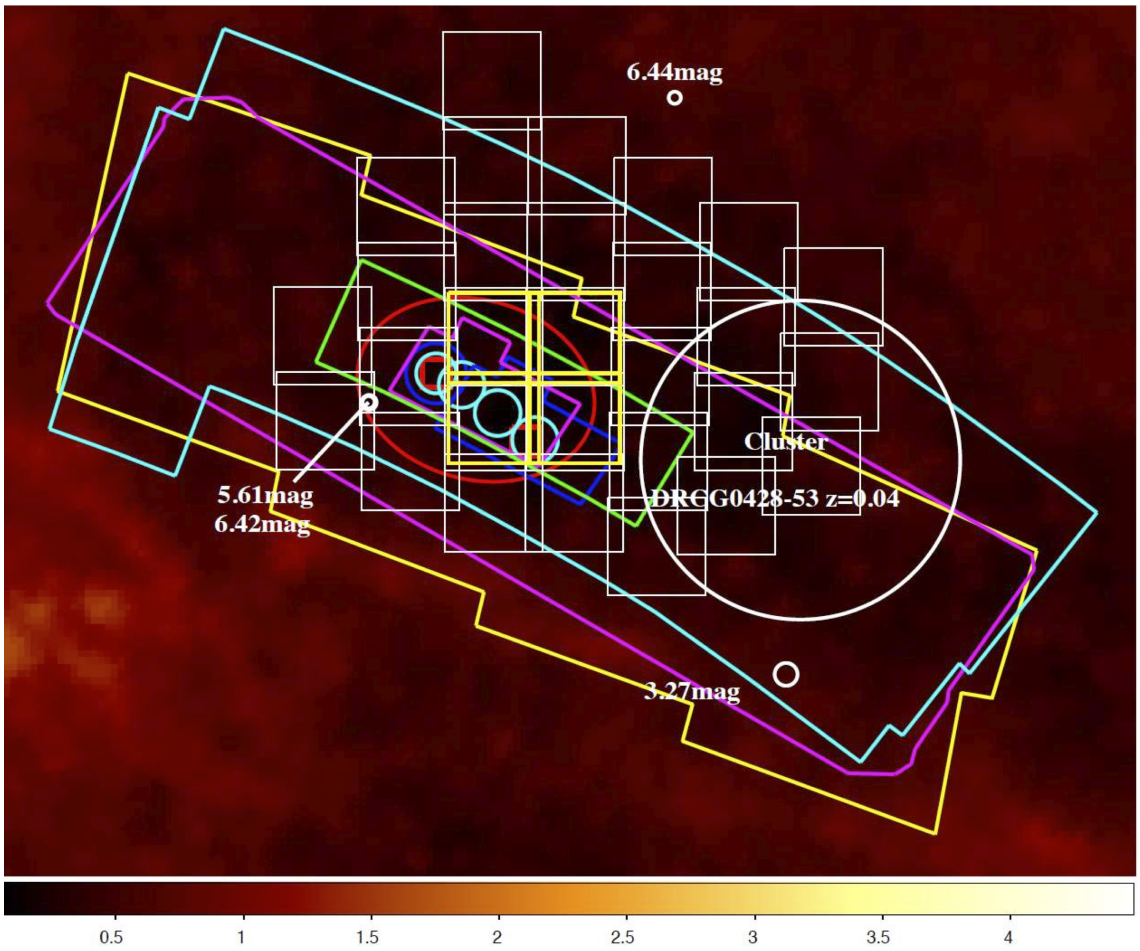

Figure 3.1: The *AKARI* Deep Field South (ADF-S). The background is the IRAS 100 μm cirrus map of the region (Schlegel et al. [1998]). The colour axis indicates $N_H \times 10^{19} cm^{-2}$. The large white circle at the right of the field is the Dressler cluster DRCG0428-53 at $z = 0.04$ (Dressler [1980]). The large cyan box shows the original 12 deg^2 ADF-S with *AKARI*-FIS observations. The large yellow box indicates the 11 deg^2 *Spitzer*-MIPS observed area. The large purple box is the BLAST area. The central irregular magenta/blue rectangles show the *AKARI*-IRC mid-infrared coverage. The white squares show the CTIO-MOSAIC R-band observed area. The red oval shows the ATCA radio observed area. The small cyan circles show the ASTE/AzTEC area.

AKARI Space Telescope in the far-infrared (Matsuhara et al. [2006]; Matsuura et al. [2011]) and covered a rectangular area of ∼12 deg^2 (see Figures 3.1 and 3.2) centred on RA 04 44 00, Dec -53 20 00.

A wide range of observations has now been made of all or part of this field at other wavelengths, including optical, near infrared, mid-infrared, submillimetre and radio. The largest catalogues (in the optical/near-infrared) found over 200,000 extragalactic sources in 1 deg^2; the 90 μm catalogue has 2,282 sources in the whole field (Shirahata et al., in preparation); the 20 cm radio catalogue has 530 sources in 2.5 deg^2 (White et al. [2012]). The multi-wavelength observations made to date will be covered in Chapter 5 and are listed in Table 5.1.

The spectroscopic observations described in this chapter covered the central 3.14 deg^2 of the ADF-S (the successful redshift identifications are shown Figure 3.9 below) and provide the results of the first spectroscopic campaign in the field. A key science goal was to generate redshifts for the preparation of a far-infrared luminosity function, since relatively few luminosity functions near the SED peak for star formation have previously been made: this is the subject of Chapter 4. Spectroscopic redshifts will also enable accurate calibration for the photometric redshifts achievable with the multi-wavelength photometric data now becoming available in this field.

The spectroscopy of active galaxies, the identification of redshifts and the methods of separating AGNs from star-forming galaxies are discussed in Section 3.2. The choice of targets, the spectroscopic observations and data reduction are set out in Section 3.3. The redshifts identified by the AAOmega observations and the flux calibration of emission lines are described in Section 3.4. The physical properties identified from spectroscopic data are described in Section 3.5 and discussed in Section 3.6. A local 90 μm luminosity function using some of this data will be presented in Chapter 4 and SED templates will be fitted to the multi-wavelength data available for these spectroscopic-redshift sources in Chapter 5.

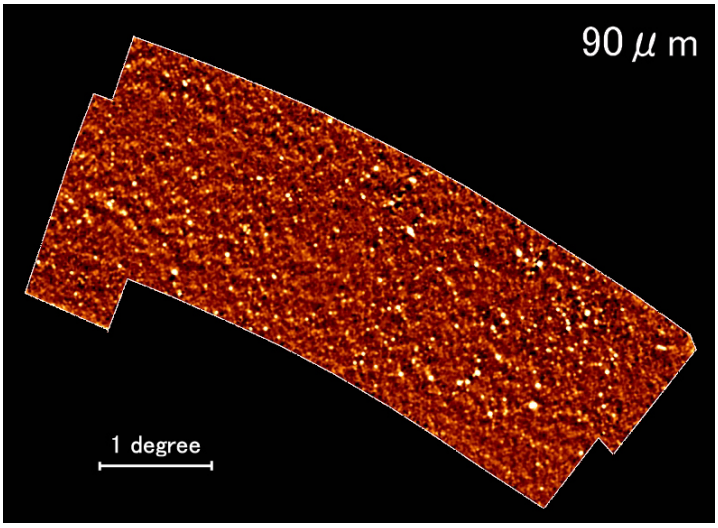

Figure 3.2: The *AKARI* 90 μm image of the ADF-S. A total of 2,282 sources were identified, down to ∼12.8 mJy with SNR>5. The confusion limit was ∼7.0 mJy.

3.2 Background: spectroscopy of active galaxies

3.2.1 Spectroscopic emission lines

Active galaxies can be studied by the emission lines in their spectra. Redshifts can be accurately measured by the shifts of well-known lines from their rest-frame wavelengths; once this is known, line fluxes can be converted to source luminosities and used to calculate the abundance of atoms and molecules and to estimate star formation rates; broad line widths can indicate rapid atomic motion typical of AGNs; the existence of particular lines will indicate the metallicity and ionisation levels of the source; and line ratios can indicate the amount of dust obscuration from the source to the observer. Continuum emission levels and breaks in the continuum (e.g. the 4000 Å break, caused by absorption by metals in stellar atmospheres) can also yield important information.

The spectroscopic observations used in this thesis have been from ground-based instruments in the optical region of the spectrum in this chapter and in Chapter 8, and from *AKARI* observations in the near-infrared region in Chapters 6 and 7. The main emission lines which have been detectable for active galaxies

with these instruments in these regions are outlined below.

Most of the sources covered in this thesis were selected from infrared and sub-millimetre catalogues, since star formation takes place in cool dense[28] molecular clouds, which absorb much of the optical/UV radiation from star formation and re-radiate it in the far infrared (as discussed in Section 1.3). To obtain accurate position coordinates for spectroscopy (and ensure they are visible in the region being observed) the targets needed to be matched to an optical (or near-infrared) catalogue.[29]

Emission lines and spectroscopic redshifts

Spectroscopic redshifts give us the most precise indicator with which to estimate the distances of objects. The alternative, photometric redshifts, are less precise and sometimes less reliable (they are discussed in Section 5.2.2 below).

A number of automatic redshift-identification routines have been used for large field studies such as the SDSS redshift surveys (for a review, see Baldry et al. [2014]). Previous codes used for AAOmega spectra include RUNZ (used for the 2dFGRS) and AUTOZ (used by GAMA). In this thesis, redshifts were identified by viewing individual spectra by eye (using IRAF or with the aid of a redshift emission-line template GUI discussed in Appendix A) so these automatic codes are not discussed further.

The main emission lines in the regions observed are shown in reference figures for emission lines in quasars in Figure 3.3 and for starburst galaxies in Figure 3.4 and are also tabulated in Table 3.1. For the work in this thesis, only atomic lines were observed, so molecular lines will not be discussed. The main emission lines seen in our observations are discussed below, grouped into wavelength regions in which they are normally detected together, starting with the longest rest-frame wavelengths.

Hα, [NII], [SII] and nearby O lines

For the optical spectroscopy in this thesis, the lines with the longest wavelengths which were observed were the first Balmer line from neutral hydrogen

[28] Molecular clouds have internal temperatures of $\lesssim$ 20K and average densities $\gtrsim 10^2$ molecules cm^{-3}.

[29] Radio interferometry catalogues can also be used to obtain more precise coordinates.

3.2.1 Spectroscopic emission lines

Table 3.1: The main emission lines observable for sources in the ADF-S which were targeted with AAOmega. See text for more details. See also Figures 3.3 and 3.4.

Emission line	Restframe wavelength(s) (Å)	Description / observation	Diagnostics		
			BPT diagram	Balmer decrement	Metallicity R23
Lyα	1216	Broad line (asymmetric)			
CIV	1549	Broad line			
CIII]	1909	Broad line			
MgII	2798	Broad line; often seen for 1.0<z<1.7 sources			
[NeV]	3426	Occasionally observed; =hard radiation			
[OII]	3727, 3729	Often observed			Yes
[NeIII]	3869	Occasionally observed			
Hγ	4340	Occasionally observed			
[OIII]	4363	Weak; rarely identified			
Hβ	4861	Often observed	Yes	Yes	Yes
[OIII]	4959, 5007	Often observed; distinctive ratio 1:3	Yes		Yes
[OI]	6300	Occasionally observed			
Hα	6563	Always observed when in range; FWHM>500 kms^{-1}=AGN	Yes	Yes	
[NII]	6548, 6583	Often observed	Yes		
[SII]	6716, 6731	Often observed			
[OII]	7325	Not observed			

(transition n=3→n=2), Hα λ6563 Å, the ionised nitrogen doublet which flanks this, [NII] $\lambda\lambda$6548, 6583 Å, and the distinctive ionised sulphur doublet [SII] $\lambda\lambda$6716, 6731 Å. All five lines were usually seen together (unless the [SII] fell outside the wavelength range observed) and where present enabled a decisive redshift determination. Hα is in the optical region for galaxies at $0 < z \lesssim 0.35$. These lines are from gas in HII regions surrounding the stars and are diagnostic of active galaxies; the ratio [NII]/Hα is used in BPT diagrams[30] to identify AGNs. The Hα line luminosity can be used to estimate the star formation rate (see Equation 2.3).

The neutral oxygen line [OI] λ6300 Å line is fairly weak, but was sometimes seen in the optical spectroscopy in this chapter. The ionised oxygen line [OII] λ7325 Å line also falls within the observed optical region and was potentially observable for low-redshift sources, but was not seen.

Hβ, [OIII] doublet

The second Balmer line (n=4→n=2) Hβ λ4861 Å was also commonly seen,

[30]BPT diagrams are discussed in Section 3.2.2.

and with the nearby doubly-ionised oxygen doublet [OIII] $\lambda\lambda$4959, 5007 Å often presents a distinctive feature. [OIII] is an important pair of lines in optical spectroscopy, and is easy to recognise since not only is it close to Hβ but the lines are typically in a 1:3 ratio (assuming Case B recombination, that all lines escape the region except Lyman lines higher than Lyα).

An important measure of dust attenuation is the Balmer decrement, defined as Hα/Hβ. This varies only slightly with temperature, and is typically close to 3 for unattenuated lines. The ratio [OIII]/Hβ is also used in BPT diagrams. The width of the [OIII] emission line is sometimes used as a proxy for stellar velocity dispersion (σ_*).

[OII], [NeIII], Hγ

The ionised oxygen lines [OII] $\lambda\lambda$3727, 3729 Å form a closely spaced doublet usually seen as a single line, but sometimes showing a distinctive width. Although near the low-wavelength end of the spectral region for low-redshift targets, which was usually quite noisy, this line was often detected, sometimes confirming an identification where other lines were tentatively detected.

The doubly-ionised neon line [NeIII] λ3869 Å is close to this [OII] line and was occasionally observed. The third Balmer line (n=5→n=2) Hγ λ4340 Å was also occasionally observed, but [OIII] λ4363 Å was not usually seen. The quadruply-ionised neon line [NeV] λ3426 Å was sometimes seen, evidence of hard radiation.

High-redshift lines observed

The ionised magnesium line MgII λ2798 Å is redshifted into optical wavelengths for higher-redshift sources ($1.0 < z < 1.7$). This is one of the strongest lines (it is a doublet, $\lambda\lambda$2797, 2803 Å), with a characteristically broad shape (see Figure 3.3), and was observed in sources in this range of redshifts. CIV λ1549 Å and CIII] λ1909 Å were also observed in high-redshift detections, and are also very broad lines. The neutral hydrogen Lyman transition (n=2→n=1) Lyα λ1216 Å is shifted into the optical region above redshifts of $z \sim 2.1$ and was one of the lines providing identification of the two highest redshifts found in this chapter; it was also seen for a source in Chapter 8.

3.2.1 Spectroscopic emission lines

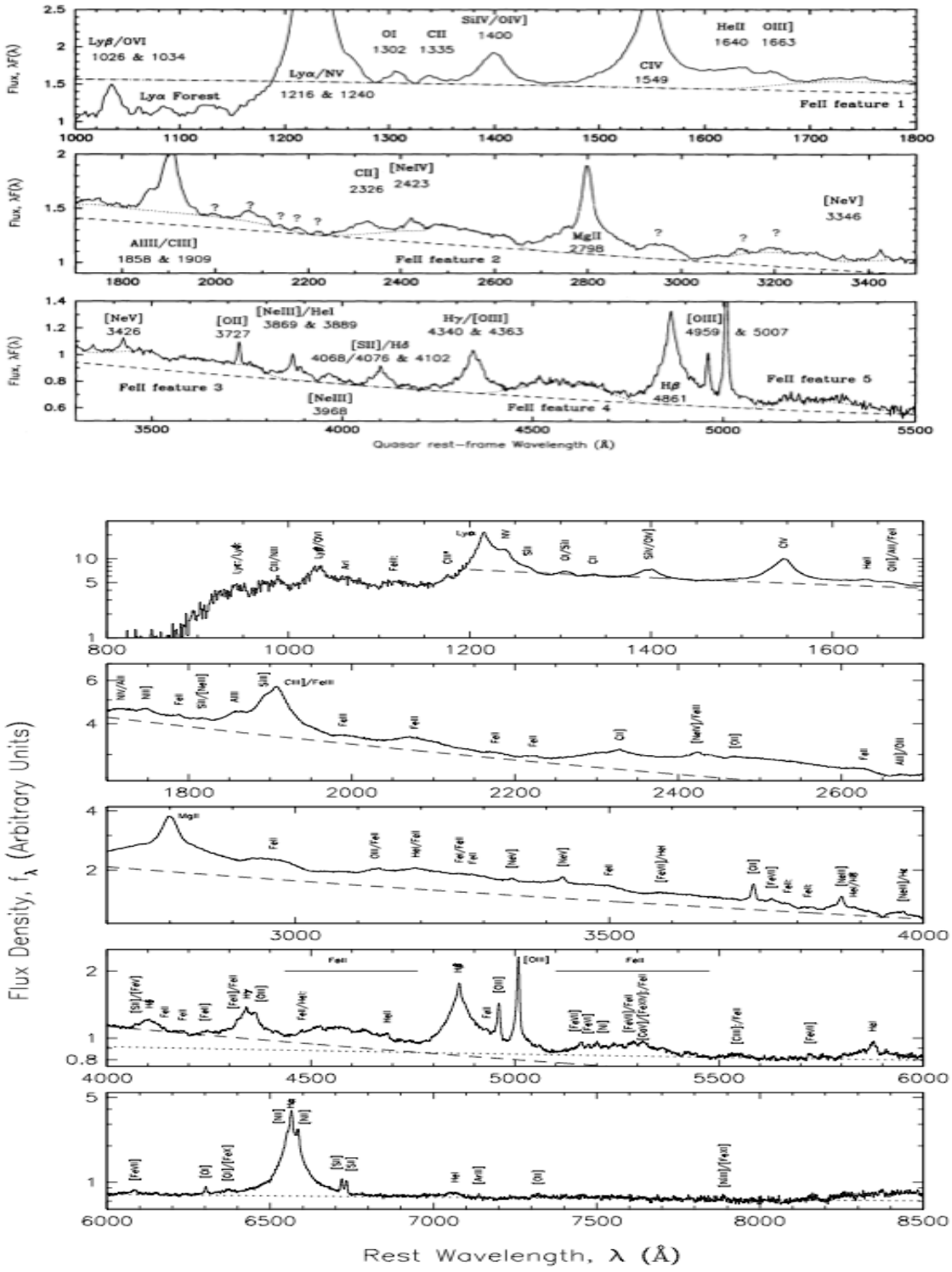

Figure 3.3: **Top:** UV/optical emission lines in quasar spectra from 1000 Å to 5500 Å from Francis et al. [1991]. The figure is based on 718 individual spectra. **Bottom:** emission lines in quasar spectra from 800 Å to 8500 Å from vanden Berk et al. [2001] based on over 2200 SDSS spectra. Star-forming galaxies have similar emission lines, although with different widths and line ratios: see Figure 3.4.

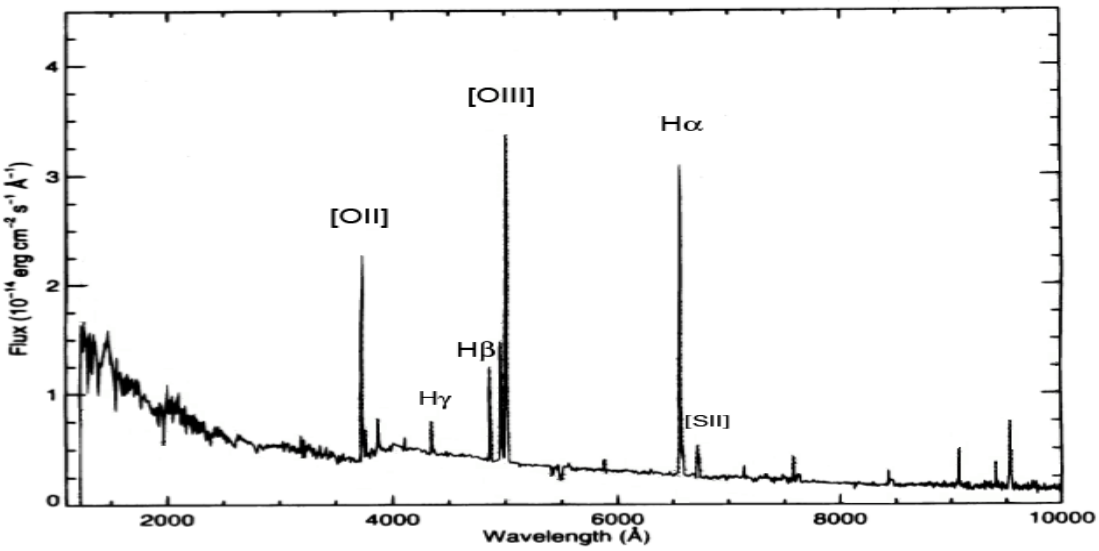

Figure 3.4: UV/optical emission lines in starburst spectra from 1500 Å to 10000 Å from Kinney et al. [1996]. The figure is based on the central regions of 35 starburst galaxies (described in Calzetti et al. [1994]) with low extinction (E(B-V)$<$ 0.1). Line identifications have been added: for identification of other emission lines, see Figure 3.3.

Metallicity

Line intensity ratios can be used to estimate metallicity. A well-known formula (referred to as R23) uses oxygen abundance (12+log(O/H)) as a tracer for metallicity (Pagel et al. [1979]; Kobulnicky and Kewley [2004]; Geller et al. [2014]):

$$\mathrm{R23} = \frac{[\mathrm{OII}]\lambda 3727 + [\mathrm{OIII}]\lambda 4959 + [\mathrm{OIII}]\lambda 5007}{\mathrm{H}\beta} \tag{3.1}$$

although this may need to be corrected for the ionisation level, to which it is also sensitive. Better estimates start with the electron temperature, which can be measured by [OIII] $\lambda 5007/\lambda 4363$; however the $\lambda 4363$ was usually too weak to be observed in the data analysed in this thesis.

3.2.2 Separating AGNs from star forming galaxies

A key question in examining mid- and far-infrared selected galaxies is to separate the luminosity from AGN accretion and the luminosity from star formation. One

method is to use line widths: the accretion disc around an AGN (and outflows in the narrow-line region) will cause Doppler broadening of the emission lines observed, and a Hα line width over $\sim$500 km s^{-1} is likely to indicate an AGN. Another commonly used method is to use line ratios: the relative strengths of the lines of highly ionised elements can be used as a proxy for the hardness of the radiation. These ratios are most reliable when the effect of relative dust obscuration is minimised (by choosing lines which are close in wavelength in the UV/optical, or FIR lines which are not affected by dust obscuration) and when the effect of differing abundances is eliminated (by using the same element). The first effect is achieved in the BPT diagram, which is described next.

BPT diagram

The Baldwin Phillips Terlevich (BPT) diagram (Baldwin et al. [1981]) uses a plot of [NII]/Hα vs. [OIII]/Hβ emission line intensity ratios[31] to distinguish AGNs from star-forming galaxies. AGNs have much harder radiation than hot stars, causing more ionisation of the nitrogen and oxygen atoms, increasing the intensities of these two forbidden lines. Two demarcation lines are often used with this plot: firstly, the Kewley line (Kewley et al. [2001a]; Kewley et al. [2001b]) to identify starburst galaxies:

$$\log_{10}([\text{OIII}]/\text{H}\beta) < 0.61/[\log_{10}([\text{NII}]/\text{H}\alpha) - 0.47] + 1.19 \tag{3.2}$$

and secondly, the Kauffmann line (Kauffmann et al. [2003]) to identify AGNs:

$$\log_{10}([\text{OIII}]/\text{H}\beta) > 0.61/[\log_{10}([\text{NII}]/\text{H}\alpha) - 0.05] + 1.3 \tag{3.3}$$

The region between the two lines is considered a composite region showing evidence of emission from both AGNs and star-forming galaxies. Earlier demarcation lines were empirical, but the Kewley starburst line was modified by the results from population synthesis models and photoionisation models to produce more

[31] Baldwin et al. [1981] also proposed various other pairs of line ratios; the advantage of the ones which have become popular is that, as well as being relatively strong, the lines in each ratio are close in wavelength, eliminating the need to estimate extinction, which varies with wavelength.

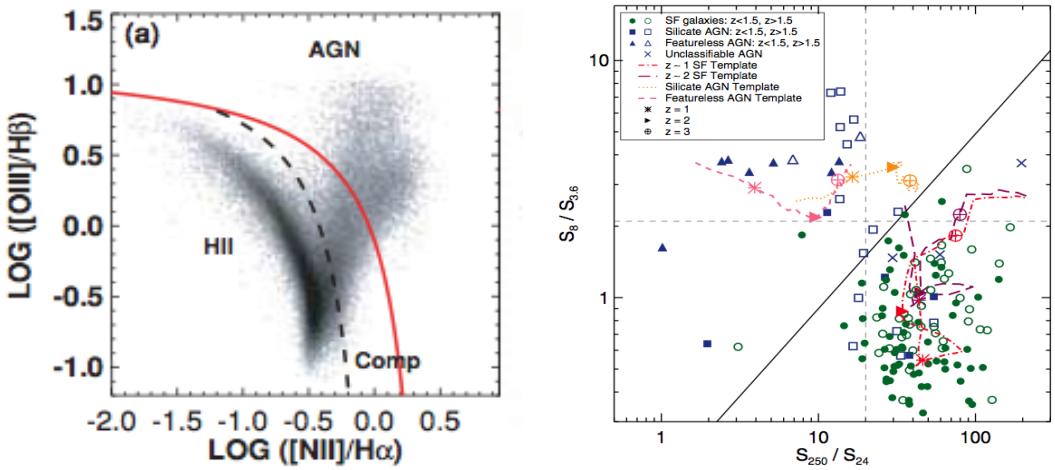

Figure 3.5: **Left:** A BPT diagram from Kewley et al. [2006] showing the Kewley (red) and Kauffmann (black dashed) demarcation lines discussed in the text, plotted over a background of $\sim 85,000$ SDSS DR4 emission-line galaxies. Starburst galaxies form a sequence on the left; the region between the two lines identifies sources with both star-formation and an AGN. **Right:** an example of a colour-colour diagram separating AGNs (blue) from star-forming galaxies (green); figure from Kirkpatrick et al. [2013].

reliable results (Kewley et al. [2001b]), in particular by placing galaxies with evidence of weak AGNs ('low-ionisation nuclear emission regions', LINERs) below the starburst line. The demarcation line is based on both the hardness of the radiation field and the metallicity of the line-emitting gases, resulting (non-trivially) in a curved boundary. The Kauffmann line is empirical. The two lines are shown in relation to $\sim 85,000$ SDSS emission line galaxies in Figure 3.5 (left). The distinction between star-forming sequence (labelled HII in the figure) and AGNs is shown to be clearly separated by the lines.

The BPT diagram diagnostic was recently confirmed out to $z \sim 1.5$ (Juneau et al. [2014]). It has recently been modified to a formula (though still using the same ratios) for higher-redshift galaxies (Kewley et al. [2013]), who also found that the usual diagram is not appropriate at $z \geq 1.5$. However, another recent study found that the BPT diagram was effective in distinguishing AGNs from starbursts out to $z = 2.3$ (Coil et al. [2015]). A variation to the BPT diagram proposed using Hβ, [OIII] and [OII] was proposed in Davies et al. [2014]. Also, a recent paper has suggested a 3-D extension of these ratios (Vogt et al. [2014]).

3.2.2 Separating AGNs from star forming galaxies

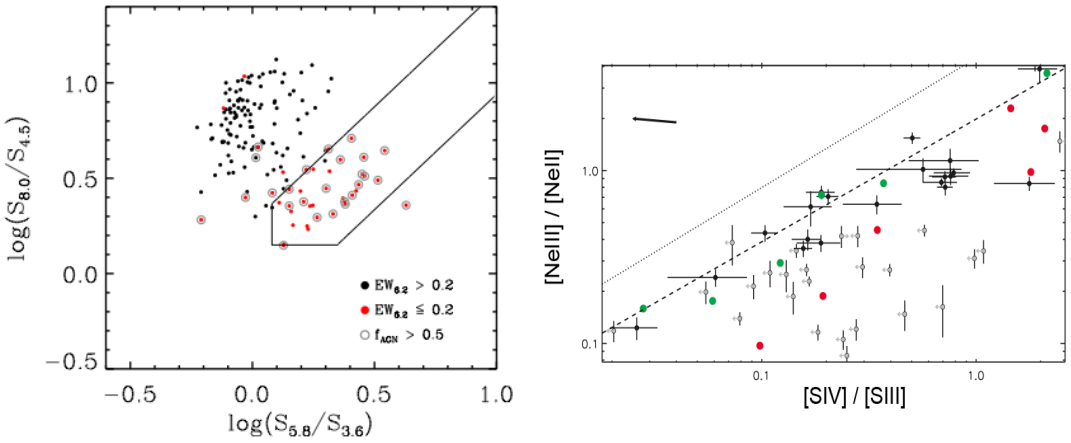

Figure 3.6: **Left:** The *Spitzer*-IRAC mid-infrared bands wedge diagnostic for AGNs of Donley et al. [2012] compared to classification of 154 galaxies from the 5MUSES sample into AGNs vs. star-forming galaxies using 6.2 μm PAH equivalent widths (Magdis et al. [2013]). Red circles show sources with $EW_{6.2} \leq 0.2$ μm (suggesting destruction of PAHs by an AGN) and black circles show sources with $EW_{6.2} > 0.2$ μm. Grey outer circles show sources with a further test: their SEDs suggest >50% L_{FIR} is due to AGN activity. **Right:** Line ratio diagnostics for sample of 53 ULIRGs (Farrah et al. [2007]): [NeIII] λ15.56 μm / [NeII] λ12.81 μm vs. [SIV] λ10.51 μm / [SIII] λ18.71 μm. Green symbols represent starbursts and red symbols represent AGNs.

An analysis to find the split between SBG- and AGN- powered galaxies in *Spitzer* 70 μm data in the Extended Groth Strip field found that although $\sim$ 13% hosted an AGN, virtually all (60 out of a sample of 61) were powered predominantly by starburst activity (Symeonidis et al. [2010]). In this chapter, $\sim$ 13% of the 192 sources for which the BPT diagram could be used (i.e., at relatively low redshifts) was found to be dominated by AGNs (see Figure 3.15). Mid-infrared selection is expected to find a higher proportion of AGNs: Toba et al. [2013], using *AKARI* IRC data, found that about 26% of their 9 μm sources and 41% of their 18 μm sources were AGNs. They found most local AGNs to be obscured, but with obscuration decreasing with increasing mid-infrared luminosity.

Evidence from mid-infrared spectroscopy

Mid-infrared spectroscopy has helped to distinguish between AGNs and starbursts. This region includes PAH features (discussed in Section 1.5) and a variety

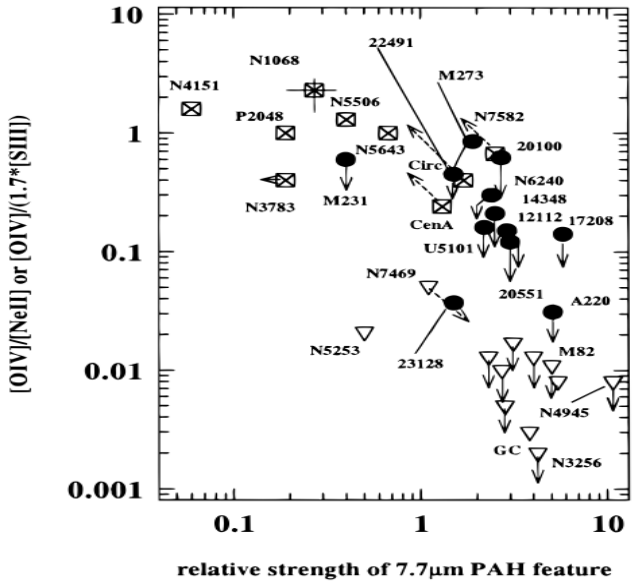

Figure 3.7: A diagnostic from Genzel et al. [1998], showing the [OIV] λ25.9 μm / [NeII] λ12.8 μm ratio plotted against the relative strength of the 7.7 μm PAH feature. Known starbursts are shown as triangles, known AGNs are squares with crosses, and ULIRGs are filled circles.

of emission lines from ionised atoms, in particular neon and sulphur, in addition to some molecules. The ratios between emission lines of atoms at different ionisation levels indicate the hardness of the radiation (i.e. the likelihood of AGN activity), in particular ratios involving [SIV] λ10.51 μm, [NeII] λ12.81 μm, [NeV] λ14.32 μm and [NeIII] λ15.56 μm (e.g. Madden et al. [2006]; Farrah et al. [2007]; Magdis et al. [2013]; see Figure 3.6, right).

The first extensive work in this region used spectroscopy from the ISO (e.g. Genzel et al. [1998]; Lutz et al. [1998]; Sturm et al. [2000]; see Figure 3.7). Many features were found, some previously unobserved; however, these emission features were largely absent in the hard radiation field close to an AGN, and also in intensely star-forming regions. Using an alternative diagnostic diagram for mid-infrared spectra and with combined ISO and *Spitzer* data, Spoon et al. [2007] has shown that most ULIRGs have simultaneous AGN and starburst activity in their nuclei.

The Great Observatories All-Sky LIRG Survey (GOALS; Armus et al. [2009]) obtained multi-wavelength data to study 202 local ($z < 0.088$) LIRGs ($10^{11} L_{\odot} <$

3.2.2 Separating AGNs from star forming galaxies

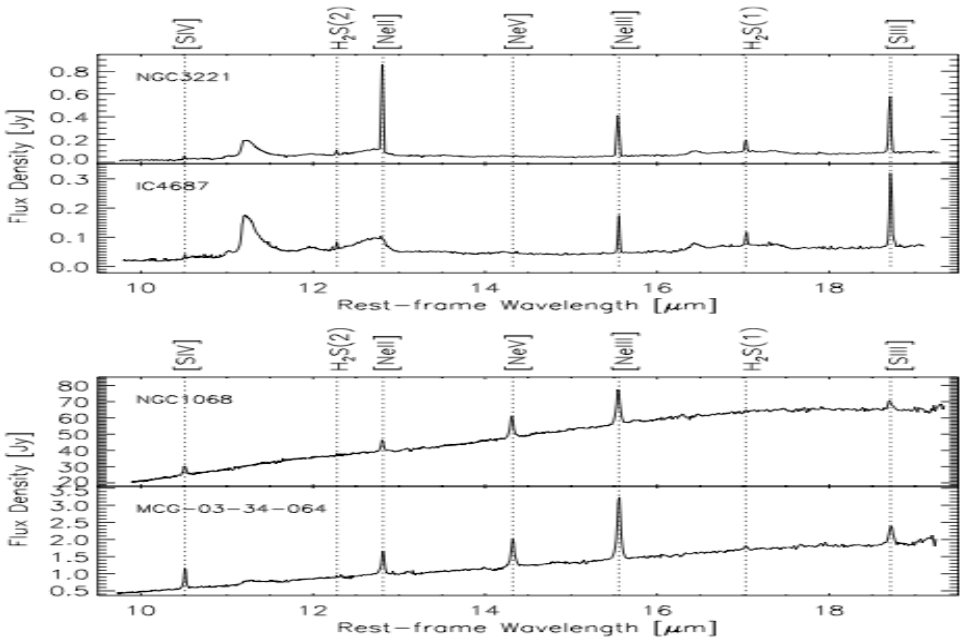

Figure 3.8: *Spitzer*-IRS mid-infrared spectra of representative starburst-dominated **(top)** and AGN-dominated **(bottom)** GOALS sources (figure from Inami et al. [2013]). Note the higher [NeV]/[NeII] line flux ratio and the absence of the PAH features (in particular at 11.3 μm) in the AGN-dominated sources.

$L_{IR} < 10^{12} L_{\odot}$) which included both AGNs and starbursts identified by optical line-ratio diagrams. It was found that the energy from LIRGs was dominated by starbursts. Petric et al. [2011], using *Spitzer* mid-infrared spectroscopy, found that ∼12% of the total energy emitted by the LIRGs came from AGNs; that 18% contained an AGN, and that in 10% AGN emission was the dominant energy source. Inami et al. [2013], also using the *Spitzer* mid-infrared spectroscopy, detected a variety of emission lines as well as PAH features (see Figure 3.8). They found that more than 75% of the galaxies were dominated by starbursts based on the [NeV]/[NeII] line flux ratios and the width of the PAH features. Far-infrared line ratios have been used with observations by *Herschel* (e.g. Rigopoulou et al. [2014]; Farrah et al. [2013]).

Other colour diagrams

Other colour-colour plots, using photometric data rather than relative emission line intensities, may be used to select or segregate types of galaxy popu-

lations. The success of this technique rests on the fact that different types of galaxies have differently shaped SEDs. Using IRAS fluxes, Helou [1986] found that for star-forming galaxies, the flux ratio 12 μm / 25 μm decreased as the flux ratio 60 μm / 100 μm increased. Soifer et al. [1987a] used a plot of 25 μm / 60 μm against 60 μm / 100 μm to separate starburst galaxies from quasars, BL Lacs and Seyferts. Star formation was characterised by warm 100 μm / 60 μm colours and AGNs by high 25 μm / 60μm colours (as would be expected from their SEDs).

In the mid-infrared the existence, equivalent widths and relative strengths of the various PAH bands can help to distinguish between AGNs and star-forming galaxies. Since these are bands rather than narrow lines, photometry from *Spitzer*-IRAC can be used since its four bands coincide to varying degrees with the PAH features (e.g. Laurent et al. [2000]; Peeters et al. [2004]; Donley et al. [2012]; Magdis et al. [2013]). For example, plotting 8.0 μm / 4.5 μm against 5.8 μm / 3.6 μm provides a successful diagnostic (see Figure 3.6, left).

Kirkpatrick et al. [2013] used a sample of 151 galaxies at $0.5 < z < 4$ with *Spitzer* spectroscopy and *Herschel* PACS and SPIRE data to evaluate the reliability of various colour plots in separating AGNs from star-forming galaxies. They found the best plots, with only $\sim$10% contamination rate, were (a) 250 μm / 24 μm against 8 μm / 3.6 μm (see Figure 3.5, right) and (b) 100 μm / 24 μm against 8 μm / 3.6 μm. Applying these diagnostics to the entire GOODS-*Herschel* survey, they found $\sim$10% of the galaxies have a significant AGN, rising to $\gtrsim$50% for the brightest sources. Huang et al. [2007] using an 8 μm selected local sample of *Spitzer* sources found that dust emission (mostly PAH) accounted for 80% of 8 μm luminosity, with AGN emission accounting for only 1%.

The IR8 ratio is also used to provide a diagnostic for AGN / SFG differentiation since PAHs are destroyed by hard radiation (this ratio was discussed in Section 2.7). Other diagnostic diagrams including colour-excitation diagrams (CEx; Yan et al. [2011]) and mass-excitation diagrams (MEx; Juneau et al. [2011]) have been proposed for cases where Hα and [NII] emission lines used in the BPT diagram are shifted out of the optical observing range (at about $z > 0.35$) or where all four lines are outside the optical range ($z \gtrsim 1$). These have not been used in this work.

3.3 AAOmega observations

3.3.1 Choice of targets

Targets were primarily chosen from sources in three *AKARI* catalogues: (a) the 90 μm catalogue (made public in 2010) of *AKARI*'s Far Infrared Surveyor Instrument (FIS; Kawada et al. [2007]; Shirahata et al. [2009]), (b) the 15 μm and (c) 24 μm catalogues of *AKARI*'s InfraRed Camera (IRC; Onaka et al. [2007]).

Three submillimetre catalogues were also used to select targets: ASTE/AzTEC at 1100 μm (Hatsukade et al. [2011]); APEX/LABOCA at 870 μm; and the Balloon-borne Large Aperture Submillimeter Telescope (BLAST; Pascale et al. [2008]; Valiante et al. [2010]) at 250 μm, 350 μm and 500 μm. These BLAST observations have now been superseded by observations by the SPIRE instrument on *Herschel* to greater depth at the same three wavelengths in the *Herschel* Multi-tiered Extragalactic Survey (HerMES; Oliver et al. [2012]), and the HerMES data will be used in the multi-wavelength work Chapter 5.

Sources were only targeted where optical counterparts could be identified. The B_J-band APM catalogue[32] (Maddox et al. [1990]) was used for optical cross-matching of the chosen sources, and optical identifications were then checked by eyeballing all the candidate sources using R-band images from the Digitised Sky Survey[33] (DSS) and (where available) images from the CTIO 4m telescope. DSS-R was chosen for eyeballing identifications of both IRC (mid-infrared) and FIS sources, partly because this was closer in wavelength to the IRC population and partly to match the available CTIO R-band data over part of the field. For the targets, a sparse sample based on the AAOmega fibre configuration was used. The area covered was π deg^2 (one AAOmega field-of-view). A few very local sources were extended optical objects, and the cross-identified *AKARI* coordinates were within the extended optical image. Where available, identifications were supported by sub-arcsecond positions from the 1.4 GHz Australia Telescope Compact Array survey (White et al. [2012]) and the *AKARI*-IRC data (Davidge et al. in preparation).

[32] http://www.ast.cam.ac.uk/∼mike/apmcat/
[33] https://archive.stsci.edu/cgi-bin/dss_form

Table 3.2: Summary of results of the spectroscopic observations with AAOmega in the ADF-S. Inactive fibres include pointings for guide stars, for the blank sky and unused fibres.

Observation date	Exposure time hr:m:s	Active fibres	Redshifts identified $z \leq 0.345$ Hα range	$0.345 < z \leq 1.0$ [OIII]/Hβ range	$1.0 < z$ [MgII] or Lyα	Total	Highest redshift
29 Oct 2007	2:30:00	262	115	32	9	156	2.357
30 Nov 2007	1:23:40	291	52	15	1	68	1.452
3 Jan 2008	2:00:00	316	44	33	3	80	2.858
27 Nov 2008(a)	1:46:40	352	75	5	3	83	1.810
27 Nov 2008(b)	0:26:40	271	63	2	1	66	1.486
Subtotal		1,492	349	87	17	453	
Multiple detections			-33	-14	-2	-49	
Total		1,492	316	73	15	404	

3.3.2 AA Omega observations

AAOmega (Saunders et al. [2004]), the fibre-fed optical spectrograph at the Anglo Australian Observatory, near Sydney, Australia, was used to obtain optical spectra of the targets which were all in the central 3.14 deg^2 of the ADF-S field. Observations were made in five observing runs over four nights between October 2007 and November 2008 as shown in Table 3.2. None of the nights was photometric. The gratings used were 385R and 580V with central wavelengths 7250 Å and 4800 Å, and wavelength resolution of $\lambda/\Delta\lambda$=1300. The AAOmega fibre spectrograph has 392 fibres available for taking simultaneous spectra. Most of the cross-identified optical sources were point sources, 94% of which fell within 10″, and all of which fell within 16″ of the *AKARI* coordinates. The *AKARI* telescope pointing error is less than 3″ (Murakami et al. [2007]). The effective beam sizes of the *AKARI* mission were 37″- 61″ (FIS) and 4.2″- 5.5″ (IRC). Artefacts in the AAOmega spectra to be avoided included various telluric lines and neon emission lines from street lighting in a local town (discussed in Chapter 4).

In total, 1,492 spectra were obtained over the five observing runs, from which spectroscopic redshifts for 404 sources were identified. Chapter 4 uses 130 of these spectroscopic-redshift sources to prepare a luminosity function of star-forming galaxies selected at 90 μm at $0 < z < 0.25$. Other studies have used ∼150 of these sources at $z < 0.25$ together with other sources from the *AKARI* 90 μm catalogue to cross-correlate with published optical data and prepare spectral en-

ergy distributions (Małek et al. [2010]; Małek et al. [2014]). The line fluxes for all the sources for which redshifts were identified are tabulated in Appendix B.

3.3.3 AAOmega data reduction

The spectra were reduced using the standard AAOmega pipeline 2dfdr data reduction software[34]. This included the removal of bad pixels, flat-fielding and use of an arc exposure for central wavelength and dispersion calibration. After sky subtraction, the two arms (blue and red) which had been reduced separately, were combined to form the final reduced file for each run. The combined spectra have a range of about 3800 Å to 8800 Å, although noise at either end of this range, particularly the blue end, often reduced the useful data to a range of about 4000 Å to 8700 Å. The flux is not calibrated in this reduction, so the available LaSilla/WFI R-band and CTIO MOSAIC II V-band photometry have been used to calibrate the flux (see Section 3.4.2).

The IRAF routine ONEDSPEC/SPLOT was then used to identify redshifts as described in Section 3.4.1 below, and to obtain other data from identified emission lines. I also wrote a graphic user interface (GUI; described in Appendix A) in IDL in order to visually identify additional emission lines by moving emission line templates across the spectra, whilst avoiding false positives by highlighting local lines and artefacts present in the data (shown in red and blue respectively in the spectra in Figures 3.10 and 3.11). As mentioned above, artefacts were found in many of the spectra (e.g. telluric lines at 5577 Å and a broad absorption feature at 7650 Å).

The quality of the spectra obtained varied widely between the different nights, as a result of varying atmospheric conditions and length of exposure times achieved for each set of targets (see Table 3.2). In a number of cases, the same object was scanned in two or three of the five observing runs. Where redshift identifications were successful, the results of each observation are shown in Appendix B.

[34]https://www.aao.gov.au/science/software/2dfdr

Table 3.3: The selection of sources for spectroscopy. For the BLAST targets, 25 were cross-matched to FIS 90 μm sources before observation, and 25 to IRC 24 μm sources.

Source	Total observations	Sources Observed	Redshifts identified z≤0.345	0.345<z≤1.0	1.0<z	Total	Success Rate
FIS 90 μm	392	319	181	7	2	190	60%
IRC 24 μm	319	157	34	38	10	82	52%
IRC 15 μm	584	522	48	24	3	75	14%
BLAST 250/350/500 μm	162	155	48	2	0	50	32%
AZTEC 1100 μm	21	12	5	2	0	7	58%
Other	14	11	0	0	0	0	
Total	1,492	1,176	316	73	15	404	34%

3.4 Data analysis

3.4.1 AAOmega observations: redshift identifications

An overall description of the emission lines available in the observed wavelength range was given in Section 3.2.1. The redshifts identified by atomic emission lines in this chapter fall into three bands, and the results are presented in this way in Tables 3.2 and 3.3. I have given the redshifts identified a quality flag of 1 to 3, with 3 being excellent (several very clear emission lines) and 1 being borderline (several lines but in a noisy spectrum usually with other unidentified lines or artefacts). A map of the sources for which redshifts were found is shown in Figure 3.9.

Firstly, sources at $z \leq 0.345$ could be identified by their Hα λ6563 Å line, which fell into our spectral range up to this redshift. The nearby [NII] $\lambda\lambda$6548, 6583 Å lines were usually also observed, as was the [SII] doublet $\lambda\lambda$6716, 6731 Å, unless it was redshifted out of range. Many other lines were also often seen, but identifications were not made without the Hα line which is expected to be the strongest in this wavelength region both for star-forming galaxies and for AGNs. Examples of these lines are shown in Figure 3.10.

Secondly, for sources at $0.345 < z \leq 1.0$, for which Hα is redshifted out of the observed wavelength range, the strongest observable lines are the three Hβ/[OIII]/ [OIII] $\lambda\lambda$4861, 4958, 5007 Å emission lines (up to about $z = 0.74$). Redshifts were only taken where there was evidence for at least two of these

3.4.1 AAOmega observations: redshift identifications

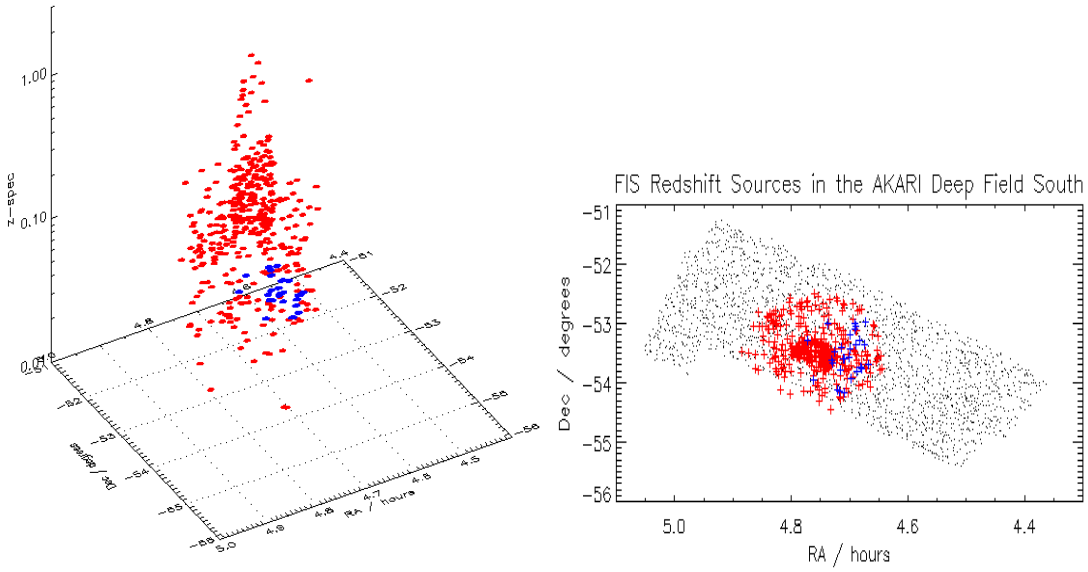

Figure 3.9: **Left:** A 3D plot of the 404 redshifts identified in the ADF-S. Cluster members are shown in blue (details of the cluster are given in Section 4.3.2). **Right:** A 2D plot of all *AKARI*-FIS sources in the ADF-S (black dots) over-plotted with spectroscopic redshift sources in red and (for cluster members) in blue.

three emission lines. Unfortunately, they sometimes coincided with artefacts in the spectra, and this is the main reason for some identifications being classed as borderline. In addition, the asymmetrical [OII] emission line resulting from the close doublet $\lambda\lambda$ 3726, 3729 Å was often found at the same redshift to support the identifications. Hγ λ4340 was not a very strong line in these sources, but was sometimes seen to support the identifications. Examples of these lines are shown in Figure 3.11.

Thirdly, after a gap in the redshift range without strong emission lines, there is a possibility of identifying several broad emission lines at redshifts $z > 1$. At about $1.0 < z < 1.7$ two strong lines are available - CIII] λ1909 Å and MgII λ 2798 Å - as well as several weaker lines. Above $z \sim 2.3$, Lyα λ1216 Å comes into range to support the CIV λ1549 Å and CIII] λ1909 Å emission lines. Such distant spectra were invariably very noisy, but these lines are broad and in some cases clear enough to be convincing. Hints of absorption lines from stellar atmospheres (e.g. MgI λ5175 Å) were seen in a few of the spectra. Examples of these

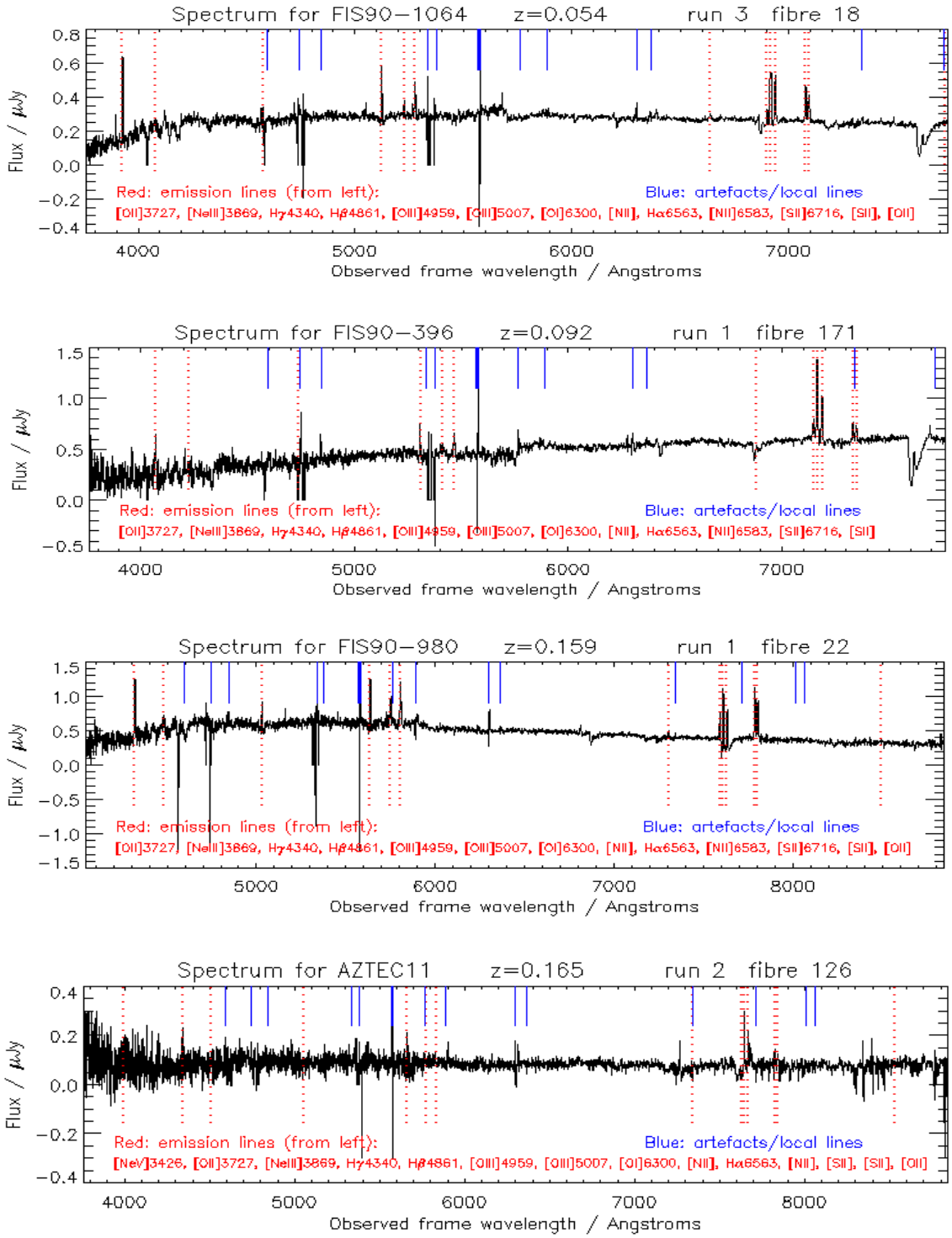

Figure 3.10: Examples of spectra at redshifts $z \leq 0.345$ (page 1 of 2) . The red vertical dotted lines are emission line templates at the given redshift. The blue vertical lines are artefacts, including lines from nearby street lighting. There are some telluric lines (e.g. the broad absorption feature at ~ 7650 Å). The spectra have not been smoothed. Note that the join between the blue and red arms of the spectrograph is visible at ~ 5700 Å in some of the spectra.

3.4.1 AAOmega observations: redshift identifications

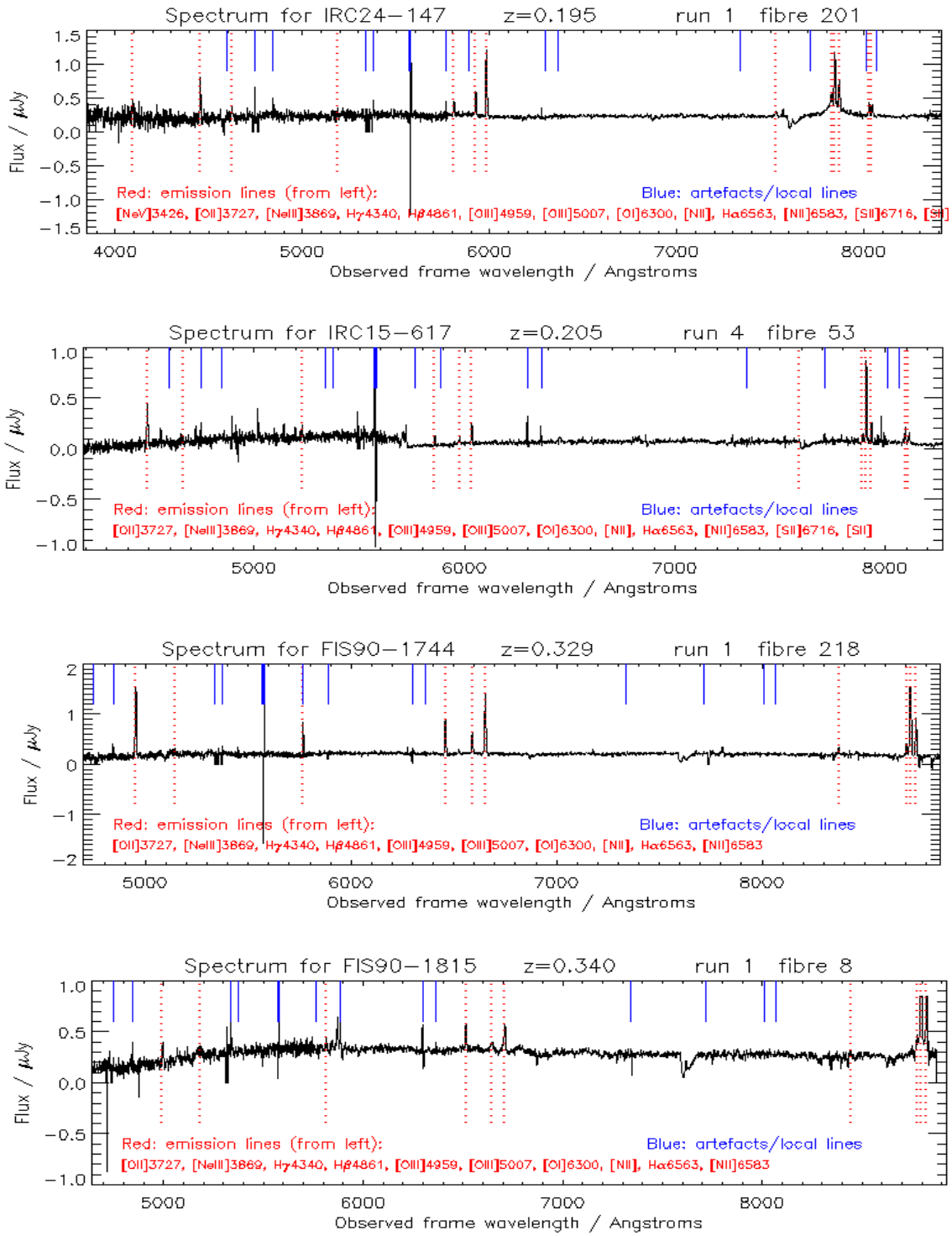

Figure 3.10: **(continued)** Examples of spectra at redshifts $z \leq 0.345$ (page 2 of 2).

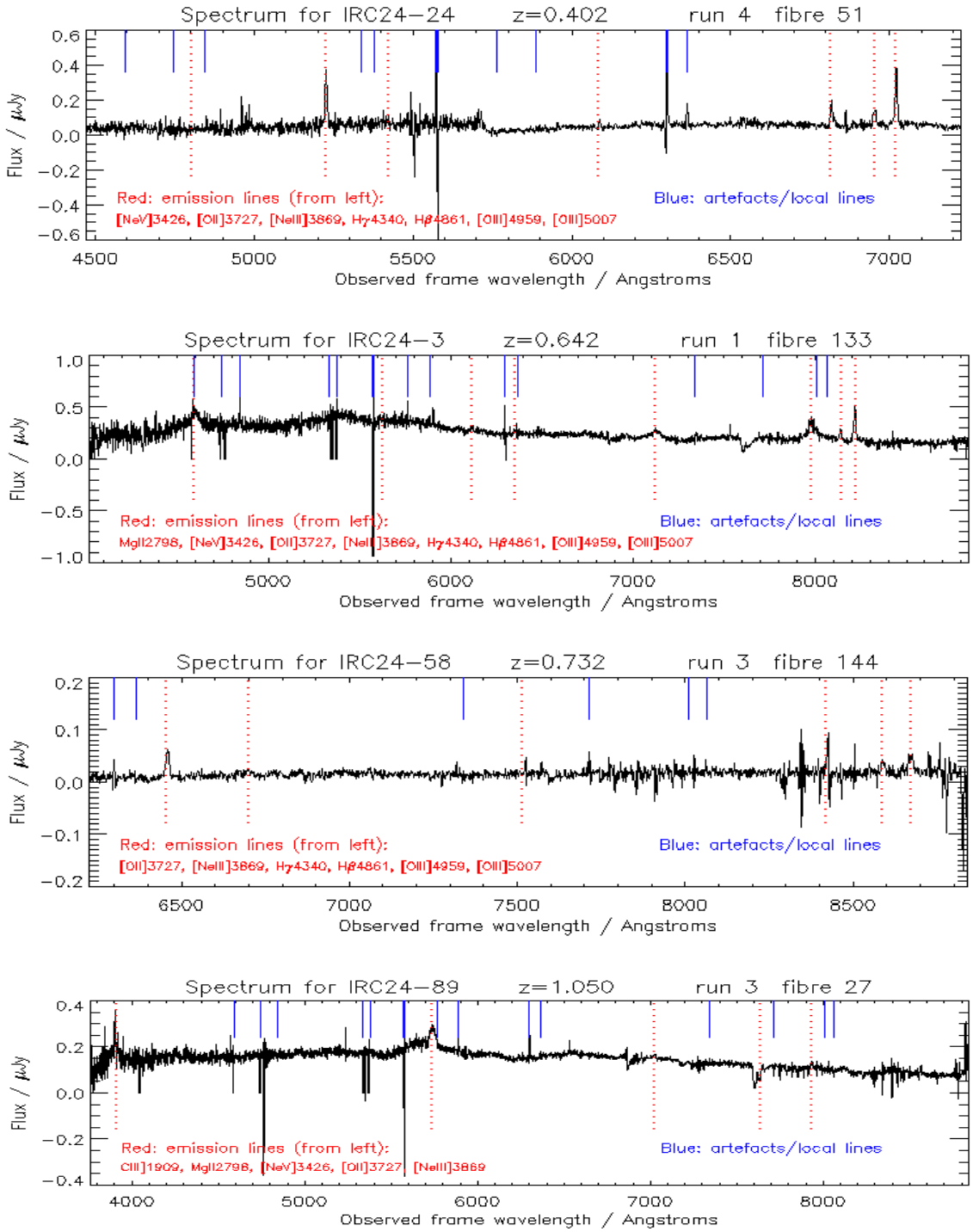

Figure 3.11: Examples of spectra at redshifts $z > 0.345$ (page 1 of 2). The red vertical dotted lines are emission line templates at the given redshift. The blue vertical lines are artefacts, including lines from nearby street lighting. There are some telluric lines (e.g. the broad absorption feature at ~ 7650 Å). The spectra have not been smoothed. Note that the join between the blue and red arms of the spectrograph is visible at ~ 5700 Å in some of the spectra.

3.4.1 AAOmega observations: redshift identifications

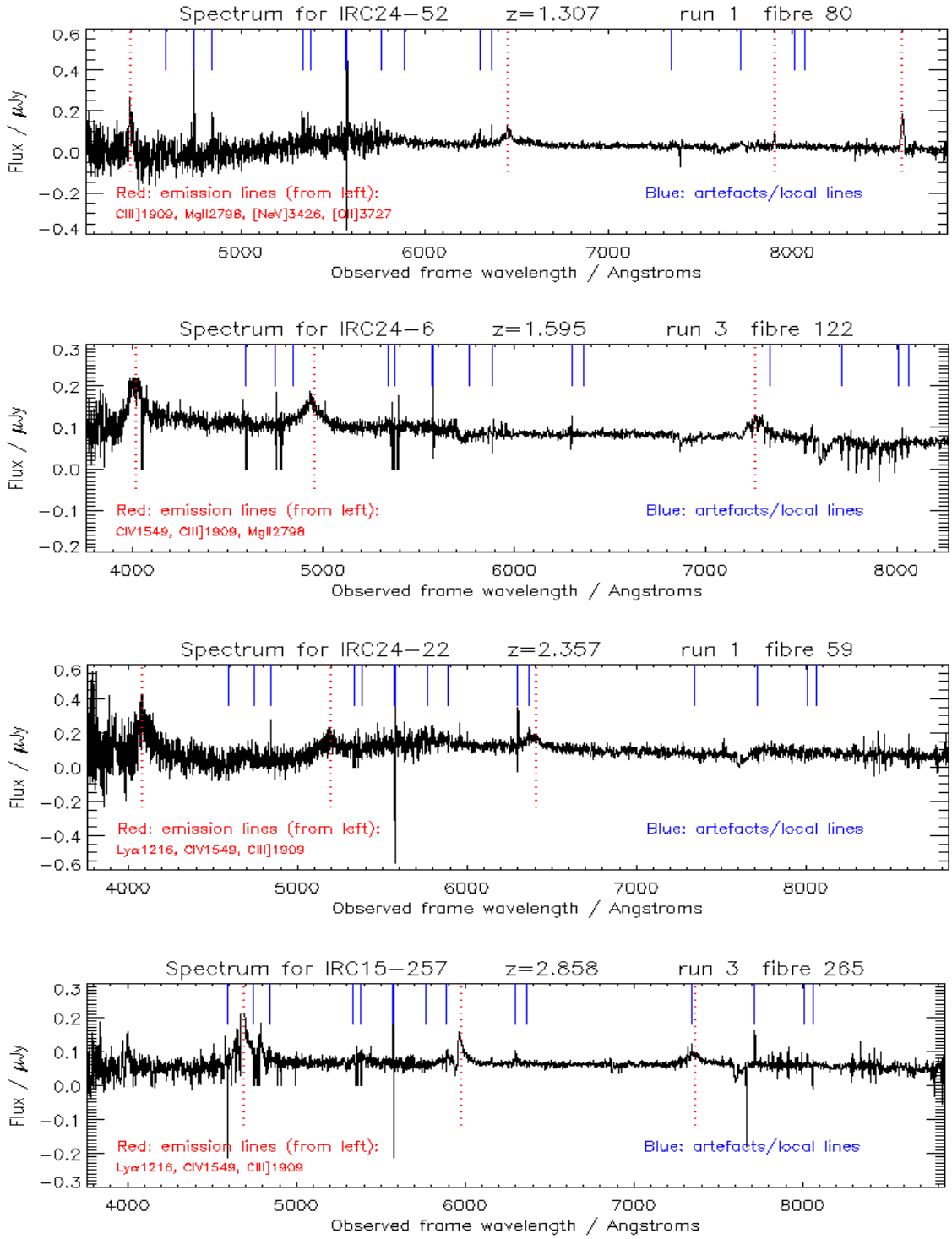

Figure 3.11: **(continued)** Examples of spectra at redshifts $z > 0.345$ (page 2 of 2). For IRC24-22, the relative fluxes of the three peaks shown are close to the predicted ratios of 100:63:29 (Francis et al. [1991]).

lines are shown in Figure 3.11.

Overall, a total of 404 redshifts were identified for the 1,176 sources targeted (see Tables 3.2 and 3.3). Detailed results have been tabulated in Appendix B: sources with $z \leq 0.345$ in Table B.1, sources with $0.345 < z \leq 1.0$ in Table B.2, and sources with $1 < z$ in Table B.3.

3.4.2 AAOmega observations: flux calibration

Flux calibration was not available in the AAOmega reduction pipeline[35]. To enable flux calibration, I have used two optical photometric catalogues: (a) the LaSilla MPG/ESO WFI R-band photometry (Baronchelli et al. [2016]) for sources for which the Hα emission line is dominant, and (b) the CTIO MOSAIC-II V-band catalogue, for which the Hβ/[OIII] emission lines are dominant (Baroncelli et al., in preparation). In each case, the spectral flux has been integrated over the wavelength range of the photometric filters. The photometric filters and the AAOmega grating throughputs used in this calculation are shown in Figure 3.12.

For the R-band calibration, I used sources with $0.0 < z < 0.115$ so that the Hα emission line would dominate the flux in the calculation. For the V-band, sources at $0 < z < 0.17$ were used so the three emission lines would form a significant part of the spectral flux. The data for each observing run and the χ^2 best-fits between the AAOmega flux and the WFI and CTIO fluxes are shown in Figure 3.13.

The R-band calibration falls within the red arm of the spectrograph and the V-band falls mostly within the blue arm (see Figure 3.12, red lines). The conversions are tabulated in in Table 3.4. The ADF-S field has also been observed in the R band by CTIO (Barrufet et al., in preparation), but the data has not yet been reduced so could not be used. It covered a wider area than the WFI data, so should give data for more accurate calibration when available.

[35]This may have been because of the difficulty in characterising the fibre throughput for all the fibres. The variation between fibres is one cause of the dispersion seen in Figure 3.13.

3.4.2 AAOmega observations: flux calibration

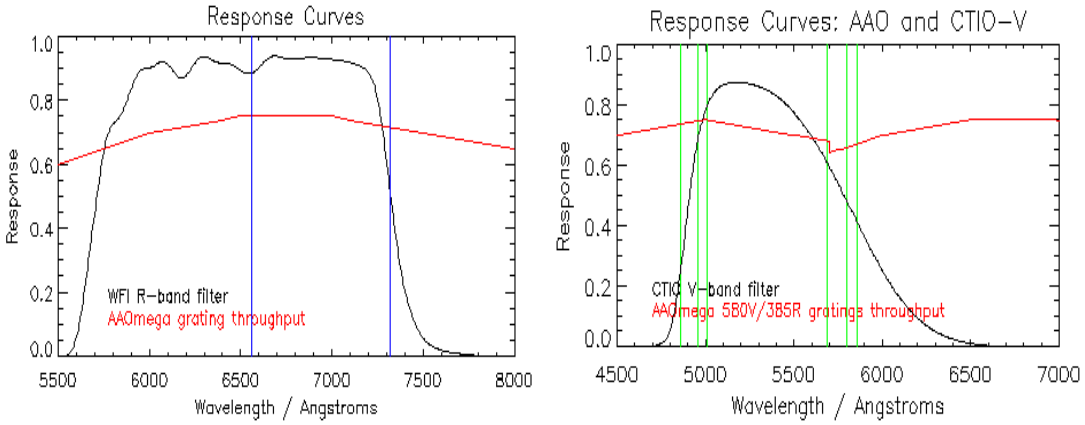

Figure 3.12: **Left:** The WFI R-band filter (black) and the AAOmega grating throughput in the same broadband range (red), both used in calibrating the AAOmega fluxes. The blue vertical lines indicate Hα line at the redshift range of the sources used in the calibration, $0.0 < z < 0.115$. **Right:** The CTIO V-band filter with the AAOmega gratings throughput. Note the discontinuity at 5700 Å in the AAOmega throughput is the join between the blue arm and the red arm. The three green vertical lines are the Hβ/[OIII] lines which dominate the emission in this region at the redshift range used in the calibration, $0.0 < z < 0.17$.

Table 3.4: Flux calibration table, from AAOmega units to mJy.

	AAOmega observing runs				
	Run 1	Run 2	Run 3	Run 4	Run 5
R-band (WFI)	1.04±0.13	0.95±0.33	0.46±0.11	2.04±0.15	8.08±1.01
V-band (CTIO)	1.06±0.12	1.26±0.37	0.54±0.11	1.26±0.17	5.53±0.61

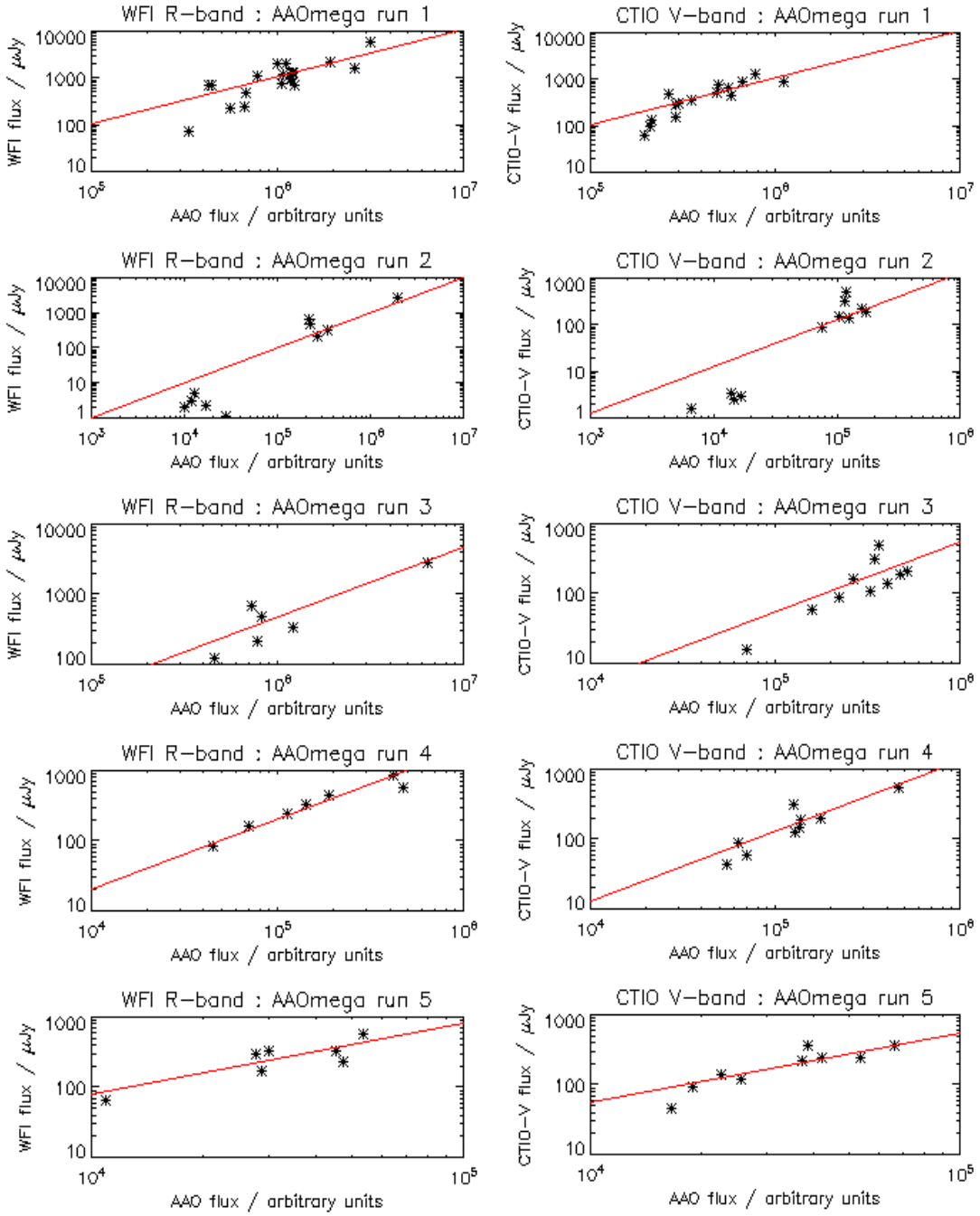

Figure 3.13: Calibration of AAOmega flux by WFI R-band photometry (for red arm) and CTIO V-band (for blue arm), for each of the 5 runs. The AAOmega fluxes were integrated across the bands shown in Figure 3.12. Linear χ^2 minimisation fits are shown with the intercept fixed at zero in each case. The fibres have varying throughputs, which is one reason for the dispersion seen. The dispersion measured for each run and each arm are used in calculating flux errors in Appendix B (see page 217).

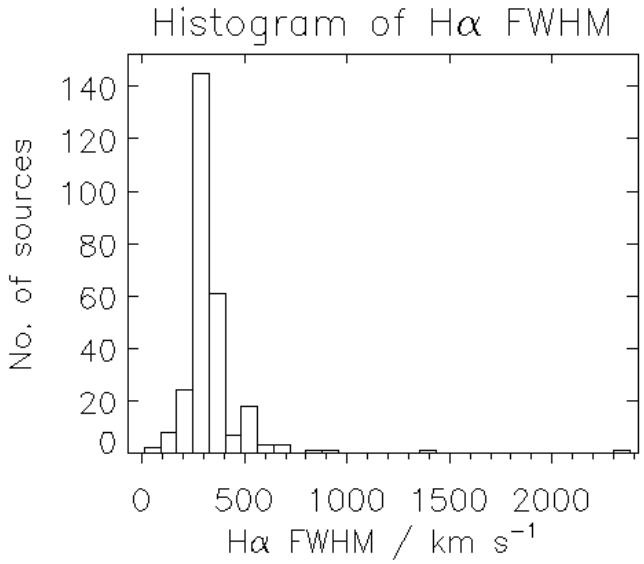

Figure 3.14: A histogram of the Hα FWHM for the 275 sources for which this could be measured. Almost all sources fall below ~ 500 km s^{-1}.

3.5 Results from analysis of spectral data

Separating AGNs and SFGs

For the 316 sources at $z \leq 0.345$, the FWHM of the Hα lines showed only two sources over 1000 km s^{-1}, and about 20 over 500 km s^{-1}, suggesting few of our sources are dominated by AGN emission. A histogram of the values for all individual sources is shown in Figure 3.14; most sources fall between 200 and 300 km s^{-1}.

An alternative empirical method for discriminating between AGN and SBG sources (discussed in Section 3.2.2) is the BPT diagram (Baldwin et al. [1981]), which plots the intensity ratio [NII] λ6583 to Hα λ6563 Å against the intensity ratio [OIII] λ5007 to Hβ λ4861 Å. The results of this are shown in Figure 3.15. The black line discriminates between AGN sources and SFG sources, based on the formula in Kauffmann et al. [2003], with a position above this line indicating an AGN. The red line, based on the formulae in Kewley et al. [2006], demarcates the area which contains AGN-SFG composite sources. This shows about 13% of sources dominated by AGN, with 28% in the intermediate region showing

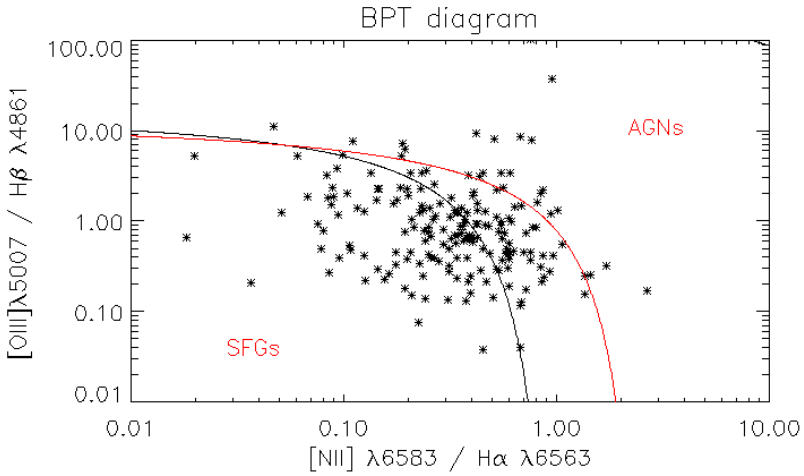

Figure 3.15: A BPT diagram for the 192 sources for which the two ratios have been determined by the AAOmega spectroscopy. The area between the black line (Kauffmann et al. [2003]) and the red line (Kewley et al. [2006]) indicates composite AGN-SFG sources.

evidence of both SFGs and AGNs. It is clear from these figures that most of the $z \leq 0.345$ sources are star-forming galaxies.

The ratio of [OIII] λ5007 /[OII] λ3727 Å was also considered as a possible AGN/SFG discriminator. However, this ratio proved unreliable: the two emission lines are not close and are from the two (blue and red) arms of the spectrograph which have different throughputs; in addition, there could be reddening intrinsic to the galaxies. This indicator usually conflicted sharply with the other indicators. In contrast, the two ratios used in the BPT diagram are each of lines which are close in wavelength, so are not affected either by throughput variations or by reddening.

Star formation rates

Star formation rates have been estimated based on Hα luminosity and on the total infrared luminosity based on the FIS flux at 90 μm, assuming an M82 spectral energy distribution (SED) and using the formulae from Kennicutt [1998b] given in Section 2.7. The result of these two calculations are plotted against each other in Figure 3.16. The expected attenuation of the Hα-based measure is not seen - in fact, the median star formation works out marginally higher,

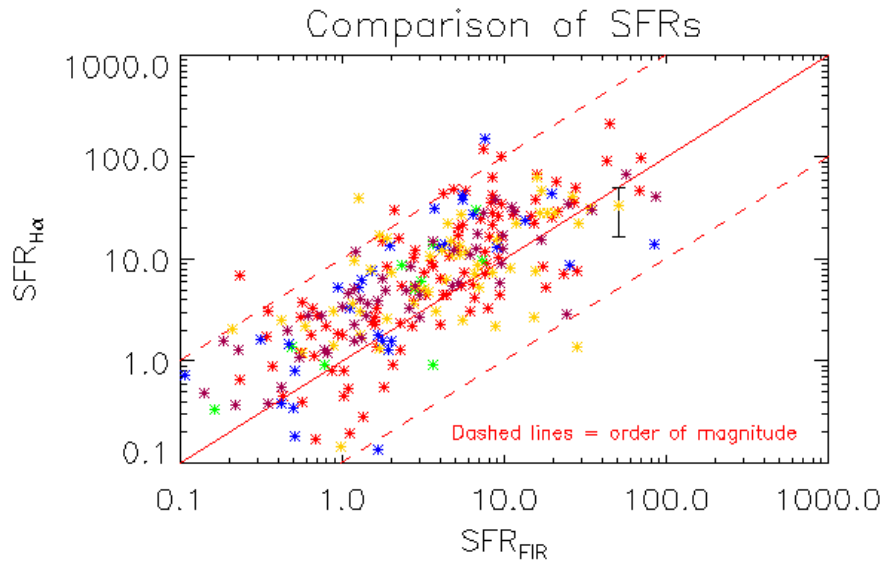

Figure 3.16: A comparison of star formation rates based on L_{FIR} (estimated from FIS 90 μm fluxes) and on $L_{H\alpha}$ for galaxies at $z \leq 0.345$. The five observing runs are colour-coded (red, green, blue, orange, brown respectively). The median star formation rates are 4.2 and 4.5 $M_{\odot}$ yr^{-1} respectively.

although well within the error (4.5 to 4.2 $M_{\odot}$ yr^{-1}, with error in the formulae alone estimated at 30%). It can be concluded that dust attenuation for these (relatively local) sources is low. Star formation rates based on total far-infrared luminosity (L_{FIR})[36] are plotted against redshifts in Figure 3.17. From this figure, it can be see that although most local sources are below the LIRG level and the typical star formation rates are shown as $0.1 - 20$ $M_{\odot}$ yr^{-1}, the sources at $z > 1$ are shown to be ULIRGs or HyLIRGs with star formation rates up to $\sim 10^3$ $M_{\odot}$ yr^{-1}.

LIRGs, ULIRGs and HyLIRGs

Using the *Spitzer*-MIPS 24 μm flux to estimate total far-infrared luminosity (based on the M82 SED) gave a total of 67 LIRGs, 11 ULIRGs and 11 HyLIRGs. However, these figures were lower if the *AKARI*-FIS 90 μm flux was used to estimate far-infrared luminosity, giving totals of 36 LIRGs and 1 ULIRG. This

[36]The estimation of star formation rates based on far-infrared luminosity is discussed in Section 2.7.

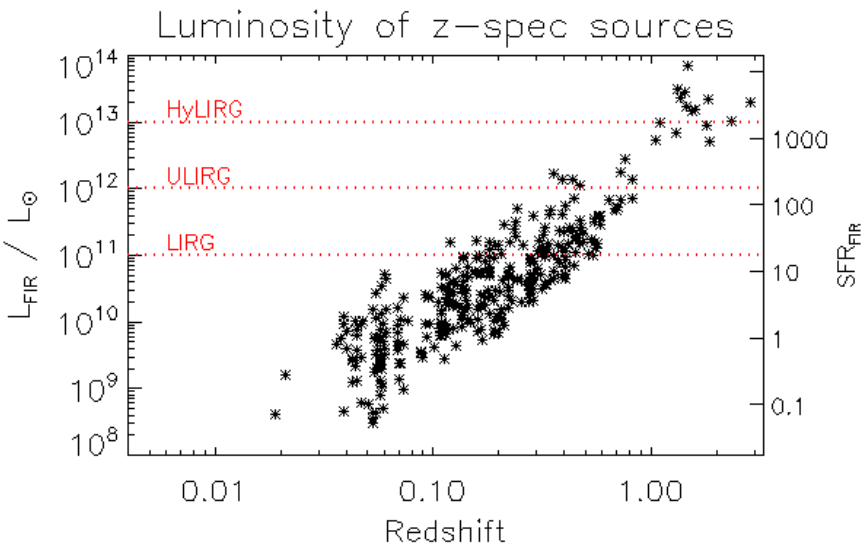

Figure 3.17: A plot of FIR luminosity and SFR based on L_{FIR} against redshift for sources detected at 24 μm by *Spitzer*-MIPS for all spectroscopic sources in the ADF-S. The L_{FIR} was estimated assuming the M82 SED, and the SFR (right-hand axis, in $M_\odot$ yr^{-1}) was estimated from this using the Kennicutt [1998b] formula (Equation 2.2).

may reflect the influence of AGNs on the 24 μm data; however, the *Spitzer* 24 μm observations reached far deeper than the *AKARI* 90 μm observations (200 μJy vs. 8.5×10^3 μJy: see Table 5.1) and is a far larger catalogue. Sources which were calculated to be ULIRGs or HyLIRGs by either method are listed in Table 3.5. It is interesting to compare this list to the ULIRGs and HyLIRGs found by SED fitting to the multi-wavelength data in Chapter 5, which are listed in Table 5.5.

Balmer decrement: dust obscuration

The Balmer decrement, the ratio between the different Balmer lines, is well known and is useful in astronomy because longer-wavelength emission lines suffer less from dimming by dust grains than shorter-wavelength lines (usually referred to as reddening). This means that measured decrements can be used as a measure of attenuation by dust, provided a simple dust screen is assumed (see Serjeant et al. [2002] for limitations to the accuracy of this assumption). The ratio Hα:Hβ is available for 266 of our spec-z sources and is plotted in Figure 3.18. It shows a mean decrement of 8.4, and a median of 5.9. (Some values are difficult to measure

Table 3.5: ULIRGs and HyLIRGs identified from either *AKARI*-FIS 90 μm flux or *Spitzer*-MIPS 24 μm flux via the M82 SED.

	Name	Luminosity			Redshift	RA (J2000)	Dec (J2000)	Figure ref.
		FIR-based (90 μm) $\log_{10}$L/L$\odot$	FIR-based (24 μm) $\log_{10}$L/L$\odot$	SED-based (Chapter 5) $\log_{10}$L/L$\odot$	z	h m s	d m s	
1	IRC15-253	12.0	11.7		0.692	04 47 28.8	-53 26 25	
2	IRC24-111		12.0		0.472	04 44 51.4	-53 27 14	3.20
3	IRC24-10		12.1		0.825	04 44 34.7	-53 43 47	
4	FIS90-219	11.8	12.1		0.395	04 51 55.2	-53 03 11	
5	FIS90-1735	11.3	12.1		0.438	04 42 52.3	-53 12 04	
6	FIS90-633	11.4	12.2		0.361	04 45 56.0	-53 16 34	3.20
7	IRC24-58	11.8	12.2		0.732	04 44 55.3	-53 34 06	3.11, 5.7
8	IRC24-90	11.7	12.4		0.760	04 47 28.4	-53 29 56	
9	IRC15-463		12.7		1.856	04 44 32.6	-53 32 24	
10	IRC24-89		12.7		1.050	04 47 22.6	-53 30 07	3.11
11	IRC24-52		12.8		1.307	04 46 23.5	-53 35 41	3.11
12	IRC15-92		12.9		1.810	04 45 55.4	-53 20 16	
13	IRC24-138		13.0		1.103	04 46 38.4	-53 24 00	
14	IRC24-22		13.0	11.0	2.357	04 46 06.8	-53 39 27	3.11
15	IRC24-6		13.2		1.595	04 45 01.0	-53 44 55	3.11
16	IRC24-167		13.2	12.1	1.541	04 45 52.0	-53 18 27	
17	IRC24-155		13.2		1.454	04 45 00.0	-53 20 46	
18	IRC15-257		13.3	12.8	2.858	04 45 24.5	-53 26 44	3.11
19	IRC24-160		13.4		1.376	04 46 14.2	-53 20 26	
20	FIS90-1845		13.4		1.833	04 43 01.3	-53 04 10	
21	IRC24-163		13.4		1.437	04 45 58.5	-53 19 27	
22	IRC24-115		13.5	11.3	1.321	04 46 04.1	-53 26 31	
23	FIS90-1700		13.9		1.486	04 38 45.4	-53 32 46	

accurately in noisy spectra, leading to some extreme values, so the median is probably the best measure of average reddening.) The expected value of the Balmer decrement varies with optical depth and temperature, but for typical nebulae is just under 3 (Osterbrock and Ferland [2006]), so there is some reddening, a factor of about two. The result does not show evidence of evolution with either redshift or with Hα luminosity, although this has been seen in other studies at higher redshifts (e.g. Domínguez et al. [2013]). As shown earlier, even less evidence of attenuation by dust was found when comparing star formation rates based on Hα luminosity with that from total infrared luminosity (see Figure 3.16).

Metallicity

Line intensity ratios can also be used to estimate metallicity. A well-known formula (referred to as R23; Pagel et al. [1979]; Kobulnicky and Kewley [2004]; Geller et al. [2014]) uses oxygen abundance as a tracer for metallicity (see Equation 3.1), although this may need to be corrected for the ionisation level, to which

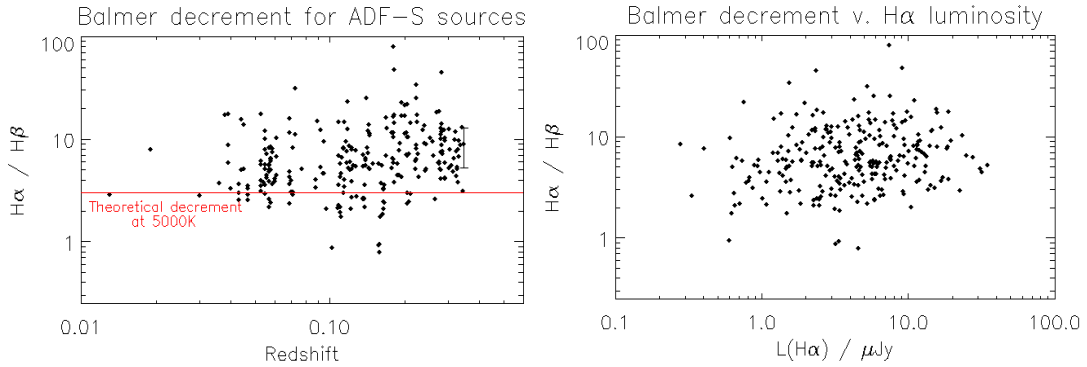

Figure 3.18: The Balmer decrement Hα/Hβ for sources at $z < 0.345$ in the ADF-S: left, as a function of redshift (with indicative error bar); right, as a function of Hα luminosity.

it is also sensitive. Figure 3.19 shows the metallicity estimated by this ratio for the sources with all these emission lines. There is no clear difference between sources with different redshifts.

Interesting spectra

The sources at $z > 1$ (see Table B.3 and Figure 3.11) are characterised by strong, broad emission lines, suggesting they are quasars. They are also U/HyLIRGS (see Figure 3.17). All but 2 of these 15 sources were IRC-selected.

Three further spectra with high ionisation lines are shown in Figure 3.20. FIS90-633 at $z = 0.361$ shows very strong [OIII] lines and clear [OII], [OI], [NeIII] and [NeV] lines. The source IRC24-111 at $z = 0.472$ is interesting with MgII and [NeV] as well as very broad Hβ and Hγ lines and clear [OII] and [OIII] lines.

The multiply-ionised neon emission lines [NeIII] λ3869 Å or [NeV] λ3869 Å were seen in 19 of the sources. A total of 21 sources showed a [NII] λ6583 Å flux higher than the Hα λ6563 Å flux.

Clusters in ADF-S

There are two known galaxy clusters in the ADF-S. Firstly, there is the well-studied cluster DC0428-53 / Abell S0463 (Dressler [1980]) at $z = 0.04$. Most of the previously-known spectroscopic redshifts in the field (from NED) are in the region of this cluster (see Figure 5.2). Secondly, a cluster at $z \sim 0.058$ was

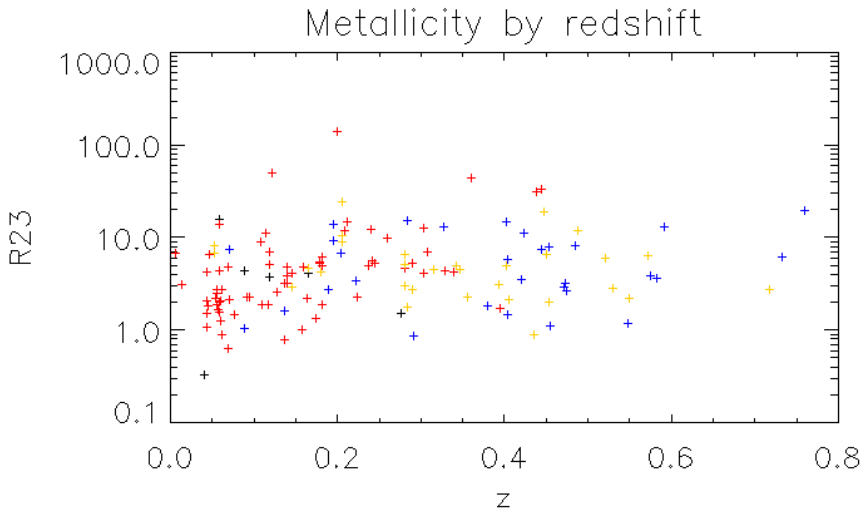

Figure 3.19: Metallicity traced by oxygen lines ratio R23 (a tracer for the metallicity Z) as a function of redshift. Colours show source selection: red for 90 μm, blue for 24 μm, brown for 15 μm, black for BLAST / AzTEC sources. Note the IRC-selected sources are at higher redshifts that FIS-selected sources.

found during the work for Chapter 4 (see Section 4.3.2). From comparison with galaxy densities in random fields of similar size, it seems that the new cluster has perhaps 300+ members (see Table 4.2 for details).

3.6 Summary

Following its selection as one of two extragalactic deep fields for observations by *AKARI*, the ADF-S has been selected for many multi-wavelength follow-up observations. This chapter has presented the results of a spectroscopic survey by the AAT/AAOmega fibre spectrograph in the central 3.14 deg^2 of the field. Spectroscopic redshifts for 404 sources were identified using emission lines in the optical region of the spectrum, with 316 of these sources being at $z \leq 0.345$, 73 at $0.345 < z \leq 1$ and 15 at $1 < z$.

The fluxes from the emission lines observed were calibrated using broadband photometric data from WFI (R-band, with Hα dominant, for the red arm) and CTIO (V-band, with Hβ and [OIII] lines dominant, for the blue arm) and are

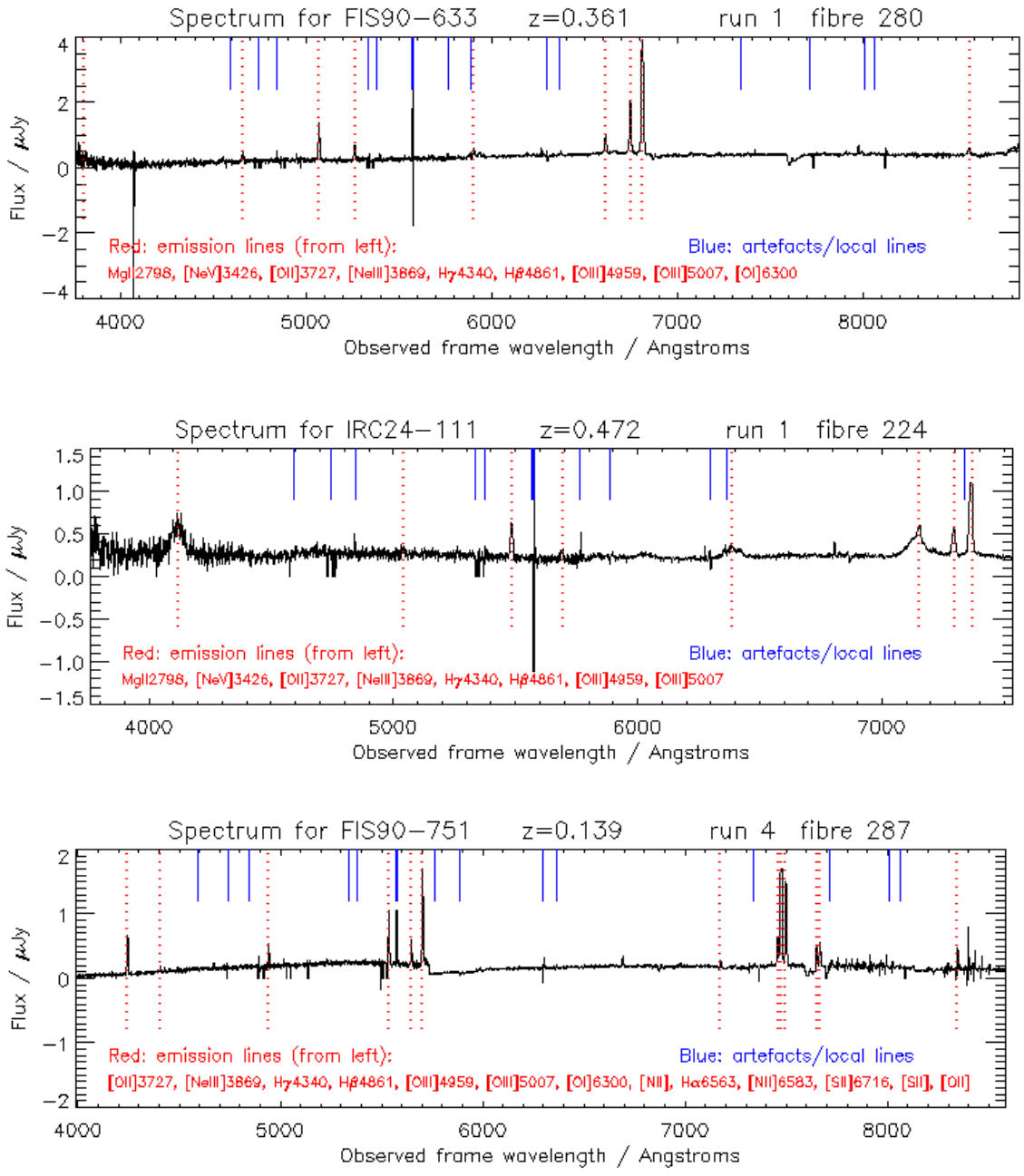

Figure 3.20: A selection of sources with strong multiply-ionised oxygen and neon lines. From top: FIS90-633 at $z = 0.361$ shows strong [OI], [OII], [OIII], [NeIII] and [NeV] lines. The unexpected similarity between the [OIII] λ4959, 5007 lines may be caused by a cosmic ray coinciding with the λ4959 line. IRC24-111 shows very broad Hβ and Hγ lines as well as MgII, [OII], [OII], [NeII] and [NeV] lines. FIS90-751 shows many strong oxygen lines, some of which are not usually seen in our sources.

tabulated in Appendix B. For the sources at $z \leq 0.345$, a BPT diagram indicated that most sources were star-forming galaxies, with only 13% being dominated by AGNs. Most of these sources have Hα FWHM between $200 - 300$ km s^{-1}. For these sources, a comparison of star formation rates calculated from the Hα luminosity and from 90 μm luminosity suggested that obscuration by dust was not significant. The Balmer decrement was also relatively modest at a median value of 5.9.

The higher-redshift sources showed considerably higher star formation rates, including 12 ULIRGs and 11 HyLIRGs, with 15 sources showing star formation rates > 1000 M$_\odot$ yr^{-1}. Two sources were found at $z > 2$ with Lyα identifications. A number of the sources (at low as well as high redshifts) showed strong [NeII] and [NeV] lines.

These spectroscopic redshifts are already being used by other studies in the field (e.g., Małek et al. [2013]; Małek et al. [2014]; Baronchelli et al. [2016]). The next chapter will present a 90 μm luminosity function based on a subset of these sources, and Chapter 5 will review the other multi-wavelength data so far available and present some SED fits of starburst galaxy templates.

Chapter 4

AKARI Deep Field South: far-infrared luminosity function of local star-forming galaxies[37]

This chapter presents a far-infrared galaxy luminosity function for the local universe, using galaxies observed at 90 μm in the AKARI Deep Field South which have redshifts $0 < z < 0.25$*, a subset of the galaxies for which spectroscopic redshifts were found as described in Chapter 3. When preparing the luminosity function, a new cluster of galaxies was discovered in the field at* $z \sim 0.06$*; excluding this cluster gave a net total of 130 local sources with which to prepare the luminosity function. Infrared and optical completeness functions were estimated using earlier Spitzer data and APM B-band optical data respectively, and the luminosity function was prepared using the* $1/V_{\mathrm{max}}$ *method. Separate luminosity functions were prepared for galaxies which show evidence of predominantly star-forming activity and galaxies which show predominantly active galactic nucleus (AGN) activity in their optical spectra. The luminosity function is in good agreement with the previous 90 μm luminosity function from the European Large Area ISO Survey (ELAIS), and a luminosity function is also presented which combines the AKARI and ISO data. The result is also in reasonable agreement with predictions based on the earlier IRAS* $60\,\mu$*m PSC-z catalogue, and with predictions by a recent backward evolution model. Recent results from the Herschel-PEP survey, published after this work, are also in reasonable agreement.*

[37]This chapter is based on research published in Sedgwick et al. [2011]. A full list of co-authors of that paper is given in Appendix C.

4.1 Introduction

There have not been many luminosity functions prepared for sources at a wavelength which is close to the SED peak for star-forming galaxies. This chapter presents a new 90 μm luminosity function for sources in the ADF-S with spectroscopic redshifts at $z < 0.25$ found in the previous chapter. Section 4.2 introduces luminosity functions, and reviews methods used to prepare them, empirical functions which describe the observations and recent research on infrared luminosity functions. Section 4.3 explains how the sources were selected for the ADF-S 90 μm luminosity function presented in this chapter. Section 4.4 describes the preparation of this luminosity function. The results are presented in Section 4.5 and discussed in Section 4.6.

4.2 Background: luminosity functions

The luminosity function is a fundamental observational tool for galaxy evolution which shows the number density of galaxies by luminosity, dependent only on the cosmological model assumed. Most other observed measures (e.g. stellar mass functions) require additional assumptions. Observed luminosity functions are considered to provide fundamental constraints on theoretical models of galaxy formation and provide a key starting point for backward-evolution models. The evolution of the luminosity function over time can enable us to distinguish luminosity evolution (i.e. galaxies becoming more or less bright over time) from number evolution (i.e. the number density of galaxies increasing or decreasing over time).

4.2.1 Selection function: completeness

In observing populations of galaxies, fainter galaxies fall below the limits of our observations as we look to increasing distances (called the Malmquist bias) and the samples are referred to as flux-limited. Most observations in extragalactic astronomy are flux-limited, so an important part of preparing the data for analysis is to estimate and compensate for the effects of incompleteness to make the

data as complete as possible. In this chapter, correction was needed for both optical (AAOmega) completeness and infrared (*AKARI*-FIS) completeness and is described in detail in Section 4.4. Instruments have a published response function, but usually it is necessary to estimate completeness by comparing to other known results from earlier studies or models.

Other selection effects may also exist in particular data samples and may need to be adjusted for. When an individual galaxy is observed, the brightest stars dominate our measurements, and it is necessary to make assumptions to account for the fainter stars: this is usually achieved by assuming an Initial Mass Function for galaxies; this is discussed in more detail in the next chapter, in Section 5.2.3. A statistical bias which may be present in flux-limited samples is the Eddington bias, which can be corrected statistically (Eddington [1913]), where an excess of sources may be identified near the limit of the observations due to statistical fluctuations in the measurement.

4.2.2 Luminosity function methods

One of the most common methods used to derive a luminosity function from observed data is the $1/\mathrm{V_{max}}$ method (Schmidt [1968]), and this is the method used in this chapter. It is a non-parametric method which requires no assumptions about the shape of the function. For each luminosity bin,

$$\Phi(\mathrm{L}) = \left(\frac{1}{\Delta \mathrm{L}}\right) \sum_{i} \left(\frac{1}{\mathrm{V_{max,i}}}\right) \tag{4.1}$$

where ΔL is the size of the luminosity bin and $\mathrm{V_{max,i}}$ is the maximum comoving volume within which the ith source would be observed and included in the catalogue. This method assumes a constant space density of galaxies, so can be biased by the existence of large scale structure. There are several alternative methods, including parametric Maximum-Likelihood methods (e.g. Sandage et al. [1979]). The completeness of the sample can be tested by checking if the mean $<\mathrm{V/V_{max}}>$ is close to 0.5, which should be the case assuming a uniform space density (Schmidt [1968]; Avni and Bahcall [1980]).

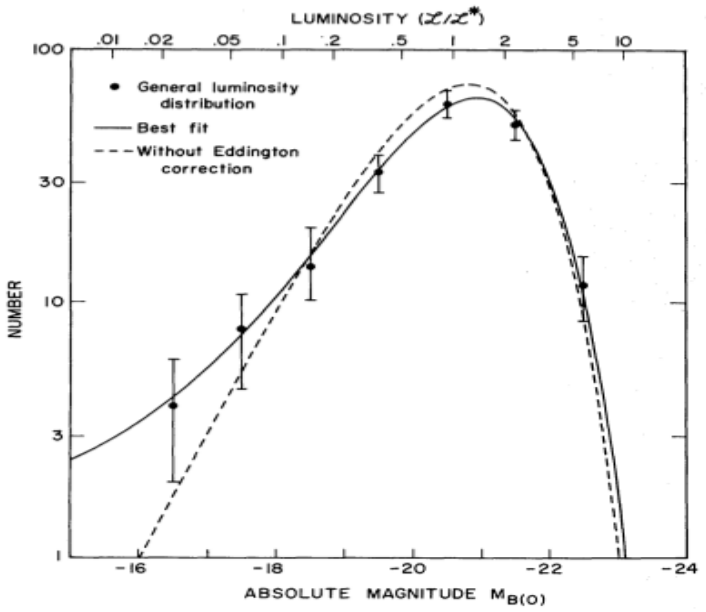

Figure 4.1: The original Schechter luminosity function from Schechter [1976]. The low-luminosity end is not usually shown in non-local observed data due to sources being below the flux limit or unknown completeness. The high end of the Schechter function often understates observed data from active galaxies.

4.2.3 Luminosity function distributions

An attempt to find a functional form for the luminosity function which successfully matches observations of local galaxies led to the famous Schechter function (Schechter [1976]) which combines a power law and an exponential function (see Figure 4.1):

$$\Phi(\mathrm{L}) = \Phi_* \left(\frac{\mathrm{L}}{\mathrm{L}_*}\right)^{-\alpha} \exp\left(-\frac{\mathrm{L}}{\mathrm{L}_*}\right) \tag{4.2}$$

where L_* is referred to as the characteristic luminosity where the transition occurs between the low-luminosity end (controlled by the power law term with index $-\alpha$) and the high-luminosity end (controlled by the exponential decay term) and where Φ_* is the number density normalization term. This is essentially an empirical fit; the Press-Schechter model of gravitational condensation which it resembles (Press and Schechter [1974]) contains simplifying assumptions which are unrealistic if applied to galaxies.

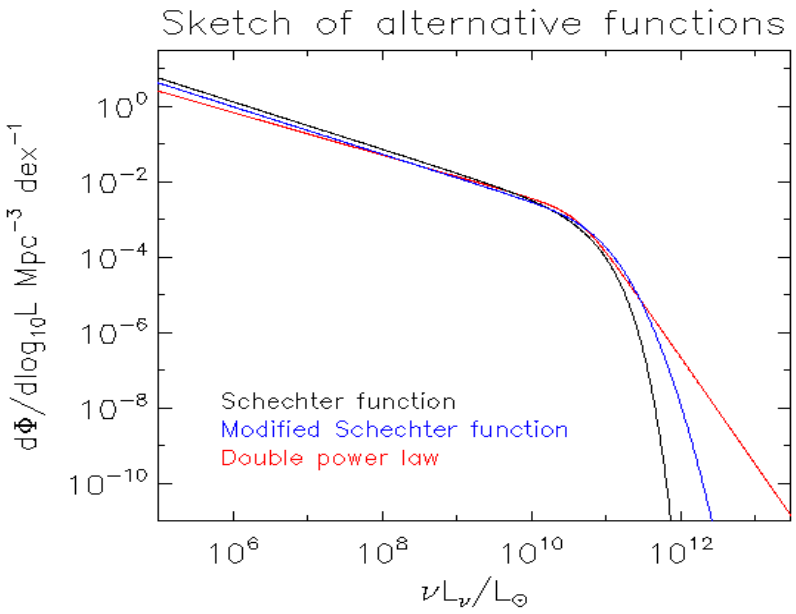

Figure 4.2: A sketch of the empirical luminosity functions given in the text, showing alternatives to the Schechter function which have shallower high-end slopes to fit observations of active galaxies.

While successful in describing quiescent and local galaxies, it has been found that the Schechter function does not successfully describe more distant active galaxies, giving a too-rapid fall-off at high luminosities. The luminosity densities of these galaxies are better fitted by a different functional form with an additional parameter covering the high luminosity end, such as a double power law (e.g. Sanders et al. [2003]; Babbedge et al. [2006]; Magnelli et al. [2009]) or a modified Schechter function introduced by Saunders et al. [1990] which behaves as a gaussian distribution in log L at the high-luminosity end (e.g. Le Floc'h et al. [2005]; Caputi et al. [2007]; Fu et al. [2010]). The contrasting high-luminosity behaviour of these functions is sketched in Figure 4.2.

The form of the double power law which is used in this chapter (following Serjeant and Harrison [2005]) is:

$$\Phi(\mathrm{L}) = \Phi_* \left[\left(\frac{\mathrm{L}}{\mathrm{L}_*} \right)^{\beta} + \left(\frac{\mathrm{L}}{\mathrm{L}_*} \right)^{\gamma} \right]^{-1} \tag{4.3}$$

The modified Schechter function introduced by Saunders et al. [1990] can be written as:

$$\Phi(\mathrm{L}) = \Phi_* \left(\frac{\mathrm{L}}{\mathrm{L}_*}\right)^{-\alpha} \exp\left[-\frac{1}{2\sigma^2}\log_{10}^2\left(1+\frac{\mathrm{L}}{\mathrm{L}_*}\right)\right] \tag{4.4}$$

Galaxies in an observed population will, of course, contain many types, from quiescent ellipticals to star-forming galaxies to AGN-dominated galaxies. Theoretical models may take account of this: for example, a backward-evolution model[38] by Gruppioni et al. [2011] which will be used later in this chapter to compare to my results (see Figure 4.9) comprised five types of galaxies: spiral galaxies, starburst galaxies, Seyfert 2s, obscured AGNs and AGN1s.

4.2.4 Previous results from infrared luminosity functions

About 40 papers on infrared luminosity functions have been published. These are listed in Table 4.1. The main consensus findings from this work to date will be discussed in this subsection. Papers which presented far-infrared luminosity functions which are most comparable to the one presented in this chapter will be discussed in Section 4.2.5.

Evolution: luminosity vs. number density

In general, a combination of luminosity evolution and number density evolution has been found in most studies of infrared luminosity functions. The characteristic luminosity peaked at $z \sim 2$, consistent with downsizing in other studies (see Section 2.4). The number density of the most massive galaxies has declined since then, whereas lower-mass galaxies have not shown a strong decline, as continuing galaxy formation balances fading with cosmic time. On a luminosity function plot of $\log(\Phi\ \mathrm{Mpc}^{-3}\ \mathrm{dex}^{-1})$ vs. $\log \mathrm{L}$, luminosity evolution vs. number density evolution is equivalent to horizontal vs. vertical movement: a sketch of this is shown in Figure 4.3.

In the near-infrared, Cirasuolo et al. [2010] found that a combination of luminosity evolution and density evolution was needed to explain the results from a sample of $\sim 50,000$ sources out to $z \sim 4$. This study also found that mas-

[38] Backward evolution models were discussed in Section 2.8.

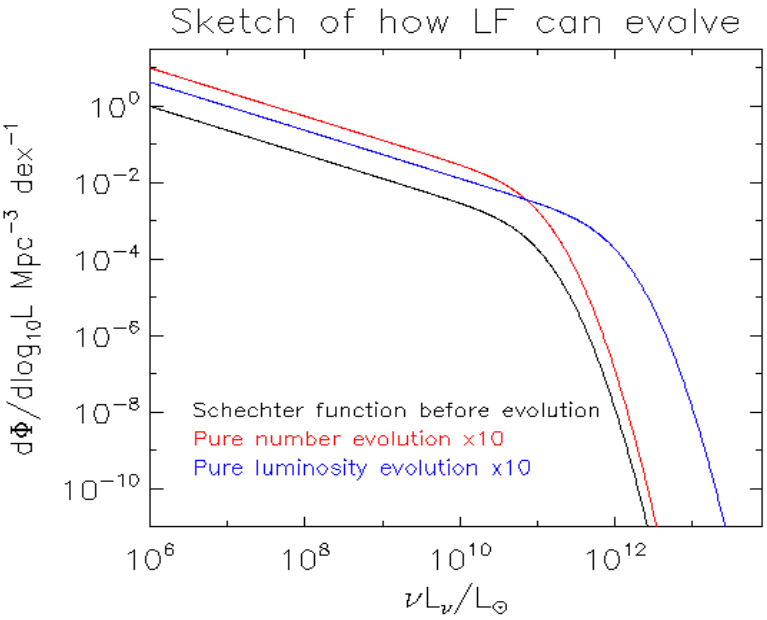

Figure 4.3: A sketch of alternative modes of luminosity function evolution. Based on an assumed Schechter function (black), number evolution only ×10 is shown in red, and luminosity evolution only ×10 is shown in blue.

sive bright galaxies formed at higher redshifts ($1 < z < 3$) and lower luminosity sources formed at lower redshifts and that theoretical models over-predicted faint galaxies and under-predicted bright galaxies. In a mid-infrared study of *Spitzer* SWIRE data out to $z \sim 4$, Babbedge et al. [2006] found that while the luminosity functions at the lower wavelengths showed moderate evolution, the luminosity function at 24 μm (reflecting star-forming galaxies and AGNs) showed much stronger evolution, particularly for luminosity. With a luminosity function of 15 μm-selected galaxies out to $z \sim$1 in the ELAIS survey, Pozzi et al. [2004] found strong evolution in both luminosity and number density for starburst galaxies in their sample (but no evolution for normal quiescent spiral galaxies).

Pérez-González et al. [2005], using an extensive sample of 8,000 galaxies based on *Spitzer* 24 μm sources with photometric redshifts out to $z \sim 3$, showed an increase in the characteristic luminosity L_* from the present out to $z = 2$, suggesting strong luminosity evolution, and included an updated version of the Madau diagram (see Figure 2.3). Also working with *Spitzer* 24 μm sources, Le Floc'h et al.

4.2.4 Previous results from infrared luminosity functions

[2005] used about 2,600 sources out to $z \sim 1.2$ to show that pure number evolution did not explain the observations, but either pure luminosity evolution, or a combination of both number density and luminosity evolution, would do so. Caputi et al. [2007]) used 1,349 *Spitzer* 24 μm-selected sources in the GOODS fields to compute an 8 μm luminosity function at redshifts $z = 1$ and $z \sim 2$, and found luminosity and number density evolution. However, Rujopakarn et al. [2010] using 4,047 *Spitzer* 24 μm sources at $0 < z < 0.6$ (and combining this with the earlier study by Magnelli et al. [2009] to extend this to $z = 1.2$) found that the evolution of the characteristic 24 μm luminosity is consistent with pure luminosity evolution of $(1+z)^{3.8\pm0.3}$ out to $z = 0.6$, and $(1+z)^{3.5\pm0.2}$ for $0 < z < 1.2$. Rodighiero et al. [2010] also used *Spitzer* 24 μm data to prepare luminosity functions at 24 μm, 15 μm, 12 μm and 8 μm. Their results suggested a rapid increase of the co-moving volume emissivity back to $z \sim 1$ and a constant average emissivity at $z > 1$ as well as showing evidence of downsizing in star formation.

In the far-infrared, Saunders et al. [1990] presented a local luminosity function of 60 μm-selected IRAS sources and found evidence of strong evolution which could be explained by evolution in either luminosity or density. This work was extended and revised by Soifer and Neugebauer [1991], Sanders et al. [2003] and Takeuchi et al. [2003], and Wang and Rowan-Robinson [2010] confirmed this evolution using a much larger sample of IRAS 60 μm sources in the redshift range $0.02 < z < 0.1$. Kim and Sanders [1998] found strong density evolution for 60 μm-selected IRAS ULIRGs. A luminosity function using *Spitzer* 70 μm sources in the ultra-deep GOODS-North pencil-beam survey (Huynh et al. [2007]; 143 sources) showed evidence for evolution in LIRGs and ULIRGs at redshifts $0.4 > z > 1.1$, but no evidence of significant evolution in normal galaxies at $z < 0.4$. Patel et al. [2013] used *Spitzer* 70 μm and 160 μm data to prepare luminosity functions to $z = 1.2$ and $z = 0.5$ respectively, finding strong luminosity evolution at both wavelengths. An early paper from the PEP survey on *Herschel* derived luminosity functions out to $z \sim 3$, detecting strong evolution out to $z \sim 2$ (Gruppioni et al. [2010]). In a joint PEP/HerMES project, Gruppioni et al. [2013][39] used PACS data at 70 μm, 100 μm and 160 μm, as well as SPIRE data, for 7,000 sources in

[39]This was published after the work in this chapter was published, and contained a figure comparing various results including the results in this chapter: see Figure 4.10.

four fields out to $z \sim 4$ to derive luminosity functions at rest-frame wavelengths 35 μm, 60 μm and 90 μm. Strong luminosity evolution was found out to $z \sim 2$, less strong luminosity evolution for $2 < z < 4$, and negative density evolution; in particular, different types of galaxies were found to evolve in different ways.

At longer wavelengths, luminosity functions based on BLAST observations at 250 μm, 350 μm and 500 μm (Eales et al. [2009]) showed a strong increase in number density of the most luminous galaxies from the present out to $z = 1$. Dye et al. [2010]) used sources in the 14 deg^2 H-ATLAS science demonstration field (2,241 sources) and showed the 250 μm luminosity function in intervals of 0.1 out to $z = 0.5$, showing significant evolution over this range. The luminosity function for $z < 0.1$ agrees very well with the prediction in Serjeant and Harrison [2005] for this wavelength. As part of the HerMES survey in smaller but deeper fields, Eales et al. [2010] looked at the evolution of the rest-frame 250 μm luminosity function and detected a total of 910 sources out to $z = 2$, finding strong evolution to $z \sim 1$ and weaker evolution beyond this redshift.

Empirical functions fitted to observed luminosity functions

Most studies fit a single function to the observed luminosity function. For local and quiescent galaxies this is usually a Schechter function (e.g. Huang et al. [2007]). Also, a Schechter function was found to fit a luminosity function of $z \sim 8$ in Schmidt et al. [2014] (part of the BoRG survey, with near-infrared observations). Fu et al. [2010] presented 8 μm and 15 μm luminosity functions for a sample consisting mainly of 24 μm-selected *Spitzer* data, finding a Schechter function a good fit in each case for star-forming galaxies (but not for AGNs which had a shallower high-end slope). A local luminosity function at 850 μm luminosity (Dunne et al. [2000]) as part of the SLUGS survey also found a Schechter function.

Most mid- and far-infrared studies needed an extra parameter (with either a double-power-law or modified Schechter function) to decrease the high-end slope for active galaxies. A double power-law was used by Soifer et al. [1987b], Rush et al. [1993], Kim and Sanders [1998], Serjeant et al. [2004], Toba et al. [2013], Babbedge et al. [2006], Huynh et al. [2007], Magnelli et al. [2009], Rujopakarn et al. [2010], Goto et al. [2010], Goto et al. [2011a], Goto et al. [2011b], Sedgwick et al. [2011], Magnelli et al. [2013] and Negrello et al. [2013]. A double power law

function was also found by Patel et al. [2013] (cited earlier) to give a better fit to their data than the modified Schechter function for luminosity functions based on *Spitzer* 70 μm and 160 μm to $z = 1.2$ and $z = 0.5$ respectively.

On the other hand, many authors have found that the modified Schechter function fitted the high-luminosity data better. These included Saunders et al. [1990], Pozzi et al. [2004], Le Floc'h et al. [2005], Takeuchi et al. [2006], Caputi et al. [2007], Wang and Rowan-Robinson [2010], Rodighiero et al. [2010], Vaccari et al. [2010] and Gruppioni et al. [2013]. A recent luminosity function for AGNs from the PEP survey was prepared by Delvecchio et al. [2014], using SED decomposition (and comparing to colour-colour diagnostics) to select AGNs; a modified Schechter function was fitted to the result.

In general, there is no disagreement about the representation of the low luminosity end of the empirical function as a power-law, and all studies show this. For example, for fitted Schechter functions the values found included -1.07 ± 0.1 (Cirasuolo et al. [2010]) and -1.38 ± 0.04 (Huang et al. [2007]). For double-power law function, Soifer et al. [1987b] found a slope of the lower-end slope was -0.8. The lower-end slope of the double-power law predictions by Serjeant and Harrison [2005] (used in this chapter) ranged from -0.704 at 70 μm to -0.458 at 850 μm.

The turnover and decline of the luminosity function at lowest luminosities has not been observable in most of the infrared studies so far; this should change as observations reach to lower flux limits in the future. New constraints have recently been obtained from the Hubble Frontier Fields survey using lensed sources to develop a UV luminosity function at $z \sim 7$ (Atek et al. [2015]). As our knowledge increases, the sum of luminosity functions for different types of galaxy (as in the Gruppioni model) is more likely to give a better fit than trying to fit a single functional form.

Contributions from LIRGs, ULIRGs and HyLIRGs

Another result confirmed by luminosity functions has been that U/Hy/LIRGs are not typically found in local galaxies. Huang et al. [2007] found the characteristic luminosity for their $z < 0.3$ sources was well below the limit for LIRGs. Goto et al. [2011a] found a tiny (0.4%) fraction of ULIRGs in a very local sample (at $z < 0.087$).

This changes with a move to higher-redshift galaxies. Goto et al. [2010] used *AKARI*-NEP Deep field observations to prepare luminosity functions at rest-frames 8 μm and 12 μm and found strong evolution toward higher redshifts, with the contribution from ULIRGs increasing by a factor of 10 from $z = 0.35$ to $z = 1.4$. Patel et al. [2013] found that luminous infrared galaxies contribute $\sim 68^{+10}_{-07}\%$ of the comoving star formation rate density at $z = 1.2$. Le Floc'h et al. [2005] found that sources between $0.5 < z < 1.0$ were dominated by LIRGs. Luminosity functions based on BLAST observations found that ULIRGs dominated the radiation at $z > 1$ (Devlin et al. [2009]). A ULIRG luminosity function was prepared by Lapi et al. [2011] for high-redshift ($z \gtrsim 1$) luminous galaxies at rest-frame 100 μm and 250 μm in the science demonstration field as part of the H-ATLAS survey. This study found strong evolution up to $z \approx 2.5$ which slows down at higher redshifts. Comparing UV-selected with submillimetre-selected galaxies, it also found that the dust-free UV bright phase is ~ 100 times shorter than the dusty submillimetre bright phase.

Table 4.1: Luminosity functions of infrared-selected sources, in order of observed wavelength: summary of some key features. See text for more details and results. Sch=Schechter function; DPL=double power law; ModS=modified Schechter function. The luminosity function in Sedgwick et al. [2011] is presented in this chapter.

Reference	Survey or telescope	Survey Area (deg^2)	Observed Wavelength (μm)	No. of sources	Redshift (z)	LF Wavelength (μm)	LF Type
Cirasuolo et al. [2010]	UKIDSS UDS	0.7	K,z′	∼50,000	$z < 4$	K band	Sch
Schmidt et al. [2014]	BoRG	0.1	V,Y,J,H	97	$z < 8$	UV	Sch
Huang et al. [2007]	*Spitzer*	6.88	8	4,867	$z < 0.3$	8	Sch
Toba et al. [2013]	*AKARI*	[SDSS]	9, 18	243; 255	local	9, 18	DPL
Pozzi et al. [2004]	ELAIS	4.12	15	150	$z < 1$	15	ModS
Babbedge et al. [2006]	SWIRE	6.5	24	102,645	$z < 4$	3.5 - 24	DPL
Pérez-González et al. [2005]	*Spitzer*	0.33	24	8,000	$z \sim 3$	12	Sch
Le Floc'h et al. [2005]	*Spitzer*	0.6	24	2,600	$z \sim 1.2$	15	ModS
Caputi et al. [2007]	*Spitzer*	0.08	24	1,349	$z \sim 2$	8	ModS
Rodighiero et al. [2010]	*Spitzer*	0.9	24	3,029	$z < 2.5$	8,12,15,24	ModS
Magnelli et al. [2009]	*Spitzer*	0.58	24, 70	10,271	$0.4 < z < 1.3$	15, 35	DPL
Rujopakarn et al. [2010]	*Spitzer*	9.0	24	4,047	$z < 0.6$	24	DPL
Fu et al. [2010]	*Spitzer*	1.12	24, 70	3,563	$0.6 < z < 0.8$	8, 14	SFG=Sch
Goto et al. [2010]	*AKARI*	0.4	2.4 - 24	4,128	$0.15 < z < 2.2$	8, 12	DPL
Soifer et al. [1987b]	IRAS	[14,500]	60	324	$z < 0.1$	60	DPL
Saunders et al. [1990]	IRAS	[82% sky]	60	2,818	local	60	ModS
Soifer and Neugebauer [1991]	IRAS	[all sky]	12,25,60,100	780	local	12,25,60,100	-
Rush et al. [1993]	IRAS	[all sky]	12, 60	893; 235	$z < 0.1$	12, 60	DPL
Kim and Sanders [1998]	IRAS	[all sky]	60	118	$z < 0.268$	bol	-
Sanders et al. [2003]	IRAS	[all sky]	12,25,60,100	629	local	bol	DPL
Wang and Rowan-Robinson [2010]	IRAS	[61% sky]	60	22,500	$0.02 < z < 0.1$	60	ModS
Serjeant et al. [2004]	ELAIS	7.4	90	151	$z < 1.1$	90	DPL
Oyabu et al. [2005]	ISO	0.9	90, 170	18	$z < 0.6$	FIR	n/a
Huynh et al. [2007]	*Spitzer*	0.05	70	143	$.04 < z < 1.1$	IR	DPL
Patel et al. [2013]	SWIRE	14.5	70, 160	634; 221	$z \sim 1.2; 0.5$	70,160,IR	DPL
Sedgwick et al. [2011]	*AKARI*	3.14	90	130	$z < 0.25$	90	DPL; model
Goto et al. [2011a]	IRAS, *AKARI*	[all sky]	9 - 160	629	$z < 0.087$	IR	DPL
Goto et al. [2011b]	*AKARI*, SDSS	[SDSS]	various	2,357	$z < 0.031$	IR	DPL
Takeuchi et al. [2006]	ISO	2.76	170	55	$z < 0.3$	170	ModS
Gruppioni et al. [2010]	*Herschel*	0.04	100,160	216; 237	$z < 3$	60,90	model
Gruppioni et al. [2013]	*Herschel*	2.36	70,100,160+	7,000	$z < 4$	35,60,90,IR	ModS
Magnelli et al. [2013]	*Herschel*	0.1	100,160	2,000	$z < 2.3$	TIR	DPL
Delvecchio et al. [2014]	*Herschel*-PEP	2.05	160	4,343	$z < 3$	agn bol	ModS
Eales et al. [2009]	BLAST	4.2	250,350,500	82	$z < 1.0$	250	-
Dye et al. [2010]	*Herschel*	14.4	250	2,241	$z < 0.5$	250	-
Eales et al. [2010]	*Herschel*	5.57	250	319	$z < 2.0$	250	-
Vaccari et al. [2010]	*Herschel*	14.7	250,350,500	753; 210; 45	$z < 0.2$	250,350,500,IR	ModS
Lapi et al. [2011]	*Herschel*	14.4	250,350,500+	3,469	$1.2 < z < 4$	100, 250	-
Dunne et al. [2000]	SLUGS	10400	60, 850	104	local	850	Sch
Negrello et al. [2013]	*Planck*	29250	350, 550, 850	328; 234; 108	local	350,550,850+	DPL
Forecasts across range of wavelengths from SED modelling:							
Serjeant and Harrison [2005]	IRAS, SCUBA		60	15,411	$z \sim 0.1$	60 - 850	DPL

4.2.5 Luminosity functions near the star-forming SED peak

This chapter will present a luminosity function of relatively local sources selected at 90 μm, which is at or close to the peak wavelengths at which radiation from star-forming galaxies reaches us after re-processing by gas and dust.[40]

The first luminosity functions at wavelengths close this peak were made with IRAS data, mostly using the 60 μm observations: Soifer et al. [1987b]; Kim and Sanders [1998]; Saunders et al. [1990]; Soifer and Neugebauer [1991]; Sanders et al. [2003]; Wang and Rowan-Robinson [2010]. *Spitzer* 70 μm observations were used in luminosity functions by Huynh et al. [2007] and more recently by Patel et al. [2013], both of which found that a double power law best fitted the data.

The closest work to this chapter has been a 90 μm luminosity function derived from the European Large Area ISO Survey (ELAIS paper IX; Serjeant et al. [2004]), based on spectroscopic redshifts of 151 ISO sources in the Northern ELAIS fields. This reached a redshift of $z \sim 1$ and a flux level of 70 mJy, and was in close agreement with the predicted double-power-law luminosity function for 90 μm from Serjeant and Harrison [2005] cited above. The evidence from the ISO ELAIS 90 μm survey suggested a calibration disagreement with the IRAS 100 μm data (Héraudeau et al. [2004]) so it is important to obtain independent estimates of the local luminosity function, particularly at 90 μm $-$ 100 μm.

AKARI's Far Infrared Surveyor Instrument (FIS; Kawada et al. [2007]) is most sensitive at 90 μm, and provides the opportunity to expand the observational evidence in this region near the SED peak for star-forming galaxies. This chapter provides a new 90 μm luminosity function, to compare with the previous ISO one, and also to combine with data from that survey to provide the best luminosity function at this wavelength so far. The present study aims to measure a local benchmark against which to compare luminosity functions of more distant star-forming galaxies based on more detailed, deeper data which will become available from new surveys from future telescopes and instruments.

[40] A wavelength peak of 90 μm equates to a temperature of about 30K for a blackbody in thermal equilibrium (Wien displacement law; $\lambda_{\rm peak} \times T_{\rm dust}$=2.9$\times$10^{-3} m K). The internal temperature of molecular clouds is thought to be $\leq$ 20K (corresponding to a peak of 150 μm). The SEDs of three representative star-forming galaxies are shown in Figure 2.2 peaking at $\sim$ 100 μm.

Results from *Herschel* appeared after my work in this chapter was published (Gruppioni et al. [2013]; Magnelli et al. [2013]). Some of these results at similar wavelengths and redshifts to mine are discussed in Section 4.6 below.

4.3 Sources for the ADF-S luminosity function

4.3.1 ADF-S 90 μm-selected sources at $z < 0.25$

The sources used in this chapter were detected in the ADF-S (Section 3.1) by the 90 μm WIDE-S band of the FIS, using its slow-scan observation mode with point-source photometry (Shirahata et al. [2009]). This reached 28 mJy at 60% completeness (our infrared completeness function is based on earlier Spitzer data: see Section 4.4 for details). By way of comparison, a 50% completeness limit of the sources used in the 90 μm luminosity function for the ELAIS Northern fields reached 70 mJy (Serjeant et al. [2004]). The FIS survey found a total of 2,282 sources at 90 μm at a signal-to-noise ratio SNR > 5 (giving a minimum flux of 12.81 mJy) in this field (Shirahata et al., in preparation). Optical identification of our targets was discussed in detail in Chapter 3. The use of the B_J-band APM catalogue in selecting sources allows a comparison with earlier ELAIS work, which also used the B_J-band.

Details of the observations, the data reduction and redshift measurement by identifying emission lines were given in Chapter 3. A total of 152 of these sources were 90 μm-selected (FIS) sources and had spectroscopic redshifts in the range $0 < z < 0.25$ and also had optical magnitudes, and these (subject to the removal of a new cluster described in 4.3.2) were used in preparing the luminosity function presented in this chapter, and are shown in Figure 4.4.

I was able to measure the FWHM of the Hα line for all the 152 selected sources, and only 10 of these showed FWHM of the Hα line over 500 km s^{-1}. A total of 105 had sufficient spectral data to plot the ratios for a BPT diagram[41], of which 39 were identified as AGNs by the Kauffmann criterion (i.e. including composite AGN/SFG sources). The net result of these two methods gave 44 optically-selected AGN sources and 108 optically-selected SFG sources out of the

[41] BPT diagrams were discussed in Section 3.2.2.

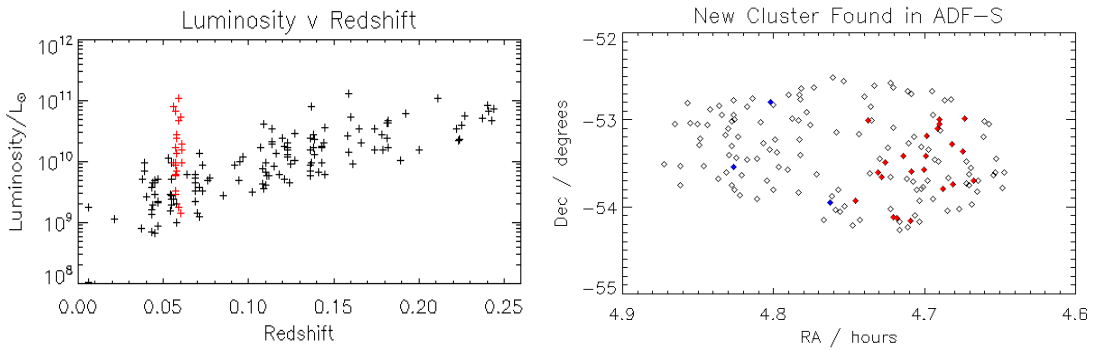

Figure 4.4: **Left:** The redshift - luminosity plane for all sources used in preparing the luminosity function, including the cluster sources (which are highlighted in red). Luminosity is $\nu L_\nu / L_\odot$ as calculated for the luminosity functions in this chapter. **Right:** A sky view of the new cluster found in the survey field. Cluster members are shown as filled red diamonds; sources in the same redshift range but not cluster members as filled blue diamonds; other redshift sources as open diamonds.

total of 152 FIS sources with $z < 0.25$ and optical magnitudes. Note, however, that many of our sources lie close to the dividing line, and the Kewley et al. [2006] criterion suggests many are AGN−SFG composite sources (Figure 3.15). Both star formation and active nuclei contribute to the bolometric energy output of these galaxies, although the BPT diagram on its own is insufficient to determine bolometric fractions.

4.3.2 New cluster of galaxies in the ADF-S

As can be seen in the luminosity / redshift plot (Figure 4.4, left), there is a group of sources bunched at about $z = 0.06$. In fact, there are 22 sources at a redshift of between $0.056 < z < 0.061$ and a separation on the sky of under 45 arcminutes, centred on (04 42 12.5, -53 30 46). This redshift range corresponds to a depth of 21 Mpc, and this angular separation corresponds to a width of about 3.2 Mpc. The cluster sources are identified in Figure 4.4; the left of this figure shows that the cluster contains relatively more luminous sources than the sample as a whole. This may have been caused by under-representation of high-luminosity galaxies at the lowest redshifts in the sample, or a region of enhanced star-formation in the outer (infalling) region of the cluster may have been sampled (Coppin et al.

[2011], but see Bai et al. [2009] and Haines et al. [2011]). Including this cluster in the sample distorts the luminosity function and causes the mean of V/V_{max} to fall well below 0.5 (this is discussed in Section 4.5.2 below). Therefore, the sources in the cluster have been excluded from the final luminosity function[42].

The comoving volume of the cluster is estimated as $\sim 10^4$ Mpc^3. For this calculation, the redshift range was converted to comoving depth per unit area and multiplied by the area of the cluster. This cluster volume is a tiny proportion (~ 0.01) of the whole field, so excluding the cluster volume from the calculations makes no significant difference to either the luminosity function or $\langle V/V_{max} \rangle$ so this adjustment has not been made. The coordinates of the cluster members are listed in Table 4.2 at the end of this chapter.

4.4 Preparation of the 90 μm ADF-S local luminosity function

Completeness as a function of flux based directly on the FIS data is still under construction (Shirahata et al., in preparation). Therefore it has been necessary to make our own assessment of the completeness of the *AKARI* data. The ultra-deep *Spitzer* 70 μm observations of the GOODS-North field reached down to a flux of 1.2 mJy (Frayer et al. [2006]). This is an order of magnitude lower than the limit of the present *AKARI* survey, so it is assumed that this will be 100% complete down to the lower end of the *AKARI* data. Frayer et al. [2006] showed that this *Spitzer* data is well fitted by the model of Lagache et al. [2004] which was used to generate number counts against which the *AKARI* completeness can be measured. However, since this data is at 70 μm an adjustment has to be made for our 90 μm case, and to do this the model described in Pearson [2001] was used, scaling the fluxes by a factor of 0.673 on the basis of that model's prediction that $N(S_{70\,\mu m} > 0.0673\,\mathrm{Jy}) = N(S_{90\,\mu m} > 0.1\,\mathrm{Jy})$. The resulting completeness ranges from 97% at 100 mJy to 60% at 28 mJy, as shown in Figure 4.5 (left).

As mentioned earlier, sources without APM B_J-band counterparts were not

[42]Note that this is not the well-known Dressler DC0428-53 cluster at $z = 0.041$, which is within the ADF-S field but outside the part of the field for which redshifts were obtained.

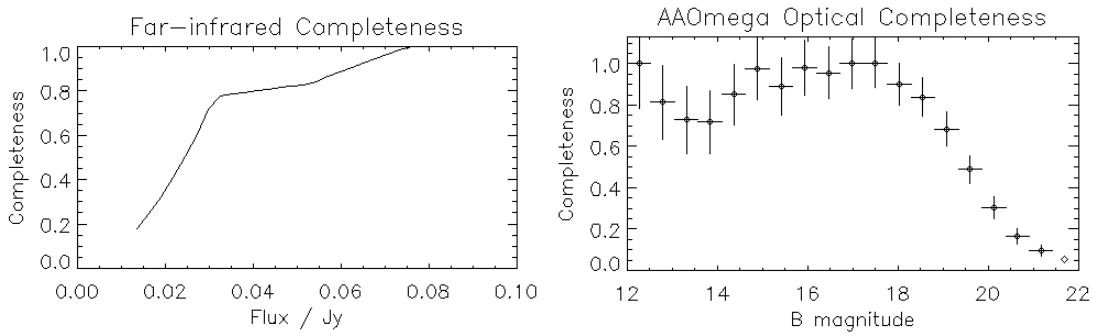

Figure 4.5: **Left:** estimated *AKARI*-FIS completeness function using Lagache model (Lagache et al. [2004]) fitted to *Spitzer* 70 μm GOODS-N data, modified for the 90 μm case by the Pearson model (Pearson [2001]) as described in the text. **Right:** estimated AAOmega optical completeness function using the APM catalogue. Vertical lines show 1σ errors, and horizontal lines show bin sizes.

selected. Using APM B_J-magnitudes, an estimate of the spectroscopic completeness as a function of magnitude was made, using the AAOmega redshift sources compared to APM sources cross-identified with the sources in the total ADF-S FIS sample before identification of redshifts. Each point in Figure 4.5 (right) shows the completeness using a range of ± 1.5 magnitudes. The 1σ error bars of the points are shown in the figure. The completeness is close to 100% down to B-band magnitude of about 18 after which it declines to 0.1 at about magnitude 21.

For galaxies with B > 21 and $z < 0.25$, I have adopted the assumption used for ELAIS (see appendix to Serjeant et al. [2001] for a detailed discussion) that such galaxies have more local counterparts, and at least one member of such a class of galaxy would be included in our sample. This would mean that its contribution to the luminosity function using the $1/V_{max}$ method would be given a weighting that exactly accounts for the increased difficulty of detecting such a class of galaxy.

To check whether or not the sample is typical of the sky as a whole - i.e. whether it is affected by large scale cosmic variance - the number per unit area was compared with that obtained in the 50 deg^2 Spitzer Wide-area Infrared Extragalactic Legacy Survey (SWIRE) at 70 μm (quoted in Frayer et al. [2009]) for > 0.1 Jy objects (following the procedure adopted in ELAIS, e.g. Serjeant et al.

[2001]). The fraction of number predicted / actual number was 1.80±0.32 so the effective luminosity density (and error) was renormalised by this fraction.

As explained above, there is a final total of 130 sources (after excluding the new cluster) for the luminosity function. For comparison, the fields used in the ELAIS IX luminosity function had a total of 151 sources (as in this case, these all had spectroscopic redshifts). More sources would obviously have been welcome, and it is hoped to obtain further AAOmega observations in the future. This survey covers a similar redshift range to the ELAIS IX survey (cf. Figure 1 of Serjeant et al. [2004]), so in addition to showing this new result (Figures 4.6 and 4.7), it seems justifiable to combine the two samples. The combined luminosity function is shown in Figure 4.8 and discussed below.

The $1/V_{max}$ luminosity function (Schmidt [1968]) was calculated following the methodology in Serjeant et al. [2004]. K-corrections were made assuming the M82 star-forming SED, except for the AGN luminosity function for which a Seyfert 2 SED template derived from SWIRE was used.

4.5 Luminosity function results

4.5.1 ADF-S luminosity function

As expected from earlier studies (Le Floc'h et al. [2005], Caputi et al. [2007]), the $z < 0.25$ sample is largely free of LIRGs and ULIRGs. The highest luminosity was 1.3 x 10^{11} $L_{\odot}$, and only two sources were over $10^{11}L_{\odot}$, the usual low-end definition of LIRGs (Sanders and Mirabel [1996]), where $\nu L_{\nu}(90\ \mu m)$ is used as a rough estimate of the bolometric infrared luminosity.

The local 90 μm luminosity function for all sources is shown in Figure 4.6, and tabulated in Table 4.3. For each luminosity bin, the space density of objects has been calculated with luminosities within ±0.15 dex.

The red line in Figures 4.6 and 4.7 is the double power-law prediction (Equation 4.3) for the local 90 μm luminosity function from Serjeant and Harrison [2005], which was based on extrapolated fluxes of 15,411 local galaxies ($z < 0.1$) in the IRAS-PSCz catalogue (Saunders et al. [2000]), where

$\log_{10} \Phi_* = -2.93\,\mathrm{dex}^{-1}\,\mathrm{Mpc}^{-3}$,

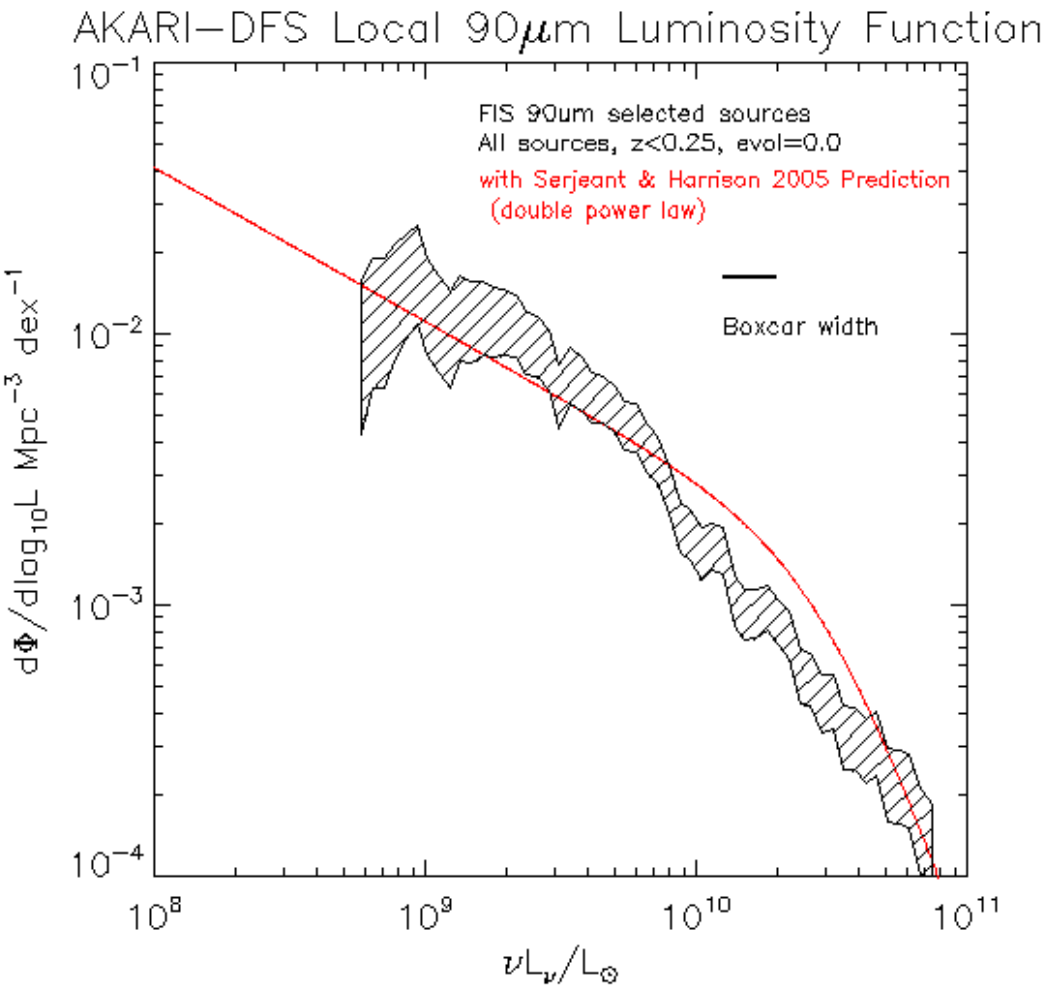

Figure 4.6: Local galaxy luminosity function using all ADF-S sources with AAOmega spectroscopic redshifts selected as described in the text. It is assumed in this figure that there is no pure luminosity evolution. The hatched area shows Poisson error bands. The line is the double power-law prediction by Serjeant and Harrison [2005].

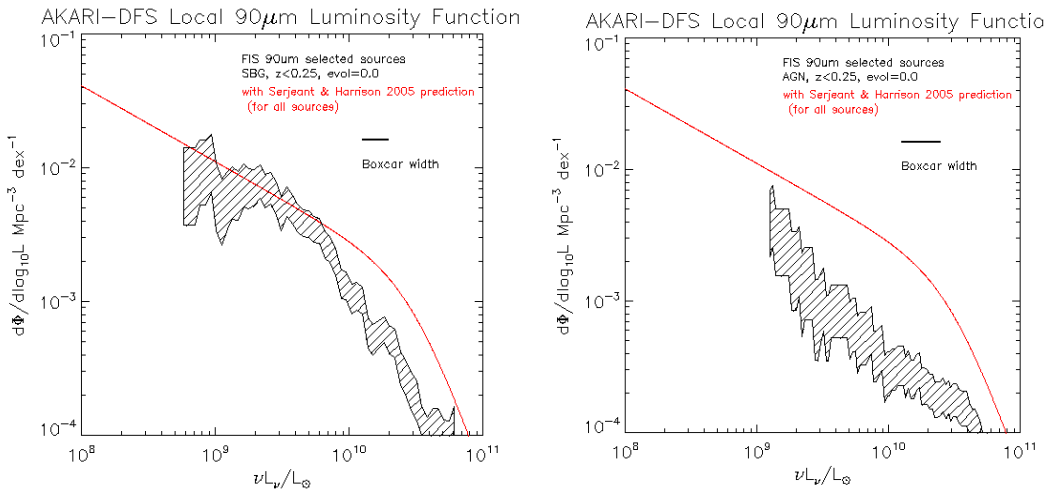

Figure 4.7: **Left:** star-forming galaxy luminosity function (with AGNs excluded). **Right:** AGN luminosity function (with SFGs excluded) as described in the text; note that only 36 AGNs were identified in the sample of 130 sources. The red line in each case is the double power-law prediction by Serjeant and Harrison [2005] for all galaxies.

$\log_{10} L_* = 23.54\,\mathrm{W\,Hz^{-1}\,sr^{-1}}$,
$\beta = 0.567$ and
$\gamma = 2.84$.

This prediction assumes pure luminosity evolution of $(1+z)^3$. Converting to the units used in this thesis (and using the more current value $H_0 = 72$ km s^{-1}Mpc^{-1}) gives the predicted $L_* = 3.06 \times 10^{10}\ L_\odot$.

The luminosity functions for star-forming galaxies (after excluding all those with any evidence of AGN activity) and for AGN sources are shown separately in Figure 4.7. In the case of AGN sources, the boxcar width is ±0.2 dex due to the lower number of data points.

4.5.2 Mean of V/V_{max}

The mean of V/V_{max} should be equal to 0.5 if the sample is complete, assuming a uniform space density. It was found that $\langle V/V_{max}\rangle = 0.478\pm0.022$ if no pure luminosity evolution is assumed. However, if $(1+z)^3$ pure luminosity evolution is assumed, $\langle V/V_{max}\rangle$ falls sharply to 0.427 ± 0.023, although the luminosity function

itself is not markedly different (compare Figures 4.6 and 4.8, left). Much of this shortfall is accounted for by the sources at $0.2 < z < 0.25$: making a cut at z=0.2 increases $\langle V/V_{max} \rangle$ from 0.427 to 0.467 for the luminosity function with pure luminosity evolution of $(1+z)^3$. (This reduces the number of sources from 130 to 119.)

This value for pure luminosity evolution has been used because earlier work has usually found pure luminosity evolution of this order, albeit with large uncertainties: for example, ELAIS IV found $(1+z)^{2.45\pm0.85}$ (Serjeant et al. [2001]) and ELAIS IX found $(1+z)^{3.4\pm1.0}$ (Serjeant et al. [2004]), both at 90 μm, and Saunders et al. [1990] found $(1+z)^{3.0\pm1.0}$ at 60 μm.

4.5.3 Combined ADF-S and ELAIS results

The 90 μm luminosity function for the Final Analysis of the northern ELAIS fields was presented in Serjeant et al. [2004] and is reproduced in the central panel of Figure 4.8. This covered three Northern ELAIS fields (totalling 7.4 square degrees) to a flux limit of 70 mJy. Completeness reached $\sim$ 100% at a flux of 150 mJy and $\sim$ 50% at 70 mJy, so it was not as deep as the ADF-S survey. The ELAIS survey was specifically designed to minimise the effects of cosmic variance (Oliver et al. [2000]) and so was spread over three fields, giving confidence that no cosmic variance renormalisation was necessary.

The left panel in Figure 4.8 shows the ADF-S luminosity function recalculated assuming pure luminosity evolution of $(1 + z)^3$ in order to compare and combine like-with-like with ELAIS, although as will be evident this makes only a slight difference to the luminosity function at this range ($z < 0.25$) of redshifts. The bottom panel of this Figure shows the combined (ADF-S and ELAIS) luminosity function.

4.6 Discussion of results

The most noticeable departure from the predicted local 90 μm luminosity function of Serjeant and Harrison [2005] described above is a deficit of galaxies close to L_* (from $\sim 10^{10} L_\odot$). This is particularly clear in the luminosity function

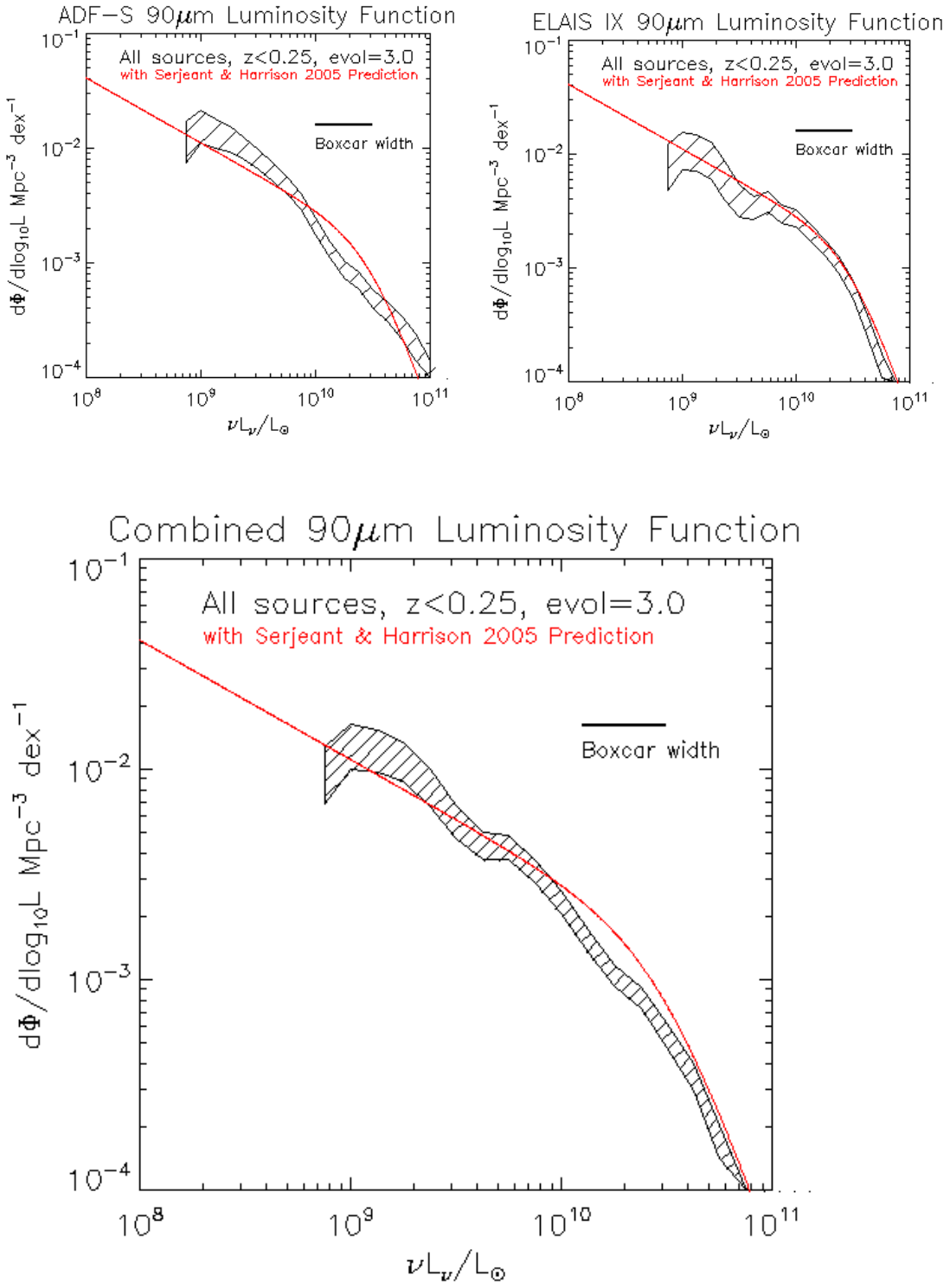

Figure 4.8: Comparison between the 90 μm luminosity functions. **Top:** ADF-S and ELAIS. **Bottom:** combined ADF-S and ELAIS. The red line shows the prediction from Serjeant and Harrison [2005]. Pure luminosity evolution of $(1+z)^3$ assumed.

where galaxies with AGN have been excluded (Figure 4.7), where it is significant at about 3σ. This may suggest that atypical large-scale structures are being sampled, and provides strong motivation for expanding the spectroscopic area to overcome these effects. To put this in context, the comoving distance across the AAOmega field at a median redshift of $z \sim 0.1$ is about 14 Mpc. The ELAIS results (Figure 4.8, middle) did not show the deficit of L_* galaxies which was found in this study[43], and the combined luminosity function (Figure 4.8, right) is close to the Serjeant and Harrison [2005] double power-law prediction.

At the faint end of the luminosity function, there is a slight excess number density when all sources are considered compared to the Serjeant and Harrison [2005] prediction (see Figure 4.6). At the bright end, the slope is shallower for AGNs than for SFGs (see Figure 4.7) indicating an increased contribution at high luminosity from AGN sources, which might be expected given the inferences from mid-infrared spectroscopy and radiative transfer models of increased AGN bolometric fractions with increasing bolometric luminosities (see for example Genzel et al. [1998] and Genzel and Cesarsky [2000]). The relative number density of AGN sources rises from under 10% of the total number density at the faint end to over 30% of the number density of all sources at the bright end.

These observations have also been compared with the theoretical prediction for the 90 μm luminosity function for $0 < z < 0.25$ galaxies from a new backward evolution model of Gruppioni et al. [2011] which uses the methodology developed in Gruppioni et al. [2008]. This comparison is shown in Figure 4.9 for all sources and for SFGs and AGNs separately. The Gruppioni model includes separate evolution for five types of galaxy: spirals (with low to moderate star formation), starbursts, low-luminosity AGNs (Seyfert 2s), AGN1s, and AGN2s (obscured AGNs). The relative number densities of the populations and their evolution are constrained by the population fractions in mid-infrared selected samples taken from ISO and IRAS (e.g. la Franca et al. [2004]; Matute et al. [2006]; see also Manners et al. [2004]), and are also constrained by early results from *Herschel*.

[43] Although the dip I found near the characteristic luminosity seems most likely due to cosmic variance, a similar dip was found recently in a *Spitzer* 70 μm luminosity function for local galaxies (Patel et al. [2013]; not commented on in that paper). Perhaps it may reflect a particular mix of different types of galaxies found. It is not seen in the recent *Herschel*-PACS study (Gruppioni et al. [2013]).

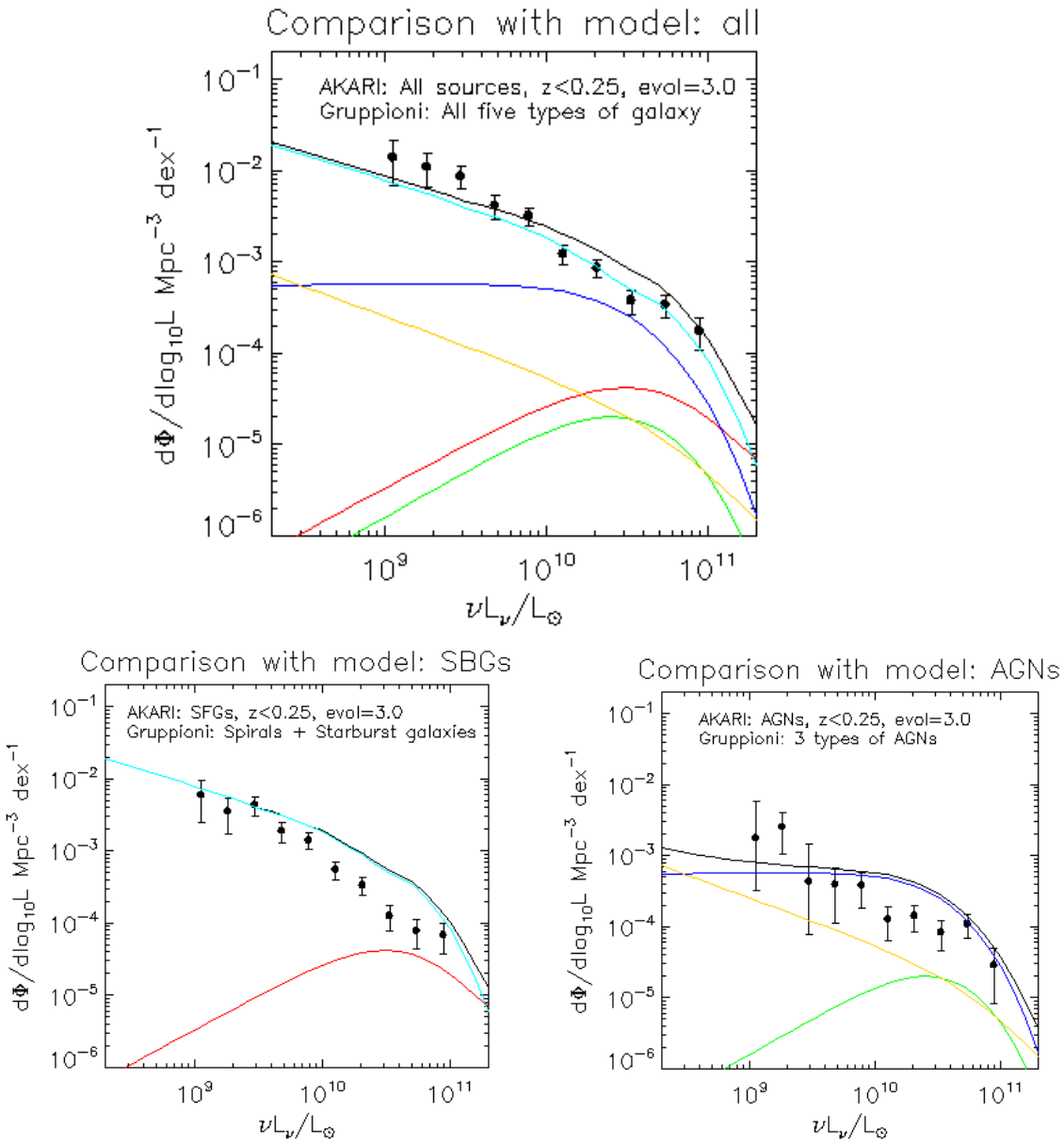

Figure 4.9: Comparison of the *AKARI* ADF-S 90 μm luminosity function with predictions from the Gruppioni et al. [2011] model. The *AKARI* data points are independent in this figure (unlike the boxcar-smoothed data in Figures 4.6 – 4.8). The plots from the Gruppioni et al. [2011] model are: black line = total, cyan = spiral galaxies, red = starburst galaxies, blue = Seyfert 2s, green = obscured AGNs and brown = AGN1 sources. The top figure shows all AKARI sources, the bottom figures show SFGs compared with the two star-forming Gruppioni classes, and AGNs compared with the three AGN Gruppioni classes.

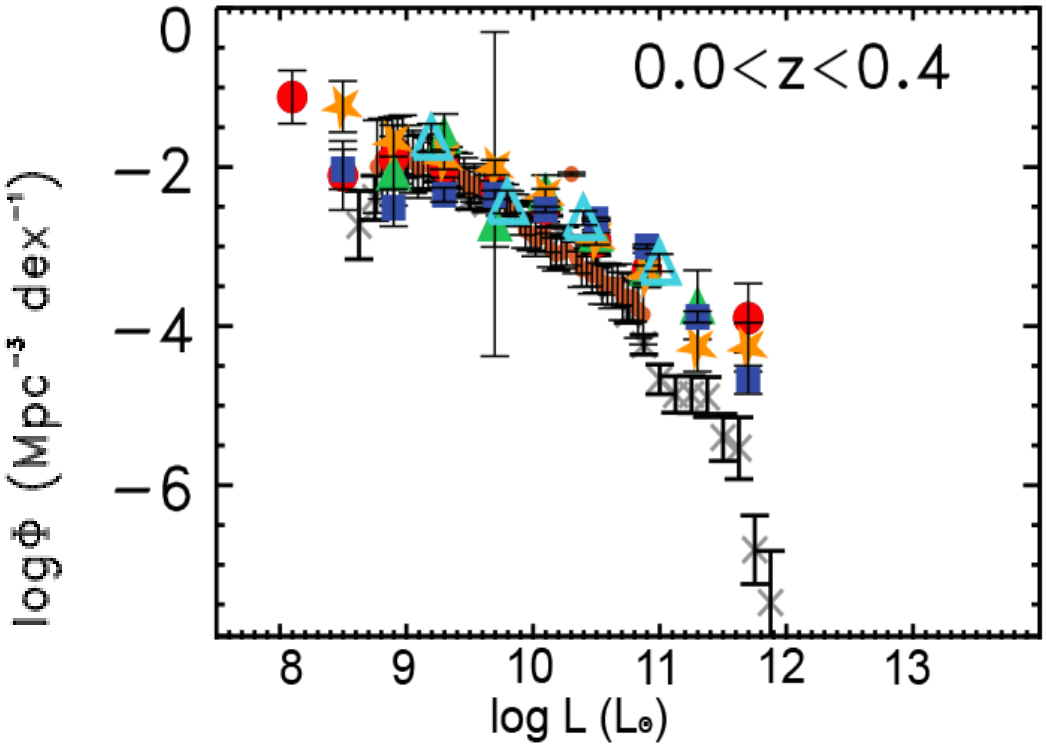

Figure 4.10: Comparison with the closest comparable 90 μm luminosity function from *Herschel*: figure from Gruppioni et al. [2013]. The *Herschel* data from four deep fields are shown as red filled circles, green filled triangles, orange filled stars and blue filled squares. The brown dots with error bars are from the LF in this thesis (Sedgwick et al. [2011]). The grey crosses are from the ELAIS local luminosity function (Serjeant et al. [2004]). The cyan open triangles are from thePEP 90 μm LF of Gruppioni et al. [2010]. Note the wider redshift range of the *Herschel* data than that used in this chapter.

In making multi-wavelength predictions for each type of object, the model uses a set of SED templates, with AGN1 being approximately flat in νL_ν, while the other AGN classes have relatively stronger far-infrared excesses. Figure 4.9 shows the detailed predictions of this model for the different classes of galaxy, showing how the contribution from the more active galaxies is predicted to increase at higher luminosity. As with the prediction by Serjeant and Harrison [2005], a slight excess is found at the low-luminosity end (although within the 1σ error bars). The dip in the *AKARI* data around L_* is not predicted by the model, but occurs for both AGNs and SBGs, suggesting it is caused by cosmic variance, as discussed above. The shallower slope in the AGN population predicted by the model is confirmed, supporting the SED assumptions of the model. Nevertheless, the AGN classification is based on emission lines at optical wavelengths so may in principle be missing AGN2s, for example, and could have misclassified AGNs and SFGs if their position on the BPT diagram does not reflect their relative bolometric contributions.

The recent results from the *Herschel* PACS Evolutionary Probe (PEP) Survey (published after the work in this chapter) explore four deep fields (GOODS-N, GOODS-S, ECDFS and COSMOS) at greater depth and redshift range. The closest comparison to my results has covered the redshift range $0.0 < z < 0.4$ at 90 μm (Gruppioni et al. [2013]; see Figure 4.10 taken from that paper which includes the results from the work in this chapter). This PEP result agrees within 1σ to the results in this chapter up to a luminosity of 10^{10} $L_\odot$, but there is significant disagreement at higher luminosities as shown in Figure 4.10. This disagreement may be due to the higher end of the redshift range ($z = 0.4$ in PEP compared to $z = 0.25$ in this chapter); that paper found significant evolution of the luminosity function in this direction with increasing redshift (the paper included galaxies up to $z \simeq 4$).

Future missions such as JWST and SPICA will improve enormously our ability to constrain the evolving bolometric luminosity function of galaxies and our assessment of the relative contributions of star formation and AGNs.

Table 4.2: The new cluster found in our redshift area of the ADF-S, centred on (04 42 12.4, -53 30 46), within a radius of 45′ of this centre, within a redshift range $0.056 < z < 0.061$. A near position search on the NASA Extragalactic Database (NED) yields 649 objects within this area, although virtually all (646) without known redshifts. For comparison, other searches on NED for the same sized area centred on positions offset by 2 degrees in RA and/or with reversed Dec typically yielded about 150−200 sources.

ID	RA(J2000) h m s	Dec(J2000) d m s	Distance from centre $\|\delta RA\|$ m s	$\|\delta Dec\|$ m s	Redshift z
FIS90-367	04 40 02.7	-53 41 44	02 09.7	10 58	0.057
FIS90-553	04 40 23.3	-52 59 07	01 49.1	31 39	0.059
BLAST500-193	04 40 29.4	-53 21 43	01 43.0	09 03	0.058
FIS90-56	04 40 52.8	-53 44 18	01 19.6	13 32	0.058
FIS90-184	04 40 54.6	-53 16 48	01 17.8	13 58	0.057
FIS90-1908	04 41 16.9	-53 47 55	00 55.5	17 09	0.057
FIS90-601	04 41 24.0	-53 03 03	00 48.4	27 43	0.060
FIS90-23	04 41 25.3	-52 59 53	00 47.1	30 53	0.061
FIS90-331	04 41 29.3	-53 05 48	00 43.1	24 58	0.057
FIS90-66	04 41 55.7	-53 11 04	00 16.7	19 42	0.061
FIS90-1767	04 41 57.3	-53 25 10	00 15.1	05 36	0.057
FIS90-2179	04 42 00.8	-53 34 22	00 11.6	03 36	0.058
FIS90-371	04 42 31.4	-53 35 28	00 19.0	04 42	0.059
BLAST500-160	04 42 33.5	-54 09 22	00 21.1	38 36	0.060
FIS90-591	04 42 51.4	-53 24 44	00 39.0	06 02	0.057
FIS90-919	04 43 04.8	-54 08 01	00 52.4	37 15	0.056
FIS90-631	04 43 14.4	-54 07 08	01 02.0	36 22	0.056
FIS90-2222	04 43 32.8	-53 29 06	01 20.4	01 04	0.057
FIS90-383	04 43 42.9	-53 39 38	01 30.5	08 52	0.058
FIS90-291	04 43 51.2	-53 36 27	01 38.8	05 41	0.057
FIS90-334	04 44 15.4	-53 00 21	02 03.0	30 25	0.061
FIS90-692	04 44 43.9	-53 55 39	02 31.5	24 53	0.059

Table 4.3: Tabulated 90 μm ADF-S $z < 0.25$ luminosity function.

Luminosity bin centre (boxcar width $\pm$0.15 dex) $\log_{10}(L/L_{\odot})$	Luminosity Density Φ Mpc^{-3} dex^{-1}	Poisson Error $\Delta\Phi$ Mpc^{-3} dex^{-1}
8.768	$1.01x10^{-2}$	$5.89x10^{-3}$
8.808	$1.27x10^{-2}$	$6.41x10^{-3}$
8.849	$1.27x10^{-2}$	$6.41x10^{-3}$
8.889	$1.48x10^{-2}$	$6.75x10^{-3}$
8.929	$1.63x10^{-2}$	$6.90x10^{-3}$
8.970	$1.80x10^{-2}$	$7.12x10^{-3}$
9.010	$1.35x10^{-2}$	$5.31x10^{-3}$
9.051	$1.16x10^{-2}$	$4.55x10^{-3}$
9.091	$1.00x10^{-2}$	$3.91x10^{-3}$
9.131	$1.15x10^{-2}$	$4.05x10^{-3}$
9.172	$1.08x10^{-2}$	$3.60x10^{-3}$
9.212	$1.11x10^{-2}$	$3.45x10^{-3}$
9.253	$1.04x10^{-2}$	$3.06x10^{-3}$
9.293	$1.04x10^{-2}$	$2.86x10^{-3}$
9.333	$9.72x10^{-3}$	$2.56x10^{-3}$
9.374	$8.42x10^{-3}$	$2.18x10^{-3}$
9.414	$8.28x10^{-3}$	$2.08x10^{-3}$
9.455	$7.29x10^{-3}$	$1.84x10^{-3}$
9.495	$5.37x10^{-3}$	$1.43x10^{-3}$
9.535	$6.30x10^{-3}$	$1.49x10^{-3}$
9.576	$5.76x10^{-3}$	$1.30x10^{-3}$
9.616	$5.10x10^{-3}$	$1.19x10^{-3}$
9.657	$4.95x10^{-3}$	$1.01x10^{-3}$
9.697	$4.56x10^{-3}$	$9.29x10^{-4}$
9.737	$3.92x10^{-3}$	$8.04x10^{-4}$
9.778	$3.79x10^{-3}$	$7.62x10^{-4}$
9.818	$3.13x10^{-3}$	$6.32x10^{-4}$
9.859	$2.85x10^{-3}$	$5.71x10^{-4}$
9.899	$2.28x10^{-3}$	$4.83x10^{-4}$
9.939	$1.60x10^{-3}$	$3.56x10^{-4}$
9.980	$1.47x10^{-3}$	$3.19x10^{-4}$
10.020	$1.24x10^{-3}$	$2.69x10^{-4}$
10.061	$1.34x10^{-3}$	$2.69x10^{-4}$
10.101	$1.32x10^{-3}$	$2.53x10^{-4}$
10.141	$8.97x10^{-4}$	$1.89x10^{-4}$
10.182	$8.03x10^{-4}$	$1.66x10^{-4}$
10.222	$8.34x10^{-4}$	$1.66x10^{-4}$
10.263	$8.91x10^{-4}$	$1.68x10^{-4}$
10.303	$8.15x10^{-4}$	$1.56x10^{-4}$
10.343	$7.24x10^{-4}$	$1.43x10^{-4}$
10.384	$5.17x10^{-4}$	$1.16x10^{-4}$
10.424	$5.21x10^{-4}$	$1.14x10^{-4}$
10.465	$4.38x10^{-4}$	$1.03x10^{-4}$
10.505	$4.49x10^{-4}$	$1.03x10^{-4}$
10.546	$3.42x10^{-4}$	$8.83x10^{-5}$
10.586	$3.40x10^{-4}$	$8.78x10^{-5}$
10.626	$3.11x10^{-4}$	$8.33x10^{-5}$
10.667	$3.32x10^{-4}$	$8.57x10^{-5}$
10.707	$2.37x10^{-4}$	$7.15x10^{-5}$
10.747	$2.34x10^{-4}$	$7.06x10^{-5}$
10.788	$2.28x10^{-4}$	$6.88x10^{-5}$
10.828	$1.61x10^{-4}$	$5.71x10^{-5}$
10.869	$1.40x10^{-4}$	$5.28x10^{-5}$

Chapter 5

AKARI Deep Field South: SEDs from multi-wavelength photometric data

The development of physical models of the evolution of star-forming galaxies is an active field of study, and should ultimately lead to an understanding of the physical processes underlying the results being found from observations. As part of this process, multi-wavelength observations of galaxies at various stages of their evolution provide essential constraints in the development of models. Indeed, observations have regularly yielded unexpected results which were not predicted by earlier models.

In particular, physical models can predict the spectral energy distributions (SEDs) of galaxies based on detailed calculations of physical processes such as radiative transfers in galaxies as they evolve, using various detailed assumptions about the evolving components of the galaxies. In this chapter, the multi-wavelength data available for the sources for which spectroscopic redshifts were found in Chapter 3 are matched to SEDs for star-forming galaxies developed from physical models. Where such templates can fit the observed data within a statistical confidence level, we may deduce properties of these galaxies from the assumptions underlying the model's predicted SED.

Optical, near-, mid- and far-infrared data are now available for the ADF-S, although much of these data cover only a part of the area covered by the spectroscopic-redshift survey. Statistically significant matches were found for 155 of the 404 spectroscopic-redshift (spec-z) sources, although this drops to 82 significant matches if sources are required to have matching points at both far-infrared and optical/near-/mid-infrared wavelengths.

5.1 Introduction

Section 5.2 provides a background to the theory and techniques of SED modelling and SED fitting. Section 5.3 outlines the multi-wavelength data available to date in the ADF-S and explains how these data were matched to the spectroscopic-redshift sources in the field. The choice of SED models and the fitting of SED templates to these data are described in Sections 5.3.3 and 5.3.4. The results are presented in Section 5.4 and discussed in Section 5.5.

5.2 Background: Spectral energy distributions

SED fitting provides a key method of estimating various parameters of a galaxy, such as redshift, mass, extinction, metallicity, and total luminosity. It can be used where multi-wavelength photometric data is available for the galaxy. As infrared astronomy has developed in recent years, model SEDs have now been extended to cover observations of dusty star-forming galaxies. To use this technique, we firstly need SED templates whose physical properties are known. The SEDs of individual well-studied galaxies may be used for purposes such as K-corrections (see Section 2.2), and empirical models of galaxy types are sometimes used as model SEDs. More often, physical models are developed (constrained by empirical data) which predict the SEDs of galaxies from known physical parameters. Secondly, a fitting routine is needed which finds the best fit of the data to the models. SED modelling and SED fitting are discussed in more detail in the following two subsections.

5.2.1 SED modelling

Three different theoretical approaches have been taken by researchers to generate model SEDs of galaxies.

The first method is called stellar population synthesis, and involves adding together the SEDs of individual stars of different types, masses, luminosities, metallicities and ages. This can be simplified by assuming an initial stellar mass function (IMF, discussed in Section 5.2.3 below) and applying this to stellar populations of differing ages and metallicities. The results need to be modified to

take account of attenuation by dust and gas in the inter-stellar medium (ISM), and this is usually done by using an empirical extinction law. Several laws have been proposed to account for the extinction of radiation from star-forming galaxies, the best-known being that of Calzetti (Calzetti et al. [1994]; Calzetti et al. [2000]):

$$\mathrm{S}(\lambda)_{corr} = \mathrm{S}(\lambda)_{obs} \times 10^{0.4\mathrm{E_s(B-V)k'}(\lambda)} \tag{5.1}$$

where the $\mathrm{E_s}$(B-V) is the colour excess of the stellar continuum and $\mathrm{k'}(\lambda)$ is the starburst reddening curve. Recent work with lensed galaxies from Herschel observations (Sklias et al. [2014]) has supported the Calzetti attenuation law. There are many population synthesis models, of which the best-known include Bruzual and Charlot [2003] and Maraston [2005]. There are problems with this approach, including our poor understanding of advanced phases of stellar evolution which will have a strong influence on the integrated light properties of galaxies, and significant degeneracies, e.g. between age and metallicity, which affect the spectra of galaxies in similar ways. These models are not ideal for the work in this chapter, since they are largely based on optical/UV data and not focussed on far-infrared fitting: for example, the Bruzual and Charlot [2003] model mainly covers a wavelength range from 3200 Å to 9500 Å (although it does cover up to 160 μm at lower resolution).

The second approach, one more directly applicable to far-infrared astronomy in which dust emission is critical, is to undertake radiative transfer (RT) calculations, modelling the interaction of radiation with dust, by absorption, scattering and re-emission (e.g. Rowan-Robinson [1992]; Efstathiou and Rowan-Robinson [1995]; Efstathiou et al. [2000b]). This approach requires extensive computations. As with population synthesis models, testing is necessarily based on data from local populations (in this case, local starburst populations). There are fewer empirical data points in the far infrared with which to measure results than are usually available in the optical. Many models and template libraries have been developed using the radiative transfer method (e.g. Chary and Elbaz [2001]; Dale and Helou [2002]). More recently, building on the dust and radiative transfer models of Rowan-Robinson and Efstathiou cited above, Siebenmorgen and

5.2.1 Background: SED modelling

Kreugel [2007] have developed a radiative transfer model for starburst nuclei and produced a library of over 7,000 SEDs covering wavelengths from optical to far-infrared. The template which best fits the observed data will give the luminosity, the proportion of OB stars, the size of the star-forming region, the dust density and visual extinction from the model. Siebenmorgen and Kreugel [2007] have shown that this procedure accurately identifies these properties of seven well-known local star-forming galaxies, including M82 and Arp 220. These should be broadly representative of most of the galaxies which are being analysed in this chapter. This library of templates has been used in a number of studies recently (e.g. for an analysis of the SEDs of Herschel HerMES/PEP sources in Symeonidis et al. [2013]), and since most of the sources I am examining are dominated by star-formation, I have chosen to use them in this chapter. They are discussed in more detail in Section 5.3.3.

A third, more complicated approach is to use N-body simulations to model the evolution of galaxies, including stars, the ISM and the dark matter halo. These models move away from the essentially static nature of other methods, but their complexity requires a significant increase in computational power. They may use a semi-analytic model to follow the evolution of gas, star and black hole processes (e.g. Springel et al. [2005]) and aim to explain far more than just the SEDs of galaxies being considered here[44]. At this stage of their development, they are not yet appropriate for the work in this chapter.

A problem with SED models is that it is difficult to model dust scattering (as opposed to absorption and emission), which is essentially a stochastic process, and can make some galaxies appear redder or bluer depending on inclination. The radiation transfer models are computationally difficult and in addition the discs are inhomogeneous on all scales. Popescu et al. [2000] and Tuffs et al. [2004] have developed models to calculate the radiation field throughout model galaxies using an iterative ray-tracing radiative transfer method.

More comprehensive details of current models are given in reviews by Casey et al. [2014] and by Walcher et al. [2011]. SED modelling is currently an active field of research. The lowest and highest wavelengths of the spectrum (X-rays and radio) are not usually included in the models, since they result from more

[44]Models of the evolution of star formation were discussed in Section 2.8.

complex processes such as supernovae, blazars, shockwaves etc.

5.2.2 Fitting model SEDs to photometric observations

Most SED template-fitting routines have a primary function of finding redshifts, and provide an alternative, cheaper method of finding galaxy redshifts than spectroscopy, which is expensive in observation time. Redshifts found by this method are called photometric redshifts. The idea was originally proposed by Baum [1962], and has become widely used in recent years as multi-wavelength surveys in deep fields have increased, and mid- and far-infrared data have been incorporated into the SED models. Unlike other properties estimated from SED fitting, photometric redshifts can be accurately verified by comparison with spectroscopic redshifts. Comparisons with spectroscopic redshifts illustrate a broad agreement but with outliers inaccurately determined by the photometric method. Work is underway to establish extensive all-sky photometric redshift catalogues (Bilicki et al. [2014]).[45]

Many template-fitting routines are publicly available[46]. Le Phare (Arnouts et al. [1999]; Ilbert et al. [2006]) allows the user to select the SED libraries to be matched, and computes the best-fit photometric redshifts and SED fits using minimum-χ^2 fitting (Equation 5.2):

$$\chi^2 = \sum_i \left[\frac{\mathrm{S_{obs,i}} - \mathrm{S_{model,i}}}{\sigma_\mathrm{i}} \right]^2 \tag{5.2}$$

taking account of the errors in the observations and the broadband filters of the instruments with which they are taken (to be convolved with the model). Various parameters can be adjusted in the Le Phare routines - for example, dust extinction models can be applied in the fitting routine. CIGALE (Burgarella et al. [2005]; Noll et al. [2009]) uses a stellar population synthesis model (the default is from Maraston [2005]) with a modified Calzetti extinction law and Dale and Helou [2002] dust emission models to derive galaxy properties where the redshift is already known. MagPhys (da Cunha et al. [2008]) uses an energy balance

[45] A photometric redshift quasar catalogue (Richards et al. [2009]) is used in Chapter 8.

[46] A list of SED fitting routines with links to download pages is available at http://www.sedfitting.org/SED08/Fitting.html.

argument to constrain SEDs from UV to far-infrared. The stellar emission is from the stellar population synthesis model of Bruzual and Charlot [2003], and dust attenuation is calculated by the model of Charlot and Fall [2000], and the attenuated starlight is then accounted for in the re-radiated infrared emission by three components: hot grains at 130−250K; grains at 30−60K; and PAHs.

The fitting routines could be modified by using Bayesian techniques to input prior information. However, in this case it is not obvious what such a prior would be, so I have just used maximum likelihood fitting, using minimum-χ^2 which is the minimum variance optimal estimator for binned data.

More directly relevant to this chapter, SED fitting can also prove a successful technique for finding various other properties of galaxies (that is, other than photometric redshifts). For example, Kartaltepe et al. [2010] with a large sample (1,503) of *Spitzer* 70 μm selected sources in the COSMOS field, used the multi-wavelength data available for this field, and a variety of templates, to prepare SEDs and infrared luminosity estimates and from these identified 31 HyLIRGs, 303 ULIRGs and 687 LIRGs in the sample.

For the sources being analysed in this chapter, which already have spectroscopic redshifts, I have chosen to use the Le Phare fitting routine. This fitting routine enables the selection of a wide variety of templates to be used and uses a straightforward chi-squared fitting of the observed fluxes with the chosen model fluxes. Since I have chosen to use the Siebenmorgen Kreugel (SK) model templates, these various parameters are built in to the large variety of templates, so these were not needed. For each source, the spectroscopic redshifts were specified in advance and for the observed fluxes, the filter response functions of the source data and errors were input. I have not included radio points since these are not accounted for in the templates. The fits can then identify other properties of the galaxies. Using the SK templates requires just a fitting without needing to specify extinction; this emerges from the best-fit template.

It is also possible to fit combinations of SEDs to data points. For example, in the UV/optical region an SED for a stellar component may be appropriate to account for unobscured stars. It may also be appropriate to combine a star-forming SED with an AGN SED for sources which show evidence of both. This has not (yet) been done for the sources in this chapter.

5.2.3 Stellar initial mass functions

Because of the different life cycles of stars of different mass, the **initial** stellar mass function (IMF) is a key assumption used in much cosmological work. This is the mass distribution of the initial population of stars born in a star-forming region within a galaxy. An IMF is needed to extrapolate from the masses of observed stars to account for the more numerous (unobserved) fainter low-mass stars. Stellar evolution, and in particular stellar lifetimes, are dominated by stellar mass. The IMF affects the evolution of a galaxy in many ways, including the generation of different amounts of metal enrichment. An IMF is assumed in SED modelling (Section 5.2.1 above).

The first stellar IMF was introduced by Salpeter [1955] for stars in the mass range 0.4 $M_\odot$ to 50 $M_\odot$, and is a simple power law[47] (Equation 5.3):

$$\Phi(\mathrm{m}) \propto \mathrm{m}^{-2.35} \tag{5.3}$$

Two more recent IMFs are sometimes used: that of Kroupa [2001], which uses a broken power law with different indices depending on mass (Equation 5.4):

$$\begin{aligned} \Phi(\mathrm{m}) &\propto \mathrm{m}^{-2.3} && \text{for } 0.5\ \mathrm{M}_\odot < \mathrm{m} \\ \Phi(\mathrm{m}) &\propto \mathrm{m}^{-1.3} && \text{for } 0.08\ \mathrm{M}_\odot < \mathrm{m} < 0.5\ \mathrm{M}_\odot \\ \Phi(\mathrm{m}) &\propto \mathrm{m}^{-0.3} && \text{for } \mathrm{m} < 0.08\ \mathrm{M}_\odot \end{aligned} \tag{5.4}$$

and that of Chabrier [2003] (Equation 5.5) which uses a log-normal distribution of stellar masses for $m < 1\ \mathrm{M}_\odot$:

$$\begin{aligned} \Phi(\mathrm{m}) &\propto \mathrm{m}^{-2.3} && \text{for } 1\ \mathrm{M}_\odot < \mathrm{m} \\ \Phi(\mathrm{m}) &\propto 0.086(1/\mathrm{m})\exp[-(\log(\mathrm{m}) - \log(0.22))^2/(2 \times 0.57^2)] && \text{for } \mathrm{m} < 1\ \mathrm{M}_\odot \end{aligned} \tag{5.5}$$

As shown in Figure 5.1, these functions are virtually identical to the Salpeter IMF for stars with M>$M_\odot$ but show the number density falling off at lower stellar

[47] This equation gives the number density as a function of mass. It is sometimes expressed as the fraction of the total mass per unit mass, in which case the exponent is -1.35.

5.2.3 Background: stellar initial mass functions

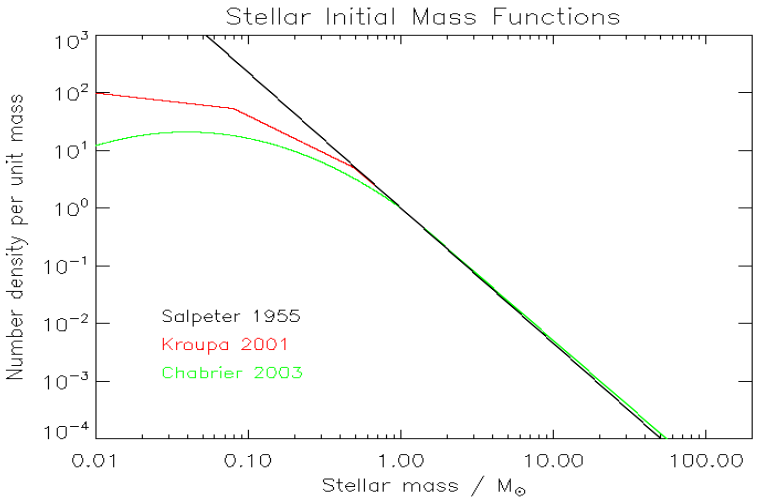

Figure 5.1: Comparative stellar initial mass functions using the formulae from Salpeter [1955], Kroupa [2001] and Chabrier [2003].

mass, suggesting that low mass stars are over-represented by the Salpeter IMF. If this is the case, then star formation rates would be over-estimated by using the Salpeter IMF. However, a recent study of a low redshift ($z = 0.116$) early-type galaxy suggests that low-mass stars may, on the contrary, be under-represented by all three IMF formulae discussed above (Läsker et al. [2013]).

To date, most of the evidence underlying these IMFs has been derived from local sources, including the Milky Way. It is not yet clear whether the IMF has a universal form that is independent of environment and redshift (see review in Bastian et al. [2010]). This is still an active field of research. In this chapter and in Chapter 7, formulae from Kennicutt [1998b] have been used which assume a Salpeter IMF to derive star formation rates.

All star formation indicators are sensitive predominantly to high-mass stars (Condon [1992]). Extrapolating star formation rates (e.g. to cover 0.1 $M_\odot$ – 100 $M_\odot$ stars) from observations will change if different IMF formulae are used, but the relative results will be unchanged.

5.3 Data analysis

5.3.1 Multi-wavelength observations in the ADF-S

Details of all the multi-wavelength data available in the ADF-S, both from dedicated surveys and public data, are shown in Table 5.1. I show how a selection of these surveys cross-match each other in Table 5.2. Some of these surveys are currently being used in a separate study (Baronchelli et al., in preparation) to find photometric redshifts of sources. Previously-known redshifts are shown in Figure 5.2 along with the redshifts found in Chapter 3.

Table 5.1: A comprehensive list of all deep data observed to date in the ADF-S (page 1 of 2). The matching radii to the AAOmega spec-z sources are shown in Table 5.3. *For the SPIRE sources, the SUSSEXtractor catalogues were used; the Starfinder catalogues gave a similar number of matches to the AAOmega sources.

Telescope, instrument and band	Wavelength (μm)	Resolution FWHM PSF (arcsec)	Survey Area (deg^2)	Confusion Limit (μJy)	Survey Depth (μJy)	Sources (no.)	Sources with AAO redshift (no.)	References	Comments
Catalogues from ADF-S projects:									
CTIO / MOSAIC-II: U	0.359	1″	0.5		0.179		144	Baronchelli+ in prep	
CTIO / MOSAIC-II: B	0.436	1″	0.5		0.165		171	Baronchelli+ in prep	
CTIO / MOSAIC-II: V	0.541	1″	0.5		0.137		183	Baronchelli+ in prep	
CTIO / MOSAIC-II: I	0.800	1″	0.5		0.170		190	Baronchelli+ in prep	
MPG / WFI : R_c	0.653		1.13		0.240	54,626	212	Baronchelli et al. [2016]	Central 1.13 deg^2
VST / OmegaCAM: g	0.470	0.216 ″+	1.0				227	Baronchelli+ in prep	Central 1 deg^2
VST / OmegaCAM: i	0.750	0.216 ″+	1.0				225	Baronchelli+ in prep	Central 1 deg^2
VST / OmegaCAM: z	0.888	0.216 ″+	1.0				234	Baronchelli+ in prep	Central 1 deg^2
Spitzer / IRAC	3.6	1.66″	7.74		3.54	341,006	371	Baronchelli+ in prep	Warm phase data
Spitzer / IRAC	4.5	1.72″	7.26		1.9	320,460	364	Baronchelli+ in prep	Warm phase data
AKARI / IRC	3.2	4.2″	3	< 1	10.6	8,399	185	Davidge+ in prep	Awaiting flux calibration
AKARI / IRC	4.1	4.2″	3	< 1	21.2	8,152	186	Davidge+ in prep	Awaiting flux calibration
AKARI / IRC	7	3.2″	3	< 1	74	2,542	136	Davidge+ in prep	Awaiting flux calibration
AKARI / IRC	11	3.5″	3	2	132	2,905	175	Davidge+ in prep	Awaiting flux calibration
AKARI / IRC	15	3.4″	0.8	16	279	2,274	176	Davidge+ in prep	Awaiting flux calibration
AKARI / IRC	24	4.1″	0.8	134	584	1,345	141	Davidge+ in prep	Awaiting flux calibration
Spitzer / MIPS	24	6″	11	24	200	40,556	366	Clements et al. [2011]	)Data analysis from 2 teams
Spitzer / MIPS	24	6″	11	24	200	92,098	360	Scott et al. [2010]	)
Spitzer / MIPS	70	18″	11	3.2 x10^3	2x10^4	1,205	159	Clements et al. [2011]	)Data analysis from 2 teams
Spitzer / MIPS	70	18″	11	3.2 x10^3	2x10^4	891	139	Scott et al. [2010]	)
AKARI / FIS	65	37″	12	3x10^3	3.5x10^4	391	27	Shirahata+ in prep	
AKARI / FIS	90	39″	12	7x10^3	8.5x10^3	2,282	179	Shirahata+ in prep	
AKARI / FIS	140	58″	12	4.5x10^4	2.8x10^4	315	13	Shirahata+ in prep	
AKARI / FIS	160	61″	12	5x10^4	6.7x10^4	216	1	Shirahata+ in prep	
Herschel / PACS	100	10″	1	1x10^2?	3x10^4?	468	95	Hadsukade+ in prep	Central 1 deg^2
Herschel / PACS	160	10″	1	2x10^3?		316	72	Hadsukade+ in prep	Central 1 deg^2
Herschel / SPIRE*	250	18.2″	7.47	24x10^3	1x10^4	21,926	263	Wang et al. [2014b]	HerMES
Herschel / SPIRE*	350	24.9″	7.47	28x10^3	1x10^4	13,605	150	Wang et al. [2014b]	HerMES
Herschel / SPIRE*	500	36.3″	7.47	31x10^3	1x10^4	6,191	51	Wang et al. [2014b]	HerMES
ASTE / AzTEC	1100	28″	0.25		4.4x10^3	198	6	Hatsukade et al. [2011]	Thin elliptic strip
ATCA	20 cm	6″	1.1, 2.5	140?	200	530	40	White et al. [2012]	
Spectroscopy:									
AAOmega	0.4-0.8		3.14				404	Chapter 3	

continued on next page

Table 5.1: (continued: page 2 of 2)

Telescope, instrument and band	Wavelength (μm)	Resolution FWHM PSF (arcsec)	Survey Area (deg^2)	Confusion Limit (μJy)	Survey Depth (μJy)	Sources in ADF-S (no.)	Sources with AAO redshift (no.)	References	Comments
Public archives which include ADF-S data:									
VISTA VHS: J	1.25	0.51″			1.23	238,500	335	)	
VISTA VHS: H	1.65	0.51″			4.65	228,805	334	) McMahon et al. [2013]	Matches for pgalaxy>0.9
VISTA VHS: K_s	2.15	0.51″			14.89	223,074	208	)	
2MASS: J	1.25	2.5″			2.1x10^3			)	
2MASS: H	1.65	2.5″			3.0x10^3			) Skrutskie et al. [2006]	
2MASS: K_s	2.17	2.5″			4.1x10^3			)	
WISE	3.4						348		
WISE	4.6						348		
WISE	12						348		
WISE	22						348		
Planck	350 - 10,000					3			
NED/Simbad							44	Małek et al. [2010], Małek et al. [2014]	
NED redshifts						212		See Fig. 5.2	
Catalogue used to find optical coordinates for AAOmega spectroscopy:									
APM / UKST B_J	0.480				9.4		350		
Catalogues used in finding targets, superseded by Herschel SPIRE:									
BLAST	250	30″	9		5x10^4	133	18	Valiante et al. [2010]	
BLAST	350	42″	9		5x10^4	90	9	Valiante et al. [2010]	
BLAST	500	60″	9		5x10^4	61	1	Valiante et al. [2010]	
Observations not yet reduced or available:									
CTIO / MOSAIC-II: R	0.663	1″	7.2		0.274			Barrufet+ in prep	Available ∼2016
CTIO / ISPI: K	2.22	3″	0.05		0.387				Not yet reduced
AKARI / IRC	9	3.5″	12	< 1	3.5x10^3				
AKARI / IRC	18	3.4″	12	66	1x10^4				
Herschel / PACS	100	10″	7.47					HerMES	Not yet published
Herschel / PACS	160	10″	7.47					HerMES	Not yet published
GALEX: FUV	0.153	6″	1.0		0.236				
GALEX: NUV	0.227	6″	1.0		0.094				
APEX /LABOCA	870	19″	0.1		6x10^3				
IMACS Magellan			0.2					Spectroscopy	

Table 5.2: A selection of the cross matches between surveys. Matching radius set to highest of each pair. Bands are in microns unless stated. For further details see Table 5.1.

Instrument:		WFI-R_c	VISTA J	IRAC	————-IRC————-				—-MIPS—-		———-FIS———-			—PACS—		———SPIRE———-			ATCA
Band:		0.653	1.25	3.6	4.1	7	11	15	24	70	65	90	140	100	160	250	350	500	20cm
Total sources:		54,626	238,500	341,006	8,152	2,542	2,905	2,274	40,556	1,205	391	2,282	315	468	316	21,926	13,605	6,191	530
Area (deg^2):		1.0	12.0	7.74	3.0	3.0	3.0	0.8	11.0	11.0	12.0	12.0	12.0	1.0	1.0	7.47	7.47	7.47	2.5
Sources/deg^2:		54,626	19,875	44,058	2,717	847	968	2,842	3,687	110	33	190	26	468	316	2.935	1,821	828	212
WFI R_c	0.653	-	6,729	1,921	373	121	143	155	486	13	8	32	1	11	13	548	305	132	26
VISTA J	1.25	6,729	-	54,775	2,236	830	1,361	877	18,036	1,069	132	1,234	84	301	210	8,713	3,919	1,198	173
IRAC	3.6	1,921	54,775	-	884	287	355	235	867	37	7	52	5	49	30	679	394	162	33
IRC	4.1	373	2,236	884	-	1,979	2,231	972	1,215	53	6	96	7	341	268	1,139	625	242	166
IRC	7	121	830	287	1,979	-	1,492	491	892	51	6	73	5	279	217	599	322	114	108
IRC	11	143	1,361	355	2,231	1,492	-	728	1,153	52	7	83	3	335	239	771	368	114	101
IRC	15	155	877	235	972	491	728	-	1,150	54	9	65	2	206	165	700	376	117	65
MIPS	24	486	18,036	867	1,215	892	1,153	1,150	-	19	0	20	1	3	1	482	260	67	0
MIPS	70	13	1,069	37	53	51	52	54	19	-	2	22	0	2	2	2	18	1	1
FIS	65	8	132	7	6	6	7	9	0	2	-	121	22	7	7	80	64	28	9
FIS	90	32	1,234	52	96	73	83	65	20	22	121	-	55	73	65	765	551	201	52
FIS	140	1	84	5	7	5	3	2	1	0	22	55	-	2	2	34	29	15	5
PACS	100	11	301	49	341	279	335	206	3	2	7	73	2	-	248	336	182	49	60
PACS	160	13	210	30	268	217	239	165	1	2	7	65	2	248	-	291	191	59	58
SPIRE	250	548	8,713	679	1,139	599	771	700	482	2	80	765	34	336	291	-	11,040	3,246	141
SPIRE	350	305	3,919	394	625	322	368	376	260	18	64	551	29	182	191	11,040	-	3,990	97
SPIRE	500	132	1,198	162	242	114	114	117	67	1	28	201	15	49	59	3,246	3,990	-	51
ATCA	20cm	26	173	33	166	108	101	65	0	1	9	52	5	60	58	141	97	51	-

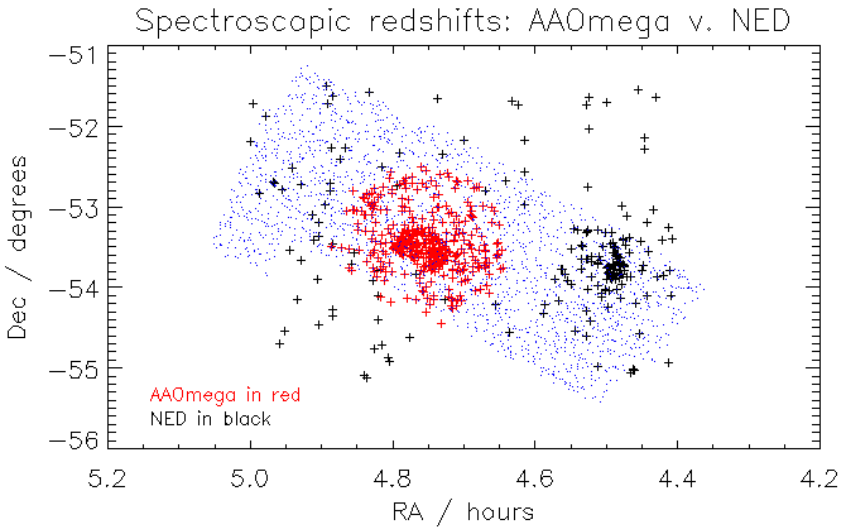

Figure 5.2: Redshifts already known in the ADF-S from the NASA/IPAC Extragalactic Database (NED, in black) compared to the spectroscopic redshifts presented in this thesis (in red). There is no overlap. The concentration at RA $\sim$ 4.5h is the Dressler cluster DC0428-53/Abell S0463 at $z = 0.04$.

5.3.2 Matching multi-wavelength data to spec-z sources in the ADF-S

It is important to set an appropriate matching radius when matching sources between catalogues: too small, and real matches will be missed; too large, and there is a risk of false positives. An empirical way of doing this, used in this chapter, is to generate a random catalogue to use alongside the real catalogue being matched. As the matching radius is increased step by step, there comes a point at which additional matches to the random catalogue become significant in relation to additional matches to the real catalogue, and therefore the matching radius has become too large and false positive matches will result. The results are tabulated in Table 5.3. As expected, a small radius was used for the optical data (which will usually have more accurate astrometry and better resolution), and a broadly increasing radius as wavelengths get longer. The final matching radii used are shown in bold in the table.

A total of 375 spec-z sources (92%) had at least 6 matches in the multi-

5.3.2 Matching multi-wavelength data to spec-z sources

Table 5.3: Finding the most appropriate matching distances to the AAOmega spec-z sources for data from the 28 catalogues used in SED fitting. Random matches use 0.2° addition to the RA coordinate. Some of the data (e.g. CTIO, VST, IRAC) was received already matched (Baronchelli et al., in prep.) so only the final matched numbers are shown. Bold font indicates the matching distance used.

Catalogue	Matches ≤1.2" actual	random	Matches ≤2.5" actual	random	Matches ≤5" actual	random	Matches ≤7.5" actual	random	Matches ≤10" actual	random
CTIO U band	**144**									
CTIO B band	**171**									
CTIO V band	**183**									
CTIO I band	**190**									
WFI R_c band	**212**	0	238	23	239	71	240	127	242	17
VST g band	**227**									
VST i band	**225**									
VST z band	**234**									
VISTA J band	**332**	0	350	7	353	20	353	36	356	65
VISTA H band	**331**	0	349	7	351	17	351	34	355	59
VISTA K_s band	**208**	0	215	4	218	12	218	29	221	48
Spitzer IRAC 3.6 μm	**371**									
Spitzer IRAC 4.5 μm	**364**									
WISE 3.4 μm			**348**							
WISE 4.6 μm			**348**							
WISE 12 μm			**348**							
WISE 22 μm			**348**							
FIS 65 μm	0	0	1	0	12	0	21	2	**27**	2
FIS 90 μm	6	0	22	0	79	1	136	1	**179**	3
FIS 140 μm	0	0	0	0	7	0	8	1	**13**	1
FIS 160 μm	0	0	0	0	1	0	1	0	**1**	0
Spitzer 24 μm	214	0	**333**	1	354	8	362	20	366	35
Spitzer 70 μm	105	0	152	0	**159**	0	162	1	164	1
PACS 100 μm	27	0	74	0	**90**	1	91	1	95	3
PACS 160 μm	15	0	51	0	66	0	**70**	0	72	1
SPIRE 250 μm	48	0	155	1	225	6	**263**	11	283	20
SPIRE 350 μm	20	0	44	2	103	4	150	5	**180**	10
SPIRE 500 μm	1	0	6	1	20	2	33	4	**51**	7

wavelength catalogues; 343 sources (84%) had at least 11 matches; 220 (54%) sources had at least 16 matches; and 130 (32%) had over 20 matches. In analysing the results of the SED fitting below, only sources with at least 6 matches have been used. In some cases, matches were found either only in the optical/near-/mid-infrared, or only in the far-infrared (taken as > 24 μm) and some of the results are shown only for the sources with matches in both wavelength regions.

5.3.3 The model SEDs used in this chapter

As discussed above in Section 5.2.1 above, the most appropriate model SEDs for these sources were judged to be those developed by Siebenmorgen and Kreugel [2007] (referred to in this chapter as the "SK templates"). Their complex models have been reduced to a template library of over 7,000 spatially integrated SEDs for star-forming galaxies. These templates have a wavelength range from 0.4 μm to 1500 μm. Their model assumes spherical symmetry and uses a range of values for five parameters: luminosity (our spec-z sources ranged from 10^{10} $L_{\odot}$ − $10^{14.7}$ $L_{\odot}$); the radius of the starburst region, the galactic nucleus (one of five discrete values: 0.35, 1, 3, 9 and 15 kpc); the visual extinction from the centre to the edge of the nucleus (also a range of discrete values: 2.2, 4.5, 6.7, 9.0, 17.9, 35.9, 72.0 and 144.0 magnitudes); the ratio of the luminosity of OB stars to the total luminosity (one of 4 values - 40%, 60%, 90% and high-luminosity objects; the 1, 9 and 15 kpc templates are for OB stars only); and finally the dust density in the hot spots (also in discrete steps, in units of hydrogen number density cm^{-3}). Siebenmorgen and Kreugel [2007] argue that the assumption of spherical symmetry and the lack of accounting for the clumpiness in the dust do not significantly affect the resulting SEDs. By finding the χ^2 best-fit template to the multi-wavelength data, we obtain a value for these 5 parameters for each source. No interpolation between templates has been done.

5.3.4 SED fitting for spec-z sources in the ADF-S

SEDs were fitted to the multi-wavelength data available for the 406 spectroscopic redshift sources presented in Chapter 3 using the library of 7,111 SED templates for star-forming galaxies given by Siebenmorgen and Kreugel [2007]. I have used 28 bands from the multi-wavelength catalogues in the SED fitting: CTIO (4 bands), WFI (1), VST (3), VISTA (3), IRAC (2), MIPS (2), FIS (4), PACS (2), SPIRE (3) and WISE (4). I did not use the IRC data which is still being reduced (Davidge et al., in preparation). I used the VISTA JHK_s data in preference to the older 2MASS data. I excluded data points which were upper limits when fitting (this was mainly mainly relevant to WISE data).

As discussed in Section 5.2.2, I chose to use the Le Phare routine (Arnouts

et al. [1999]; Ilbert et al. [2006]) to find the χ^2 best fit to the multi-wavelength data, fixing the redshift since these sources all have spectroscopic redshifts. Examples of the SED fits for a selection of sources are given at the end of this chapter in Figures 5.6, 5.7 and 5.8 for low-redshift, high-redshift and submillimetre-selected sources respectively.

5.4 Results of SED fitting

In total, 155 of our spec-z sources had SED fits to SK templates with a χ^2 value above the 95% confidence level. The results are summarised in Table 5.4. Histograms of the total luminosity of sources are shown in Figure 5.3. At $z \leq 0.345$, for which the Hα emission line was within the observed wavelength range, most sources show relatively low luminosity ($\sim 70\%$ at $10^{10}\mathrm{L}_{\odot}$), whereas at $z > 0.345$, sources range from $10^{10}\mathrm{L}_{\odot}$ up to $10^{11.5}\mathrm{L}_{\odot}$. In each case, there are a few outliers at $> 10^{12}\mathrm{L}_{\odot}$. Some of these sources had matches involving only optical/NIR/MIR catalogues, and some had matches to FIR data only. A total of 82 sources had matches at **both** ends of the wavelength range. The histograms for these in Figure 5.3 (bottom row) show sources spread more evenly up to $\sim 10^{11}\mathrm{L}_{\odot}$, without the outliers at higher luminosity.

The parameters of the model take discrete values, and the values for four of these parameters (the radius of the starburst region, the ratio of the luminosity of OB stars to total luminosity, visual extinction $\mathrm{A_V}$, and dust density) are shown as a function of the fifth parameter, luminosity, in Table 5.4. None of our sources was fit by the largest two starburst radius models, 9 kpc or 15 kpc. Sources were split between 40%, 60% and 90% OB ratio. Most sources showed relatively low extinction (80% had $\mathrm{A_V} \leq 4.5$), which confirms the relatively low extinction found from the spectroscopy in Chapter 3. $\mathrm{A_V}$ is plotted against luminosity in Figure 5.4. Most also showed the lowest value for dust density.

Although not used in our SED fitting, the matched radio observations confirm the well-known radio-far-infrared correlation (Figure 5.5). The parameter $q_{\mathrm{FIR}} = 2.36 \pm 0.27$, comparable to other recent studies (e.g. Pannella et al. [2015]).

Table 5.4: Parameters of the best-fit Siebenmorgen-Kreugel models. Sources are selected with (a) at least 6 matching points and (b) a best-fit χ^2 value above the 95% confidence level. The parameters have a range of discrete values as shown.

	Luminosity ($\log_{10}$L/L$\odot$)								
	10.0 ≤10.2	10.2 ≤10.4	10.4 ≤10.6	10.6 ≤10.8	10.8 ≤11.0	11.0 ≤12.0 (LIRGs)	12.0 ≤13.0 (ULIRGs)	13.0 and over (HyLIRGs)	Total
Radius of nucleus in model (kpc)									
0.35	31	5	4	2	2	3	2	2	51
1	7	4	3	0	3	1	1	2	21
3	48	8	10	5	3	8	1	0	83
9	0	0	0	0	0	0	0	0	0
15	0	0	0	0	0	0	0	0	0
Total	86	17	17	7	8	12	4	4	155
Ratio OB:total luminosity									
OB40	27	7	12	3	2	4	2	0	57
OB60	41	7	4	3	4	3	0	0	62
OB90	18	3	1	1	2	5	1	0	31
HL	0	0	0	0	0	0	1	4	5
Total	86	17	17	7	8	12	4	4	155
Visual extinction (A_V)									
2.2	71	13	7	1	4	3	4	1	104
4.5	5	0	4	5	2	2	0	3	21
6.7	3	3	1	1	0	1	0	0	9
9.0	2	1	2	0	1	2	0	0	8
17.9	0	0	2	0	1	1	0	0	4
35.9	2	0	0	0	0	2	0	0	4
72.0	2	0	1	0	0	1	0	0	4
144.0	1	0	0	0	0	0	0	0	1
Total	86	17	17	7	8	12	4	4	155
Dust density (No. of hotspots cm^{-3})									
100	68	9	14	4	7	5	2	1	110
1000	13	3	2	0	1	1	1	1	22
2500	1	3	1	1	0	0	0	0	6
5000	1	1	0	1	0	2	0	0	5
7500	0	0	0	1	0	0	0	0	1
10000	3	1	0	0	0	4	1	2	11
Total	86	17	17	7	8	12	4	4	155
Total SEDs fitted	86	17	17	7	8	12	4	4	155
Poor fit / no fit									249
Total									404

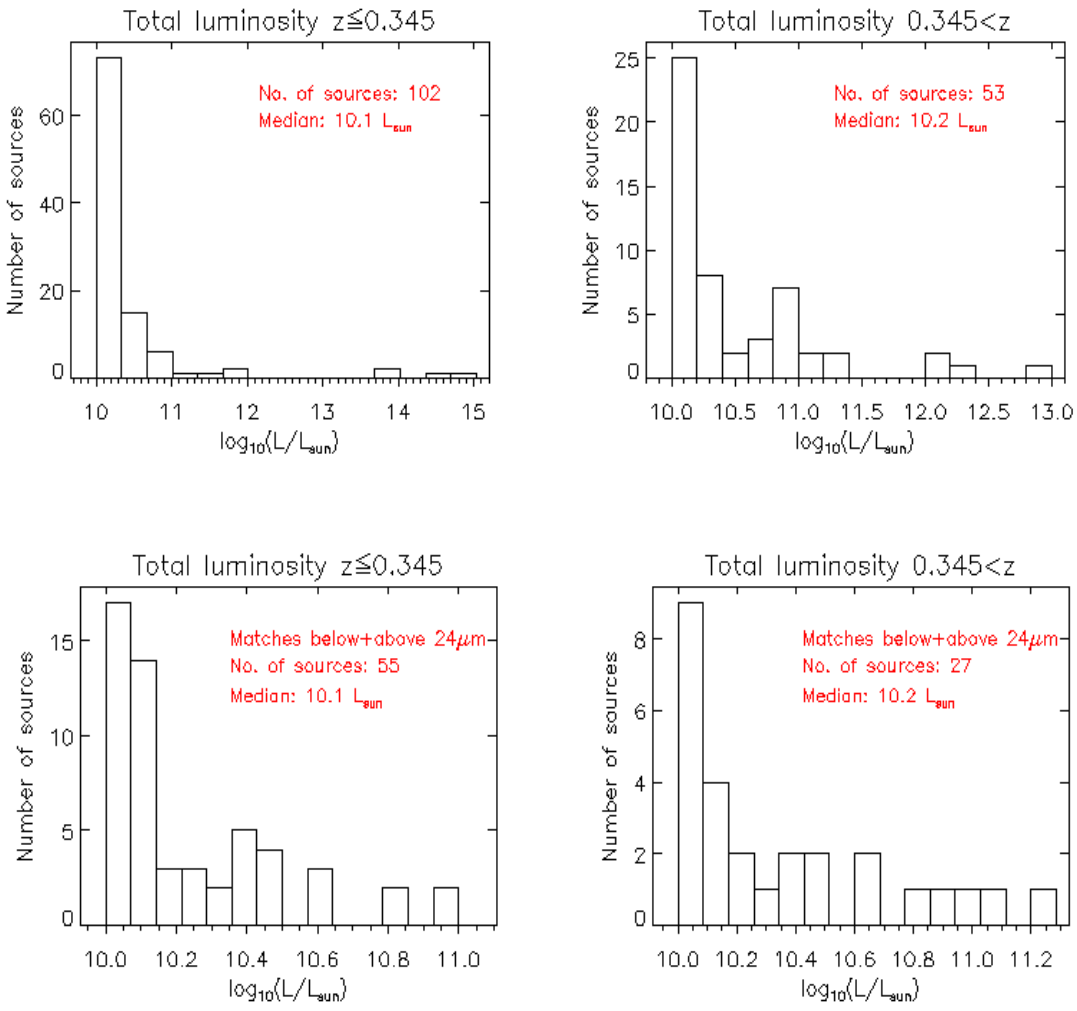

Figure 5.3: Histograms of total luminosities from the minimum-χ^2 best-fit Siebenmorgen template SEDs, split into two redshift groups: $z \leq 0.345$, for which Hα is within the observed wavelength range, and $z > 0.345$. These spec-z sources have (a) at least 6 matching points and (b) χ^2 values above the 95% confidence level; in addition, for the bottom histograms (c) matching points above **and** below 24 μm. As expected, there are more high luminosity sources at high redshift, although the median luminosity is not significantly higher.

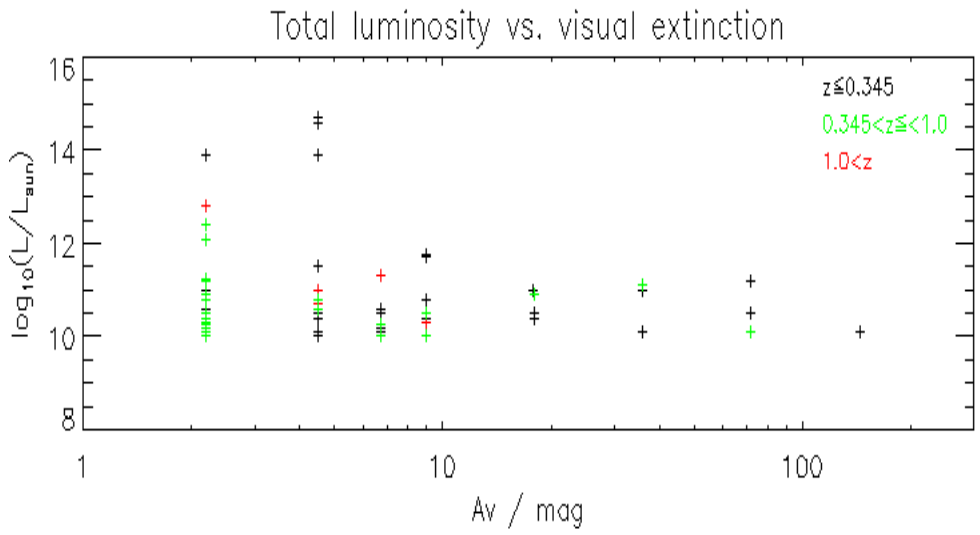

Figure 5.4: Luminosity vs. extinction from SED fittings. These spec-z sources have (a) at least 6 matching points; (b) χ^2 values giving >95% confidence level. High-z sources show less extinction, but there is no clear relation between luminosity and extinction.

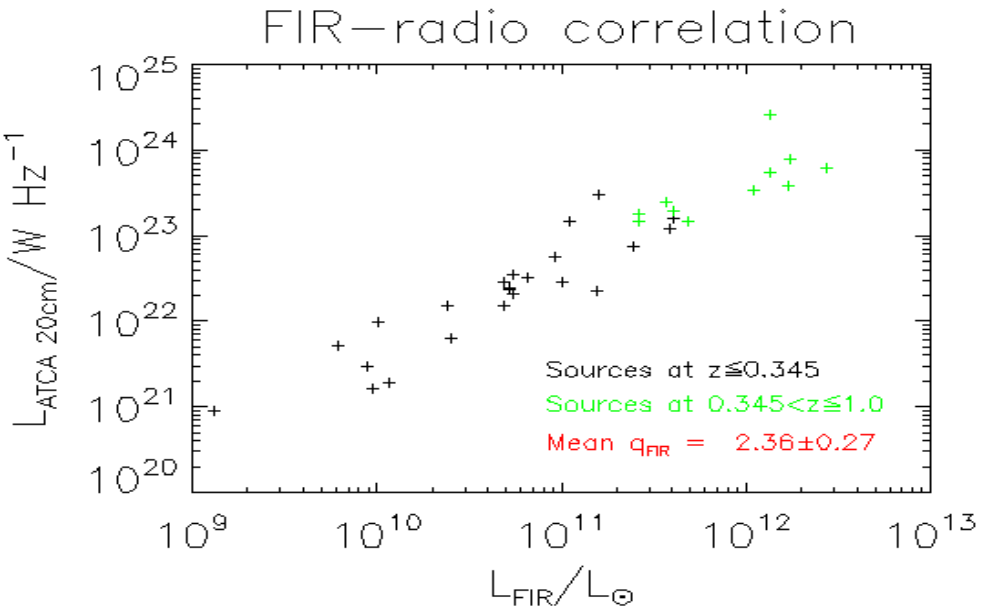

Figure 5.5: The well-known far-infrared−radio correlation is demonstrated by our 90 μm-selected sources. L_{FIR} is estimated from the 90 μm flux using the M82 SED. The parameter q_{FIR} is calculated using Equation 2.4.

5.5 Discussion and future work

The *AKARI* Deep Field South (ADF-S) was chosen as one of the two deep fields for observations by *AKARI* because it is a relatively cirrus-free field (based on the COBE / IRAS 100 μm map of dust by Schlegel et al. [1998]) near one of the ecliptic poles which would be easily observed on its orbit (Matsuhara et al. [2006]). Follow-up observations at a wide range of wavelengths have now been made in the field (and more are ongoing). With the identification of over 400 spectroscopic redshifts for the infrared sources (described in Chapter 3), this chapter has presented a first look at establishing properties of the far-infrared sources in the field by fitting SED models to the data available so far.

Since most of the redshifts found were for far-infrared or submillimetre selected sources (see Table 3.3) it seemed reasonable to choose a star-forming galaxy model for this exercise. The success in fitting 155 of our 404 sources (nearly 40%) at a 95% confidence level would seem to vindicate our choice of the Siebenmorgen-Kreugel model templates. Since the redshifts were known, the fitting by a simple χ^2-square minimisation seemed appropriate, so the choice of fitting routine was not critical: I used the Le Phare routine for this purpose, which worked well.

The results have broadly confirmed expectations. The low level of cirrus in the field was confirmed by the results, with 67% of the sources showing the lowest level of extinction (A_V=2.2) built into the model. The dust density was also at the lowest model value for most (71%) of the sources. Most galaxies (87%) showed luminosity $\leq 10^{11} L_\odot$. The SK template fits identified 12 LIRGs, 4 ULIRGs and 4 HyLIRGs, which are shown in Table 5.5. Only 3 of these had 90 μm fluxes. Most had 24 μm fluxes, which usually led to comparable luminosity estimates, except for the 4 HyLIRGs, where the 24 μm-based luminosity estimates were far lower than the SK-based estimates.

The SEDs generally showed no hint of a drop below the starburst SEDs in the PAH-silicate region 3 μm - 13 μm, giving no hint of extinction by AGN (or extreme starburst) activity (cf. discussion in Section 2.7). The WISE 12 μm data points are available for most of the matched SEDs, but this is a broad band so the fine structure of these features is not seen. The existence of MIR emission confirms the BPT analysis presented in Chapter 3 (see Figure 3.15) that star-

Table 5.5: LIRGs, ULIRGs and HyLIRGs in SED fits. Luminosity estimated from far-infrared flux is also shown, based on [a] *AKARI*-FIS 90 μm flux (there are only three cases), and [b] *Spitzer*-MIPS 24 μm flux.

	Name	Luminosity			Redshift	RA	Dec	No. of SK matched points	Figure Ref.
		SK model ($\log_{10}$L/L$\odot$)	FIR-based (90 μm)[a]	FIR-based (24 μm)[b]					
1	AzTEC13	11.0	-	-	0.025	04 44 07.7	-53 39 46	10	
2	FIS90-751	11.0	10.5	11.0	0.139	04 44 08.4	-52 50 58	17	3.20
3	FIS90-50	11.0	11.0	10.7	0.109	04 41 26.8	-53 28 34	6	
4	IRC24-22	11.0	-	13.0	2.357	04 46 06.8	-53 39 27	19	3.11
5	IRC24-104	11.1	-	10.9	0.381	04 44 09.2	-53 28 04	10	
6	FIS90-485	11.2	9.8	9.5	0.055	04 50 04.3	-52 56 34	6	
7	IRC24-113	11.2	-	11.1	0.404	04 46 19.4	-53 26 53	16	
8	IRC24-32	11.2	-	11.6	0.577	04 45 09.7	-53 37 52	16	5.7
9	IRC24-115	11.3	-	13.5	1.321	04 46 04.1	-53 26 31	15	
10	IRC15-265	11.5	-	-	0.030	04 45 58.5	-53 27 09	7	
11	IRC15-286	11.7	-	-	0.117	04 45 52.9	-53 27 41	12	
12	IRC15-596	11.7	-	-	0.205	04 43 36.9	-53 35 56	8	
13	IRC24-84	12.1	-	11.6	0.591	04 43 48.1	-53 30 30	16	
14	IRC24-167	12.1	-	13.2	1.541	04 45 52.0	-53 18 27	10	
15	IRC15-69	12.4	-	-	0.717	04 47 04.8	-53 19 31	13	
16	IRC15-257	12.8	-	13.3	2.858	04 45 24.5	-53 26 44	14	3.11
17	IRC24-168	13.9	-	9.0	0.073	04 46 21.0	-53 18 29	9	
18	IRC24-54	13.9	-	9.6	0.128	04 44 06.2	-53 34 28	13	
19	IRC24-79	14.6	-	10.3	0.191	04 44 27.4	-53 31 17	10	
20	IRC15-547	14.7	-	8.8	0.051	04 45 09.3	-53 34 44	13	

forming galaxies dominate the low-redshift ($z < 0.345$) sources. As would be expected, the *Herschel*-SPIRE points (usually at least for 250 μm and 350 μm) were found in the SED fits for BLAST-selected sources (Figure 5.8).

Further work should be possible with the *AKARI* data. The reduction of the CTIO R-band data (Barrufet et al., in prep.) will improve the calibration of the AAOmega data and is currently under way. It hoped to expand spectroscopic coverage; currently spectroscopic observations of several quasars in the field are planned with the 10 metre Southern African Large Telescope (SALT). Further work which is now in progress includes the reduction of the IRC observations at mid-infrared wavelengths (Davidge et al., in prep.). It has been proposed that the ADF-S may be targeted by *Euclid*. The location of the ADF-S as a low-cirrus field with available multi-wavelength datasets should make it an ideal field for deep observations by the powerful telescopes (such as E-ELT and CCAT) now being built in the southern hemisphere.

5.5 Discussion and future work

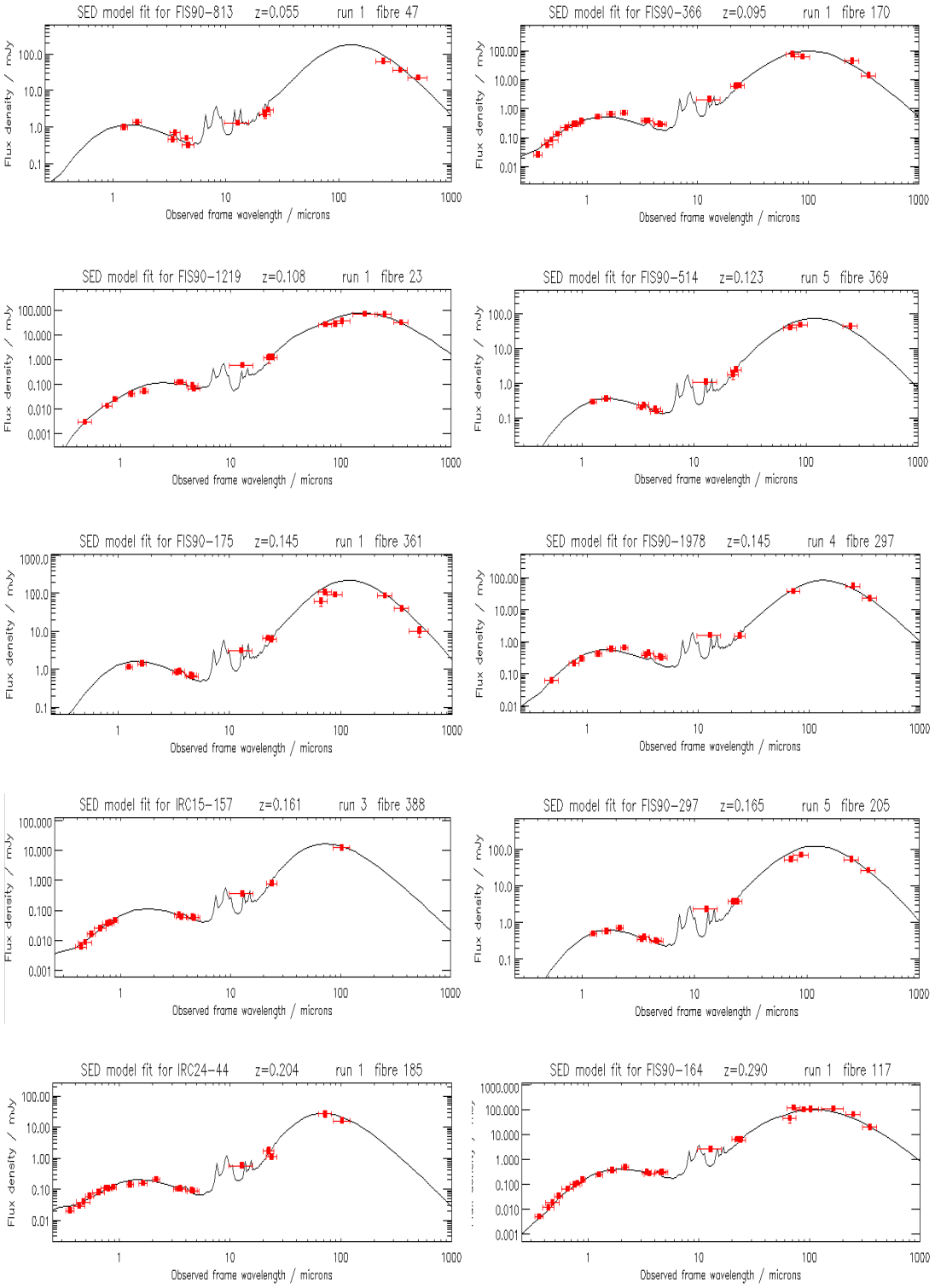

Figure 5.6: Examples of low-redshift ($z \leq 0.345$) SED fits to the SK starburst templates. For details of matched catalogues used, see text. Minimum χ^2 with the Le Phare fitting routine was used.

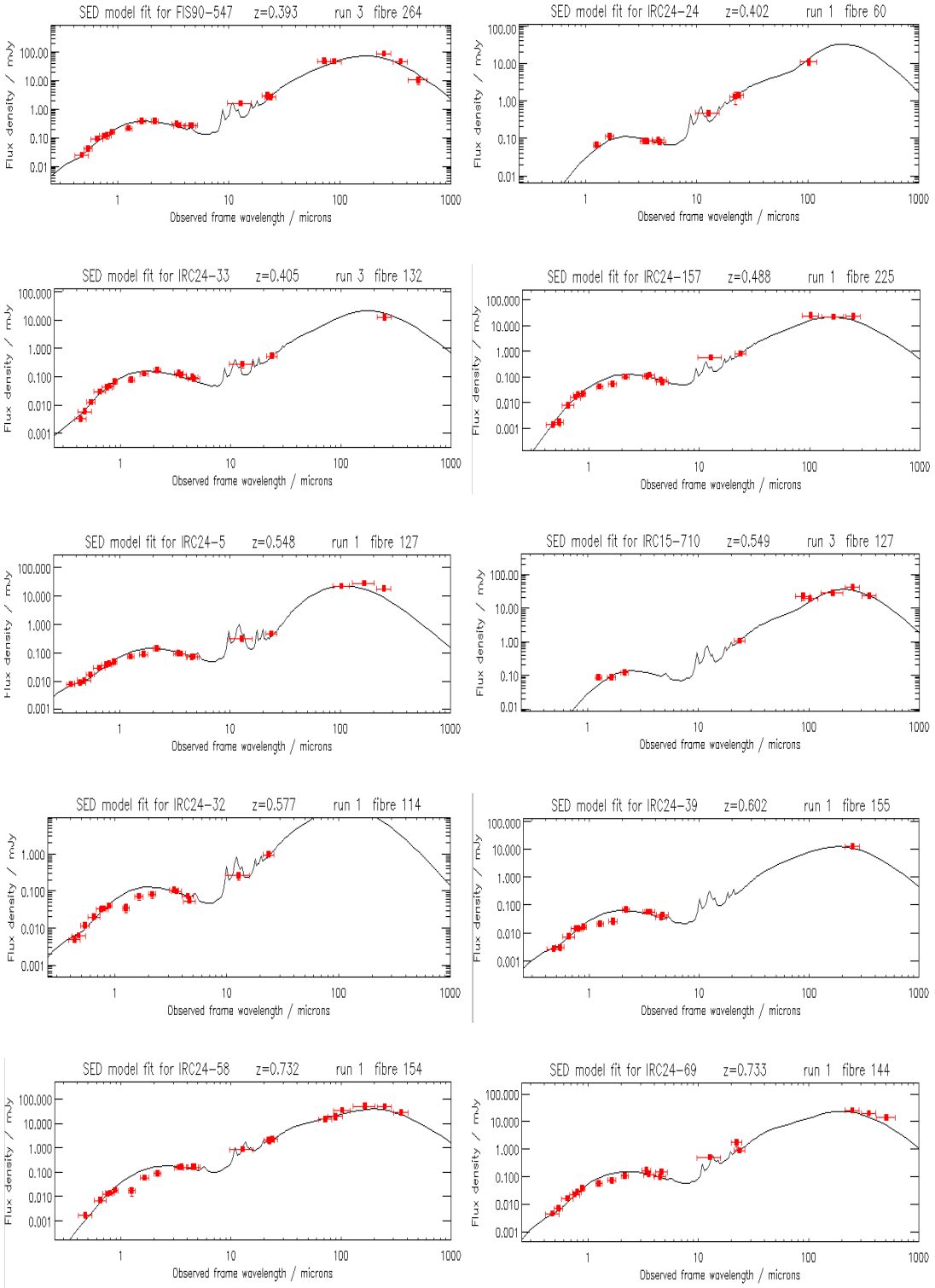

Figure 5.7: Examples of high-redshift ($z > 0.345$) SED fits to the SK templates. See caption to Figure 5.6 for further details.

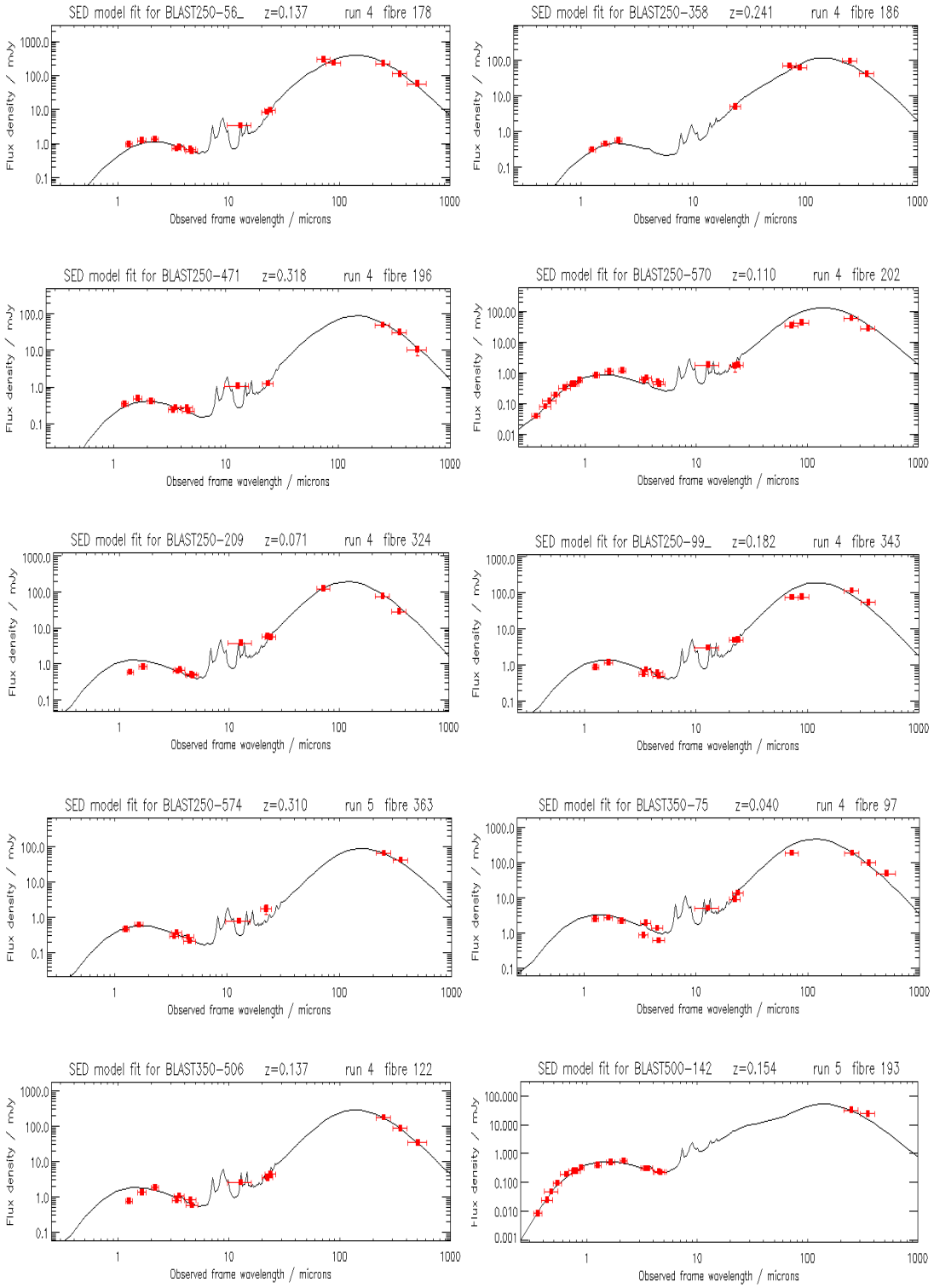

Figure 5.8: Examples of SED fits for submillimetre-selected sources to the SK templates. See caption to Figure 5.6 for further details.

Chapter 6

AKARI-FUHYU project: near-infrared spectroscopy of submillimetre-selected galaxies

As outlined in Chapter 2, many questions remain to be answered about the evolution and extinction of ultra-luminous starbursts, and their co-existence and interaction with AGNs. Insight into these questions can in principle be achieved with spectroscopy of Hα and Pa-α emission lines; however above $z \sim 2.5$ the Hα lines are shifted out of the atmospheric windows available for near-infrared ground-based spectroscopy. AKARI offered a spectroscopic capability beyond the ground-based K-band, and this chapter reports on the results of the spectroscopic phase of the AKARI-FUHYU project, in which observations were made in the wavelength region 2.5 μm - 5 μm during in the warm phase of the AKARI mission. This wavelength region has very poor visibility for ground-based instruments (mainly due to absorption by water vapour in the atmosphere) and has not been covered by other infrared space missions since ISO some twenty years ago.

Observations were made of 43 well-known submillimetre galaxies, most of which had known redshifts, with about 10 pointings for each target. Sources were identified for about two-thirds of the observed targets, and in most cases these showed continuum emission in their spectra. By stacking the multiple pointings for each target, a total of six tentative Hα emission line detections have been obtained. When these are stacked together, the resulting emission line has a signal-to-noise ratio (SNR) of 6.5. Four of these detections (two radio galaxies and two submillimetre galaxies associated with one of them, at redshifts of $z > 3.5$) will be the examined in more detail in Chapter 7. I also made a tentative detection of a Pa-α line for one submillimetre source.

Spectra for 29 Spitzer 70 μm-selected galaxies were also obtained. I was less successful in finding emission lines in these targets, which were observed later in

the mission (when the detectors had warmed further) and with fewer pointings (usually six) per target. These galaxies are at lower redshifts and luminosities that the submillimetre galaxies, and I found only one tentative Pa-α detection at a SNR of 2.5.

6.1 The *AKARI*-FUHYU mission program

The *AKARI* "Follow-Up Hayai-Yasui-Umai" mission program (FUHYU; Pearson et al. [2010]) used the InfraRed Camera to target known sources in well-studied fields to maximise the legacy value of *AKARI* data. The specific objective of the program was to add *AKARI* data to contemporary data rich fields, in particular to fill vital wavelength gaps in existing data. The choice of fields was necessarily constrained by *AKARI's* orbit. Previous papers published in this program covered imaging in the Lockman Hole field (Serjeant et al. [2010b]) and in the GOODS-N field (Pearson et al. [2010]; Negrello et al. [2009]). Spectroscopic work in the project was deferred to the warm phase of *AKARI* (since it can be performed in non-photometric conditions) and is the subject of this chapter and Chapter 7. The primary objective of this phase was to carry out aperture spectroscopy of high-redshift ultra-luminous submillimetre galaxies.

Data collection and reduction is discussed in Section 6.2. Data analysis is covered in Section 6.3. The results for submillimetre-selected galaxies are presented in Section 6.4. The later observations of *Spitzer* 70 μm-selected galaxies are briefly described in Section 6.5, and the stacking of spectra for different targets is presented in Section 6.6. The results are discussed in Section 6.7.

6.2 Data collection and reduction

The *AKARI Space Telescope* is described in Section 1.2. After the cryogen ran out, a number of projects continued into the warm post-cryogen phase when the temperature of the telescope and instruments rose from $\sim$ 6K to $\sim$ 40K. The InfraRed Camera (IRC; Onaka et al. [2007]) was designed for wide-field deep imaging and low-resolution spectroscopy in *AKARI*'s pointing mode, and was used for these observations as discussed in detail below.

Table 6.1: Submillimetre-selected targets in redshift ranges of strongest potential emission lines in the observed wavelength region 2.5 μm$< \lambda <$ 5.0 μm.

Redshift range	Strongest potential emission line	Restframe wavelength (nm)	Targets (no.)	Pointings (no.)
$0.4 < z < 1.6$	Pa-α	1875	4	40
$1.6 < z < 2.8$	Pa-β	1282	13	133
$2.8 < z < 2.9$	Pa-γ	1093	2	20
$2.9 < z < 6.7$	Hα	656	22	221
Unknown z			2	17
Total			43	431

In total, 43 high-redshift submillimetre galaxies were targeted and observed. The targets chosen were mostly well-known from submillimetre observations, and included a number of High-redshift Radio Galaxies (HzRGs). The redshifts of most of these sources had already been established, either from optical spectroscopy or using the photometric redshift technique described in Section 5.2.2. The submillimetre-selected targets are summarised in Table 6.1 by redshift, and results will be presented batched in this way, by the strongest potential emission line detection for each source. The fields in which these targets are located covered many of the well-known deep fields[48] with substantial multi-wavelength data available, and are shown in Table 6.2.

6.2.1 *AKARI* observations

The *AKARI* IRC-NIR instrument was used during the warm phase of the mission. This instrument used a filter wheel to select either one of three imaging filters or one of two dispersion elements. The NIR has an InSb photodiode detector array, using refractive optics to achieve a nearly diffraction-limited performance. The detectors are free of hysteresis effects for these observations, though prone to charged particle impact effects which have to be removed by comparison between multiple short observations. The detector responsivity is highly linear at these flux densities, and no other detector-based artefacts were relevant for these observations. The InSb detectors have been used in both the *Spitzer* and *AKARI*

[48]Deep fields were discussed in Section 2.3.

6.2.1 *AKARI* observations

Table 6.2: Deep fields in which the submillimetre-selected targets were observed in the FUHYU Phase III project (in order of declination; J2000 coordinates).

Deep fields	Central coordinates RA	Dec	Targets	Pointings
GOODS-N	12 36 49	+62 12 58	3	30
Lockman Hole	10 52 43	+57 28 48	4	40
EGS	14 17 52	+52 29 46	4	36
SSA 13	13 12 17	+42 38 05	6	67
ELAIS N2	16 39 44	+41 15 43	3	30
Boötes	14 32 06	+34 16 48	2	22
SSA 22	22 17 00	+00 20 00	3	26
XMM-LSS-SXDF	02 18 00	-07 00 00	3	30
E-CDFS	03 32 28	-27 48 30	5	50
HzRGs + nearby SMGs			7	70
Other			3	30
Total			43	431

missions even in the absence of cryogen, although at lower sensitivity. This is an important advantage of this detector technology. For a reference image, the *N3* image filter (at ~ 3 μm) was used which had a field of view of approximately $10' \times 10'$ across 512×412 pixels giving a pixel scale of $1.46''$. For spectroscopy, the grism *NG* was used which dispersed between 2.5 μm $-$ 5.0 μm across 291 pixels, giving 0.0097 μm per pixel (Ohyama et al. [2007]). The spectral resolution was $\mathrm{R} = \lambda_{\mathrm{min,max}}/\Delta\lambda = 80 - 160$. The *NG* used a $1' \times 1'$ aperture which is referred to as *Np* (which selects the grism and the point source aperture) and was dedicated for spectroscopy of point sources. The PSF FWHM was $4.7''$ in imaging mode and $\sim 6.7''$ in spectroscopic mode.

For the observations, the spectroscopy Astronomical Observing Template (AOT) *IRCZ4* was selected, in the configuration *b;Np*. In Phase III, this configuration gives a quoted 5σ detection limit for point sources of ~ 2 mJy and a line sensitivity of $\sim 5{\times}10^{-18}$ Wm^{-2} for a 10 minute integration for each pointing. Our measured sensitivity was $\sim 4{\times}10^{-18}$ Wm^{-2} at 5σ for 10 minutes. Each pointing consisted of a reference image (for examples, see Figures 7.2 and 7.3 in the next chapter) and at least 8 exposure frames for the *NG* grism, bracketed between 10 dark frames with the shutter closed (see Onaka et al. [2009] for further details). Each frame exposure was ~ 70 seconds, giving an integrated exposure time for each pointing of ~ 9.3 minutes. A total of 10 pointings per source were carried out whenever possible. The observations were made between 2 June 2008 and 9

May 2010.

6.2.2 Data reduction pipeline

The data reduction pipeline for the warm phase was produced in IDL by the *AKARI* team, and is described in the Phase 3 Manual, Version 1.1 (Onaka et al. [2009]). The pipeline includes steps for dark subtraction, saturation masking, monochromatic flat-fielding and background subtraction, wavelength calibration and flux calibration. The calibration data is provided by *AKARI* and used automatically by the pipeline.

The pipeline, $IRC\_SPECRED$, is designed to be run at least twice: firstly without, then with, the *Np_spec* keyword. The first run creates an image shift database for the spectroscopy sub-frames. The second pass attempts to automatically find the target and complete the reduction. Often, the algorithm to find the target fails (it can fail even when there is a clear target in the image) so the position of the target has first to be selected by eye and specified in a table and the pipeline run a third time. If this third run proves necessary, the pipeline fine-tunes the coordinates of the target specified. As advised in the manual, the pipeline was run without slit flat-fielding. The target specified, whether automatically or by eye, then becomes the centre of the $1' \times 1'$ image from which the spectra are extracted.

A number of serious problems were experienced with the *AKARI* pipeline in reducing the data for the targets. An error was found in handling spacecraft jitter between the sub-frames for each pointing (this error has now been corrected by the *AKARI* team). The sky subtraction needed additional work, and so we decided to write our own pipeline to run alongside the *AKARI* pipeline.

The new pipeline includes dark subtraction, saturation masking (physical detector saturation is detected by scaled values from a short exposure and is masked out), wavelength calibration and spectral response calibration using the calibration data from the IRC pipeline. New routines were written to handle sky subtraction in which a sixth-order polynomial was fitted in the dispersion direction to remove a banding pattern across the frame, and a second-order polynomial in the image direction. Routines were also written to handle de-glitching and to

6.2.2 Data reduction pipeline

estimate the offsets between sub-frames caused by spacecraft jitter during each pointing using the simultaneous imaging data.

The new pipeline included IDL routines for zerofootprint drizzling (described in Section 6.3.2) and for noise-weighted feature extraction which were previously developed for the SCUBA Half Degree Extragalactic Survey (SHADES; Serjeant et al. [2008]), using a Gaussian with a FWHM kernel in the expanded grid of 10 and 15 pixels in the wavelength and spatial directions respectively. This equates to a FWHM kernel of 2 and 3 pixels in the original data. The spectroscopic flat fields provided in the calibration data have low signal-to-noise and were found to increase the rms of our data slightly, so flat-fielding was not performed, following guidance in the manual (Onaka et al. [2009]). The new pipeline is described in detail in Appendix A (Section A.2.1). I also wrote an IDL graphic user interface (GUI; see Section A.2.2) routine to visualise various elements of the reduction on an interactive basis and to see instantly the results of changing various parameters, and to compare the results of the new pipeline with those of the *AKARI* pipeline quickly and easily (see Figure 6.1 for an example). Finally, the results were stacked by coadding the noise-weighted pointings for each target. The reduced spectra had lower noise and fewer artefacts than those from the *AKARI* pipeline.

Some of the resulting stacked spectra showed a cyclic pattern which was difficult to remove. I therefore tried to find a better solution by combining all the sub-frames of all the pointings for each target in a single mega-zero-footprint grid and performing source extraction from this grid. However, the final results were still very noisy and did not yield any further detections, except in one case (see Figure 6.2).

Both the new pipeline and the *AKARI* pipeline were run for all sources. The *AKARI* pipeline continued to be used to identify the coordinates of the targets, and also to generate the image for use in the GUI. The spectra obtained by our new pipeline were superior and are used in the rest of this chapter.

6.3 Data analysis

6.3.1 Near-infrared spectroscopy

AKARI had a spectroscopic facility in the near-infrared, a region not covered spectroscopically since the ISO-SWS in the mid-nineties, and which will not be covered again until the launch of the *James Webb Space Telescope* in some four or five years' time. All but two of the submillimetre-selected targets in this chapter had known redshifts, in the range $0.66 < z < 4.73$. The strongest emission lines which will be shifted into this wavelength range for these targets will be the Pa-α line (for galaxies at redshifts of $0.4 < z < 1.6$) and the Hα emission line (for galaxies at $2.9 < z < 6.7$) as shown in Table 6.1. This subsection gives a brief outline of these and other emission lines which were looked for to identify active galaxies at these high redshifts. Much of the discussion on spectroscopy in Chapter 3 (Section 3.2.1) is also relevant to this chapter.

Balmer lines: Hα falls within the observed wavelength range for sources at $2.9 < z < 6.7$. A total of 22 of our targets (all submillimetre-selected) could potentially show Hα emission lines. No Hβ or higher-frequency Balmer lines were detected.

Paschen lines: The Pa-α λ1.875 μm line (transition n=4→n=3) falls into our wavelength range for $0.4 < z < 1.6$, and 4 of our targets were at redshifts where Pa-α could potentially be detected. Pa-α is intrinsically ~ 10 times weaker than Hα, but is the strongest potential line for some of the sources targeted in this chapter. Only two tentative detections were made at low SNRs (see Figures 6.2 and 6.5). We did not detect any Pa-β or Pa-γ lines although 15 of our targets fell within the wavelength range where one of these would have been the strongest line.

Brackett lines: No Brackett lines (transitions down to n=4) were detected. The strongest Brackett emission which was potentially observable for our targets in the observed wavelength range would have been Br-α λ4.051 μm (for sources at $0 < z < 1.23$).

Other lines: We also looked for PAH and silicate features (e.g. the 3.3 μm PAH emission feature), which could have fallen within our wavelength range for some of the targets. However, none of these features was detected in any of our sources.

6.3.2 Stacking, drizzling, zerofootprinting

Averaging, coadding and stacking

When multiple measurements are made of a single source (in this chapter, there were $\sim$ 8 sub-frames for each pointing, and $\sim$ 10 different pointings for each target), the simplest way to combine the measurements is by averaging. The measurements will usually first need to be realigned to a common reference frame. Our problems with spacecraft jitter between sub-frames are discussed in Appendix A, Section A.2.1. When the measurements are registered to a common frame, noise-weighted and averaged, this is normally called coadding (although this term is sometimes used more loosely to refer simply to noise-weighted averaging).

Stacking is a statistical technique which is powerful in finding a category of sources in observations at wavelengths where individual sources are not detected, or have a low signal-to-noise ratio. Provided the source coordinates are known, the source flux can be obtained by averaging many different observations at these coordinates. This can produce a better signal-to-noise ratio than the unstacked observations, since the noise levels integrate down. Stacking is used to combine our observations of Hα sources in Section 6.6 below.

Shift-and-add, drizzling

Where the fields of view of the individual observations are not exactly aligned, whether deliberately offset (called dithering) or as the result of observations taken at slightly different CCD alignments or orientations with respect to the target, a technique called shift-and-add takes the pixels of the observed flux and places each of them, after resampling, into a finer output grid.

An alternative method of combining such observations, which can better preserve information for undersampled (i.e. the pixel size larger than the Nyquist scale, which in turn is about half the FWHM of the point-spread-function) data,

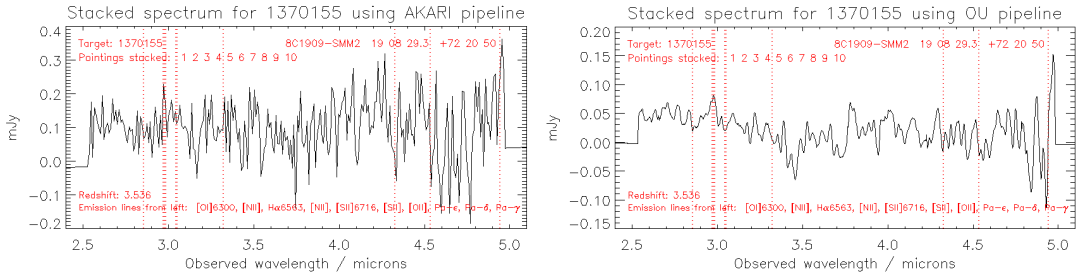

Figure 6.1: Pipelines compared for the stacked spectrum of the submillimetre target 1370155: **left,** after using the *AKARI* pipeline; **right,** after using the new pipeline which used zerofootprint drizzling (discussed in Section 6.3.2).

places the observed flux into a smaller area in the output grid; this is called variable-pixel linear reconstruction, or more commonly, drizzling. Drizzling can reconstruct a sharper image than would be obtained by shift-and-add. Drizzling was developed for the *Hubble Space Telescope*, and is described in Fruchter and Hook [2002]. A finer output grid is set up, and the information in the different input grids are aligned and "drizzled" into the output grid. This has the effect of recovering the small scale structure up to the Nyquist scale.

Zerofootprint drizzling

Zerofootprint drizzling is an extreme example of drizzling: the flux for each detector pixel is assigned to the single point in the zerofootprint map. This could be described as the detector pixel's view of the sky at each point. Although the zerofootprint map is noisier than a shift-and-add map, a source extraction routine (mathematically equivalent to convolutions) then finds the maximum signal-to-noise best-fit point source at each point in the map. The technique was developed for the SCUBA observations (Scott et al. [2002]; Serjeant et al. [2003]). In this chapter, where the technique is used on 2D spectral maps, the convolution kernel is the IRC's point-spread-function in the spatial direction and a Gaussian at the wavelength resolution in the dispersion direction. By using this technique, the signal-to-noise of the resulting spectra can be maximised. An example comparing the *AKARI* pipeline with the new pipeline using zerofootprint drizzling for one of the submillimetre targets is shown in Figure 6.1.

6.4 Results for submillimetre galaxies

Of the 43 submilllimetre-selected sources targeted, a clear reference image was obtained for 29 sources. Given the low SNR for clear sources, it is unlikely that a meaningful spectrum can be extracted for sources without a clear image, although in three further cases, a column flux profile peak could be used to identify the position of the target.

In the proposal for the FUHYU program, it was thought that Paschen lines would most likely be observed (see Table 6.3 for targets in this redshift range). There were four potential Pa-α sources among the submillimetre targets, two with clear images and two with column flux peaks. A tentative identification was made of an emission line in one of these sources (at SNR ~ 2; see Figure 6.2). A further 15 sources were at redshifts where the strongest potential emission line was Pa-β or Pa-γ ($1.5 < z < 3.0$), but no trace of these relatively weak emission lines was found.

More success was achieved with the detection of Balmer lines, even though sources are at higher redshifts and so expected to be fainter. Of the 22 potential H-α sources (see Table 6.4), 15 showed either an image (sometimes faint) or a peak in their column flux profiles. Most spectra for these sources showed continuum emission. Four Hα detections which were made at SNRs of $2.5 - 10.0$ will be investigated in detail in Chapter 7. Two further tentative Hα detections (at SNRs of 3.0 and 2.0) are reported below. A multi-source stack of all six sources with tentative Hα detections gave a SNR of 6.5 and is described below in Section 6.6.

The sub-sections below discuss the results for each target, firstly those with potential Paschen lines and then those with potential Hα lines.

Submillimetre sources with potential Paschen lines ($0.4 < z < 2.9$)

Only four submillimetre sources were targeted with redshifts in the Pa-α range, of which one showed a tentative detection. Brief comments about the four sources are given below. There were also thirteen Pa-β targets, and two Pa-γ targets, but none showed convincing detections. Table 6.3 shows the details of all these Paschen line targets.

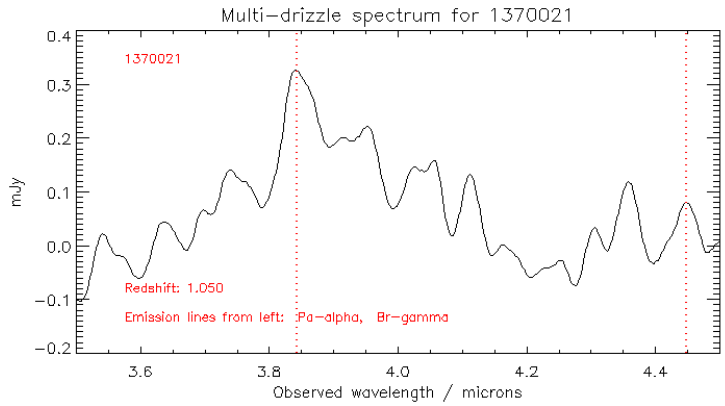

Figure 6.2: Multi-drizzle spectrum of the first ten (1370021) pointings for SSG1. The peak coincides with the emission line for Pa-α at $z = 1.05$, which agrees with the *Spitzer*/IRS redshift which matched several PAH features at 7 μm - 15 μm rest-frame wavelengths (Khan et al. [2009]). The SNR is 2.0.

SSG1 ($z = 1.05 \pm 0.01$): The redshift for this source was established with *Spitzer*/IRS mid-IR spectroscopy, which identified PAH features at 7.7, 8.6, 11.3 and 12.7 μm (Khan et al. [2009]). There was a clear but faint source in the *AKARI* image for each pointing. The stack of the first 10 pointings (observations made earlier than the final 2) showed a peak at a wavelength equivalent to Pa-α at $z = 1.05$, at an SNR of about 2 (see Figure 6.2) when the multi-drizzle sky subtraction was used in the reduction.

SXDF850.36 ($z = 0.92$ or $z \sim 3.6$): There was no clear source in the *AKARI* image, although there was a column flux profile peak in most pointings (not 7, 8, 9). Stacked spectra showed no convincing line detection, either of Hα at $z \sim 3.6$ or of Pa-α at $z = 0.92$. The photometric redshift for this source of $z = 0.92$ came from NED (although the reference there is incorrect, so unknown) (2010). Private correspondence (C. Pearson) suggested a redshift of $z \sim 3.6$ for this source.

LOCK850.05 ($z = 1.2$): Although the target was not visible in the $1' \times 1'$ IRC image, most of the pointings showed a peak in the column fluxes. Pointings 7 and 8 were not usable. The spectra showed no hint of Pa-α emission at this redshift (photometric redshift from Dye et al. [2008]).

SMMJ141742.04+523025.7 ($z = 0.661$): Redshift known from Chapman et al. [2005]. This was a clear source. There were possible Pa-α identifications in pointings 1, 4 and 5, but there was no convincing line in the stacked spectrum.

Table 6.3: Submillimetre sources for which the strongest potential emission lines are Pa-α ($0.4 < z < 1.6$) or Pa-β ($1.6 < z < 2.8$) or Pa-γ ($2.8 < z < 2.9$). References: (a) Aretxaga et al. [2007]; (b) Bertoldi et al. [2000]; (ce) Coe et al. [2006]; (ch) Chapman et al. [2005]; (ch2) Chapman et al. [2004]; (cm) flux data from Charmandaris et al. [2004]; (dy) Dye et al. [2008]; (e) Eales et al. [2003]; (k) Khan et al. [2009]; (i) Ivison et al. [2007]; (lf) Le Fevre et al. [2004]; (se) Serjeant et al. [2010b]; (sm) Smail et al. [2004]; (v) Valiante et al. [2007]; (wa) Watabe et al. [2009]; (we) Weiss et al. [2009a].

Object	RA (J2000)	Dec (J2000)	Observation ID	Pointings	Redshift (z)	Flux mJy (μm)	References
Boötes field:							
SSG1	14 32 06.6	+34 16 13.4	1370021, 1371003	12	1.05 spec	23.2 (350)	k
SSG2	14 32 06.1	+34 16 48.4	1370022, 1371004	10	1.97 phot	17.1 (350)	k
MAMBO/VLA targets close to Abell 2125:							
MMJ154127+6615	15 41 26.9	+66 14 37	1370151	10	2.25 est	10.7 (870)	b, cm, e
MMJ154127+6616	15 41 27.3	+66 16 17	1370152	10	2.79 phot	14.6 (870)	b, cm, wa, v
E-CDFS:							
LESS-25	03 33 02.2	-27 56 44.1	1370017	10	2.79	12.0 (870)	we, lf
LESS-37	03 32 42.6	-27 46 47.4	1370018	10	2.839 phot		we, ce
XMM-LSS-SXDF:							
SXDF850.7	02 17 38.9	-05 05 28.0	1370007	10	2.6 phot	7.1 (850)	i, a
SXDF850.36	02 18 32.3	-04 59 47.2	1370010	10	0.92 phot	5.4 (850)	i, se
Lockman Hole field:							
LOCK850.05	10 53 02.6	+57 18 27.0	1370003	10	1.2 phot	8.1 (850)	dy, i
SSA13 field:							
SMMJ131231+424609	13 12 31.1	+42 46 09.0	1370035, 1301012	14	2.713 spec	4.9 (870)	sm, ch
SMMJ131215+423900	13 12 15.3	+42 39 00.9	1370043, 1371010	12	2.565 spec	4.4 (870)	sm, ch
SMMJ131222+423814	13 12 22.4	+42 38 14.1	1370044	10	2.565 spec	3.0 (870)	sm, ch
SMMJ131212+424422	13 12 12.7	+42 44 22.5	1370034, 1371009	11	2.805 spec	5.6 (870)	sm, ch
Extended Groth Strip:							
SMMJ141742+523025	14 17 42.0	+52 30 25.7	1370091	8	0.661 spec	2.6 (870)	sm, ch
SMMJ141809+522803	14 18 09.0	+52 28 03.8	1370036	10	2.712 spec	4.3 (870)	ch
SMMJ141800+512820	14 18 00.5	+51 28 20.8	1370072, 1371013	8	1.913 spec	5.0 (870)	ch
GOODS-N field:							
SMMJ123600+620253	12 36 00.10	+62 02 53.5	1370037	10	2.710 spec	6.9 (870)	ch
SMMJ123616+621513	12 36 16.15	+62 15 13.7	1370042	10	2.578 spec	5.8 (870)	ch, ch2
ELAIS N2 field:							
SMMJ163706+405313	16 37 06.51	+40 53 13.8	1370054, 1371014	9	2.374 spec	11.2 (870)	ch

Submillimetre sources with potential Hα lines ($2.9 < z < 6.7$)

Twenty-two sources were targeted which have redshifts in this range: see Table 6.4 for details. The 15 sources for which a clear detection was made are described below. In Section 6.6 I will describe the results of stacking together all the potential Hα sources with clear images.

LOCK850.63 ($z = 4.73$): This is a very strong source, with a decreasing continuum with strong emission lines. There is a strong peak at $z = 5.55$ in pointing 8, and at $z = 5.850$ in pointing 9. However, stacking the sources (excluding pointing 6 which was not usable) smoothed out these emission lines. Dye et al. [2008] gives a 90% uncertainty range for the photometric redshift of 4.64 - 4.89. Earlier, Aretxaga et al. [2007] calculated two photometric redshifts of $3.9^{+2.6}_{-1.7}$ and $2.6^{+2.0}_{-0.6}$ giving a range of $1.5 < z < 6.7$.

LESS-88 ($z = 4.06$): This looked at first to be a promising result, with a clearly visible source and strong column flux peaks. Pointing 8 showed a possible Hα line. However, the stack of all pointings showed no convincing Hα line and had a high noise level. The multi-drizzle stack showed no convincing line either. Pointing 6 was faulty.

SMMJ131201.17+424208.1 (aka SSA13 # 290) ($z = 3.405$): This was a very clear and bright source in six of the ten pointings. It was at the top of the $1' \times 1'$ frame and just missed in the other four pointings. Some pointings show a possible Hα line, but at slightly differing redshifts. The stacked spectrum of good pointings did not show Hα.

SMMJ141813.54+522923.4 ($z = 3.484$): This was an extremely faint source near the edge of the aperture but with a column flux profile peak in most pointings. Hints of Hα were seen in individual pointings; the stacked spectrum showed a weak (but unconvincing) peak around Hα.

SMMJ123712.05+621212.3 ($z = 2.910$): A double source (Chapman et al. [2004]). This was a very clear source in the *AKARI* image. There was a hint of a possible Hα line at the extreme edge of the stacked spectrum (just at 2.5 μm) but noise at the edge made this unconvincing.

SMMJ163627.94+405811.2 ($z = 3.180$): Hints of Hα at this redshift in most pointings and in the stacked spectrum. Pointings 7 and 9 not usable. This seemed a promising result, although the noisy spectrum and other nearby peaks (see Figure 6.3) made the SNR of the Hα line only 2.0.

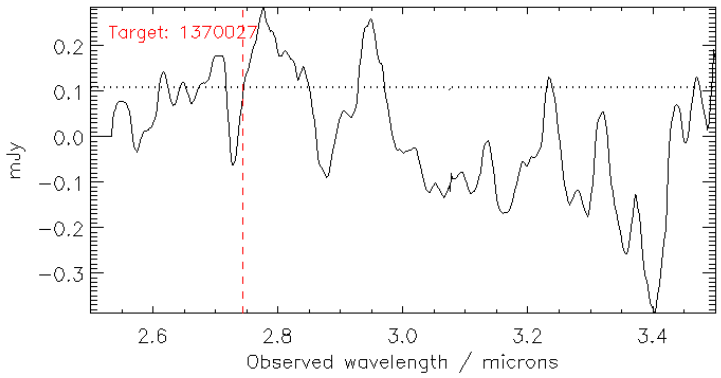

Figure 6.3: Spectrum of SMMJ163627+405811, with a tentative identification of Hα at the already known redshift $z = 3.180$. The peak is offset from expected peak and the target was on the edge of the aperture. SNR is 2.0 using the continuum level shown in the figure.

LAB 5 ($z = 3.090$): This is one of the largest submillimetre-detected Lyman-alpha blobs (LABs; Geach et al. [2005]). The $1' \times 1'$ image for LAB5 did not show a clear source, and although there was a peak in the column fluxes in some of the pointings, the spectra were poor and the stacked spectra showed no expected emission lines.

LAB 10 ($z = 3.090$): This LAB has a significant 850 μm flux, showing an SFR of ~ 1600 M$_\odot$ yr^{-1}, and may be related to obscured activity in the source; it is within $\sim 5''$ of an extended continuum source (Geach et al. [2005]). A clear source in the IRC image, with a good Hα identification in several pointings. The stacked spectrum showed a peak but also a stronger nearby peak. If we exclude the second peak from the calculation of the continuum, the SNR of the possible Hα line is 3.0 (see Figure 6.4).

Abell Cluster 1835: SMMJ14009+0252 ($z = 2.934$): This was one of the brightest submillimetre sources found by SCUBA and is magnified by the Abell Cluster 1835 lens at $z = 0.25$ (Ivison et al. [2000b]). It is also a radio source at 1.4GHz but not visible at optical wavelengths (Ivison et al. [2000b]). The redshift was determined from its CO line emission by Weiss et al. [2009a]. The potential Hα line is unfortunately very close to the bottom edge of our wavelength range. There was a hint of Hα in several pointings, but not in the stacked spectrum. Pointing 4 was not usable.

Radio source 8C1909+722 ($z = 3.536$) and 3 nearby submm sources SMM1-3: Hα emission was found for the radio galaxy and two (SMM1 and SMM2) of the three submillimetre sources. These are described and analysed in Chapter 7. The line width

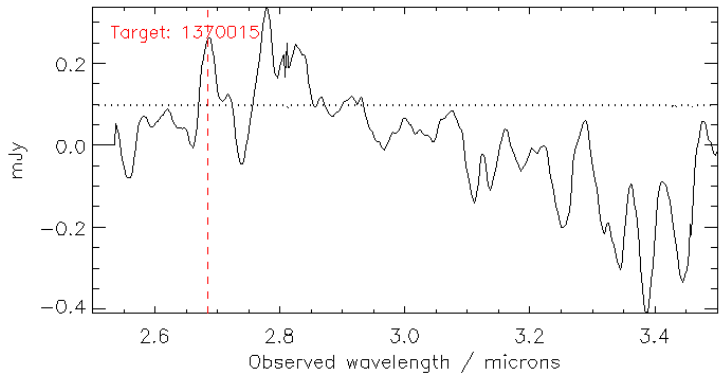

Figure 6.4: Spectrum of LAB10 showing expected Hα emission line at $z = 3.09$ ($\lambda_{\rm obs} = 2.68\,\mu$m). This would be more convincing if it wasn't for the even higher peak alongside.

showed that the HzRG is a quasar.

8C1435+635 ($z = 4.261$): This radio galaxy was clearly identified. Pointing 7 showed a clear Hα peak at this redshift, but most pointings did not. I was not able to detect a clear Hα emission line in the stacked spectrum.

4C60.07 ($z = 3.788$): I also found Hα emission from this radio galaxy, which is covered in Chapter 7. The width of the line showed that this is also a quasar.

4C41.17 ($z = 3.792$): This was a very clear source. However, the spectra of the seven pointings and of the stack was of poor quality with no clear Hα line.

ELAIS N2-23, unknown redshift: There were several peaks in the spectra, but no identifiable pattern of emission lines.

SSA 21a-C1 (LBG at $z \sim 3$)): A faint source, but most pointings showed clear column flux peaks. There were peaks in the stacked spectrum (there was a broad line which could be Hα is $z \sim 3.65$). With only the one line and the redshift unknown with any precision, I cannot claim an identification.

Table 6.4: Submillimetre sources with potential Hα emission lines ($2.9 < z < 6.7$). References: (a) Aretxaga et al. [2007]; (ch) Chapman et al. [2005]; (cp) Coppin et al. [2010]; (db) de Breuck et al. [2001]; (d) Dye et al. [2008];(ge) Geach et al. [2005]; (gr1) Greve et al. [2005]; (gr2) Greve et al. [2007]; (ha) Hainline et al. [2006]; (hi) Hildebrandt et al. [2005]; (i) Ivison et al. [2007] (SHADES targets); (i2) Ivison et al. [2000b]; (i3) Ivison et al. [2000a]; (i4) Ivison et al. [2008]; (r) Roettgering et al. [1997]; (sm) Smail et al. [2004]; (sp) Spinrad et al. [1995]; (st) Stevens et al. [2003], flux data from SCUBA on JCMT; (sz) Szokoly et al. [2004]; (w) Weiss et al. [2009b], taken from the LABOCA Extended Chandra Deep Field South Survey (LESS); (w2) Weiss et al. [2009a]. * asterisk indicates the 5 sources in this project covered in Sedgwick et al. [2013]. ** double asterisk indicates redshifts confirmed by this project. † The L_{FIR} calculation is described in Section 7.3.3.

Object	RA (J2000)	Dec (J2000)	Observation ID	Pointings	Redshift (z)	Flux mJy (μm)	L_{FIR}† $10^{13} L_{\odot}$	Hα detection	References(s)
Lockman Hole:									
LOCK850.01	10 52 01.2	+57 24 45.8	1370001	10	3.38 spec	8.8 (850)	0.62		i, cp
LOCK850.02	10 52 57.0	+57 21 08.3	1370002	10	3.1 phot	13.4 (850)	0.96		i, a, d
LOCK850.63	10 51 54.3	+57 25 02.6	1370005	10	4.73 phot	3.6 (850)	0.25		d, a, i
XMM-LSS-SXDF:									
SXDF850.1	02 17 30.6	-04 59 36.7	1370006	10	3.1 phot	10.4 (850)	0.75		i, a
E-CDFS:									
LESS-31	03 32 53.7	-27 37 39.6	1370020	10	3.44 phot				hi
LESS-68	03 31 51.9	-27 53 26.6	1370013,1371001	9	2.94 spec	5.5 (870)	0.42		w, sz
LESS-88	03 31 31.0	-27 32 34.4	1370019, 1371002	11	4.06 phot	6.7 (870)	0.49		w, hi
SSA13 field:									
SMMJ131228.30+424454.8	13 12 28.3	+42 44 54.8	1370032, 1371011	10	2.931 spec	3.4 (870)	0.26		sm, ch
SMMJ131201.17+424208.1	13 12 01.2	+42 42 08.1	1370026	10	3.408 spec	6.2 (870)	0.46		ha, gr1, sm, ch
EGS / CDFS-14:									
SMMJ141813.54+522923.4	14 18 13.5	+52 29 23.4	1370025	10	3.484 spec	3.6 (870)	0.27		sm, ch
GOODS-N field:									
SMMJ123712.05+621212.3	12 37 12.05	+62 12 12.3	1370033, 1371008	10	2.914 spec	8.0 (870)	0.62		sm, ch
ELAIS N2:									
SMMJ163627.94+405811.2	16 36 27.94	+40 58 11.2	1370027	10	3.180 spec	6.5 (870)	0.49	yes	sm, ch
SSA 22 field:									
LAB5	22 17 11.7	+00 16 44.9	1370014	10	3.090 spec	5.2 (850)	0.37		ge
LAB10	22 18 02.3	+00 25 56.9	1370015	10	3.090 spec	6.1 (850)	0.44	yes	ge
Abell Cluster 1835:									
SMMJ14009+0252	14 00 57.57	+02 52 49.1	1370012	10	2.934 spec	15.6 (850)	1.13		w2, i2
HzRGs and associated SMGs:									
8C1909+722 HzRG*	19 08 23.3	+72 20 10.4	1370153	10	3.536 spec	34.9 (850)	2.45	yes	st, db
8C1909+722 SMM1*	19 08 27.4	+72 19 28.0	1370154	10	3.536**	23.0 (850)	1.61	yes	st
8C1909+722 SMM2*	19 08 29.3	+72 20 49.6	1370155	10	3.536**	8.7 (850)	0.61	yes	st
8C1909+722 SMM3*	19 08 16.1	+72 20 24.0	1370156, 1371006	13	3.536 assoc	4.3 (850)	0.30		st
8C1435+635 HzRG	14 36 37.4	+63 19 13.1	1370157	10	4.261 spec	6.0 (850)	0.42		st, sp
4C60.07 HzRG*	05 12 54.8	+60 30 51.7	1370162	10	3.788 spec	23.8 (850)	1.66	yes	st, i4, r
4C41.17 HzRG	06 50 52.1	+41 30 30.8	1370163	7	3.792 spec	12.0 (850)	0.84		st, i3, gr2, r

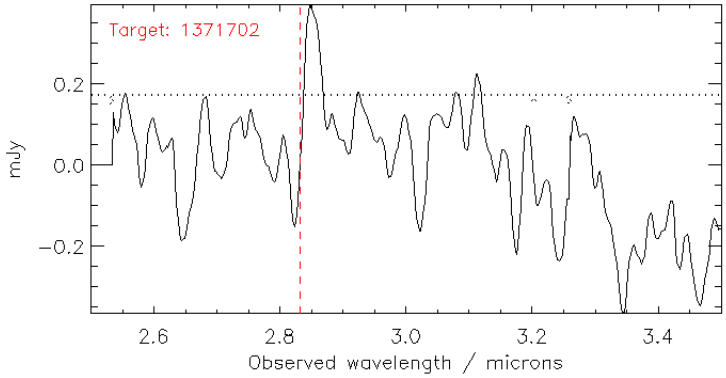

Figure 6.5: Spectrum of 70Bootes1, a *Spitzer*-selected target, with a tentative identification of Pa-α slightly offset from the known redshift $z = 0.510$. Brand et al. [2008] estimated the redshift from PAH features in the MIR spectrum at $z = 0.501$; this is slightly different from the $z = 0.510$ shown in Weedman and Houck [2008]. The SNR of this tentative detection is 2.5.

.

6.5 Results for *Spitzer*-selected galaxies

A total of 29 *Spitzer* 70 μm-selected sources were observed in the final stages of the FUHYU mission program, when the instruments would have been warmer as *AKARI* neared the end of its scientific lifetime (the final science was completed in May 2011). Up to 6 (rather than 10) pointings were made of each of these targets. The results were poorer than for the submillimetre targets discussed earlier.

The strongest detectable line for these observations was the Pa-α λ1875 Å line, available for $0.4 < z < 1.6$ sources in our observed wavelength region. In total, nine sources were observed with redshifts in this range (4 in the Extended Groth Strip, 2 in the Lockman Hole and 3 in the Boötes field). Only six of these nine were actually observed in the images or column flux peaks, and only one of these showed a tentative detection, shown in Figure 6.5. As stated in Section 6.2.1, the line sensitivity for our observations was $\sim 5{\times}10^{-18}$ Wm^{-2}. The forecast flux from a Pa-α line for a ULIRG of luminosity $5{\times}10^{12}$ L$_\odot$ (Pearson et al. [2008]) at the limits of our range, $z = 0.4$ and $z = 1.6$, would be $5{\times}10^{-17}$ and $2{\times}10^{-18}$ respectively. Although the lower-redshift flux is within our sensitivity (and the detection in Figure 6.5 was at $z = 0.510$) the higher-redshift flux is not. It is also likely that the sensitivity will have reduced by the time these observations were made, some two years into the warm phase. The

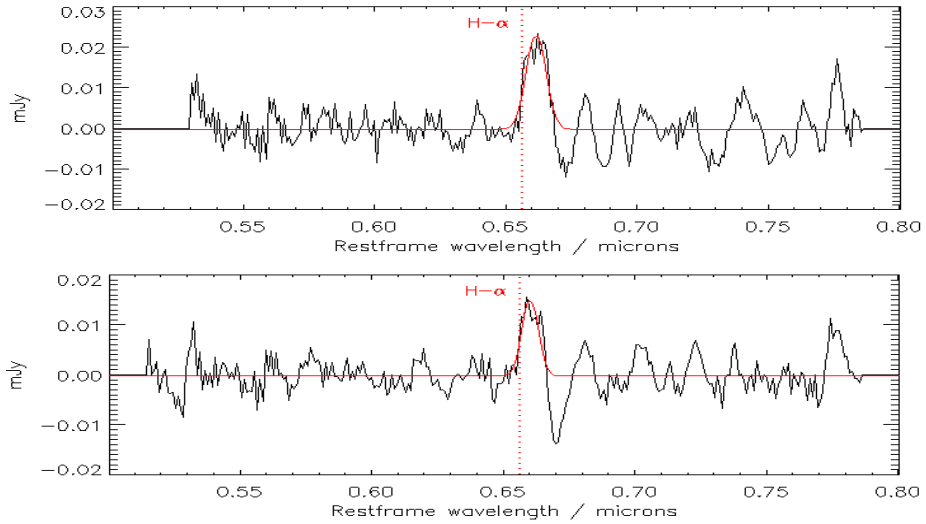

Figure 6.6: **Top:** The multi-source stacked spectrum of sources spanning Hα which had line detections (see Table 6.5, top). A total of 58 pointings are included. The continuum has been subtracted using a 30-bin boxcar median. The SNR of the Hα line is 6.5. **Bottom:** The multi-source stacked spectrum of all targets with potential Hα lines, a total of 143 pointings. The SNR of the Hα line is 4.0.

non-detections may perhaps suggest the sources are not HyLIRGs and/or do not show evidence of strong AGN emission.

The next strongest emission line observable was the Br-α λ4051 Å line, and 11 targets had redshifts which would put this line in our observed wavelength range: 9 in the *Spitzer* First Look Survey field (FLS; Frayer et al. [2006]), one in the Boötes field and one in the Extended Groth Strip. In the context of our results for Pa-α , it is not surprising that this relatively weak line was not detected for any of these sources.

6.6 Multi-source stacking

Stacking of Hα sources

In total, 15 of the 22 targets in the redshift range with the possibility of detecting Hα (all submillimetre-selected) had a clear source detection, either from the *AKARI* reference image or from a clear peak in the column flux profile. The spectra for these sources were converted to restframe wavelengths and stacked in two groups: those with a Hα line detection, and all such sources. Details are shown in Table 6.5. The individual

Table 6.5: Multi-source stacking: targets with potential Hα lines which were identified sources from either the reference image or from a column flux profile peak. All are submillimetre-selected sources. See Section 6.4 for comments on each target.

Object	Type / Field	Redshift (z)	Observation ID	Pointings to stack	SNR
Sources with line detections					
8C1909+722 HzRG	HzRGs +	3.536 spec	1370153	1-10	3.1
8C1909+722 SMM1	HzRGs +	3.536 spec	1370154	1-10	10.0
8C1909+722 SMM2	HzRGs +	3.536 spec	1370155	1-10	2.4
4C60.07 HzRG	HzRGs +	3.788 spec	1370162	1-10	2.5
SMMJ163627.94+405811.2	ELAIS N2	3.180 spec	1370027	1-6 ,8, 10	2.0
LAB10	SSA 22	3.090 spec	1370015	1-10	3.0
Subtotal				*58*	6.5
Sources without line detections					
LESS-88	ECDFS	4.06 phot	1370019, 1371002	1-5, 7-9; 1-2	
LOCK850.63	LH	4.73 phot	1370005	1-5, 7-10	
SMMJ131201.17+424208.1	SSA 13	3.405 spec	1370026	1,3,4,6,7,9,10	
SMMJ141813.54+522923.4	EGS	3.484 spec	1370025	1-10	
SMMJ123712.05+621212.3	GOODS-N	2.914 spec	1370033, 1371008	1-5; 1-5	
SMMJ14009+0252	Abell Cluster 1835	2.934 spec	1370012	1-3, 5-10	
8C1909+722 SMM3	HzRGs +	3.536 assoc	1370156, 1371006	1-10;1-3	
8C1435+635 HzRG	HzRGs +	4.261 spec	1370157	1-10	
4C41.17 HzRG	HzRGs +	3.792 spec	1370163	1-7	
Subtotal				*85*	2.9
Total pointings				*143*	4.0

pointings taken in each case have been co-added after noise-weighting, and the result is shown in Figure 6.6. This shows a clear Hα detection for the 6 sources with line detections, with an SNR of 6.5. There is also a peak for the stack of all potential Hα sources, for which the SNR is 4.0.

Stacking of Pa-α sources

For targets with potential Pa-α detections, we have identified the sources in 10 of the 13 sources targeted (including both submillimetre-selected and *Spitzer*-selected), with tentative lines detected in two of them (see Table 6.6 for details). The number of pointings involved was low, however, and no Pa-α line was seen in the stacked spectrum of all the sources.

6.7 Discussion and conclusions

This was an ambitious project to observe the spectra of well-known sources in a wavelength region which had not been observed spectroscopically since ISO-SWS, and which will not be accessible again until JWST spectroscopy in about five years' time. These

6.7 Discussion and conclusions

Table 6.6: Multi-source stacking: targets with potential Pa-α lines which were identified sources from either the reference image or a column flux profile peak. *The *Spitzer* source labelled Lockman 63 is not the same as the Lockman 63 targeted as a submillimetre source.

Object	Field / Type	Redshift (z)	Observation ID	Pointings to stack	SNR
Sources with line detections					
SSG1	Boötes	1.05 spec	1370021	1-10	2.0
70Bootes1	Boötes	0.501 pah	1371702	1-6	2.5
Total pointings				*16*	
Sources without line detections					
SMMJ141742+523025	EGS	0.661 spec	1370091	1-8	
EGS70-41	EGS	0.450 spec	1371713	1-2	
EGS70-126	EGS	0.420 spec	1371740	1, 4, 5	
EGS55	EGS	0.670 spec	1371767	1-2	
EGS1-5	EGS	0.530 spec	1372277	1-2	
LOCK850.05	Lockman Hole	1.2 phot	1370003	1-6, 9-10	
Lockman 63*	Lockman Hole	1.15 phot	1371955	1-2	
SXDF850.36	XMM-LSS-SXDF	0.92 phot	1370010	1-10	
Total pointings				*27*	

observations were taken in the *AKARI* warm phase, when the quality of observations had been degraded by factor of two (and more in the later stages of the project), which meant that only the strongest emission lines were observable. The quality of the spectra obtained was in most cases extremely poor. Sub-frame multi-pointing drizzling was also tried as an alternative way to reduce the noise, and one further detection was achieved with this. The most significant exception to this was the detection of Hα emission in two high-redshift radio galaxies and associated submillimetre galaxies, which is described in more detail in the next chapter.

A significant number of targets did not show in the reference image, although continuum emission was present in most of the pointings, suggesting that real fluxes were being observed from the sources (as well as noise). Some sources could nevertheless be targeted for spectroscopy in the aperture if they showed a clear peak in their column flux profile. I could not obtain spectra for a significant number of sources: 7 of the 22 Hα sources and 5 of the 13 Pa-α sources could not be identified at all. Only Hα and Pa-α lines could realistically be identified, given the quality of the observations. (No targets with Hβ / [OIII] as potential strongest potential lines were targeted.) Lines from targets with relatively weak lines like Brackett lines in the observed wavelength region were not observed. With only a single convincing emission line detected for any source, this work did not yield any new redshifts (other than the two discussed in the next chapter).

For the submillimetre-selected sources, 6 (tentative) Hα line identifications were made. Although most were at modest SNRs, the stack of all 6 gave an SNR of 6.5, and the stack of all 15 potential Hα sources (i.e. those with clear targets in the reference image and with the appropriate redshift) showed a line with an SNR of 4.0. This confirms that submillimetre galaxies are active with starburst and/or AGN activity. This is discussed in more detail in the next chapter for the most interesting detections. Table 6.4 shows that three of the successful identifications were the three most luminous objects observed, and the average luminosity of successful identifications was over twice that of non-detections. For these distant targets, dust obscuration was clearly a factor in non-detection.

The results for the *Spitzer*-selected sources, taken in the later stages of the project when the instruments were even warmer, and with fewer pointings, were almost non-existent.

For the 10 sources whose Pa-α line would fall in the observed wavelength range, only 2 (tentative) line identifications were made, and the stack including non-detected sources did not show a result for Pa-α.

A more detailed discussion of the physical interpretation of these results will be given in the next chapter, including their relation to high-redshift [CII] lines.

Chapter 7

Detection of Hα emission from $z > 3.5$ submillimetre luminous galaxies with *AKARI*-FUHYU spectroscopy[49]

This chapter presents tentative Hα emission line detections of four submillimetre-detected galaxies at $z > 3.5$: the radio galaxies 8C1909+722 and 4C60.07 at signal-to-noise ratios (SNRs) of 3.1 and 2.5, and two submillimetre-selected galaxies (SMGs) near the first of these at SNRs of 10.0 and 2.4, made with the AKARI Space Telescope as part of the FUHYU mission program. These are the highest-redshift Hα detections in such galaxies, made possible by AKARI's unique near-infrared spectroscopic capability. The two radio galaxies had known redshifts and surrounding structure, and I have detected broad Hα components indicating the presence of dust-shrouded quasars. I conclude that powerful AGNs at $z > 3.5$ occur in peaks of the star-formation density fields, supporting a close connection between stellar mass build-up and black hole mass assembly at this redshift. I also show that 4C60.07 is a binary AGN. The Hα detections of the two SMGs are the first redshift determinations for these sources, confirming their physical association around their companion radio galaxy. The Hα-derived star formation rates (SFRs) for the SMGs are lower than their far-infrared derived SFRs by a factor of ∼10, suggesting a level of dust obscuration similar to that found in studies at redshifts $\sim 1 < z < 2.7$.

7.1 Introduction

As discussed in Section 2.5, finding the explanation for the close connection between active galactic nuclei (AGNs) and star formation in galaxies is a key question in cos-

[49]This chapter is based on research published in Sedgwick et al. [2013]. A full list of the co-authors of that paper is given in Appendix C.

mology. The discovery of high-redshift submillimetre galaxies (see Section 1.6) and their possible association with high-redshift radio galaxies (HzRGs) (e.g. Stevens et al. [2003]; Chapman et al. [2005]) implies that there are regions of intense star-formation which also show strong radio emission at high redshift. Detection of emission lines from these galaxies in the infrared can be used to confirm this connection, and to provide an independent measure of star formation and AGN activity.

Near-infrared spectroscopy of high-redshift radio and submillimetre galaxies has previously been made in the K-band (Swinbank et al. [2004]). However, spectroscopy at longer near-infrared wavelengths between 2.5 μm and 5.0 μm is a region which has been relatively unexplored: it has poor sensitivity from the ground and was previously covered in space only with ISO-SWS (see Table 1.2), and was not, in particular, covered by *Spitzer*. This gave *AKARI*, which had a spectroscopic facility in this region, the unique possibility of detecting Hα emission from active galaxies at $3.0 < z < 6.5$.

The *AKARI* FUHYU program was described in Chapter 6. The near-infrared spectroscopic campaign which was part of this campaign was carried out during *AKARI's* warm phase and details of the observations, data reduction and general results were presented in that chapter. The most interesting result, the detection of powerful Hα emission in four high redshift radio and submillimetre galaxies, is described in this chapter. The targets observed are described in Section 7.2. Results are presented in Section 7.3 and discussed in Section 7.4.

7.2 Targets observed

Observations were made of two HzRGs, and three submillimetre sources potentially associated with one of them (see Table 7.1 and Figure 7.1). The submillimetre mapping of these radio sources by the Submillimeter Common-User Bolometer Array (SCUBA) instrument on the James Clerk Maxwell Telescope (JCMT) was described by Stevens et al. [2003], who suggested that the submillimetre sources observed were associated with the nearby radio source on the basis of their number densities and positions relative to the radio jets.

8C1909+722 and companions. The redshift ($z = 3.536 \pm 0.0003$) was reported in de Breuck et al. [2001] based on a deep Keck optical spectrum showing strong Ly-α emission at $\lambda_{\rm obs} = 5516 \pm 0.3$ Å with FWHM = 1200 $\pm$ 90 km s^{-1}. This field was included in an 850 μm survey of the environments of HzRGs which detected three

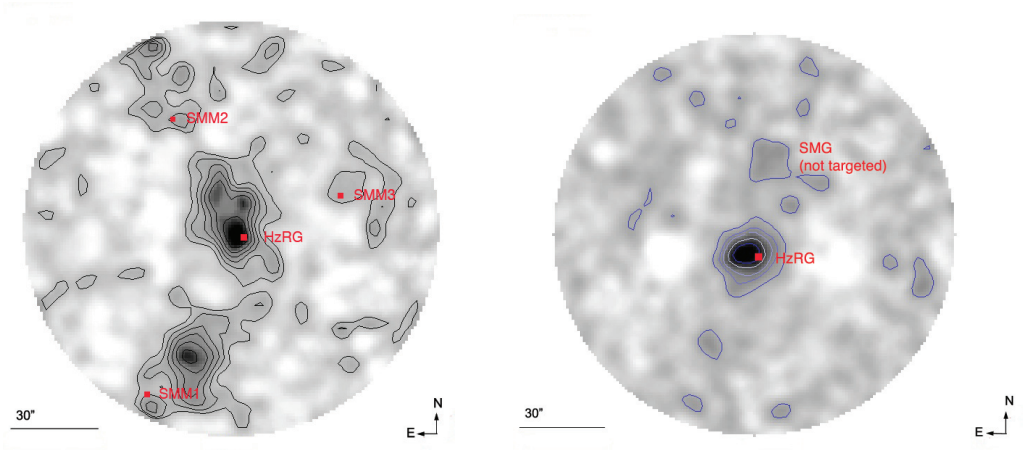

Figure 7.1: **Left:** SCUBA 850 μm image and contours (at 0.5, 1, 1.5, 2, 2.5 and 3 σ) for 8C1909+722 with the positions of the four *AKARI* spectra marked in red. **Right:** SCUBA 850 μm image and contours (at 1, 2, 3 and 4 σ) for 4C 60.07 with the position of the *AKARI* spectrum marked in red. This does not resolve the sources within the central contour (see Figure 7.3 for SMA 870 μm contours). The SCUBA maps are from Stevens et al. [2003].

nearby submillimetre galaxies (Stevens et al. [2003]). Two of the three submillimetre sources (SMM1 and SMM2) were later detected at 350 μm with SHARC-II on the Caltech Submillimeter Observatory (Greve et al. [2006]). A recent study using JVLA and IRAM PdBI radio observations and *Herschel* data at 100 μm - 500 μm (Ivison et al. [2012]) found a large red dust feature aligned with the radio jet and SMM1, and concluded that SMM1 probably shared the same node or filament of the cosmic web as the radio galaxy, although it did not detect convincing ^{12}CO emission from SMM1. Redshifts for these SMGs were not previously known.

4C60.07. The redshift for this galaxy ($z = 3.788 \pm 0.004$) is based on the Ly-α emission line (Roettgering et al. [1997]) at $\lambda_{\rm obs} = 5831 \pm 9$ Å with FWHM = 2880 $\pm$ 940 km s^{-1}. Dust emission was detected at 850 μm and 1.25 mm (Papadopoulos et al. [2000]), and CO J = 1 − 0 emission (Greve et al. [2004]). A detailed SMA, *Spitzer* and VLA study by Ivison et al. [2008] suggested an early-stage merger between the host galaxy of an AGN (the HzRG) and a companion starburst/AGN (which they labelled 'B'; see Figure 7.3). They proposed that the second submillimetre source, which they labelled 'A', although of roughly equal integrated flux as source 'B', and which is coincident with very narrow CO emission, might be comprised of cold dust

7.2 HzRGs and associated submillimetre sources: targets observed

Table 7.1: Sample of high-redshift radio galaxies and submillimetre-selected sources. The 850 μm flux data from SCUBA and the target coordinates are from Stevens et al. [2003].

Source	RA (J2000)	Dec (J2000)	Redshift (z)	850 μm Flux (mJy)	AKARI NIR Spectroscopy Observation ID	AKARI NIR Spectroscopy Dates	AKARI NIR Spectroscopy Exposure (mins)
8C1909+722 HzRG	19 08 23.3	+72 20 10.4	3.536 ±0.0003	34.9 ±3.0	1370153	8/2008(1), 8/2009(9)	93
SMMJ190827+721928 (SMM1)	19 08 27.4	+72 19 28.0	...	23.0 ±2.5	1370154	8/2008(10)	93
SMMJ190829+722050 (SMM2)	19 08 29.3	+72 20 49.6	...	8.7 ±2.4	1370155	8/2009(10)	93
SMMJ190816+722024 (SMM3)	19 08 16.1	+72 20 24.0	...	4.3 ±2.1	1370156	8/2008(5), 2/2009(2), 8/2009(3), 2/2010(3)	120
4C60.07 HzRG	05 12 54.8	+60 30 51.7	3.788 ±0.004	23.8 ±3.5	1370162	6/2008(9), 6/2009(1)	93

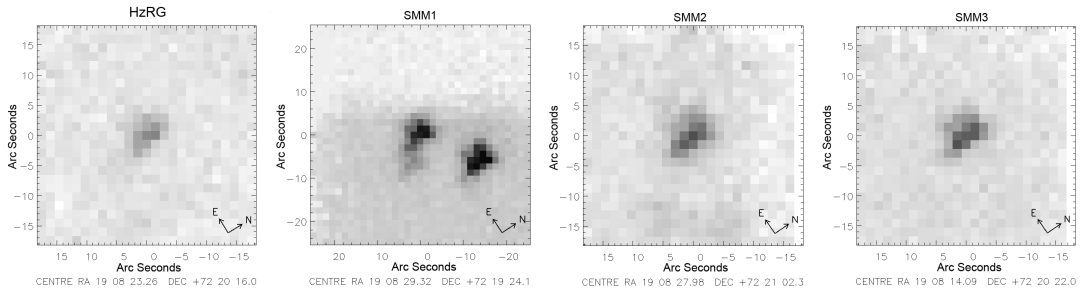

Figure 7.2: *AKARI* 3 μm images of the 8C1909+722 radio galaxy and its three companion submillimetre galaxies. The figures are centred on the positional centroids of the spectra, and each is a median stack of the pointings taken for each source using the N3 filter. The dispersion direction is horizontal and the FWHM of the kernel used in the source extraction is equivalent to a width of 2 and 3 pixels in the wavelength and spatial directions respectively.

and gas, and may represent a short-lived[50] tidal structure caused by the merger.

At the redshifts of the targets considered in this chapter, the Hα hydrogen recombination line falls within the 2.5 μm - 5.0 μm observed wavelength range. However, Hβ was outside this range. No other emission lines were detected. I used the reference image of the larger $10' \times 10'$ N3 band field which is attached to the $1' \times 1'$ grism field, smoothed with a 5×5 median boxcar, to confirm the identification of the sources with images from public archives.

[50]Short-lived on a dynamical timescale. In this case, this would be disc diameter / velocity of interaction - e.g. 10 kpc / 10^3 km s^{-1} $\sim 10^7$ years.

7.3 Results

Figure 7.4 shows the spectra of the five targeted sources, four of which appear to have Hα emission. The spectra have been stacked by co-adding the noise-weighted pointings for each source. These spectra were smoothed in the source extraction routine during the data reduction described in Section 6.2.2, and were not otherwise smoothed. The signal-to-noise ratios (SNRs) of these detections are 3.1 and 2.5 for the HzRGs and 10.0 and 2.4 for the submillimetre galaxies (see Table 7.2). Although two of these SNRs are relatively modest, the redshifts for the two HzRGs were already known from Ly-α and other emission lines (see Section 7.2) and all four Hα line identifications were observed at the wavelengths corresponding closely to these redshifts. Noise levels were estimated in each data frame from RMS values, propagated formally into the coadd, and used in the noise-weighted matched filter line detection. The mathematical formalism for error propagation in the optimal noise-weighted matched filter is given in Serjeant et al. [2003]. The estimated noise as a function of wavelength shown in Figure 7.4 was verified by splitting the spectra for each source into two halves (taking alternate sub-frames within all the pointings for the source) and subtracting the totals of the two spectra obtained. The SNR for each Hα detected shown in Table 7.2 was calculated as the mean of this estimated noise across the wavelengths covered by the emission line divided into the total flux of the emission line.

7.3.1 Spectra of the HzRGs

The spectrum for the radio galaxy 8C1909+722 HzRG shows a broad Hα emission line at an observed wavelength that is consistent with its redshift, as shown in Figure 7.4 (top). The spectrum was taken from the centre of the target.

For the radio galaxy 4C60.07, Figure 7.3 shows the *AKARI* 3 μm image overplotted with the SMA 870 μm contours from Ivison et al. [2008]. There are two submillimetre peaks, the weakest (labelled 'A') coincident with the 3 μm peak, and the strongest ('B') offset by about 3″. The stacked spectrum for this radio source has a broad Hα emission line at 'B' (see Figure 7.4, bottom). I did not detect an Hα line at 'A'.

The FWHM of the Hα lines for the two HzRGs are shown in Table 7.2 and are 9400±1600 km s^{-1} and 4800±1000 km s^{-1} respectively, levels which show that dust-shrouded quasars are present in these sources.

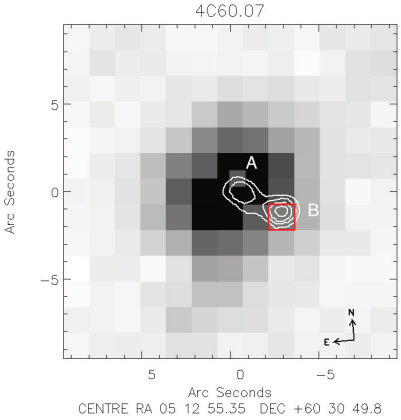

Figure 7.3: A blow-up of the *AKARI* 3 μm image of 4C60.07, overlaid by contours (at 3.5, 4.5, 5.5 and 6.5 σ) from the SMA 870 μm image for the centre of 4C60.07 from Ivison et al. [2008] which resolve the two submillimetre sources close to the HzRG. The labelling of the submillimetre sources 'A' and 'B' follows Ivison et al. [2008]. The radio source overlaps 'A' and is centred $< 0.5''$ north-east of it. A red square marks the positional centre of the *AKARI* spectrum. The dispersion direction is horizontal and the FWHM of the kernel used in the source extraction was equivalent to a width of 2 and 3 pixels in the wavelength and spatial directions respectively.

7.3.2 Spectra of submillimetre galaxies near 8C1909+722

SMM1 shows considerable structure, both in the submillimetre (see Figure 7.1) and at 3 μm (see Figure 7.2). The second-brightest of the submillimetre peaks shows an Hα emission line, but the other peaks do not. The emission line confirms that SMM1 is at the same redshift as the radio galaxy.

SMM2 also shows Hα emission (see Figure 7.4), again at the same redshift ($z = 3.536$), confirming that this galaxy is also associated with the radio galaxy. The spectrum for SMM2 is taken from the centre of the target in the *AKARI* 3 μm image.

SMM3 does not show a peak at the expected wavelength, although these is a strong peak about 0.05 μm lower (if this is Hα, then $z = 3.464$). I have not taken this as a convincing Hα emission line. Unlike SMM1 and SMM2, this galaxy is not aligned with the radio jets.

Stevens et al. [2003] suggested that the radio galaxy, the nearby submillimetre galaxies and other clumps had formed as a single galaxy cluster; it has now been confirmed that this association is correct in the case of two of these submillimetre sources.

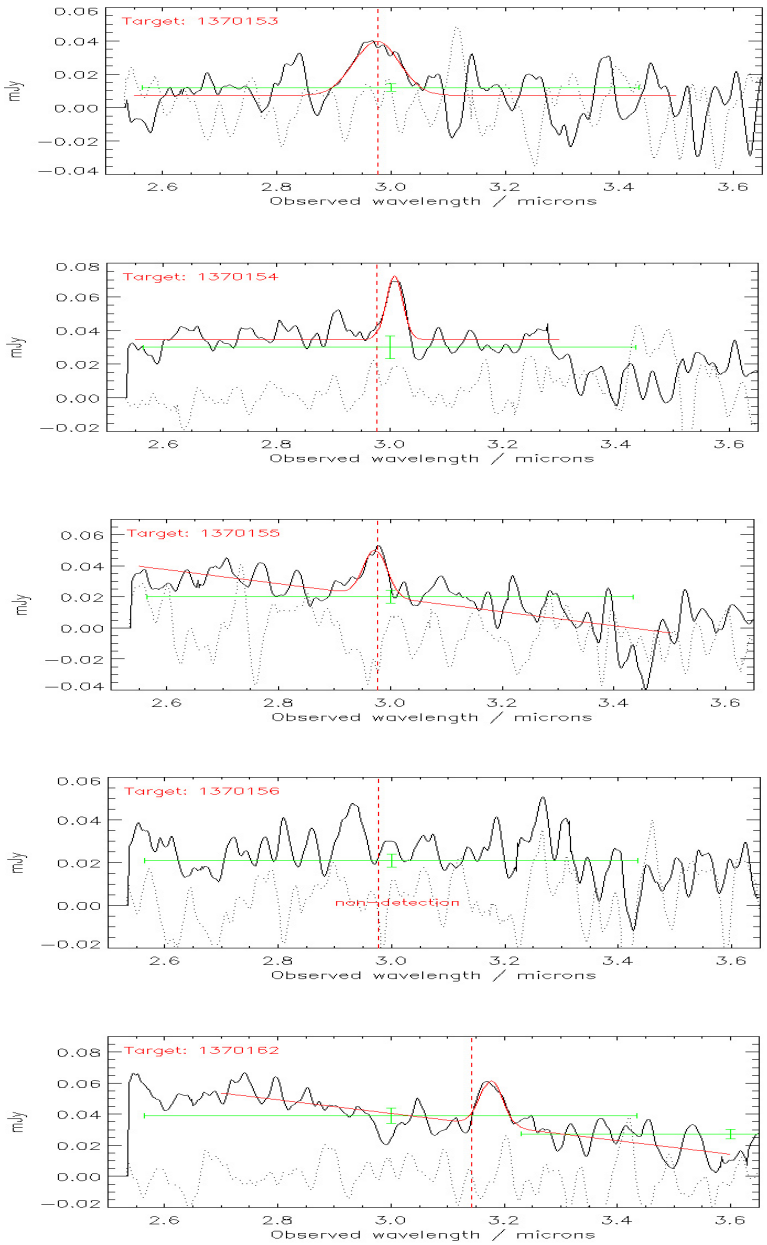

Figure 7.4: From top: 8C1909+722 HzRG, SMM1, SMM2, SMM3 (non-detection) and 4C60.07. The dashed red vertical lines show the position of Hα emission lines at the expected redshifts. The solid red lines show the gaussian least-squares fits to the Hα line and continuum in the wavelength region shown. The dotted grey lines show the noise levels as a function of wavelength, calculated as described in the text. The green points at 3.0 μm are from the *AKARI* broadband photometry (the reference image). The green point at 3.6 μm for 4C60.07 is from *Spitzer* IRAC broadband photometry. *Spitzer* photometry for 8C1909+722 is an order of magnitude higher and may include flux from another source; 0.8 μm Keck photometry (de Breuck et al. [2001]) is the same order of magnitude as the *AKARI* data.

7.3.3 Star formation rates

I have used the Hα emission lines to estimate the star formation rates of the submillimetre galaxies, using the formula from Kennicutt [1998b]:

$$\mathrm{SFR}/(\mathrm{M}_{\odot}\mathrm{yr}^{-1}) = 7.9 \times 10^{-35}\mathrm{L}_{\mathrm{H}\alpha}/\mathrm{W} \tag{7.1}$$

assuming a Salpeter IMF and solar abundances.[51] The results for the two submillimetre galaxies for which Hα lines were detected are 260 ± 80 $\mathrm{M}_{\odot}$ yr^{-1} and 300 ± 100 $\mathrm{M}_{\odot}$ yr^{-1} respectively (see Table 7.2). No adjustment has been made for dust extinction.

An alternative measure of the SFRs can be obtained by using the 850 μm luminosity (Table 7.1) to estimate the 60 μm luminosity, then using the 60 μm luminosity to obtain an estimate of the far-infrared luminosity $\mathrm{L}_{\mathrm{FIR}}$ (8 μm - 1000 μm), as discussed in Section 2.7. I have assumed the SED of the submillimetre galaxy SMMJ2135-0102 (the 'Eyelash') for these estimates, and then used the formula for estimating the star formation rate from Kennicutt [1998b]:

$$\mathrm{SFR}/(\mathrm{M}_{\odot}\mathrm{yr}^{-1}) = 4.5 \times 10^{-37}\mathrm{L}_{\mathrm{FIR}}/\mathrm{W} \tag{7.2}$$

The results of this calculation[52] are shown in Table 7.2.

The SFRs estimated from Hα are lower than the SFRs estimated from $\mathrm{L}_{\mathrm{FIR}}$ by factors of about 11 (for SMM1) and 4 (for SMM2), suggesting dust obscuration. Swinbank et al. [2004] found an $\mathrm{SFR}_{\mathrm{FIR}}/\mathrm{SFR}_{\mathrm{H}\alpha}$ ratio of ~ 10 in a study of submillimetre to radio galaxies in the redshift range $z = 1.408$ to $z = 2.692$. Takata et al. [2006] found close agreement between the two methods of estimating SFRs after adjusting the Hα-based estimates for dust extinction by an average factor of 2.9±0.5 in a study of submillimetre-selected ULIRGs at $0.9 < z < 2.7$. Figure 7.5 shows that the SMGs have

[51] The main limitations to using Hα to measure star formation by this formula are its sensitivities to uncertainties in extinction and to the assumed IMF. Extinction is discussed further in Section 7.4; functions used to estimate the IMF are discussed in Section 5.2.3. Subject to these uncertainties, in particular after an adjustment for the estimated extinction, it should be applicable at redshift $z \sim 3.5$.

[52] Using $\mathrm{L}_{\mathrm{FIR}}$ to measure star formation in star-forming galaxies is not only sensitive to the choice of assumed IMF, but also assumes high dust opacity. Although this assumption will eventually break down at very high redshifts, it should hold for the redshifts considered here, and perhaps up to $z \sim 6$ (Barger et al. [2014]). Recent studies using ALMA have been investigating non-extreme 'normal' galaxies at very high redshift. A galaxy at $z = 7.5$ was shown to be dust-shrouded with a dust-to-gas ratio similar to that of the Milky Way (Watson et al. [2015]); however continuum thermal emission was not detected in three galaxies at $6.8 < z < 7.1$, which appeared similar to local low-metallicity galaxies (Maiolino et al. [2015]).

Table 7.2: Estimates of star formation rates and line widths. Estimates of SFR(Hα) for the SMGs are based on Hα emission luminosities, and deconvolved FWHM are based on the width of the Hα lines for the HzRGs. No adjustment for extinction has been made. FIR luminosities and SFRs are based on the 850 μm flux (see Table 7.1) assuming an SMMJ2135-0102 SED. SFR(Hα)s for the HzRGs are not quoted due to line contamination from their AGNs. Redshifts in italics were identified by this work.

Source	Redshift (z)	Flux(Hα) (10^{-19}Wm^{-2})	SNR(Hα)	$L_{H\alpha}$ (10^{36}W)	$SFR_{H\alpha}$ ($M_\odot yr^{-1}$)	L_{FIR} ($10^{13}L_\odot$)	SFR_{FIR} ($M_\odot yr^{-1}$)	FWHM(Hα) (km s^{-1})
HzRGs								
8C1909+722 HzRG	3.536	7.9	3.1	8.6 ±2.8	...	2.5 ±0.2	4300 ±1500	9400 ±1600
4C60.07 HzRG	3.788	2.8	2.5	3.6 ±1.4	...	1.7 ±0.3	2900 ±1000	4800 ±1000
SMGs								
8C1909+722 SMM1	*3.536*	3.1	10.0	3.3 ±0.3	260 ± 80	1.6 ±0.2	2800 ±1000	...
8C1909+722 SMM2	*3.536*	3.5	2.4	3.8 ±1.6	300 ±100	0.6 ±0.2	1100 ± 500	...
8C1909+722 SMM3	...	<0.02	...	< 0.02	...	0.3 ±0.2	500 ± 300	...

luminosities and dust extinction at comparable levels with these earlier studies. The total FIR luminosity calculated above also shows that SMM1 and the two HzRGs are HyLIRGs ($L_{FIR} > 10^{13}L_\odot$), and SMM2 is a ULIRG.

7.4 Discussion and conclusions

These are the first (tentative) detections of Hα emission lines in HzRGs / SMGs at $z > 2.8$.

The Hα lines in the two HzRGs are broad. Broad Hα emission lines in HzRGs are not rare (Larkin et al. [2000]; Nesvadba et al. [2011]) and indicate that these sources should be classified as reddened quasars rather than galaxies. Rawlings et al. [1995] found a similar result for 3C 22, and suggested that other slightly reddened quasars may also be misclassified as HzRGs, leading to misleading estimates of stellar populations in the host galaxy. This is because the restframe UV emission from the Broad Line Region is preferentially extinguished, so optical observations of high-redshift objects can lead to misclassification. This is a particular problem in studies using near-/mid-infrared photometry of sources which may otherwise appear to be narrow-line AGNs.

For 4C60.07, the detection of a broad Hα line was at the location of the submillimetre source 'B' (see Figure 7.3). Ivison et al. [2008] suggested that 'B' was a gas-rich starburst/AGN on the basis of the red mid-infrared colours. The discovery that 'B' is a quasar supports the argument that binary AGNs at close separations may be due

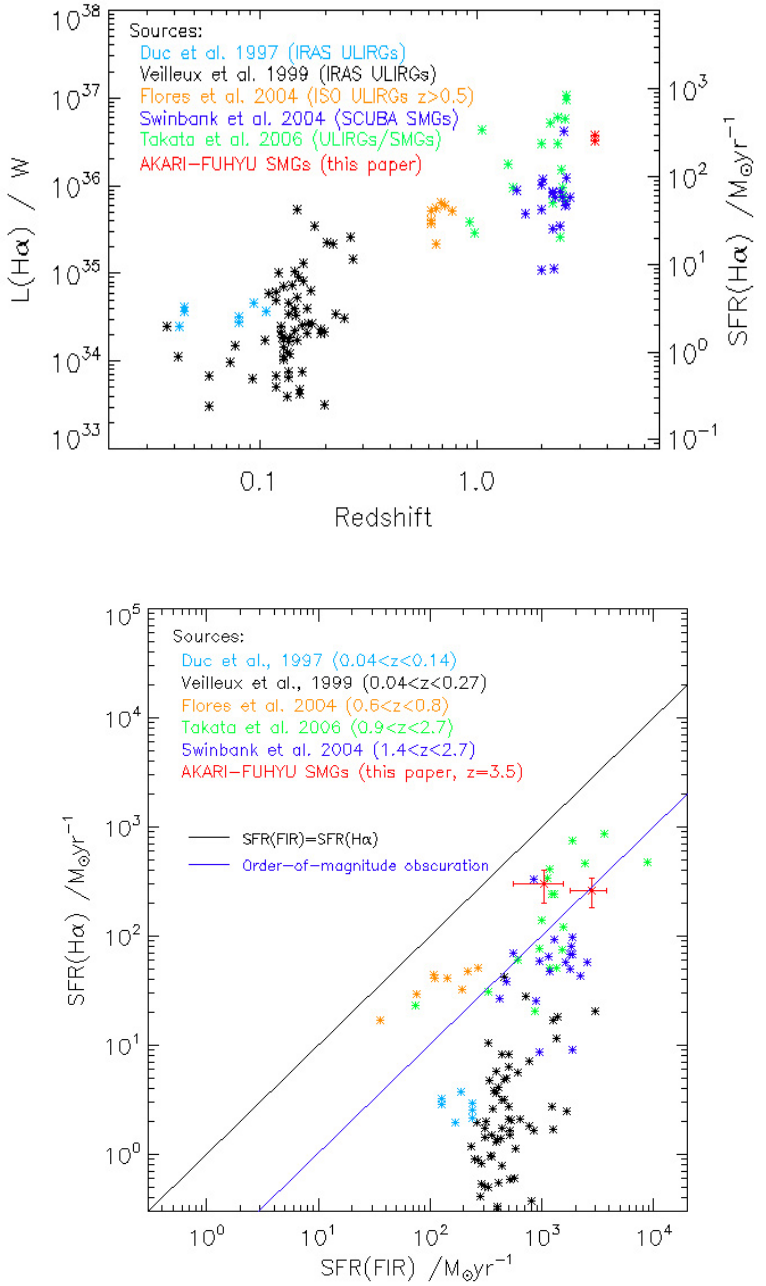

Figure 7.5: **Top:** Hα luminosity for the two SMGs as a function of redshift in comparison with earlier studies. **Bottom:** Star formation rates based on Hα luminosity versus far-infrared luminosity of the two SMGs compared that to those of recent studies. Takata et al. [2006] and Flores et al. [2004] data are shown before correction for extinction. Duc et al. [1997] and Veilleux et al. [1999] have been adjusted to the cosmological assumptions used in this thesis. Some sources show evidence of AGNs; all are SMGs. My results are shown in red.

to the triggering or enhancement of AGN activity during mergers. The unexpectedly high prevalence of binary quasars at high redshifts (Djorgovski [1991]; Hennawi et al. [2010]) provided strong support for this idea. A recent study of binary quasars found that simple halo occupation distribution models under-predict quasar clustering at small separations (Kayo and Oguri [2012]). That such a well-studied source had not previously been shown to be a quasar adds to the evidence that there is a higher fraction of binary AGN/quasars at high redshift than previously realised. The Hα luminosity and FWHM results for the two HzRGs are both consistent with those of lower redshift radio galaxies (e.g. Nesvadba et al. [2011]).

The detection of Hα emission lines at the same redshift from two submillimetre galaxies in the region of 8C1909+722 provides confirmation of their association with the HzRG. The extent of the system is $\sim$ 700 kpc (based on Stevens et al. [2003]), suggesting that this may be evolving into a cluster of galaxies or possibly a single galaxy. The complex SMM1 is $\sim$ 80 kpc in extent and appears to be in the process of merging. In the 8C1909 field we have the first confirmation of multiple U/HyLIRGs in a proto-cluster region at $z > 3$, giving a combined SFR[53] of $\sim$ 8000 $M_{\odot}yr^{-1}$.

The high levels of star formation in the two SMGs are shown with previous results in Figure 7.5. The Hα luminosities and $SFR_{FIR}/SFR_{H\alpha}$ ratios are comparable to those found in recent studies at $0.9 < z < 2.7$ suggesting similar levels of dust obscuration.

These results can also be used to see whether the empirical Calzetti extinction law[54] (Calzetti et al. [2000]) can extend to high redshifts. Observed at low redshifts, this is:

$$S(H\alpha)_{corr} = S(H\alpha)_{obs} \times 10^{0.4 \times 3.327 E(B-V)} \tag{7.3}$$

E(B-V) can be estimated using the recent result (again, for local galaxies) of Domínguez Sanchez et al. [2012]):

$$E(B-V) = 0.29 \times \log_{10}(L_{IR}/L_{\odot}) - 2.54 \tag{7.4}$$

These calculations give factors of 61 and 53 (compared to my estimates of 11 and 4 respectively) for the dust extinction for the two radio galaxies. A more representative sample may be able to extend this phenomenological extinction law to much higher

[53]The four galaxies being considered may grow to have a stellar mass of $\sim 10^{12} M_{\odot}$ so this rate of star formation could only be sustained for $\sim 10^{7}$yr, about 0.1% of the age of the universe. Clearly the chance of finding such intensively active regions is small.

[54]The Calzetti extinction law was discussed in connection with SED modelling in Section 5.2.1.

redshifts. The same calculation applied to the galaxy sample at $1.4 < z < 2.7$ used by Swinbank et al. [2004] (discussed above) gives a decrement of 23, a factor of about three higher than that calculated in this chapter.

The NIRSpec on the JWST, which will have about an order of magnitude increase in spectral resolution (see Table 1.2) should significantly extend the results from spectroscopic observations in the near infrared. Moreover, its angular resolution of $\sim 0.1''$ (corresponding to ~ 1 kpc at the peak of cosmic star formation history) will isolate star-forming regions in the galaxies. In the meantime, ALMA observations of molecules such as HCN, HNC, HCO^+ and H_2O lines can distinguish photon-dominated regions from X-ray-dominated regions (diagnostics of starbursts and AGNs respectively). *Herschel* surveys such as H-ATLAS (Eales et al. [2010]) are already providing bright submillimetre targets for exactly such studies. Fine structure lines from [CII] and [NII] can provide key information on active regions[55]. The detection of [CII] $\lambda 157.7$ μm and the non-detection of [NII] far-infrared emission lines in an H-ATLAS study of a lensed submillimetre galaxy at $z = 3.0$ (Valtchanov et al. [2011]) provided evidence of the dominance of star formation, since [CII] lines can be produced by a relatively modest FUV flux, unlike [NII] emission since nitrogen has a higher ionisation potential.

[55]These far-infrared emission lines were discussed briefly in Section 1.2.

Chapter 8

AKARI all-sky bright source catalogue: finding lensed quasars by excess far-infrared luminosity

As discussed in earlier chapters, understanding the relationship between black hole accretion and star formation has been one of the key topics of research in cosmology in recent years. Another key topic has been the discovery of gravitational lenses and the opportunity they provide to explore high-redshift galaxies. One recent result which may throw light on both these issues has been the discovery of a shallow correlation between the optical and far-infrared luminosity of quasars which implies a steep slope at the high-luminosity end of the far-infrared quasar luminosity function. Not many sources which are known to be quasars from their optical luminosity have known far-infrared luminosity, and this discovery was first made using stacking analysis of sources observed at a variety of far-infrared wavelengths.

This chapter describes work done to confirm this correlation by identifying quasars in the AKARI far-infrared all-sky survey Bright Source Catalogue. I have cross-matched these far-infrared sources to sources in currently available published quasar catalogues, not only well-known spectroscopic quasar catalogues such as that from SDSS, but also to a recent much larger photometric quasar catalogue. About 300 matches were identified within a 10″ matching radius; however optical images of these matches showed that most of them were either hotspots in the arms of local spiral galaxies, or cirrus, or that their far-infrared flux was liable to have been contaminated by a local source. A final count of 22 uncontaminated sources showed a broad confirmation of the optical - far-infrared correlation for quasars, and the sources at $z > 1$ showed evidence of magnification, suggesting a new method with which to identify gravitational lenses. Gravitationally-lensed quasars are not only very interesting objects in their own right, but can also provide high-redshift probes of dark matter halos in the lensing object. As an initial test of these ideas, I observed seven of these sources spectroscopically, and found confirmation of high-redshift quasars for three of them.

8.1 Introduction: *AKARI* all-sky survey

The *AKARI* all-sky survey mission provides the first census of the infrared sky since that of IRAS in 1983. The all-sky Bright Source Catalogue (BSC; Yamamura et al. [2010]) covered about 98% of the sky and identified a total of 427,071 point sources, making more sensitive far-infrared photometry of large samples of rare objects (such as quasars) possible. A map of these sources is shown in Figure 8.1 (left). The 90 μm WIDE-S band was the most sensitive (0.55 Jy in normal mode; 1.8 Jy in Correlated Double Sampling mode for bright sky regions). The dominant uncertainty is in the calibration, so fluxes are only quoted to 20% uncertainty according to the Bright Source Catalogue Release Notes. The image pixel size is $8''$, which has meant that some matches may be contaminated by picking up IR radiation from nearby local galaxies (discussed below in Section 8.5.3).

The availability of the *AKARI* all-sky far-infrared survey offers an opportunity to identify known quasars with high far-infrared luminosity. There is a correlation between optical and far-infrared (FIR) luminosity for quasars, known from earlier studies (discussed in Section 8.2) which also offers a possibility of detecting gravitational lenses among these matched sources, where the FIR luminosity is magnified beyond the predicted value. New, more extensive photometric quasar catalogues are being developed, and these should enable the method discussed in this chapter to quickly identify many more lenses in the future.

The background to finding quasars with evidence of star formation and the discovery of the optical−far-infrared correlation are discussed in Section 8.2. A background to gravitational lenses is given in Section 8.3. The various quasar catalogues used in this chapter are described in Section 8.4. The methods used in this work are discussed in 8.5. The results and spectroscopic follow-up observations are presented and discussed in Section 8.6. There is a summary and discussion of planned future work in Section 8.7.

8.2 Background: quasar host galaxies and the optical−far-infrared correlation

It has proved difficult to detect the far-infrared emission from a significant number of quasar host galaxies. In any case, as discussed in Section 8.4 below, large catalogues

of quasars are a fairly recent development.

Only 21 quasars were detected in the IRAS all-sky Point Source Catalogue (which was sensitive only down to 1.5 Jy for point sources at 100 μm). In addition, pointed observations of 179 quasars were made with IRAS which used repeated observations to reach a sensitivity greater than the all-sky survey by a factor of about five (Neugebauer et al. [1986]), and 74 were detected (most at $z < 1$), although these included radio-loud quasars who infrared emission was not thermal and did not peak in the far-infrared. The matching was hindered, especially at 100 μm, by Galactic infrared cirrus and neighbouring infrared sources, a problem I also found with the *AKARI* 90 μm matching (see Section 8.5.3). Identifying quasars in IRAS did confirm the existence of substantial amounts of dust. Using IRAS data, Sanders et al. [1989] found no obvious relationship between the optical emission and the infrared emission for Palomar-Green quasars[56].

For high-redshift quasars, far-infrared emission is redshifted into the submillimetre and millimetre windows available to ground-based instruments, such as SCUBA (at 850 μm) and MAMBO (at 1200 μm) and there have been a number of studies using ground-based instruments targeting optically-selected, optically-bright, radio-quiet quasars at high redshifts (see Table 8.1). Radio-loud quasars are also detected at these wavelengths, and are excluded from or separated in these studies which focus on the far-infrared thermal radiation from star formation, to avoid potentially contaminating the results with detected synchrotron emission. Observation of molecular lines would also confirm the existence of dusty thermal emission.

The first studies (Isaak et al. [1994]; McMahon et al. [1994]; Omont et al. [1996]) found six quasars at $z > 4$ with FIR luminosity, and confirmed that these quasars each contained a dust mass $\sim 10^8$ $M_\odot$, suggesting starbursts. Confirmation that the emission is thermal (from cool dust) is shown by the spectral index between observations at different wavelengths: e.g. for the quasar in Isaak et al. [1994] this is 2.7±0.4 between 850 μm and 1100 μm, which could not be explained by synchrotron emission (although heating by the AGN is not ruled out). The far-infrared radiation from this source was confirmed to be thermal by the identification of CO emission (Ohta et al. [1996]). Omont et al. [1996] also identified at least one gravitational lens in the six detections. These data were used by Priddey and McMahon [2001] to prepare an SED for $z > 4$ radio-quiet quasars, which peaked at ~ 75 μm and suggested star formation rates of $\sim 10^3$ $M_\odot yr^{-1}$, with a timescale for star formation of $0.5 - 1$ Gyr.

Finding a quantitative relationship between the luminosity from black hole accretion

[56]The Palomar-Green quasar catalogue is discussed below in Section 8.4.1.

8.2 Quasar host galaxies and the optical−far-infrared correlation

Table 8.1: Submillimetre and millimetre studies of high-redshift optically-luminous radio-quiet quasars. Wavelengths of submm/mm detectors used in these studies: UKT14 = 1100, 800, 450 μm; MPIfR = 1250 μm; MAMBO = 1200 μm; SCUBA = 850, 450 μm. PSS = Palomar Sky Survey.

Reference	Sample source	Sample size	Quasars detected	Instrument	Redshift (z)	Sensitivity 1σ (mJy)	$<M_B>$	L_{FIR} ($L_\odot$)
Isaak et al. [1994]	APM	9	1	UKT14 / JCMT	>4.2			
McMahon et al. [1994]	APM	5	1	MPIfR/ IRAM	>4	1.5		$\sim10^{14}$
Omont et al. [1996]	APM	22	6	MPIfR / IRAM	$\gtrsim$4	1.5	-27.8	
Priddey and McMahon [2001]			7	(data from previous studies)				
Omont et al. [2001]	PSS	63	18	MAMBO / IRAM	>3.8	1.5	-27.9	$\sim10^{13}$
Carilli et al. [2001]	SDSS	41	16	MAMBO / IRAM	>3.6	1.4	-27.0	$\sim5\times10^{12}$
Isaak et al. [2002]	APM+	38	8	SCUBA / JCMT	$\geq$4	3.3	-27.5	$\sim10^{13}$
Omont et al. [2003]	Hamburg+	35	9	MAMBO / IRAM	1.8−2.8	$\sim$3	-28.0	$\sim10^{13}$

and the luminosity from star formation in quasars has been limited in the past by the number of sources for which both sets of data are available. With an SDSS-derived sample of 41 quasars, Carilli et al. [2001] detected 16 sources with MAMBO; combining centimetre and millimetre observations, they concluded the observations came from thermal dust emission; SED fitting implied star formation rates between 500 and 2000 $M_\odot yr^{-1}$. The SCUBA Bright Quasar Survey detected 8 out of 38 high-redshift ($z \gtrsim 4$) quasars at 850 μm, but again found no strong evidence for a relation between the 850 μm flux and optical magnitude (Isaak et al. [2002]). With a new sample of 35 quasars, Omont et al. [2003] detected 9 with MAMBO 1200 μm observations. They found far-infrared luminosities of $\sim10^{13}$ $M_\odot$ implying star formation rates of 10^3 $M_\odot yr^{-1}$. They also applied a statistical survival analysis to the optical and far-infrared/submillimetre luminosities for the results of all of these surveys (43 detections and 95 non-detections at $2 \lesssim z \lesssim 4$) but found no clear evidence for an optical−far-infrared correlation.

As more data became available, the relationship between far-infrared and optical emission for quasars became clearer. Using stacking analysis of sources observed at a variety of far-infrared and submillimetre wavelengths, a clear relationship has been established (Serjeant and Hatziminaoglou [2009]; Serjeant et al. [2010a]; Bonfield et al. [2011]) and is discussed in Section 8.5.1. As the number of known quasars continues to increase rapidly (see Section 8.4) and with the availability of the *AKARI* all-sky far-infrared catalogue, the work in this chapter suggests that it has become possible to use this relationship to identify sources which have greater FIR luminosity than predicted, which may be caused by gravitational lensing.

8.3 Background: finding gravitational lenses

Gravitational lenses have become a key research area recently, since they afford not only the opportunity to investigate very distant galaxies not otherwise observable (e.g. Smail et al. [1997]), but also provide unique evidence on key cosmological parameters. Their importance is due their magnification of the lensed object, typically by an order of magnitude, and the fact that the surface brightness of the lensed object is conserved. They also afford an opportunity to investigate the mass of the lensing object through its effect on the lensed object. Lensing is achromatic (independent of wavelength) so the spectrum of the lensed source is unaltered. If chromatism is observed, it may be caused by structure in the extended source itself leading to differential magnification (Blain [1999]; Serjeant [2012]; Hezaveh et al. [2012]).

Lenses were originally identified morphologically, by their multiple images or distinctive arcs, or (in the occasional head-on alignment) by an Einstein ring (e.g. King et al. [1998]). However, the number of lenses which can be found by this means is limited. Lenses have also been discovered by identifying emission lines in spectra at higher redshift than the galaxy being observed (e.g. the Sloan Lens ACS (SLACS) survey of SDSS galaxies, Bolton et al. [2006]). Recent developments in identifying lensed systems by their strong 500 μm flux (with data available from *Herschel*-SPIRE) have generated a great deal of exciting work in the far-infrared and submillimetre (Negrello et al. [2010]; Gonzalez-Nuevo et al. [2012]; Vieira et al. [2013]; Negrello et al. [2014]). The original diagram from Negrello et al. [2010] which demonstrates this method is shown in Figure 8.2 (right). Clusters of galaxies can also provide significant gravitational lenses (Kneib and Natarajan [2011]). The new Hubble Frontier Fields survey (discussed in Section 2.3) is based on finding lensed galaxies magnified by well-known clusters of galaxies. New space facilities (e.g. *Euclid*; Laureijs et al. [2011]) should find and explore further new lensed systems.

An idea for a new method for identifying gravitational lenses is explored in this chapter, in a way similar to the idea used in Negrello et al. [2010]: quasars which show far-infrared luminosity above that predicted by the L_{FIR} - $L_{optical}$ relation are unusual sources and likely to be gravitationally lensed.

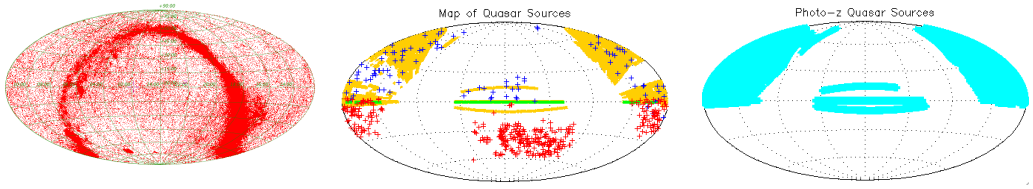

Figure 8.1: **Left:** sources in the *AKARI* FIS Bright Source Catalogue. **Middle:** sources in the four spectroscopic quasar catalogues. Sloan QSOs in yellow microdots, 2SLAQ in green microdots, Palomar-Green in blue pluses, Hamburg/ESO in red pluses. **Right:** sources from the Richards et al. [2009] photometric quasar catalogue. Hammer-Aitoff projection.

8.4 Quasar catalogues

This section describes the quasar catalogues which I have matched to the *AKARI* far-infrared all-sky Bright Source Catalogue: firstly, the well-known spectroscopic quasar catalogues, and secondly the less accurate but much larger (and still developing) photometric quasar catalogues.

8.4.1 Spectroscopic quasar catalogues

Sloan QSO Surveys

The seventh edition of the Sloan Digital Sky Survey (SDSS; York et al. [2000]) Quasar Catalogue (Schneider et al. [2010]), based on the SDSS Seventh Data Release (DR7) contains 105,783 spectroscopically confirmed quasars. Quasar candidates were first identified by the UV-excess method using the Sloan photometry (quasars can be distinguished from stars by a colour-colour plot of u-g against g-r: see Figure 8.2, left). For inclusion in the final quasar catalogue, candidates are then observed spectroscopically and required to meet four conditions: (i) have absolute i-band magnitude brighter that -22, (ii) have apparent magnitudes fainter than 15 (to avoid saturation and cross-talk in the spectra), (iii) have at least one emission line with FWHM larger than 1000 km s^{-1} or have interesting/complex absorption features[57], and (iv) have highly reliable redshifts. The area covered by the catalog is ∼9380 deg^2. The quasar redshifts range from 0.065 to 5.46, with most at $z < 2$. Most sources are in the northern galactic hemi-

[57]This is quoted from Schneider et al. [2010] and not defined further in that paper!

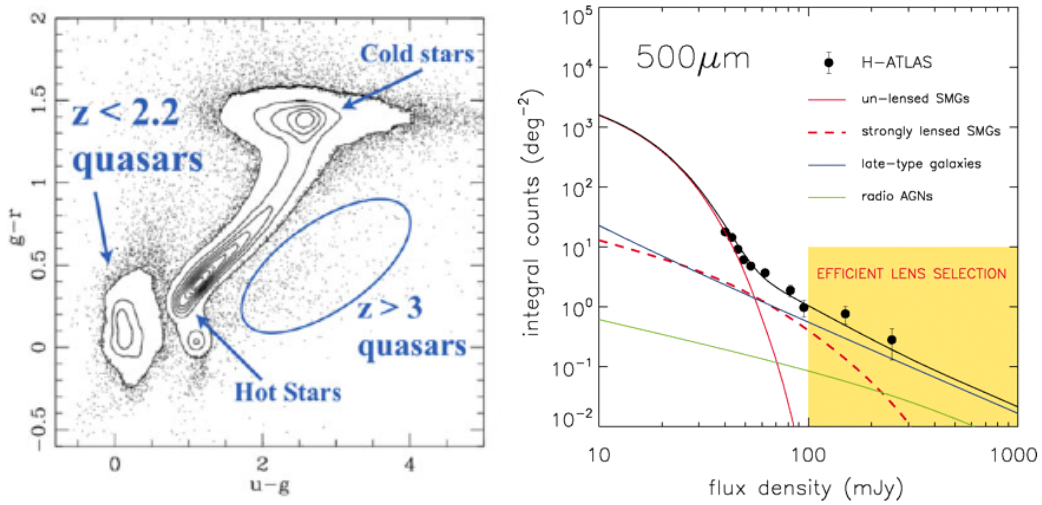

Figure 8.2: Selection of quasars: **Left:** the UV-excess method used by SDSS to distinguish quasars from stars. Figure from Ivezic et al. [2014]; further details of SDSS selection algorithm in Richards et al. [2002]. **Right:** the selection of gravitational lenses at submillimetre wavelengths discussed in Section 8.3. Figure from Negrello et al. [2010].

sphere (see Figure 8.1). Three classes of Active Galactic Nuclei (AGN) not included in DR7 are Seyfert galaxies, Broad Absorption Line (BAL) Quasars and BL Lac objects. The DR7 quasar catalogue is cumulative with respect to earlier catalogues. However, I have found matches in the DR5 quasar catalogue (Schneider et al. [2007]) which are missing from the DR7 quasar catalogue and have retained these. Since the work in this chapter was completed, SDSS-III has released a cumulative quasar catalogue (DR12), which contains 294,512 quasars (Alam et al. [2015]; see Table 8.2).

2SLAQ Survey

The 2dF-SDSS LRG and QSO survey (2SLAQ) contains QSOs selected from SDSS photometry and observed with the 2dF spectrograph on the Anglo-Australian Telescope, covering 191.9 deg^2. The survey contains 14,183 galaxies of which 12,702 are QSOs with a redshift range of ∼0.8 to 4.8 (most are at $z < 2.6$), and apparent magnitudes $18 < g < 21.85$, and it includes 'any broad line (type 1) AGN, irrespective of luminosity' (Croom et al. [2009]). The survey area was RA 9h to 15h, and Dec +0° 54′ to -1° 18′ (see Figure 8.1).

Table 8.2: Selection criteria and redshift ranges in current and planned quasar catalogues. The acronyms are expanded in the text.

Catalogue	Area deg^2	Quasars	Magnitude or magnitude	Redshift	Methods of quasar selection; data used
Spectroscopic catalogues					
P-G BQS	10,714	109	$B < 16.16$	$0.025 < z < 2.046$	Colour U-B<-0.44; M_B<-23.0
Hamburg/ESO	3,700	415	$13.0 < B_J < 17.5$	$0 < z < 3.2$	Colour U-B<-0.18
2SLAQ	192	12,702	$18.0 < g < 21.85$	$0.8 < z < 4.8$	M_i<-22; various colour cuts
SDSS DR7qso	9,380	105,783	$15.0 < i < 21.0$	$0.065 < z < 5.46$	FWHM>1000 kms^{-1}; M_i<-22
SDSS DR12qso	9,380	294,512	$g < 22$ or $r < 21.85$	$2.15 < z < 3.5$	Various algorithms; time variability
Photometric catalogue matched in this chapter					
Richards et al. [2009]	8,417	1,015,082	$14.4 < m_i < 21.3$	to z∼6	NBCKDE algorithm; SDSS+MIR data
Photometric catalogues recently released and planned					
Ho et al. [2015]	11,000	1,615,226	$i < 21.5$	$0.5 < z < 2.5$	XD; SDSS+BOSS data
Abraham et al. [2012]	9,380	2,430,625	$14 < i < 22$	no z yet	Machine learning classifier; SDSS data
Brescia et al. [2015]	14,555	3,602,210	$i < 22.0$		MLPQNA algorithm; SDSS DR10 data
DiPompeo et al. [2015]	12,500	5,537,436	no limit	$z < 5$	XD; WISE+SDSS data
Ivezic et al. [2014]	18,000	10,000,000	$r \sim 27.5$	$z < 7$	LSST (2021); time variability

Palomar-Green Bright Quasar Survey

The Palomar-Green (PG) Bright Quasar Survey is the famous set of 114 objects identified from the Palomar-Green survey over an area of 10,714 deg^2 of UV-excess objects which are brighter than B∼16.16 magnitude (Schmidt and Green [1983]). I have selected 109 of the quasars from this survey, using the coordinates and flux values from Serjeant and Hatziminaoglou [2009]. The redshift range is $0.025 < z < 2.046$. These are also shown in Figure 8.1.

Hamburg/ESO Survey for Bright QSOs

The Hamburg/ESO (HE) survey for bright QSOs is comprised of 415 bright QSOs and Seyfert 1 nuclei taken from the Hamburg/ESO survey (Wisotzki et al. [2000]). The survey was essentially in the southern hemisphere, and the sources had optical magnitudes in the approximate range $13 < \mathrm{B_J} < 17.5$ and redshifts within $0 < z < 3.2$. The range of this survey is shown in Figure 8.1, and covered over 3,700 deg^2 in the sky.

8.4.2 Photometric quasar catalogues

Spectroscopy is time-consuming and expensive, so developing methods for identifying quasars from photometry has the potential to identify larger numbers of quasars more quickly and cheaply.

Distinguishing galaxies from stars can be readily achieved by looking at the morphology of the source. However, distinguishing quasars from stars is much more difficult (this is of course the origin of their name as quasi-stellar objects). Until recently, most studies of quasars have used one or more of the spectroscopic quasar catalogues discussed in the previous subsection. Early attempts to provide a more extensive quasar catalogue not reliant on spectroscopic data identified quasars by the UV-excess method, but achieved an efficiency of only about 50% (e.g. Croom et al. [2001]). However, several projects are now underway, using techniques such as Bayesian selection algorithms and neural networks to make the identifications from photometric catalogues (primarily the SDSS catalogue data releases) and provide greater identification efficiency.

The Richards catalogue

The most extensive photometric quasar catalogue which includes (photometric) redshifts which was available when I did the work described in this chapter is the Non-parametric Bayesian Classification Kernel Density Estimator (NBCKDE; Richards et al. [2009]) which is based on SDSS Data Release 6 (DR6; Adelman-McCarthy et al. [2008]), and this is the catalogue used in this chapter. It has 1,172,157 quasar candidates and estimates the identification efficiency is about 80%. It assigns a classification of either quasar or star to each object in the SDSS catalogue, using training sets for each classification. For quasars the training set uses colours[58] from the five optical bands (u, g, r, i and z) from the SDSS DR5 quasar catalogue of 77,429 quasars. Since most objects will be stars, they use a Bayesian prior to exclude stars (see Richards et al. [2009] for details).

The Richards catalogue comes with a quality flag between ±6, with values below 0 being suggested by Richards as unreliable for statistical work on quasars. Following this, I have worked only with quasar candidates with this flag (called 'good' in the catalogue) which is zero or positive. This removed 157,075 from the full list of 1,172,157 quasar candidates, leaving 1,015,082 quasar candidates.

Other methods of selecting quasars

A different approach to developing a photometric quasar catalogue has been taken recently by Abraham et al. [2012]. This used a machine learning classifier, with a training set of spectroscopically confirmed objects, on the six million unresolved photometric detections in SDSS DR7, and found 2.4 million quasars. Unfortunately there

[58]Colour diagrams were discussed in Section 3.2.2.

are no redshifts yet, although the authors are currently working to obtain photometric redshifts for a later release. The Abraham method confirmed the classification of over 99% of the Richards quasars by its difference boosting neural network (DBNN) learning method. Success has also been claimed recently by Brescia et al. [2015] with their Multi Layer Perception with Quasi Newton Algorithm (MLPQNA) machine learning method, claiming 3.6 million candidate quasars/AGNs, and also by Ho et al. [2015] and by DiPompeo et al. [2015] using Extreme Deconvolution (XD) methods. These catalogues will be used in future work on this project.

The time variability of quasars (several tenths of a magnitude on time scales over a few months) provides another method of quasar selection, and can be distinguished from that shown by variable stars (Kozłowski et al. [2010]). This method will be viable with optical imaging by the forthcoming Large Synoptic Survey Telescope (LSST), which will provide hundreds of detections per object and is expected to generate a photometric quasar catalogue of over 10 million quasars to $z \sim 7$ (Ivezic et al. [2014]). A summary of these catalogues is given in Table 8.2.

Compilations of quasar catalogues

Veron-Cetty and Veron [2010] have published a quasar catalogue (their 13th edition) of 133,336 quasars (as well as 6,517 Seyferts). Many of these are also in the official SDSS QSO catalogues (the latest data release they used was DR7), but other published sources of quasars are also included. Comparison to the *AKARI*-BSC did not find any new matches using this catalogue.

A more recent compilation has just been published (Flesch [2015]) of 510,764 quasars. This has corrected some duplications and positional errors in the Veron-Cetty and Veron [2010] catalogue, and added some more recent catalogues, in particular SDSS DR10. It includes the Richards et al. [2009] catalogue and many other catalogues from papers which identified quasars. Optical magnitudes have been updated based on the author's use of DSS images. I have not (yet) used this compilation.

Comparison to similar studies with IRAS

IRAS 60 μm and 100 μm sources yielded 179 quasars (Neugebauer et al. [1986]). These were obtained by repeated scanning by IRAS of pre-selected positions[59], unlike the present study. Also, identifications were accepted within $1'$ of an optical or radio

[59] A similar study was undertaken with *AKARI*, finding 155 quasars at $3.3 < z < 6.4$, which was published after this thesis was submitted (Jun et al. [2015]).

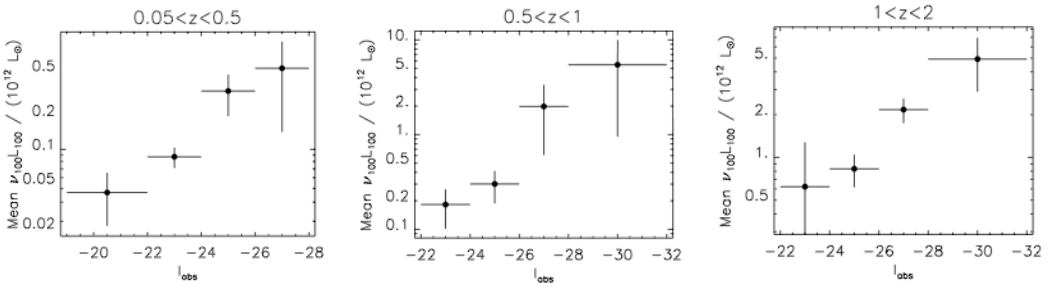

Figure 8.3: The optical−far-infrared correlation for quasars. The quasars were selected from SDSS DR5, Palomar-Green and several submillimetre quasar catalogues; the 100 μm luminosity is estimated from IRAS, ISO, *Spitzer*, SCUBA and MAMBO data assuming an M82 SED. Figures from Serjeant and Hatziminaoglou [2009].

image in a relatively clear field. This is a far wider tolerance than in the present study.

About 30% of the sources in the Palomar-Green Bright Quasar Survey were found in the IRAS 25 μm and 60 μm bands, and about 80% were found in the ISO Data Archive in the mid infrared (Haas et al. [2003]). This paper found that the starbursts which were found to accompany quasars at high redshift in earlier studies did not occur in its sample of local AGN sources.

The HyLIRGs found in Rowan-Robinson [2000] were not all quasars, but about 50% were shown to be AGNs based on their optical spectra. Many of these sources have been identified as lenses (e.g. the Cloverleaf quasar, Barvainis et al. [1995]). Rowan-Robinson and Wang [2010] estimate that 10% - 30% of the 179 HyLIRGs in the IIFSCz catalogue are significantly lensed, although probably only a minority of these are quasars.

8.5 Data analysis of FIR-luminous quasars

8.5.1 Optical−far-infrared correlation for quasars

Serjeant and Hatziminaoglou [2009] matched far-infrared data from IRAS, ISO, *Spitzer*, SCUBA and MAMBO to various quasar catalogues (including that from SDSS DR5), finding a correlation dependent on redshift (see Figure 8.3). They found a relationship between FIR luminosity and I-band optical luminosity of roughly $L_{FIR} \propto L_{opt}^{0.5}$. A science demonstration phase Herschel paper by Serjeant et al. [2010a] used stacking analysis to make a first estimate of star-formation history of quasar host galaxies back

8.5.1 Optical−far-infrared correlation for quasars

to $z \sim 5$, using 511 quasars from the Sloan QSO and 2SLAQ quasar catalogues. As well as finding strong evidence of downsizing in the formation of such galaxies, this paper proposed an empirical formula (Equation 8.1) for the correlation between the I-band optical luminosity (primarily due to the quasar) and the 100 μm far-infrared luminosity (primarily due to star formation):

$$\log_{10}\frac{\nu \mathrm{L}_\nu(100\mu\mathrm{m})}{10^{12}\mathrm{L}_\odot} = \alpha(\mathrm{M_I} + \beta) \tag{8.1}$$

with the parameter values for $z < 4$ being

$$\alpha(z) = (0.0371 \pm 0.0048)z - (0.235 \pm 0.018) \tag{8.2}$$

$$\beta(z) = (-1.19 \pm 0.30)z + (27.42 \pm 0.37) \tag{8.3}$$

and using a value of $z = 4$ for sources with $z > 4$.

I have converted the Serjeant formula from 100 μm to 90 μm for comparison later in this chapter with far-infrared sources in the *AKARI*-BSC catalogue, using a factor of 1.197 which is the the $\nu \mathrm{L}_\nu$ ratio at these two wavelengths from the SED of M82 (see Figure 2.2).

The relative optical and far-infrared luminosity functions resulting from the Serjeant relation for $z = 1$ are shown in Figure 8.4. At the high-luminosity end of the functions, the far-infrared luminosity falls off sharply compared to the optical luminosity. This fall-off is even sharper at higher redshift. Figure 8.4 also shows predictions of the lensed population, showing a clear excess over the far-infrared number density at high luminosities. The predictions are based on formalism of Blain [1996], Perrotta et al. [2002] and Perrotta et al. [2003] and assume a singular isothermal sphere for the lenses and a magnification ranging from 2 up to maxima (due to finite source sizes) of 10 and 30 (blue and green lines respectively in Figure 8.4).

The relationship does not appear to exist in AGN of lower luminosity (Rosario and Lutz [2013]; Rosario et al. [2013]). The anisotropy of quasar emission is a significant factor which may distort results unless some account can be made of their orientation: a recent study of accretion disk anisotropy by DiPompeo et al. [2014] suggests the bright end may be overstated by as much as a factor of two.

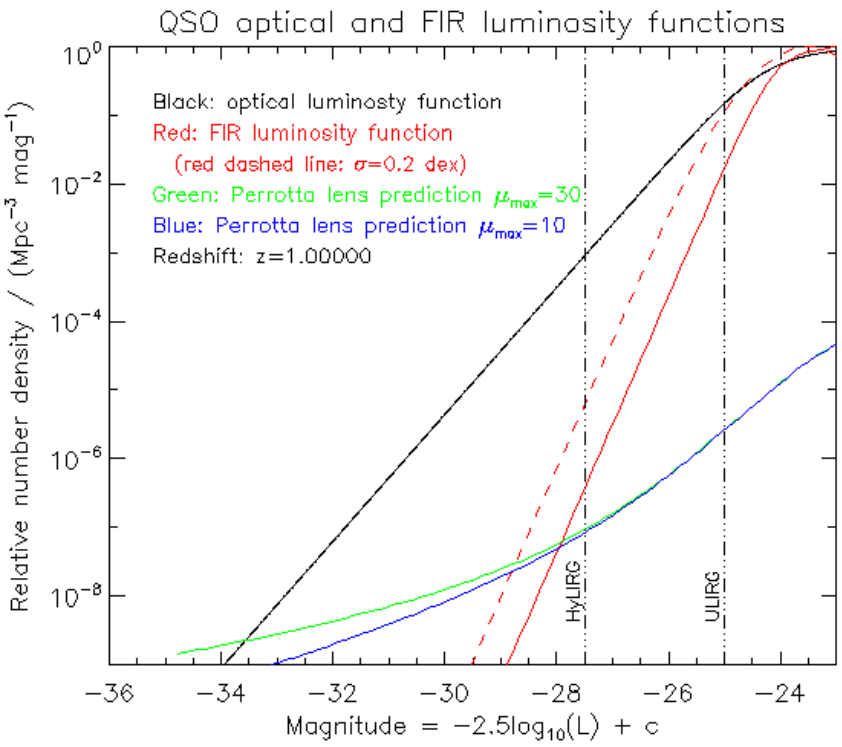

Figure 8.4: Relative optical and FIR luminosity functions for quasars for $z = 1$ assuming a flat universe. The optical luminosity function is from Croom et al. [2004]. The FIR luminosity function is calculated from the Serjeant et al. [2010a] relation for 100 μm (equation 8.1). Note the relative drop in the FIR LF at higher luminosity. The lensed predictions are based on the formalism of Blain [1996], Perrotta et al. [2002] and Perrotta et al. [2003].

8.5.2 Avoiding false positives: setting a tight matching radius

One way of avoiding false positives when matching sources with a catalogue is by 'randomising' the coordinates of sources in the catalogue (e.g. by swapping the hemisphere for declination, or adding a fixed amount to the right ascension) to find the angular matching distance at which a similar result starts to occur for these randomised coordinates[60]. An appropriate matching distance should clearly be chosen before this point is reached.

To see how many matches would be expected within various distances from a catalogue of random positions, the Sloan quasar catalogue was 'randomized' by translating the galactic longitude by $+5°$, $-5°$, $+10°$, $-10°$, followed by a reflection in the latitude plane. The mean of the results of matching four such random catalogues with the *AKARI* BSC was compared with the actual number of matches found in searches within these distances. The result suggests that all matches within $5''$ are likely to be real, but once the distance reaches $15''$, matches are likely to contain nearly 50% of false positives (for SDSS DR7 and 2SLAQ; less than 25% for the Richards catalogue). I have therefore only taken matches which are under $10''$ apart as genuine matches.

From the four spectroscopic quasar catalogues, 33 quasars were found in the *AKARI* BSC. From the Richards et al. [2009] photometric quasar catalogue, 584 matches were found in total, of which 256 had quality flags greater or equal to zero.

8.5.3 Review of images to avoid local FIR sources

I have examined optical images from the SDSS archive of all these 289 matches (33 from spectroscopic quasar catalogues, 256 from the Richards photometric catalogue). Roughly ninety per cent of them showed extended local features (see examples in Figure 8.5): some FIR sources were either in local spiral or irregular galaxies (some were bright spots in spiral arms, suggesting HII regions) or within the *AKARI* pixel size of about $8''$ of an extended local source. Some sources were in diffuse emission suggestive

[60] A similar technique was used to check the reality of the new galaxy cluster found in the ADF-S (see Table 4.2) and to find a realistic matching radius when cross-correlating sources in the different catalogues used in Chapter 5. Various statistical methods are available (e.g. Monte Carlo methods) to check whether a result could have occurred at random, and measure the statistical significance of the result. I have not used them in this thesis, so I will not describe them here.

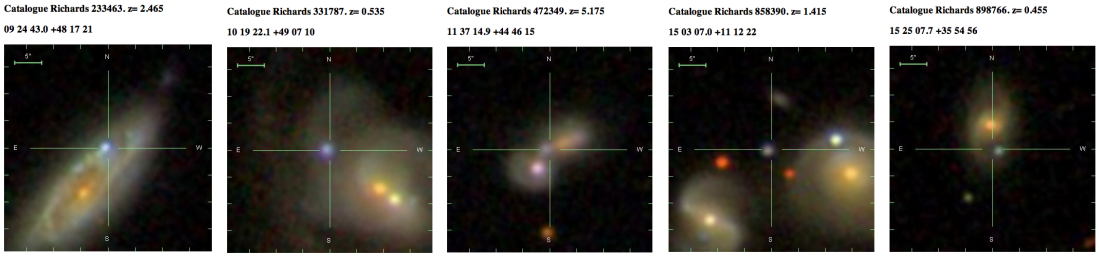

Figure 8.5: SDSS images of quasar-FIR matches rejected as false positives because of extended local features as discussed in Section 8.5.3. Sources which were clearly just local galaxies were also rejected.

of dust. Such local sources within this angular distance may contribute to the FIR flux, contaminating the data, and are not considered further.

The SDSS images of the final 22 sources are shown in Figures 8.8 and 8.9 at the end of this chapter. Coordinates, fluxes and other details are shown in Table 8.3. The SDSS images do not have sufficient angular resolution to show the possible lensed system, and deeper follow-up observations are planned. Figures 8.8 and 8.9 also show the *AKARI* 90 μm images; all but two of the 22 candidates are clearly shown.

8.6 Results

8.6.1 FIR luminosity: actual vs. prediction

We have used the optical luminosities of the sources and their (in most cases photometric) redshifts to predict the FIR luminosity using the Serjeant relation (Equation 8.1), and this is plotted as a function of redshift together with the actual 90 μm luminosity from *AKARI* in Figure 8.6. K-corrections in the far infrared have been made using the M82 SED, and in the optical by using the power law $S_\nu \propto \nu^{-0.5}$. The i-band magnitudes used are mostly SDSS asinh magnitudes, which are close (within 0.01 magnitudes) to the AB magnitude system. For non-SDSS sources, we have used the HST NICMOS conversion tool[61] to convert to i-band AB magnitudes assuming the same power law. The actual values of FIR luminosity derived from the *AKARI* data are close to the predicted values for $z < 1$, showing a similar slope to that predicted. For sources at $z > 1$, however, we see clear evidence of magnification, suggesting these sources may be

[61] http://www.stsci.edu/hst/nicmos/tools/conversion_form.html

8.6.1 FIR luminosity: actual vs. prediction

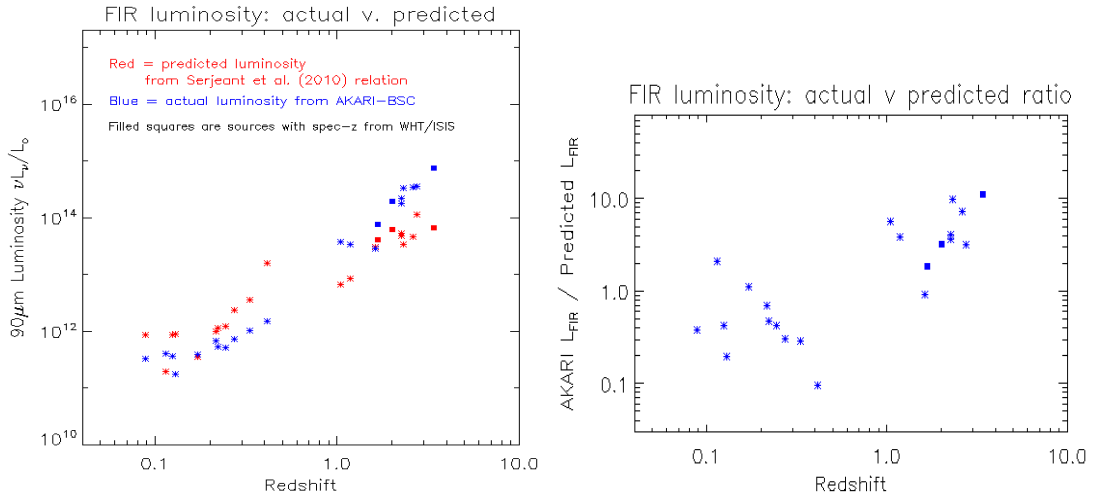

Figure 8.6: **Left:** actual *AKARI* BSC luminosity (blue points) vs. prediction using the Serjeant et al. [2010a] relation (red points) for our final shortlist of 22 matches. Magnification is seen for sources at $z > 1$, suggesting these may be gravitational lenses. Note also that low-redshift sources show a deficit to predicted values. **Right:** The same data plotted as a ratio. In each figure, the squares are the spec-z values from the work described in Section 8.6.2 replacing the photo-z values.

behind gravitational lenses. As shown in Figure 8.4, magnification by a lens would give a higher FIR luminosity relative to the optical luminosity, since the intrinsic optical-FIR relation is non-linear, so the same magnification applied to both optical and FIR luminosities would produce an FIR excess compared to the unlensed prediction. (If the FIR region is significantly more extended, the differential magnification would reduce the FIR, so differential magnification is unlikely in itself to cause an FIR excess.) This may therefore provide a new method for identifying lenses - by selecting quasars with strong FIR luminosity.

Table 8.3: Final list of quasars matched to the *AKARI* FIS-BSC catalogue, including lens candidates (in order of declination). The quality flag for Richards sources is given in parenthesis after the catalogue name (range: -6 to +6). For the three sources with both spec-z and photo-z, the spec-z value has been used in Figure 8.6.

AKARI FIS-BSC RA (J2000)	Dec (J2000)	Flux 90μm Jy	QSO Catalogue	QSO Ref	QSO catalogue RA (J2000)	Dec (J2000)	Redshift (z)	Mag i	Radio source	Distance (arcsecs)
Sources with $z < 1$:										
10 50 28.8	+00 28 06	0.791	SDSS DR5	33042	10 50 28.5	+00 28 08	0.216	18.122	yes	4.79
11 42 03.5	+00 51 35	0.452	SDSS DR5	39180	11 42 03.4	+00 51 36	0.245	18.128	yes	1.57
12 07 21.0	+02 17 02	0.580	SDSS DR5	42361	12 07 21.4	+02 16 58	0.222	17.948	no	7.41
12 57 39.2	+08 09 35	0.510	(Richards (3)	627748	12 57 39.4	+08 09 32	0.935	17.226	yes	4.28
			(SDSS DR7	63649	12 57 39.3	+08 09 32	0.272	17.292		4.27
04 44 29.0	+12 21 12	2.256	SDSS DR7	9603	04 44 28.8	+12 21 12	0.089	15.811	yes	3.76
15 02 32.0	+14 21 32	1.686	Richards (0)	857373	15 02 31.9	+14 21 35	0.115	19.279	yes	2.35
08 57 06.4	+19 08 55	0.481	(Richards (3)	186533	08 57 06.2	+19 08 54	0.305	17.077	yes	1.88
			(SDSS DR7	21306	08 57 06.4	+19 08 54	0.331	17.143		1.90
08 54 48.8	+20 06 32	0.434	Richards (3)	182648	08 54 49.0	+20 06 31	0.415	14.983	yes	1.13
16 34 59.5	+20 49 42	0.579	SDSS DR7	96210	16 34 59.8	+20 49 36	0.129	16.733	yes	7.77
15 22 38.2	+33 31 35	1.259	SDSS DR5	62583	15 22 38.1	+33 31 36	0.125	16.742	yes	0.98
Sources with $z > 1$:										
12 26 58.1	+00 26 18	0.691	2SLAQ	10613	12 26 58.9	+00 25 15	1.186	20.935	no	13.11
09 41 01.0	+14 36 22	0.771	Richards (1)	262979	09 41 00.7	+14 36 14	3.875	18.889	yes	8.52
10 36 23.1	+15 45 06	0.486	Richards (0)	362063	10 36 23.0	+15 45 12	2.255	20.014	no	5.46
07 35 31.9	+17 26 53	0.492	Richards (2)	61550	07 35 31.9	+17 27 01	1.265	20.358	no	7.68
08 22 30.3	+18 35 18	0.533	Richards (2)	128255	08 22 30.7	+18 35 11	1.845	19.101	yes	8.16
15 08 42.7	+28 10 23	0.575	Richards (0)	868490	15 08 42.7	+28 10 32	2.625	20.817	no	9.28
08 17 54.6	+31 28 20	0.598	Richards (0)	120548	08 17 55.2	+31 28 26	2.255	19.743	yes	8.46
08 30 03.9	+32 50 33	0.229	Richards (2)	140774	08 30 03.1	+32 50 36	1.625	19.582	no	9.06
10 35 17.0	+59 44 33	0.852	Richards (0)	360011	10 35 16.3	+59 44 31	2.315	21.152	no	5.99
16 12 24.7	+59 46 16	0.529	Richards (1)	988617	16 12 24.5	+59 46 11	2.735	18.097	no	5.98
10 12 58.3	+63 04 20	1.120	Richards (1)	320216	10 12 57.4	+63 04 20	1.045	20.836	no	6.22
Source with spec-$z < 1$ and photo-$z > 1$:										
15 09 14.0	+17 57 16	0.732	(Richards (0)	869418	15 09 13.7	+17 57 13	2.225	19.326	yes	4.46
			(SDSS DR7	84424	15 09 13.8	+17 57 10	0.171	16.440		6.15

Table 8.4: Spectroscopic follow-up observations of seven $z > 1$ sources with WHT/ISIS.

Date	Target(s)	i-band magnitude	Position angle (°)
11 May 2014	R869418	19.3	145
19 Jun 2014	R988617	18.1	80
29 Jan 2015	R262979	18.9	0
...	R362063	20.0	50
31 Jan 2015	R61550	20.4	0
...	R120548	19.7	50
...	R128255	19.1	0

8.6.2 Spectroscopic follow-up for 7 sources

As a first step to following up these initial results, I have obtained optical spectroscopy for 7 of the most FIR-luminous $z > 1$ sources with $i < 20.5$ with the Intermediate dispersion Spectrograph and Imaging System (ISIS) single-slit spectrograph on the William Herschel Telescope. The long slit was used ($\sim 4'$ in length and $\sim 22''$ in width). I observed simultaneously in the blue (3200−5300 Å) and red (5300−9706 Å) arms using the R158B and R158R gratings respectively with exposure time for each target of 1800s. Observations were made over four nights (see Table 8.4). The night of 29 Jan 2015 was described as poor seeing. Optical and FIR images for the seven sources are included in Figure 8.9.

I had problems with the blue arm, which in some cases did not reach its full wavelength extent, leaving a gap between the two arms at ~ 5300 Å. The data were reduced using well-known IRAF routines. Most targets showed more than one source, and a spectrum was extracted for each source.

The results are summarised in Table 8.5. Of the seven targets, one yielded no source (it was taken on the night with very poor seeing and was one of the fainter i-magnitude targets) and one proved to be a star. Of the other five targets, local sources ($z \sim 0.1$) were identified in four, and high-redshift quasars ($1.7 < z < 3.4$) tentatively identified in three. The spectra for the three quasars are shown in Figure 8.7.

Table 8.5: Results from initial follow-up spectroscopy with WHT/ISIS. One of the seven targets showed no source, and one was a star. Of the other five, four showed a local source (or sources) and three showed tentative detections of quasars.

Richards photo-z catalogue					WHT / ISIS spectroscopy			
Target	RA (J2000)	Dec (J2000)	Photo-z	Quality	Source	Redshift (z)	Lines identified	Comments
R61550	07 35 31.9	+17 27 01	1.265	+2	A	0.097	Hα, [SII]	Local source
					B	3.440	Lyβ, Lyα, CIV, AlIII	[Lensed] quasar
					C	-	Blue arm only	Star
R128255	08 22 30.7	+18 35 11	1.845	+2	A	0.113	Hα, [SII], Hβ etc	Local source
					B	1.684	CIV, AlIII, MgII	[Lensed] quasar
					C	0.376	Hα; red arm only	Local source
R262979	09 41 00.7	+14 36 14	3.875	+1	A	2.010	CIV, AlIII, CIII], MgII	[Lensed] quasar
R988617	16 12 24.5	+59 46 11	2.735	+1	A	0.102	Hα, [SII], [OIII], [OII] etc	Local source
					B	0.102	Hα, [SII], [OIII], [OII] etc	Local source
					C	0.102	Hα, [SII], [OIII], [OII] etc	Local source
R120548	08 17 55.2	+31 28 26	2.255	0	A	0.125	Hα, [SII], [OIII] etc	Local source
					B	-	None	
R869418	15 09 13.7	+17 57 13	2.225	0	A	-	Absorption spectrum	Star
					B	-	None	
R362063	10 36 23.0	+15 45 12	2.255	0	A	-	None	No source observed

8.6.2 Spectroscopic follow-up

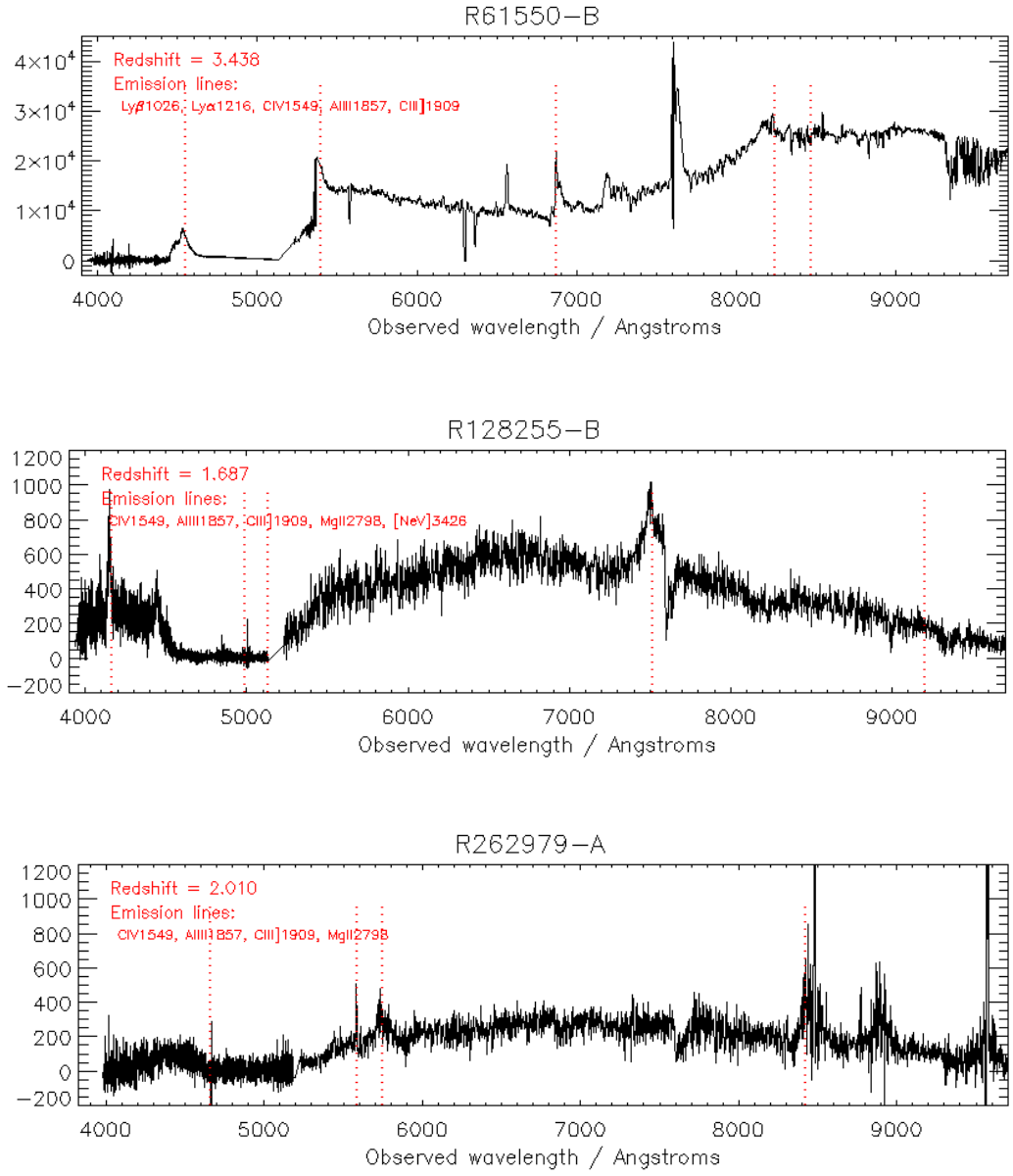

Figure 8.7: Spectra for the three tentative quasar identifications from WHT/ISIS spectroscopy. For R128255 (centre) the potential CIII] emission line falls in the gap between the two arms. Expected quasar emission lines at each redshift are vertical red dotted lines. The small gap between the two arms at ~ 5300Å is where the blue arm observations did not cover its full range. The spectra have not been flux-calibrated.

8.7 Discussion and future work

Finding extremely rare objects such as FIR-luminous quasars requires a large catalogue of quasars. A relatively small number of quasars ($\sim 10^5$) have been identified spectroscopically to date. This number can be increased by an order of magnitude by using photometric quasar catalogues, and by doing this I have increased the shortlist of quasar candidates in the *AKARI* all-sky Bright Source Catalogue from 33 to 256. Even so, many of these matches have turned out to be local sources. Further quasar catalogues are expected shortly, both spectroscopic[62] and photometric, which means that this work can be greatly extended in the near future. As shown in Table 8.2, improvements in photometric catalogues based on SDSS should improve in quantity by a factor of about 5, and with better training sets being developed, higher accuracy in quasar identification is now claimed. The quasar catalogue from LSST (Ivezic et al. [2014]) promises even larger quasar catalogues in the future using the time variability of quasars to assist detection and is expected to yield a factor of ten more in a different region of the sky.

In this chapter, it was the Richards photometric quasar catalogue, with over a million quasars, which yielded most of the 22 FIR-luminous quasars identified. A serious problem with using this photometric quasar catalogue has been contamination by local sources, which need to be eliminated by visual inspection. Our spectroscopic follow-up campaign on seven of the high-redshift targets, however, suggests that a significant fraction of these rare objects have been correctly identified, with three of the seven targets identified as quasars.

The work described in this chapter provides evidence supporting the optical−far-infrared correlation for quasars. Since this relation predicts a steep slope for the far-infrared luminosity function at high luminosities, whereas lens model predictions such as Perrotta et al. [2002] predict a shallower slope due to magnification bias, this leads to the prediction that most quasars with $L_{FIR} \gtrsim 5 \times 10^{13} L_{\odot}$ will be lensed. I have found evidence of magnification for the sources considered in this chapter at $z > 1$. This provides another method for finding gravitational lenses.

In addition, the *AKARI* BSC is not the only extensive source of far-infrared luminous sources. Many HyLIRGs found previously in the IRAS far-infrared all-sky catalogue (Rowan-Robinson [2000]) were later found to be lensed quasars. The *Herschel* Astrophysical Terahertz Large Area Survey (H-ATLAS; Eales et al. 2010) covered

[62] There have been further SDSS quasar catalogue data releases since the work in this chapter.

a total of 550 deg^2 and probed significantly deeper sources than *AKARI* with catalogues at 100, 160, 250, 350 and 500 μm. An earlier method of identifying gravitational lenses from high flux in H-ATLAS 500 μm source counts is already known and has proved to be highly efficient in identifying lenses (Negrello et al. [2010]). We are now planning to match the H-ATLAS sources at FIR and submillimetre wavelengths to the spectroscopic and photometric quasar catalogues. Follow-up observations, both optical spectroscopy and JCMT-SCUBA-2 submillimetre bolometric imaging, on matches of these catalogues to quasar catalogues are planned. With the sources from H-ATLAS, the final count of lensed quasars identified using this technique may reach $\sim$ 50-100.

Quasars found by this method will be from high-redshift lenses, and potentially good dark matter halo probes. Identifying lenses by excess emission line flux in relation to predicted steep high-luminosity decline is a possible future extension of the idea described in this chapter: for example, up to $\sim 10^5$ strong lenses are predicted to be discovered by excess Hα emission with *Euclid* (Serjeant [2014]).

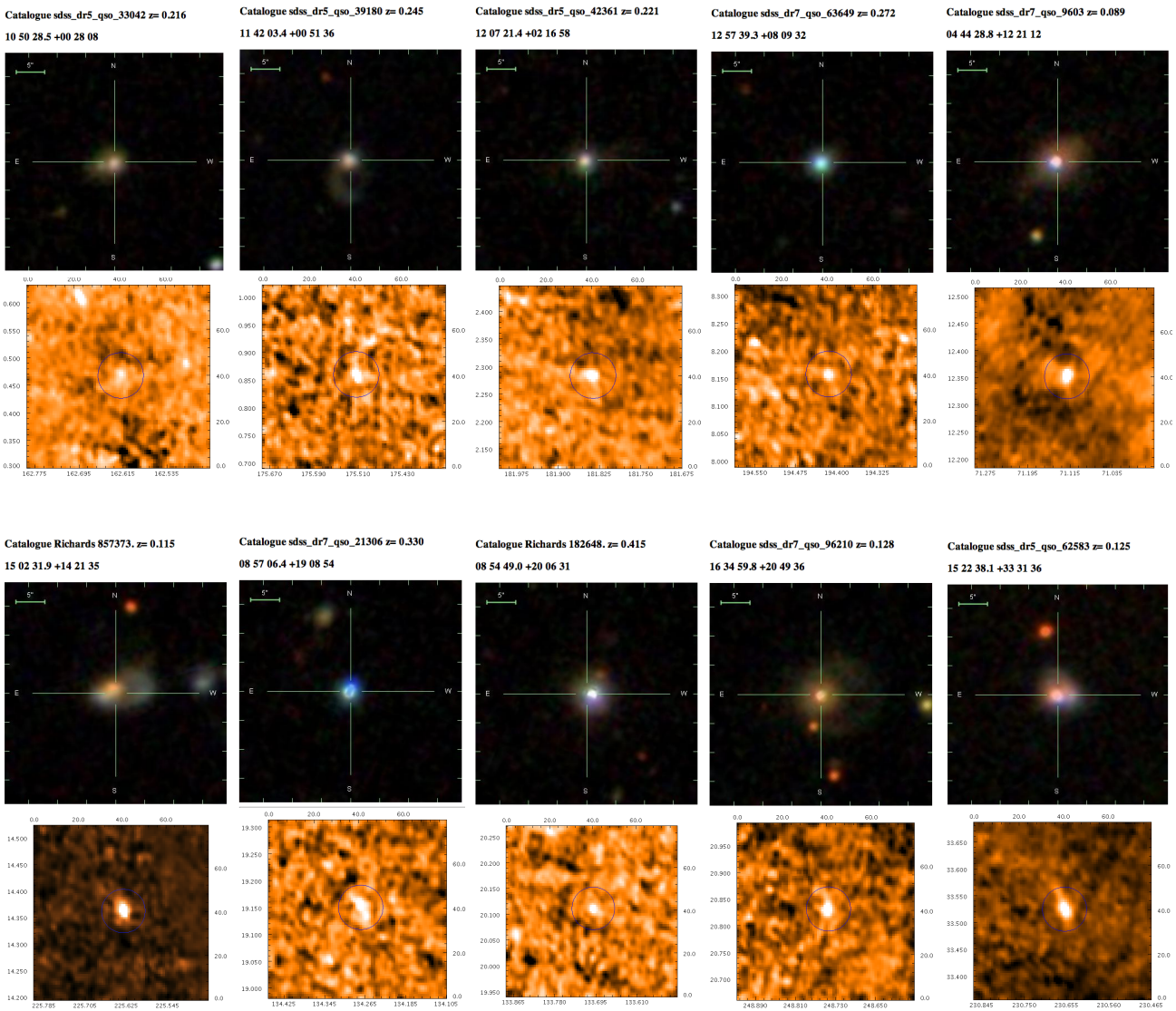

Figure 8.8: SDSS images and *AKARI* 90 μm images of sources at $z < 1$: matches between quasar catalogues and the *AKARI* FIR-BSC which are not (and are not within about 8″ of) local extended sources.

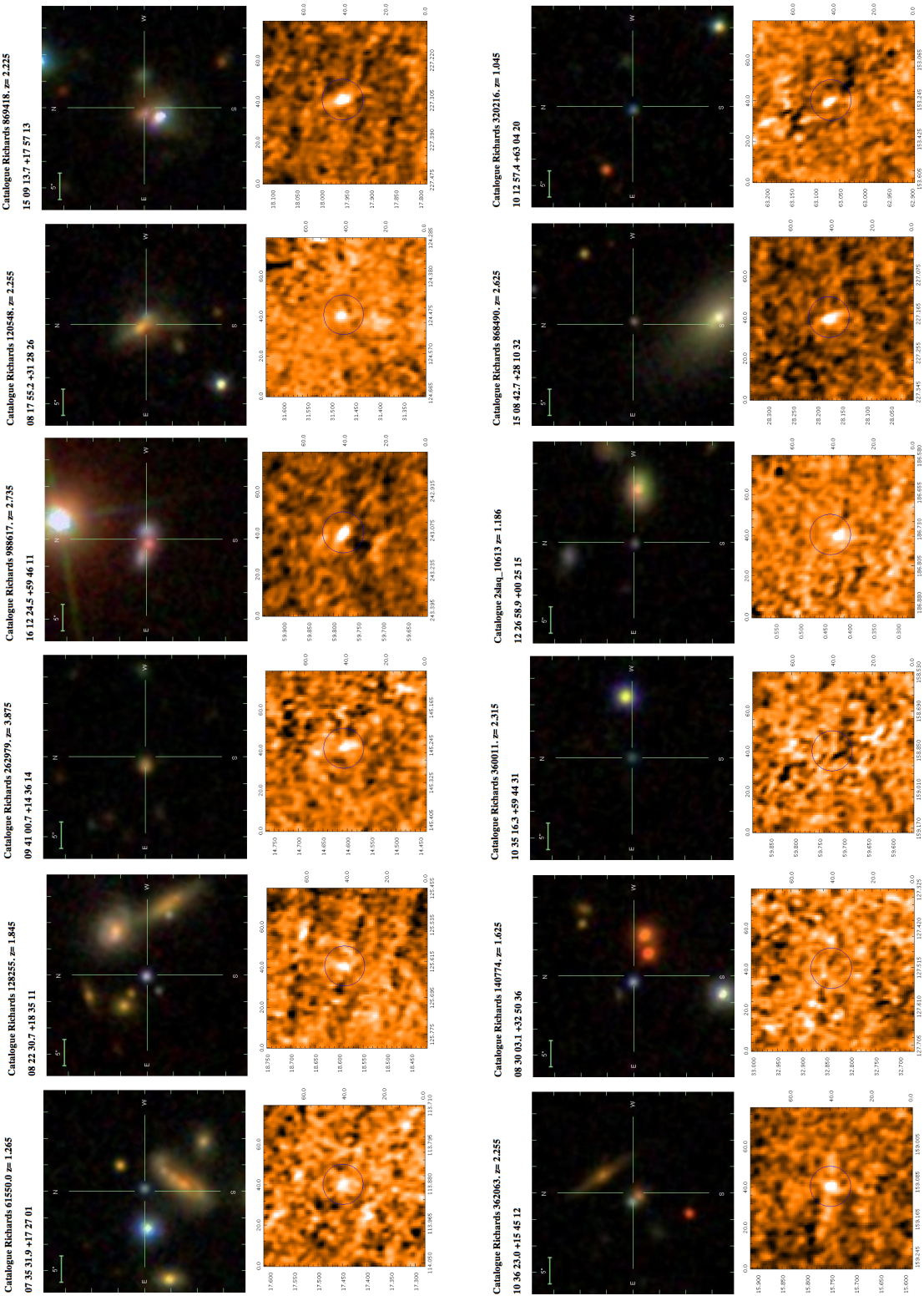

Figure 8.9: SDSS and *AKARI* 90 μm images of the 12 sources at $z > 1$ matched between quasar catalogues and the *AKARI* FIR-BSC. The first seven sources have been followed up with WHT/ISIS spectroscopy.

Appendix A: Graphic User Interfaces for spectroscopy

I have designed a Graphic Use Interface (GUI) in IDL for two of the science projects in this thesis. Although similar in design, each was designed and used for a different purpose, and this Appendix describes each of them briefly and shows some examples.

Firstly, I will describe the GUI used for the AAOmega optical spectroscopy in Chapter 3. The reason this was written was initially to help in identifying redshifts by enabling a template of potential emission lines to be moved over the spectrum, which I found to be much quicker and more productive than using IRAF for this purpose. The GUI also enabled the calculation of line widths and fluxes (in a similar manner to IRAF), and in addition showed the multi-wavelength data and the fitted SEDs for each source.

Secondly, I will explain the reasons for the GUI used in the *AKARI*-FUHYU near-infrared spectroscopic project (Chapters 6 and 7), which was written to compare the results of our own pipeline with those from the AKARI pipeline for each pointing, and also to see graphically the effect on the reduced spectra of altering some of the parameters used in the two pipelines.

A.1 AAOmega GUI

As described in Chapter 3, the observations from the AAOmega spectrograph were reduced using the standard AAOmega pipeline (2dfdr). I originally used the IRAF routine ONEDSPEC/SPLOT to identify redshifts and to calculate fluxes and line widths from identified emission lines. I later designed the GUI described here, because it enabled the interactive fitting of redshift templates over the spectra, which was particularly useful for noisy spectra and for detecting line patterns and supporting lines at distant parts of the spectrum. Telluric lines and local artefacts which survived the reduction process could be over-plotted to avoid misidentifying them as real observations.

I was also able to include widgets to boxcar-median smooth the data for any boxcar length, and to adjust the sigma-clipping which was needed to remove extreme values which also survived the standard reduction, but needed to be set a different levels for some of the spectra which showed strong (artificial) continuum variability. I included a zoom feature enabling a closer look at lines, and a cursor-sensitive widget to calculate

line widths (for FWHM) and line fluxes (less continuum). These calculations were checked against those from the IRAF SPLOT routine and found to be in agreement.

The GUI also shows the multi-wavelength data available for each source, and plots the best-fit SED from the Siebenmorgen Kreugel starburst templates using the χ^2-minimising Le Phare software, also showing the various parameters from the fitted template.

A schematic diagram of the GUI design in shown in Figure A.1 and an example of the GUI is shown in Figure A.2. When the GUI was written, redshifts had already been identified for 389 sources using IRAF. Additional redshifts (15) were found using the GUI and some changes made to earlier redshifts. When the routine is launched for a specified source, the redshift and multi-wavelength data is read in and the widget structure set up. Then the Analysis and Display routines are called to show the first spectrum and SED. The spectrum, the overlaid expected emission lines at its redshift (at zero redshift if none identified) and the data shown can be modified by any of six widgets shown on the right hand side of Figure A.1 and described below. A keyword option enables data files for line fluxes and widths to be updated.

The **reload** widget simply enables the user to move on to the next source. This can be specified by run and fibre, or the next source in the observing run can be chosen, or the next source with an identified redshift can be chosen. If the end of a run is reached, it automatically moves to the next run, and wraps around from the final (fifth) run to the start of the first run. The whole process described earlier then repeats itself for the new source, taking less than one second to do so. This widget is situated on the bottom left hand side of the widget (see Figure A.2).

Extreme values have survived the AAOmega reduction in some cases, and in order to show the spectrum they need to be clipped out. I have set a default to clip values at 7σ when displaying the spectra, but in some cases a higher value is needed (e.g. where the blue and red arms have not been joined very well and the continuum is at different levels in each). The **clipping** widget enables the clipping level to be changed in the analysis routine.

The **smoothing** widget allows the user to smooth the spectrum by median boxcar smoothing to a specified degree, or to show the spectrum unsmoothed.

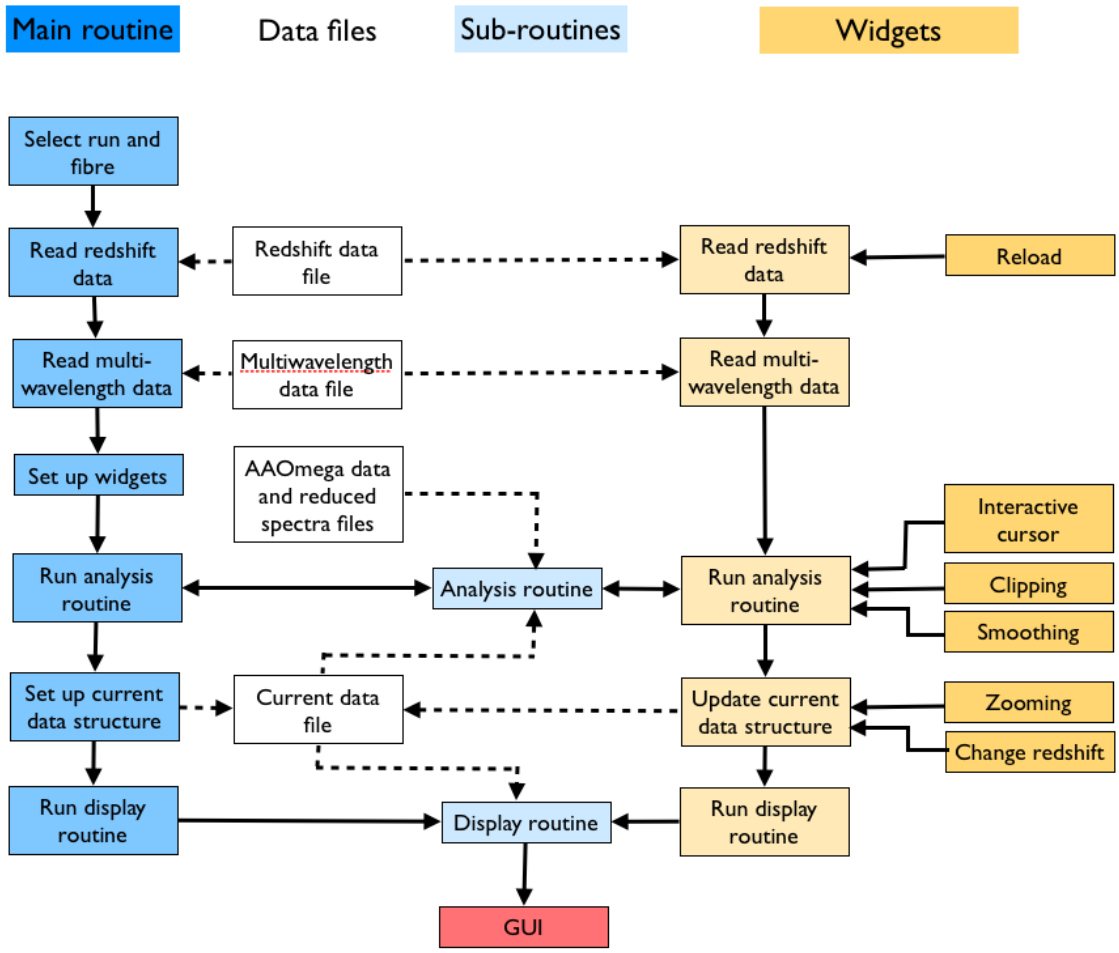

Figure A.1: Schematic diagram of the AAOmega graphic user interface (GUI). The six widgets are shown on the right hand side and are described in the text. The interactive cursor widget calculates fluxes and widths and shows the results in the GUI itself.

A.1 AAOmega GUI

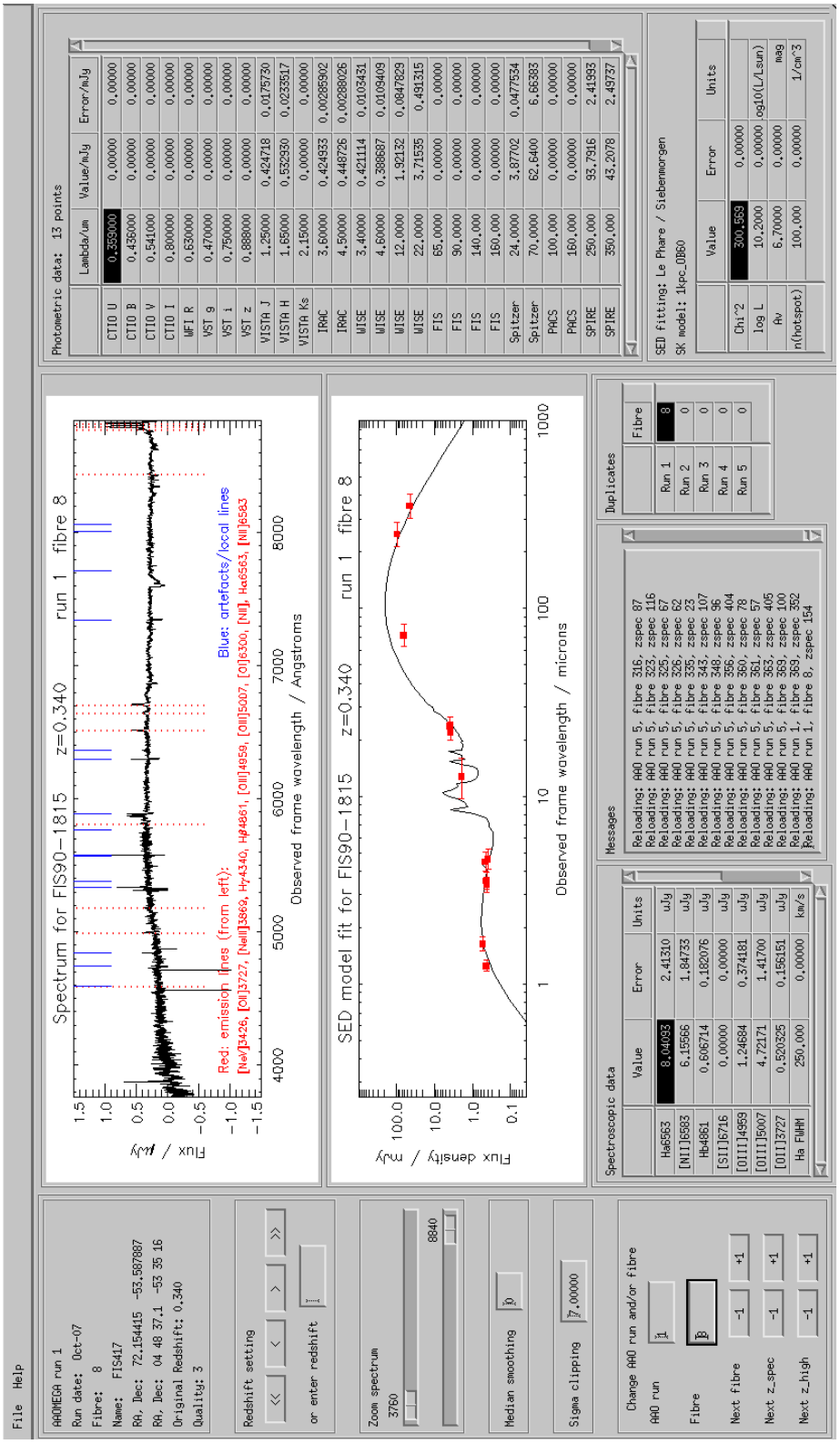

Figure A.2: The AAOmega graphic user interface: this figure shows an example of the interactive routine allowing various adjustments to be reflected quickly in the resulting spectrum. The blue lines are artefacts, some being telluric lines and others being lines from lighting in a local town, and are shown to avoid false identifications. The widgets are described in the text.

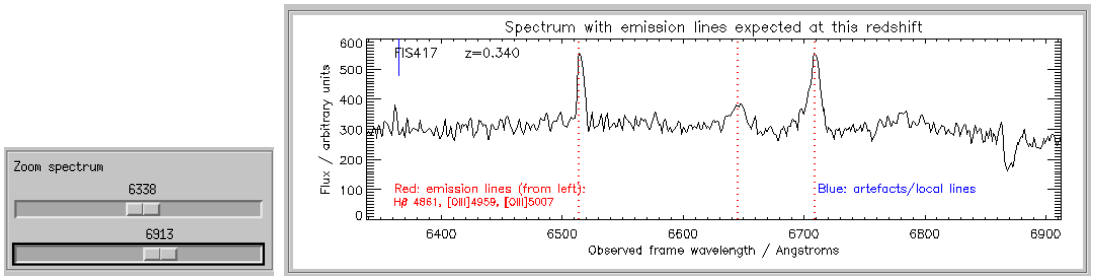

Figure A.3: Example of the sliding widget in the AAOmega GUI, zooming in to the [OIII] and Hβ lines in the same spectrum as that shown in Figure A.2.

It is important to be able to zoom in to see potential emission lines in more detail, and this is also helpful in accurately setting the limits for calculating the line and continuum fluxes and line width as described below. This is done by the **sliding** widget, which allows zooming in to any extent by moving the two (upper and lower) sliders in the GUI. An example of this is shown in Figure A.3. This widget does not require the analysis routine to be re-run, but just the display routine.

The **redshift** widget also operates only at the level of the display routine, and overprints red dotted lines on the spectrum corresponding to expected emission lines at the specified redshift. A new redshift can be entered as a number, or can be increased or decreased slowly or quickly with a selection of buttons. The names of the expected emission lines shown are printed at the bottom of the spectrum. Also shown are blue lines representing commonly found artefacts in the spectrum, resulting from emission by street lighting in a nearby town or telluric lines.

Finally, the **interactive cursor** widget causes calculations of width and flux to be made from clicking and releasing the cursor within the spectrum. By choosing points at half the maximum flux, an estimate of FWHM is obtained, converted to km s^{-1}, and printed in the messages box in the GUI. Similarly, the flux can be estimated by clicking and releasing at the bottom of either side of the emission line, choosing at the continuum level; the resulting emission line luminosity (converted from the spectrum flux to μJy as described in Section 3.4.2) is shown together with the continuum level and the flux minus the continuum. The main cause of error in the flux is likely to be in the estimation of the continuum level, which is often not clear-cut (e.g. one side of the line may differ from the other). The calculation of errors in the flux is shown on Page 217. The interactive cursor does not require either the analysis routine or the display routine to be re-run.

The IDL GUI widgets work by using a continually updated current data file, an IDL structure, which is read by each widget and updated with the input values. Pointers are used for components in the structure which may vary in size. This is shown as 'current data file' in Figure A.1. The other data files used are self-explanatory and shown as uncoloured boxes in the second column of the figure. These other data files are not updated during use of the GUI.

The GUI also shows the multi-wavelength data for this source in a table, and plots the data with a best-fit SED from the Le Phare fitting routine, using the spectroscopic redshift from the spectrum and the Siebenmorgen starburst templates as discussed in Chapter 5. The parameters from this fit are also shown in a table. The SED is generated and modified within the Le Phare routines and is not interactive in the GUI.

A.2 *AKARI*-FUHYU GUI

This section describes the design of the *AKARI*-FUHYU GUI, which was used to compare the results of two alternative reduction pipelines on the data in Chapters 6 and 7, and to fine-tune the reductions of the raw data for each. The original reduction using the *AKARI* pipeline proved very disappointing, as described in detail in Section 6.2.2, and after we had written our own reduction routines, it was helpful to be able to compare the results of the two pipelines instantly by clicking a button, and also to assess the effect of altering some of the parameters in the two pipelines. Firstly, I will outline the pipelines used to reduce the data, which will place the GUI in context.

Originally, the *AKARI* Phase III spectroscopic pipeline was run for each pointing for each source, with two or three iterations as described in the manual (Onaka et al. [2009]). The third run is necessary if the pipeline does not automatically identify the source. This was normally the case: the target usually had to be identified manually in the $1' \times 1'$ point source aperture reference image. The *AKARI* pipeline for warm-phase data is described in Onaka et al. [2009] and is not described further here.

The disappointing quality of the spectra obtained from the *AKARI* reduction led us to write a new pipeline (referred to as the OU pipeline). There were problems in the *AKARI* pipeline with the registration of sub-frames for each pointing, and more work was needed on sky subtraction to reduce the noise, much of which probably instrumental. In our GUI, I have built in an option to compare our pipeline's results directly with those from the *AKARI* pipeline for each pointing. The target coordinates from these *AKARI* reductions were used as input into the OU pipeline; the GUI allows

these to be fine-tuned by looking at the column flux profiles. After this, the results were stacked by coadding the noise-weighted pointings for each source; this is not discussed further here.

A.2.1 Outline of the OU pipeline

This subsection outlines the steps in the reduction; the following subsection will describe how the GUI was used to review the results and modify the reduction. After reading in the raw data from the AKARI observations, the target coordinates and the calibration data, the following steps were performed.

Dark field subtraction: Each pointing included 10 dark frames in a sequence of 5 darks, 4 spectroscopic observations (sub-frames), one reference image, 4 or 5 more spectroscopic observations, and 5 further darks. I took the median of the 10 dark frames and subtracted this median from each of the eight or nine spectroscopic sub-frames.

Identify target coordinates: The third *AKARI* pipeline iteration employed a fitting routine around the target specified. I usually had to specify the target coordinates by visual inspection of the reference image since this was not usually identified correctly by the pipeline. I added a further interactive option in the GUI (using the **position** widget described below) to fine-tune the centre of the target by showing the target in relation to the column flux profile.

Saturation masking: There is a short exposure as well as the long exposure for every sub-frame for each pointing. As described in the *AKARI* manual (Onaka et al. [2009]), saturation is identified in the short exposure for each sub-frame, and the corresponding pixel in the long exposure is masked.

Flat-fielding: Although I included an option to apply the flat field data to our observations, I found that this did not improve the data, and following guidance in Onaka et al. [2009] I eventually decided not to use this in our reduction.

De-glitching: The aim is to remove hot pixels and cosmic rays. Readings are set to the median for any pixel across all sub-frames for that pixel where (a) the ADU reading was over a maximum above the median, or (b) where the reading was greater than 10 standard deviations. The same was applied to pixels where the reading was less than a minimum value. These thresholds were monitored and could be varied.

Sky subtraction: It proved very difficult to reduce the noise in our spectra. The main

source of this was probably due to the instruments in the warm phase, more than the radiation from the background sky, and sometimes showed a cyclic pattern. I tried to remove this by fitting various functions to the background data (after masking our source). This included fitting polynomials of various orders, median boxcar fitting, and other functions. The one which gave best results was a polynomial of order 6 in dispersion direction and of order order 2 in spatial direction. The columns used and the columns masked out in the sky subtraction could be varied using the **skysub** widget described below.

Registration of sub-frames: The next step was to align the eight or nine sub-frames with each other. This was done by matching against the fourth (∼middle) frame, as in the *AKARI* pipeline. The jitter of the telescope meant that sometimes the target could move out of frame. I used a routine called **pixshift.pro** which was written earlier for the SCUBA Half Degree Extragalactic Survey (SHADES; Serjeant et al. [2008]).

Zerofootprint drizzling: This is a technique (similar to drizzling which was developed for the HST) where a large grid (×5 magnification of each axis in our case) is set up and the flux of each pixel is inserted into it. A detailed description of zerofootprint drizzling is given in Section 6.3.2. Additional de-glitching is done at this stage to ensure no pixel has a value greater than 10σ.

Extraction of sources: It is then necessary to extract the sources from this big grid, and again I used a routine previously written for SCUBA (see Serjeant et al. [2003]) called **scuba_src_ext.pro**, using a Gaussian FWHM kernel of [15, 30] pixels across pixels of [31, 61]. Note the [x,y] axes are in the [spatial, dispersion] directions. The **gaussian** widget in the GUI described below enabled the centre and width of the fitted gaussian to be varied and the results evaluated. Note that the pixels here are of the magnified grid.

Wavelength calibration and spectral response: The wavelength axis is calibrated and the flux adjusted for the spectral response of the instrument using the *AKARI* calibration data.

A.2.2 Details of the FUHYU GUI

The GUI was designed to show the extracted spectrum for each pointing for each source, to compare between the two pipelines for each pointing, to fine-tune the position at which the spectrum was extracted and see the results of varying certain parameters

used in the two pipelines. A schematic diagram of the FUHYU GUI design in shown in Figure A.4 and an example of the GUI is shown in Figure A.5.

When the GUI is launched, the pipeline (*AKARI* or OU; default is OU), the target identification numbers (both main ID and pointing subid) and the redshift (if unknown, $z = 0$) need to be specified. Any previously saved sky subtraction data (indicating which columns are used for the data and which for the sky subtraction) are read in, and if no file exists then a file is set up to save the results of this run. Similarly, the peak and width of the Gaussian used to extract the source from the expanded grid in the OU pipeline is read in, and if it was not previously saved a new file is created to save the results. The offsets for the sub-frames for each pointing are also read in.

The widget layout is then established, the analysis routine is run, the current data file set up (for use by the widgets) and the display routine displays the resulting spectrum for the specified pointing and pipeline in the GUI. It also shows the *AKARI* reference image, and three external images where available for comparison. There is also an ongoing message log of the changes made, and a table of the shifts applied when the sub-frames are registered.

The analysis routine, which is called both in the initial run and by several of the widgets, performs the following steps. Firstly, it reads in the output from the selected pipeline, using the header information to calibrate the wavelength axis in microns. It then runs the sky subtraction procedure using the parameters specified in the sky subtraction data file (where relevant, as modified by the widget). It returns the flux profile in the spatial direction across the aperture before and after the sky subtraction, and the mask used for the sky fit, all of which will be shown in the GUI. It then runs the routine to extract the spectrum by fitting a gaussian using the peak and width parameters in the gaussian data file (as modified by the widget, where relevant); there is also an option to use a single column for the extraction of the spectrum. The wavelength calibration is adjusted if a row other than the central row is selected in the fine-tuning of the source coordinates. It clips extreme values at 5σ and includes an option for boxcar median smoothing. It also reads in the *AKARI* reference image for the pointing and any external images which are available (*Spitzer*, SDSS, 2MASS, DSS or WISE) for the source.

I will next discuss the eight widgets in more detail.

The **skysub** widget allows various changes to parameters used in the sky subtraction in the OU pipeline: which columns to use for sky subtraction and which to mask out; also the sky subtraction can be turned on or off to see the effect on the spec-

trum. The mask for the sky subtraction is shown in a figure (the central figure in the second column, see Figure A.5). Three spatial flux profiles are also shown in the second column, which will normally show a peak where the source can be identified and help to select which columns should be used for sky subtraction: total flux before sky subtraction, median flux before sky subtraction, and median flux after sky subtraction.

The **gaussian** widget enables the peak and width (sigma) of the gaussian which is applied to rows across the source to be altered; also, it can be turned off and a single column used to extract the spectrum. Both this widget and the previous **skysub** widget widget amend the relevant data files, so the next run for this pointing will show the latest parameters selected; they then run the analysis routine, update the current data structure used by all widgets, and run the display routine.

The **pipeline** widget enables an immediate comparison of results between the two pipelines, enabling an instantaneous switch between them. The **source or pointing** widget will change to another pointing of the present source, or to another source.

A key point in this work was the correct identification of the source coordinates from which to extract the spectrum. The **position** widget enables the exact position from which the spectrum is extracted to be altered by specifying the row (which is the spatial coordinate) and the column (which affects the offset of the spectrum, necessitating an adjustment to the wavelength calibration as discussed above in the description of the analysis routine). Adjustment of the position is based on the displayed column flux profile. The reference image originally used to identify the coordinates is also shown.

Boxcar median smoothing is possible by use of the **smoothing** widget. The length of the boxcar can be specified, or the smoothing can be turned off. The **colour table** widget is relevant only to the images shown, which sometimes look clearer with or without the use of a colour table. These last five widgets cause the analysis routine to be re-run with appropriate keywords, then update the current data file and run the display routine as shown in Figure A.4.

Finally, the effect of altering the redshift is controlled by the **redshift** widget, which shows the key expected emission lines overplotted on the spectrum for the specified redshift. As with the other GUI, a specific redshift can be entered, or the redshift increased or decreased rapidly (by ± 0.03) or slowly (by ± 0.001) using buttons. This does not require the analysis routine to be re-run.

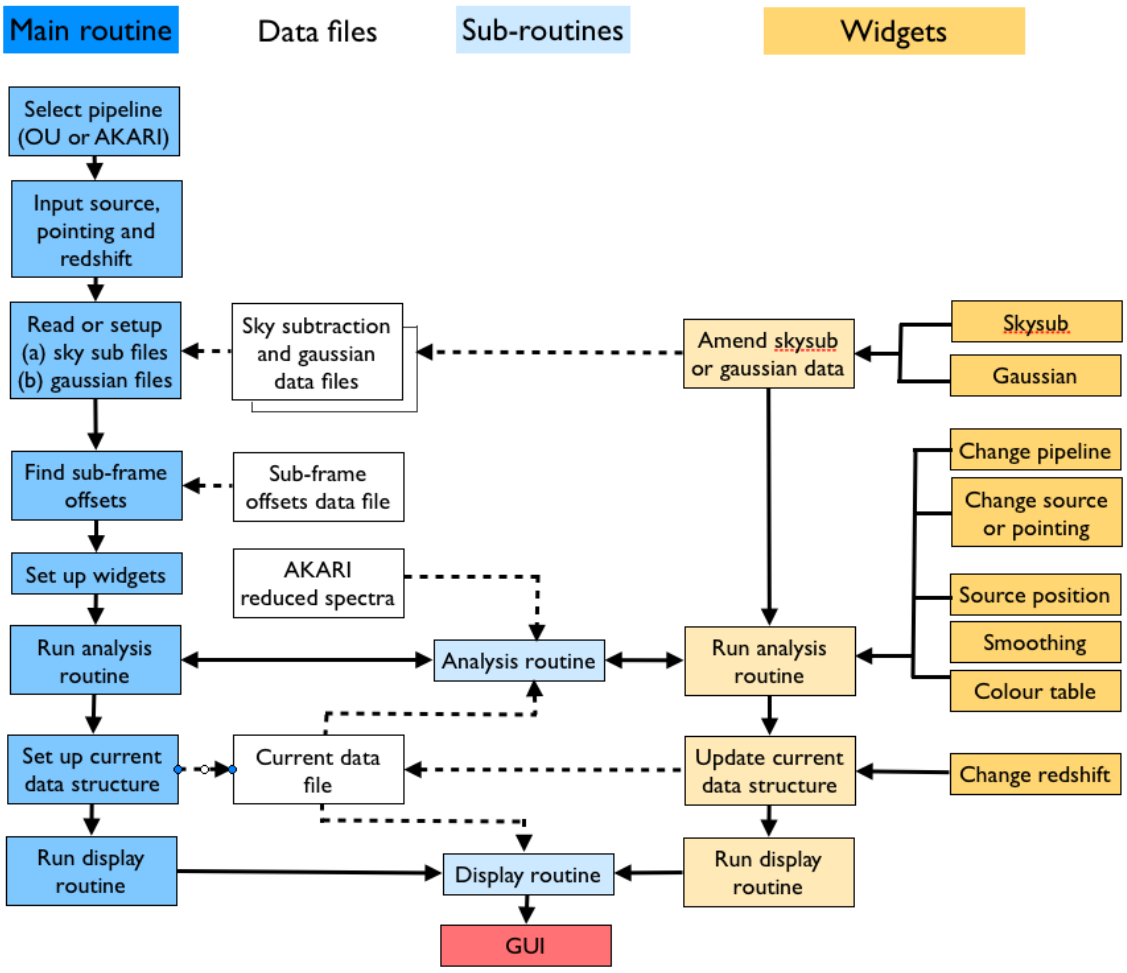

Figure A.4: Schematic diagram of the *AKARI*-FUHYU spectroscopy GUI. The *AKARI* pipeline is run first (as described in the text) to obtain the target's coordinates; these can be fine-tuned by the **position** widget based on the profiles shown in the GUI. The columns used in sky subtraction can be amended using the **skysub** widget. The **pipeline** widget enables instant comparison between the *AKARI* and OU pipelines for a source. All the widgets are described in more detail in the text.

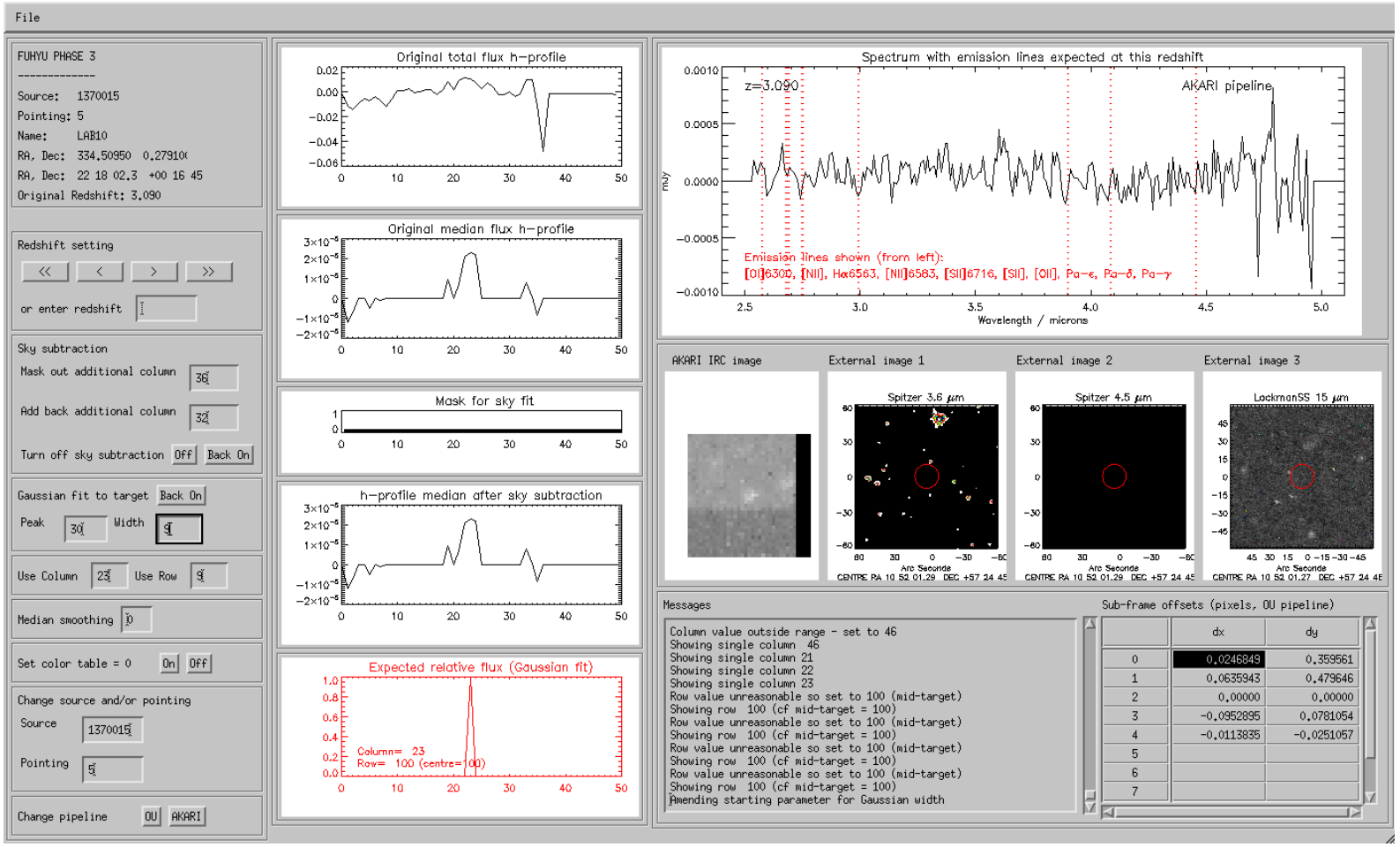

Figure A.5: The *AKARI*-FUHYU graphic user interface: this figure shows an example of the interactive routine allowing various adjustments to be reflected quickly in the resulting spectrum. Note this shows a single pointing: up to 10 pointings are later coadded for the final spectrum of the source.

Appendix B: ADF-S spectroscopic data with AAOmega

Details of the emission lines for the 404 sources for which spectroscopic redshifts were identified (as described in Chapter 3) are given in this appendix, in three tables:

Table B.1: sources with redshifts $z \leq 0.345$

Table B.2: sources with redshifts $0.345 < z \leq 1.0$

Table B.3: sources with redshifts $1.0 < z$

Results are in order of RA in each table.

Abbreviations in tables:

z_{spec} = spectroscopic redshift identified in this work

Q = quality of redshift identification on a scale of 1 (tentative) up to 3 (excellent)

osr = outside spectroscopic range

abs = absorption line instead of expected emission line

diff = difficult to measure in noisy part of spectrum

cl = member of the new cluster found (see Section 4.3.2)

... = duplicate observation(s); results from the best spectrum are shown first

A note on errors:

The flux errors shown in the tables comprise the following (combined in quadrature):

a) the 1σ error in the flux calibration fit described in Section 3.4.2

b) the WFI R-band or CTIO V-band flux error

c) the AAOmega flux error (estimated at 10%)

d) the error in calculating the continuum at the emission line (estimated 20%)

e) the error in identifying the start and end points of the emission line (estimated 20%)

Table B.1: Sources with $z \leq 0.345$, page 1 of 7, showing the main emission lines identified. For notes, see page 217.

ID	RA (J2000)	Dec (J2000)	AAO Fibre	z_{spec}	Q	[OII] 3727Å S μJy	[OII] 3727Å ΔS μJy	Hβ 4861Å S μJy	Hβ 4861Å ΔS μJy	[OIII] 4958Å S μJy	[OIII] 4958Å ΔS μJy	[OIII] 5007Å S μJy	[OIII] 5007Å ΔS μJy	Hα 6563Å S μJy	Hα 6563Å ΔS μJy	[NII] 6582Å S μJy	[NII] 6582Å ΔS μJy	[SII] 6716Å S μJy	[SII] 6716Å ΔS μJy
BLAST500-329	04 38 42.3	-53 45 05	4-181	0.303	3	1.18	0.35	0.39	0.12	0.16	0.05	0.25	0.08	2.98	0.90	1.27	0.38	0.93	0.28
FIS90-660	04 38 54.2	-53 46 45	5-182	0.043	3	1.66	0.50	1.46	0.44	0.40	0.12	0.95	0.29	2.55	0.76	0.05	0.01	0.84	0.25
FIS90-559	04 39 02.4	-53 13 17	5-218	0.157	3	1.37	0.41	1.43	0.43	0.00	0.00	0.00	0.00	5.74	1.72	3.93	1.18	0.59	0.18
BLAST350-310	04 39 07.0	-53 34 49	4-191	0.053	3	0.00	0.00	0.18	0.05	0.00	0.00	0.60	0.18	0.68	0.20	0.00	0.00	0.49	0.15
FIS90-297	04 39 08.2	-53 26 43	5-205	0.165	3	1.83	0.55	1.61	0.48	0.00	0.00	0.18	0.06	3.69	1.11	2.48	0.74	0.83	0.25
FIS90-297	04 39 12.0	-53 27 11	5-198	0.069	3	1.73	0.52	1.31	0.39	0.00	0.00	0.00	0.00	3.28	0.98	2.27	0.68	0.46	0.14
FIS90-502	04 39 12.1	-53 36 25	5-189	0.043	3	0.95	0.28	6.67	2.00	1.64	0.49	7.54	2.26	13.63	4.09	3.68	1.10	1.88	0.56
BLAST500-133	04 39 16.2	-53 38 12	4-187	0.069	3	1.99	0.60	1.38	0.41	0.16	0.05	4.38	1.31	3.66	1.10	1.41	0.42	0.84	0.25
FIS90-67	04 39 25.3	-53 02 51	5-230	0.006	3	osr		7.56	2.27	10.16	3.05	40.71	12.22	10.41	3.12	1.03	0.31	0.35	0.10
FIS90-1	04 39 36.8	-53 00 50	4-234	0.006	3	osr		1.72	0.52	0.00	0.00	1.52	0.46	6.03	1.81	2.91	0.87	2.60	0.78
FIS90-616	04 39 38.7	-53 11 31	5-223	0.243	3	0.00	0.00	2.09	0.63	0.00	0.00	0.00	0.00	7.06	2.12	0.49	0.15	0.70	0.21
FIS90-1339	04 39 51.5	-53 42 08	5-185	0.136	3	0.38	0.11	0.69	0.21	0.00	0.00	0.00	0.00	3.36	1.01	3.23	0.97	0.00	0.00
FIS90-244	04 39 53.5	-53 49 47	5-173	0.240	3	18.37	5.51	1.92	0.58	1.85	0.56	3.67	1.10	12.02	3.61	2.43	0.73	2.15	0.65
FIS90-1079	04 39 53.8	-54 04 32	5-158	0.269	1	0.00	0.00	0.19	0.06	0.00	0.00	0.00	0.00	2.38	0.72	0.00	0.00	0.00	0.00
FIS90-367 cl	04 40 02.7	-53 41 44	5-175	0.057	3	2.34	0.70	3.60	1.08	0.25	0.08	3.46	1.04	6.45	1.94	2.40	0.72	1.68	0.50
FIS90-467	04 40 08.0	-53 58 19	5-161	0.069	3	1.28	0.38	3.66	1.10	0.26	0.08	0.79	0.24	5.89	1.77	0.74	0.22	0.65	0.19
BLAST250-274	04 40 10.2	-53 33 01	4-193	0.054	3	0.44	0.13	0.00	0.00	1.24	0.37	3.80	1.14	0.62	0.19	0.60	0.18	0.00	0.00
BLAST250-471	04 40 11.6	-53 32 05	4-196	0.318	3	1.16	0.35	0.43	0.13	0.00	0.00	0.66	0.20	2.63	0.79	0.74	0.22	0.00	0.00
BLAST250-358	04 40 12.7	-53 37 38	4-186	0.241	3	2.22	0.66	0.65	0.20	0.13	0.04	1.33	0.40	5.49	1.65	0.57	0.17	0.47	0.14
BLAST250-221	04 40 13.1	-53 45 11	4-176	0.138	1	0.19	0.06	0.65	0.20	0.00	0.00	0.26	0.08	1.47	0.44	0.50	0.15	0.05	0.02
BLAST250-56	04 40 19.2	-53 43 35	4-178	0.137	1	0.36	0.11	0.00	0.00	0.00	0.00	0.00	0.00	1.63	0.49	1.63	0.49	0.00	0.00
FIS90-354	04 40 19.5	-53 28 40	5-195	0.123	3	5.43	1.63	4.95	1.49	0.00	0.00	4.54	1.36	9.32	2.80	4.29	1.29	1.59	0.48
FIS90-553 cl	04 40 23.3	-52 59 07	4-240	0.059	3	2.03	0.61	2.18	0.65	0.00	0.00	1.25	0.38	10.91	3.27	6.54	1.96	1.84	0.55
BLAST500-193 cl	04 40 29.4	-53 21 43	4-212	0.058	3	0.40	0.12	1.42	0.43	0.00	0.00	0.58	0.17	4.43	1.33	0.55	0.16	0.68	0.20
BLAST250-508	04 40 36.9	-54 01 20	4-155	0.211	3	7.02	2.11	0.87	0.26	1.17	0.35	4.58	1.37	7.82	2.35	1.45	0.44	0.53	0.16
BLAST250-602	04 40 43.1	-53 32 48	4-190	0.265	3	0.87	0.26	0.21	0.06	0.00	0.00	0.27	0.08	0.33	0.10	0.04	0.01	0.00	0.00
BLAST500-44	04 40 43.5	-53 45 08	4-172	0.058	3	0.13	0.04	0.20	0.06	0.00	0.00	0.47	0.14	0.63	0.19	0.09	0.03	0.16	0.05
FIS90-17	04 40 44.8	-53 45 22	5-254	0.013	3	osr		4.63	1.39	3.30	0.99	10.85	3.26	9.22	2.77	1.70	0.51	1.05	0.31
FIS90-700	04 40 47.3	-53 41 23	1-181	0.110	3	0.00	0.00	0.00	0.00	0.00	0.00	0.00	0.00	1.31	0.39	1.40	0.42	0.77	0.23
FIS90-56 cl	04 40 52.8	-53 44 18	1-178	0.058	3	2.44	0.73	1.35	0.41	4.54	1.36	11.73	3.52	11.52	3.46	7.80	2.34	3.48	1.04
FIS90-184 cl	04 40 54.6	-53 16 48	1-212	0.057	3	0.79	0.24	0.00	0.00	0.00	0.00	0.00	0.00	3.08	0.93	2.76	0.83	0.17	0.05
FIS90-262	04 40 55.8	-52 45 44	4-254	0.123	3	0.84	0.25	1.73	0.52	0.00	0.00	0.23	0.07	5.49	1.65	1.71	0.51	1.15	0.35
FIS90-2096	04 41 02.7	-53 40 10	5-187	0.109	3	2.20	0.66	2.87	0.86	0.00	0.00	0.11	0.03	4.48	1.35	2.03	0.61	1.17	0.35
FIS90-167	04 41 04.9	-54 02 48	3-158	0.055	3	0.92	0.28	0.54	0.16	0.00	0.00	0.00	0.00	6.46	1.94	2.51	0.75	1.58	0.48
...	...	...	2-156	0.055	3	0.00	0.00	0.00	0.00	0.00	0.00	0.00	0.00	4.61	1.38	1.79	0.54	0.42	0.13
FIS90-121	04 41 10.6	-52 46 42	4-258	0.160	3	0.62	0.19	0.58	0.17	0.00	0.00	0.09	0.03	0.62	0.19	0.84	0.25	0.91	0.27
FIS90-532	04 41 12.6	-53 44 48	2-176	0.181	1	0.00	0.00	0.00	0.00	0.00	0.00	0.00	0.00	1.97	0.59	0.00	0.00	0.00	0.00
FIS90-841	04 41 15.6	-53 37 18	3-185	0.110	3	2.78	0.84	1.17	0.35	0.00	0.00	0.50	0.15	5.87	1.76	3.48	1.05	1.31	0.39
...	...	...	2-190	0.110	3	0.31	0.09	0.96	0.29	0.00	0.00	0.00	0.00	4.33	1.30	1.71	0.51	1.33	0.40
FIS90-1908 cl	04 41 16.9	-53 47 55	1-173	0.057	3	0.92	0.28	0.43	0.13	0.00	0.00	0.00	0.00	2.49	0.75	0.20	0.06	0.44	0.13
FIS-546	04 41 17.9	-53 07 40	1-221	0.254	2	0.00	0.00	0.14	0.04	0.00	0.00	0.26	0.08	1.52	0.46	0.10	0.03	0.67	0.20
BLAST500-142	04 41 21.1	-53 31 52	5-193	0.154	1	0.00	0.00	0.00	0.00	0.00	0.00	0.00	0.00	5.41	1.62	0.00	0.00	0.26	0.08
FIS90-501	04 41 21.3	-53 07 23	4-239	0.178	3	5.06	1.52	0.65	0.19	0.00	0.00	0.27	0.08	4.69	1.41	4.04	1.21	2.44	0.73
FIS90-1954	04 41 21.6	-53 21 06	1-207	0.060	3	0.00	0.00	0.00	0.00	0.00	0.00	0.00	0.00	1.35	0.40	0.96	0.29	0.58	0.18
FIS90-601 cl	04 41 24.0	-53 03 03	1-230	0.060	3	2.23	0.67	2.23	0.67	0.44	0.13	1.96	0.59	9.44	2.83	3.43	1.03	3.28	0.98
FIS90-23 cl	04 41 25.3	-53 59 53	1-229	0.061	3	2.64	0.79	2.22	0.67	0.36	0.11	3.10	0.93	23.45	7.04	5.95	1.79	8.69	2.61
BLAST350-127	04 41 25.7	-53 28 21	4-201	0.109	3	1.62	0.49	5.17	1.55	0.00	0.00	2.83	0.85	11.47	3.44	3.35	1.01	1.49	0.45
FIS90-50	04 41 26.8	-53 28 34	1-197	0.109	3	1.24	0.37	0.63	0.19	0.00	0.00	0.19	0.06	4.44	1.33	2.62	0.78	1.16	0.35
FIS90-331 cl	04 41 29.3	-53 05 48	1-226	0.057	3	3.40	1.02	0.62	0.19	0.00	0.00	0.40	0.12	3.04	0.91	1.70	0.51	1.13	0.34
BLAST250-570	04 41 34.8	-53 27 14	4-202	0.110	3	0.40	0.12	0.36	0.11	0.00	0.00	0.00	0.00	1.28	0.39	1.35	0.41	0.84	0.25

continued on next page

Table B.1: **(continued)** Sources with redshifts $z \leq 0.345$, page 2 of 7. For notes, see page 217.

ID	RA (J2000)	Dec (J2000)	AAO Fibre	z_{spec}	Q	[OII] 3727Å S μJy	[OII] 3727Å ΔS μJy	Hβ 4861Å S μJy	Hβ 4861Å ΔS μJy	[OIII] 4958Å S μJy	[OIII] 4958Å ΔS μJy	[OIII] 5007Å S μJy	[OIII] 5007Å ΔS μJy	Hα 6563Å S μJy	Hα 6563Å ΔS μJy	[NII] 6582Å S μJy	[NII] 6582Å ΔS μJy	[SII] 6716Å S μJy	[SII] 6716Å ΔS μJy
FIS90-97	04 41 39.0	-53 54 21	1-162	0.045	3	3.61	1.08	0.00	0.00	0.00	0.00	0.39	0.12	1.76	0.53	1.74	0.52	0.70	0.21
FIS90-1848	04 41 39.9	-52 56 21	4-249	0.161	3	1.09	0.33	0.68	0.21	0.00	0.00	0.05	0.02	1.57	0.47	0.35	0.11	0.27	0.08
FIS90-561	04 41 41.4	-52 40 36	5-265	0.143	3	0.28	0.09	0.00	0.00	0.00	0.00	0.48	0.15	2.52	0.76	2.61	0.78	0.20	0.06
FIS90-177	04 41 52.5	-53 42 13	1-176	0.040	3	0.00	0.00	0.00	0.00	0.00	0.00	0.00	0.00	1.33	0.40	1.23	0.37	0.79	0.24
FIS90-1156	04 41 53.7	-53 55 12	1-156	0.057	3	0.00	0.00	0.21	0.06	0.00	0.00	0.00	0.00	1.74	0.52	0.74	0.22	0.00	0.00
FIS90-66 cl	04 41 55.7	-53 11 04	1-220	0.061	3	1.50	0.45	1.85	0.56	0.00	0.00	0.42	0.13	12.87	3.86	1.99	0.60	3.77	1.13
FIS90-1767 cl	04 41 57.3	-53 25 10	3-197	0.057	3	0.90	0.27	0.84	0.25	0.00	0.00	0.41	0.12	5.55	1.66	3.23	0.97	1.66	0.50
...	...	...	2-205	0.057	3	0.00	0.00	0.78	0.23	0.00	0.00	0.00	0.00	3.54	1.06	0.92	0.28	0.94	0.28
FIS90-2179 cl	04 42 00.8	-53 34 22	5-186	0.058	3	0.50	0.15	3.58	1.07	3.13	0.94	12.05	3.62	5.88	1.76	1.21	0.36	0.83	0.25
FIS90-731	04 42 02.8	-53 46 08	3-171	0.222	3	0.78	0.23	0.39	0.12	0.00	0.00	0.21	0.06	4.34	1.30	0.95	0.29	0.39	0.12
...	...	...	2-166	0.222	3	2.57	0.77	1.04	0.31	0.00	0.00	0.50	0.15	7.53	2.26	0.81	0.24	0.86	0.26
BLAST350-465	04 42 06.7	-53 47 28	4-159	0.136	3	3.11	0.93	3.02	0.91	1.06	0.32	5.47	1.64	4.84	1.45	1.56	0.47	0.58	0.17
FIS90-2057	04 42 08.2	-53 18 56	5-221	0.102	3	0.89	0.27	5.27	1.58	0.00	0.00	0.00	0.00	3.19	0.96	0.47	0.14	0.32	0.10
BLAST250-104	04 42 11.3	-54 10 11	4-133	0.070	3	1.38	0.42	3.33	1.00	0.46	0.14	5.17	1.55	6.32	1.90	2.68	0.80	0.76	0.23
FIS90-1222	04 42 11.8	-53 31 31	3-190	0.053	3	0.70	0.21	0.18	0.05	0.00	0.00	0.12	0.04	0.83	0.25	0.32	0.10	0.63	0.19
...	...	...	2-197	0.053	3	0.34	0.10	0.00	0.00	0.00	0.00	0.17	0.05	0.51	0.16	0.13	0.04	0.17	0.05
FIS90-108	04 42 12.6	-53 55 52	3-157	0.044	3	0.89	0.27	0.57	0.17	0.10	0.03	1.43	0.43	10.41	3.12	2.76	0.83	3.36	1.01
...	...	...	2-154	0.044	3	1.54	0.56	0.00	0.00	0.00	0.00	0.35	0.11	8.39	2.52	3.07	0.92	3.64	1.09
FIS90-2116	04 42 18.5	-53 48 30	5-155	0.123	3	0.91	0.27	0.00	0.00	0.00	0.00	0.00	0.00	2.07	0.62	0.70	0.21	0.95	0.29
BLAST250-302	04 42 21.8	-54 06 11	4-134	0.114	3	2.75	0.82	3.55	1.06	0.00	0.00	0.00	0.00	6.62	1.99	3.30	0.99	1.43	0.43
FIS90-505	04 42 25.9	-53 11 26	4-244	0.138	3	2.54	0.76	3.86	1.16	0.00	0.00	0.00	0.00	5.26	1.58	1.80	0.54	0.36	0.11
FIS90-545	04 42 27.5	-53 19 42	5-225	0.260	3	5.58	1.67	0.79	0.24	0.47	0.14	1.66	0.50	5.14	1.54	2.11	0.63	0.71	0.21
FIS90-366	04 42 27.6	-53 42 27	1-170	0.095	3	1.51	0.45	0.60	0.18	0.00	0.00	0.41	0.12	5.88	1.77	1.52	0.45	2.16	0.65
FIS90-27	04 42 31.2	-52 42 02	4-270	0.159	3	3.01	0.90	1.03	0.31	0.00	0.00	0.17	0.05	0.60	0.18	1.60	0.48	1.47	0.44
FIS90-371 cl	04 42 31.4	-53 35 28	1-182	0.059	3	2.49	0.75	1.50	0.45	0.00	0.00	0.68	0.20	11.52	3.46	2.03	0.61	3.78	1.13
BLAST500-160 cl	04 42 33.5	-54 09 22	4-131	0.060	3	1.07	0.32	3.15	0.94	0.17	0.05	2.69	0.81	7.57	2.27	5.87	1.76	1.09	0.33
FIS90-2017	04 42 33.9	-53 47 11	5-144	0.304	3	7.00	2.10	0.62	0.19	0.05	0.02	0.70	0.21	3.38	1.02	1.07	0.32	0.83	0.25
FIS90-868	04 42 36.0	-53 06 42	4-247	0.140	3	3.38	1.01	1.87	0.56	1.38	0.42	4.28	1.29	6.37	1.91	0.93	0.28	0.82	0.25
FIS90-1691	04 42 37.4	-53 16 01	3-228	0.043	3	1.34	0.40	0.00	0.00	0.00	0.00	1.03	0.31	2.38	0.72	4.58	1.37	1.45	0.43
...	...	...	2-228	0.043	3	0.77	0.23	0.00	0.00	0.00	0.00	0.98	0.30	0.61	0.18	3.72	1.12	1.24	0.37
FIS90-58	04 42 39.2	-54 13 49	5-128	0.055	3	2.57	0.77	11.07	3.32	0.00	0.00	4.16	1.25	22.53	6.76	13.43	4.03	2.07	0.62
FIS90-350	04 42 39.4	-52 40 29	4-271	0.174	3	7.49	2.25	2.98	0.90	0.00	0.00	0.09	0.03	0.00	0.00	9.00	2.70	4.13	1.24
BLAST350-208	04 42 40.8	-53 36 08	4-174	0.058	3	0.00	0.00	0.05	0.02	0.00	0.00	0.00	0.00	0.28	0.08	0.09	0.03	0.11	0.03
FIS90-1143	04 42 42.4	-53 40 45	5-172	0.137	3	1.82	0.55	1.62	0.49	0.00	0.00	0.00	0.00	2.96	0.89	2.37	0.71	0.05	0.02
FIS90-1744	04 42 44.2	-53 20 50	1-218	0.329	3	9.31	2.79	4.81	1.44	4.34	1.30	7.08	2.12	18.78	5.64	4.38	1.32	osr	
BLAST250-361	04 42 45.4	-53 36 55	4-156	0.088	3	2.61	0.78	1.36	0.41	0.75	0.22	2.49	0.75	3.36	1.01	0.30	0.09	0.78	0.23
FIS90-1737	04 42 45.8	-52 46 31	4-273	0.308	3	3.60	1.08	0.65	0.20	0.16	0.05	0.85	0.26	2.25	0.68	0.75	0.22	0.00	0.00
FIS90-591 cl	04 42 51.4	-53 24 44	3-208	0.058	3	0.87	0.26	0.25	0.08	0.00	0.00	0.00	0.00	1.48	0.45	0.64	0.19	0.41	0.12
...	...	...	2-202	0.057	3	0.00	0.00	0.00	0.00	0.00	0.00	0.00	0.00	0.97	0.29	0.41	0.12	0.23	0.07
BLAST500-266	04 42 57.3	-53 47 12	4-151	0.059	3	0.50	0.15	0.36	0.11	1.08	0.32	4.01	1.20	0.81	0.24	0.04	0.01	0.23	0.07
FIS90-1477	04 42 57.6	-53 53 21	5-143	0.111	3	3.43	1.03	1.23	0.37	0.00	0.00	0.00	0.00	1.48	0.44	0.63	0.19	0.47	0.14
FIS90-1145	04 42 58.4	-54 16 02	5-122	0.182	3	4.56	1.37	2.17	0.65	0.00	0.00	0.39	0.12	5.65	1.69	1.10	0.33	0.79	0.24
FIS90-1563	04 42 59.4	-53 46 47	3-170	0.223	3	0.50	0.15	0.28	0.08	0.07	0.02	0.07	0.02	2.92	0.88	1.00	0.30	0.12	0.04
...	...	...	2-158	0.223	3	0.69	0.21	0.00	0.00	0.00	0.00	0.00	0.00	2.20	0.66	1.26	0.38	0.13	0.04
BLAST350-346	04 42 59.4	-54 10 16	4-125	0.136	3	2.60	0.78	4.12	1.24	0.14	0.04	0.52	0.16	6.75	2.03	4.62	1.39	0.16	0.05
BLAST350-506	04 43 04.6	-54 14 04	4-122	0.137	3	1.13	0.34	1.99	0.60	0.00	0.00	0.98	0.29	3.21	0.96	1.44	0.43	0.00	0.00
FIS90-919 cl	04 43 04.8	-54 08 01	5-121	0.056	3	0.57	0.17	0.31	0.09	0.00	0.00	0.00	0.00	1.52	0.46	0.52	0.16	0.20	0.06
FIS90-621 cl	04 43 14.4	-54 07 08	1-139	0.056	3	2.26	0.68	1.60	0.48	0.00	0.00	0.94	0.28	6.89	2.07	2.78	0.83	2.54	0.76
FIS90-318	04 43 15.0	-53 05 25	5-260	0.121	3	1.26	0.38	1.12	0.33	0.00	0.00	0.24	0.07	4.65	1.39	2.18	0.66	0.51	0.15
FIS90-1196	04 43 15.3	-52 37 34	4-278	0.173	3	0.79	0.24	0.80	0.24	0.09	0.03	0.20	0.06	0.00	0.00	1.95	0.58	1.04	0.31

continued on next page

Table B.1: **(continued)** Sources with redshifts $z \leq 0.345$, page 3 of 7. For notes, see page 217.

ID	RA (J2000)	Dec (J2000)	AAO Fibre	z_{spec}	Q	[OII] 3727Å S μJy	[OII] 3727Å ΔS μJy	Hβ 4861Å S μJy	Hβ 4861Å ΔS μJy	[OIII] 4958Å S μJy	[OIII] 4958Å ΔS μJy	[OIII] 5007Å S μJy	[OIII] 5007Å ΔS μJy	Hα 6563Å S μJy	Hα 6563Å ΔS μJy	[NII] 6582Å S μJy	[NII] 6582Å ΔS μJy	[SII] 6716Å S μJy	[SII] 6716Å ΔS μJy
FIS90-1340	04 43 19.8	-54 01 43	2-134	0.112	3	0.85	0.26	0.56	0.17	0.00	0.00	0.00	0.00	4.39	1.32	0.70	0.21	0.37	0.11
...	...	...	3-134	0.112	3	0.00	0.00	0.00	0.00	0.00	0.00	0.00	0.00	4.14	1.24	1.31	0.39	1.58	0.47
FIS90-396	04 43 21.5	-53 39 33	1-171	0.092	3	1.39	0.42	1.12	0.34	0.14	0.04	1.00	0.30	6.19	1.86	3.39	1.02	2.04	0.61
FIS90-382	04 43 21.6	-52 34 47	4-280	0.158	3	4.30	1.29	5.81	1.74	0.11	0.03	1.46	0.44	3.34	1.00	4.81	1.44	3.31	0.99
FIS90-1274	04 43 26.6	-53 19 13	3-215	0.179	3	0.95	0.28	0.59	0.18	0.28	0.08	1.98	0.59	4.48	1.34	1.04	0.31	1.43	0.43
...	...	...	2-217	0.179	3	1.03	0.31	0.76	0.23	0.00	0.00	0.76	0.23	4.44	1.33	1.43	0.43	1.44	0.43
FIS90-599	04 43 28.2	-53 25 31	5-211	0.328	1	0.70	0.21	0.25	0.07	0.00	0.00	0.00	0.00	1.36	0.41	0.85	0.26	osr	
IRC15-540	04 43 30.0	-53 34 23	2-182	0.301	1	0.00	0.00	0.13	0.04	0.00	0.00	0.00	0.00	0.89	0.27	0.00	0.00	0.00	0.00
IRC24-76	04 43 30.3	-53 31 32	1-194	0.187	1	0.00	0.00	0.24	0.07	1.68	0.51	0.00	0.00	1.12	0.34	0.00	0.00	0.00	0.00
BLAST250-433	04 43 30.9	-52 59 35	4-275	0.115	3	2.10	0.63	1.25	0.37	0.00	0.00	0.00	0.00	3.15	0.95	2.58	0.78	0.46	0.14
IRC24-44	04 43 31.7	-53 36 04	1-185	0.204	3	8.21	2.46	1.70	0.51	0.37	0.11	2.92	0.88	12.31	3.70	2.18	0.65	1.97	0.59
FIS90-2222 cl	04 43 32.8	-53 29 06	5-204	0.057	3	0.62	0.19	1.22	0.37	0.00	0.00	0.00	0.00	1.84	0.55	0.78	0.23	1.12	0.34
IRC15-596	04 43 36.9	-53 35 56	4-167	0.205	3	0.83	0.25	0.05	0.02	0.07	0.02	0.42	0.13	0.75	0.23	0.08	0.02	0.17	0.05
BLAST500-253	04 43 39.7	-53 51 15	4-127	0.331	3	0.63	0.19	0.10	0.03	0.00	0.00	0.11	0.03	0.61	0.18	0.37	0.11	osr	
FIS90-383 cl	04 43 42.9	-53 39 38	1-167	0.058	3	1.18	0.36	1.31	0.39	0.16	0.05	0.73	0.22	8.75	2.63	9.34	2.80	3.75	1.13
IRC15-612	04 43 44.0	-53 37 03	3-180	0.280	1	0.00	0.00	0.00	0.00	0.00	0.00	0.00	0.00	1.87	0.56	0.65	0.20	0.20	0.06
...	...	...	2-173	0.280	1	0.00	0.00	0.00	0.00	0.00	0.00	0.00	0.00	0.55	0.16	0.25	0.08	0.00	0.00
FIS90-1933	04 43 47.5	-53 26 35	5-213	0.110	1	1.34	0.40	0.47	0.14	0.00	0.00	0.85	0.26	0.71	0.21	0.00	0.00	0.14	0.04
IRC24-183	04 43 48.6	-53 40 20	5-149	0.088	3	1.38	0.41	1.85	0.55	0.16	0.05	0.40	0.12	4.26	1.28	1.63	0.49	0.98	0.29
IRC24-20	04 43 48.6	-53 40 35	1-160	0.245	3	1.08	0.32	0.29	0.09	0.16	0.05	0.00	0.00	1.54	0.46	0.97	0.29	0.66	0.20
IRC15-470	04 43 49.7	-53 32 32	2-179	0.173	1	0.00	0.00	0.00	0.00	0.00	0.00	1.05	0.32	2.95	0.88	0.00	0.00	0.00	0.00
AZTEC-1	04 43 50.3	-53 43 06	2-151	0.035	1	0.00	0.00	0.00	0.00	0.00	0.00	0.00	0.00	2.23	0.67	0.00	0.00	0.00	0.00
FIS90-291 cl	04 43 51.2	-53 36 27	1-159	0.057	3	1.05	0.31	1.25	0.38	0.26	0.08	0.76	0.23	7.17	2.15	1.72	0.52	1.49	0.45
FIS90-409	04 43 51.2	-53 11 36	1-227	0.324	3	1.22	0.37	0.29	0.09	0.00	0.00	0.00	0.00	2.31	0.69	1.12	0.33	osr	
IRC15-581	04 43 53.8	-53 35 26	3-172	0.053	3	4.48	1.35	4.14	1.24	7.33	2.20	21.67	6.50	15.19	4.56	0.93	0.28	2.41	0.72
IRC15-709	04 43 54.7	-53 42 07	2-177	0.334	1	0.00	0.00	0.00	0.00	0.00	0.00	0.00	0.00	2.77	0.83	0.00	0.00	osr	
IRC15-529	04 43 55.7	-53 34 11	3-209	0.205	3	2.26	0.68	0.98	0.29	0.43	0.13	1.28	0.38	3.43	1.03	0.81	0.24	1.77	0.53
...	...	...	2-161	0.205	3	1.85	0.56	0.69	0.21	0.0	0.02	0.37	0.11	2.76	0.83	0.50	0.15	0.25	0.08
BLAST250-336	04 43 56.7	-54 26 44	4-109	0.119	3	1.96	0.59	0.78	0.24	0.17	0.05	0.77	0.23	2.52	0.76	1.54	0.46	0.42	0.12
FIS90-159	04 44 00.2	-52 36 20	4-289	0.127	3	2.01	0.60	1.72	0.52	0.21	0.06	2.14	0.64	5.80	1.74	2.19	0.66	0.46	0.14
IRC24-54	04 44 06.2	-53 34 28	2-157	0.128	1	0.71	0.21	0.17	0.05	0.00	0.00	0.00	0.00	0.64	0.19	0.00	0.00	0.09	0.03
FIS90-125	04 44 06.2	-53 00 44	1-258	0.043	3	3.76	1.13	4.50	1.35	0.40	0.12	0.67	0.20	16.89	5.07	3.51	1.05	6.77	2.03
AZTEC-13	04 44 07.7	-53 39 45	2-167	0.025	1	0.00	0.00	0.00	0.00	0.00	0.00	0.00	0.00	0.56	0.17	0.00	0.00	0.00	0.00
IRC15-180	04 44 07.7	-53 23 28	2-213	0.122	1	0.28	0.08	0.23	0.07	0.00	0.00	0.00	0.00	0.66	0.20	0.00	0.00	0.00	0.00
FIS90-751	04 44 08.4	-52 50 58	4-287	0.139	3	7.69	2.31	7.05	2.12	3.70	1.11	15.58	4.67	27.53	8.26	14.40	4.32	1.90	0.57
AZTEC- 7	04 44 10.6	-53 46 02	3-133	0.277	3	0.19	0.06	0.46	0.14	0.15	0.05	0.35	0.10	2.81	0.84	0.55	0.16	0.50	0.15
...	...	...	2-145	0.277	2	0.00	0.00	0.59	0.18	0.00	0.00	0.00	0.00	2.43	0.73	0.65	0.20	0.28	0.08
IRC15-703	04 44 12.0	-53 42 11	4-128	0.261	3	3.80	1.14	0.28	0.08	0.00	0.00	0.08	0.02	1.19	0.36	0.17	0.05	0.55	0.17
IRC15-680	04 44 12.2	-53 40 54	4-132	0.201	3	2.26	0.68	0.15	0.04	0.00	0.00	0.07	0.02	1.95	0.59	0.40	0.12	0.00	0.00
IRC15-207	04 44 14.3	-53 25 15	2-210	0.132	1	0.00	0.00	0.00	0.00	0.00	0.00	0.00	0.00	0.99	0.30	0.00	0.00	0.00	0.00
FIS90-334 cl	04 44 15.4	-52 00 21	4-286	0.061	3	2.25	0.68	11.52	3.46	0.78	0.23	7.30	2.19	31.96	9.59	13.06	3.92	4.97	1.49
IRC24-46	04 44 16.8	-53 36 05	3-174	0.089	3	1.25	0.38	0.07	0.02	0.00	0.00	0.00	0.00	1.20	0.36	0.73	0.22	0.14	0.04
...	...	...	1-137	0.089	1	0.00	0.00	0.00	0.00	0.00	0.00	0.00	0.00	0.90	0.27	0.71	0.21	0.00	0.00
...	...	...	2-171	0.089	3	0,.65	0.19	0.00	0.00	0.00	0.00	0.23	0.07	0.92	0.28	0.67	0.20	0.16	0.05
FIS90-487	04 44 19.6	-53 26 02	1-190	0.208	3	1.28	0.38	0.47	0.14	0.91	0.27	3.44	1.03	3.48	1.05	0.66	0.20	0.79	0.24
IRC15-233	04 44 20.0	-53 25 54	2-196	0.208	3	1.07	0.32	0.72	0.22	0.00	0.00	0.33	0.10	2.37	0.71	1.44	0.43	0.83	0.25
BLAST500-190	04 44 20.3	-53 35 02	5- 208	0.193	1	0.00	0.00	0.00	0.00	0.00	0.00	0.00	0.00	3.38	1.01	0.00	0.00	0.07	0.02
FIS90-576	04 44 22.2	-52 44 05	1-278	0.123	3	5.03	1.51	2.30	0.69	0.00	0.00	1.94	0.58	18.70	5.61	14.97	4.49	3.66	1.10
IRC15-218	04 44 22.2	-53 25 25	2- 242	0.316	1	0.11	0.03	0.00	0.00	0.00	0.00	0.00	0.00	1.27	0.38	0.00	0.00	osr	
IRC15-168	04 44 23.5	-53 23 35	3-256	0.327	3	0.50	0.15	0.40	0.12	0.00	0.00	0.25	0.08	2.42	0.73	0.90	0.27	osr	

continued on next page

Table B.1: **(continued)** Sources with redshifts $z \leq 0.345$, page 4 of 7. For notes, see page 217.

ID	RA (J2000)	Dec (J2000)	AAO Fibre	z_{spec}	Q	[OII] 3727Å S μJy	[OII] 3727Å ΔS μJy	Hβ 4861Å S μJy	Hβ 4861Å ΔS μJy	[OIII] 4958Å S μJy	[OIII] 4958Å ΔS μJy	[OIII] 5007Å S μJy	[OIII] 5007Å ΔS μJy	Hα 6563Å S μJy	Hα 6563Å ΔS μJy	[NII] 6582Å S μJy	[NII] 6582Å ΔS μJy	[SII] 6716Å S μJy	[SII] 6716Å ΔS μJy
IRC24-79	04 44 27.4	-53 31 17	2-218	0.191	1	0.00	0.00	0.00	0.00	0.00	0.00	0.00	0.00	0.27	0.08	0.00	0.00	0.00	0.00
AZTEC-11	04 44 32.7	-53 41 36	3-139	0.165	3	2.06	0.62	0.22	0.06	0.00	0.00	0.00	0.00	1.26	0.37	0.67	0.20	0.74	0.22
...	...	...	2-126	0.165	3	0.60	0.18	0.94	0.28	0.00	0.00	0.00	0.00	1.08	0.32	0.64	0.19	0.25	0.07
IRC15-229	04 44 32.7	-53 25 38	3-196	0.053	3	4.40	1.32	0.95	0.28	0.35	0.10	1.33	0.40	3.95	1.18	1.41	0.42	2.39	0.72
...	...	...	2-253	0.053	3	1.80	0.54	0.76	0.20	0.26	0.08	0.74	0.22	3.45	1.04	0.64	0.19	2.27	0.68
AZTEC-14	04 44 34.4	-53 35 32	2-137	0.039	1	0.00	0.00	0.00	0.00	0.00	0.00	0.06	0.02	0.23	0.07	0.00	0.00	0.00	0.00
BLAST350-23	04 44 34.7	-54 09 19	4-105	0.111	3	0.19	0.06	1.00	0.30	0.00	0.00	0.39	0.12	2.91	0.87	1.11	0.33	0.83	0.25
FIS90-709	04 44 36.0	-52 52 43	4-288	0.149	3	1.36	0.41	2.41	0.72	0.00	0.00	0.00	0.00	8.58	2.58	3.44	1.03	1.59	0.48
FIS90-421	04 44 36.3	-53 09 35	1-239	0.044	3	0.35	0.10	1.12	0.34	0.00	0.00	0.23	0.07	5.70	1.71	0.21	0.06	2.64	0.79
FIS90-179	04 44 36.7	-53 46 33	1-140	0.164	3	2.38	0.71	1.81	0.54	1.07	0.32	0.50	0.15	3.42	1.03	3.18	0.95	1.47	0.44
BLAST500-74	04 44 37.8	-54 43 32	4-106	0.276	3	1.99	0.60	0.37	0.11	0.00	0.00	0.54	0.16	1.38	0.42	0.95	0.28	0.80	0.24
IRC15-268	04 44 38.5	-53 27 12	2-201	0.204	3	2.13	0.64	0.14	0.04	0.00	0.00	0.00	0.00	2.21	0.66	0.26	0.08	0.36	0.11
IRC15-492	04 44 40.7	-53 33 18	4-153	0.145	3	0.54	0.16	0.29	0.09	0.08	0.02	0.23	0.07	0.94	0.28	0.08	0.02	0.48	0.14
FIS90-2202	04 44 40.9	-53 15 26	4-259	0.170	3	1.49	0.45	0.59	0.18	0.00	0.00	0.00	0.00	4.64	1.39	2.16	0.65	1.31	0.39
FIS90-251	04 44 41.4	-53 04 02	5-287	0.195	3	0.93	0.28	0.00	0.00	0.00	0.00	0.00	0.00	0.80	0.24	0.62	0.18	0.00	0.00
FIS90-692 cl	04 44 43.9	-53 55 39	1-130	0.206	1	0.00	0.00	0.18	0.06	0.00	0.00	0.00	0.00	1.29	0.39	0.00	0.00	0.00	0.00
FIS90-1085	04 44 44.5	-52 40 14	4-294	0.280	3	2.59	0.78	1.28	0.39	0.00	0.00	0.43	0.13	8.04	2.41	1.82	0.55	1.44	0.43
IRC15-187	04 44 45.1	-53 24 17	5-220	0.192	1	0.00	0.00	0.00	0.00	0.00	0.00	0.00	0.00	1.53	0.46	0.00	0.00	0.00	0.00
IRC15-617	04 44 45.9	-53 37 25	4-53	0.205	3	4.64	1.39	0.60	0.18	0.25	0.08	1.38	0.41	3.96	1.19	0.90	0.27	0.47	0.14
IRC24-1	04 44 46.9	-53 47 08	1-136	0.222	2	0.64	0.19	0.22	0.07	0.00	0.00	0.03	0.01	1.07	0.32	0.30	0.09	0.08	0.02
...	...	...	2-128	0.223	2	0.00	0.00	0.00	0.00	0.00	0.00	0.00	0.00	1.04	0.31	1.34	0.40	0.00	0.00
IRC24-147	04 44 47.1	-53 21 46	1-201	0.195	3	3.81	1.14	1.30	0.39	1.87	0.56	12.23	3.67	5.70	1.71	2.38	0.71	1.02	0.31
IRC24-27	04 44 47.3	-53 38 21	1-163	0.183	1	0.00	0.00	0.00	0.00	0.00	0.00	0.00	0.00	0.42	0.13	0.11	0.03	0.00	0.00
IRC15-140	04 44 49.2	-53 22 13	4-252	0.281	3	2.07	0.62	0.37	0.11	0.00	0.00	0.44	0.13	2.73	0.82	0.26	0.08	0.00	0.00
FIS90-636	04 44 51.1	-54 12 46	5-106	0.071	3	0.94	0.28	0.68	0.21	0.00	0.00	0.85	0.26	1.34	0.40	0.47	0.14	0.24	0.07
IRC24-165	04 44 53.5	-53 18 47	1-251	0.281	3	0.66	0.20	0.21	0.06	0.00	0.00	0.09	0.03	2.78	0.83	1.35	0.40	0.64	0.19
IRC15-460	04 44 54.8	-53 32 25	3-140	0.165	3	1.05	0.31	0.34	0.10	0.15	0.05	0.43	0.13	1.00	0.30	0.34	0.10	0.52	0.16
IRC15-176	04 44 56.8	-53 23 51	2-243	0.281	3	2.50	0.75	0.49	0.15	0.14	0.04	0.61	0.18	2.72	0.82	0.14	0.04	1.03	0.31
IRC24-31	04 44 58.2	-53 38 06	3-126	0.222	3	0.71	0.21	0.36	0.11	0.06	0.02	0.45	0.13	2.21	0.66	0.50	0.15	0.50	0.15
...	...	...	1-165	0.222	3	0.96	0.29	0.17	0.05	0.14	0.04	0.15	0.05	1.00	0.30	0.46	0.14	0.24	0.07
IRC24-131	04 45 00.0	-53 24 33	1-223	0.070	3	13.91	4.18	4.31	1.29	3.93	1.18	14.03	4.21	17.33	5.20	1.44	0.43	1.58	0.47
BLAST350-75	04 45 08.6	-54 18 23	4-97	0.040	3	osr		6.97	2.09	0.42	0.13	1.85	0.55	14.23	4.27	1.21	0.36	1.49	0.45
IRC15-547	04 45 09.3	-53 34 44	2-85	0.051	1	0.00	0.00	0.00	0.00	0.00	0.00	0.00	0.00	0.34	0.10	0.00	0.00	0.07	0.02
FIS90-1978	04 45 10.7	-52 45 43	4-297	0.145	3	0.46	0.14	0.42	0.13	0.00	0.00	0.00	0.00	2.85	0.86	2.53	0.76	2.45	0.74
FIS90-563	04 45 11.2	-53 59 37	1-113	0.055	3	2.05	0.62	2.10	0.63	0.38	0.11	1.58	0.48	11.05	3.32	2.77	0.83	1.54	0.46
FIS90-1009	04 45 11.7	-52 33 29	5-305	0.110	3	0.87	0.26	2.40	0.72	0.53	0.16	3.13	0.94	3.17	0.95	1.35	0.40	1.09	0.33
IRC15-370	04 45 12.3	-53 30 10	3-271	0.180	3	0.81	0.24	0.27	0.08	0.07	0.02	0.27	0.08	1.87	0.56	1.03	0.31	0.21	0.06
...	...	...	2-203	0.180	2	0.00	0.00	0.00	0.00	0.00	0.00	0.00	0.00	2.21	0.66	0.31	0.09	0.55	0.17
IRC15-172	04 45 12.4	-53 23 35	3-262	0.281	3	1.02	0.31	0.80	0.24	0.39	0.12	1.01	0.30	4.75	1.43	2.21	0.66	1.39	0.42
IRC24-9	04 45 13.1	-53 43 51	2-105	0.165	1	0.67	0.20	0.88	0.26	0.00	0.00	0.67	0.20	2.46	0.74	1.32	0.40	0.86	0.26
IRC24-7	04 45 14.7	-53 44 29	1-124	0.311	3	0.44	0.13	0.00	0.00	0.20	0.06	0.07	0.02	2.57	0.77	1.06	0.32	0.18	0.05
BLAST500-75	04 45 17.4	-53 19 26	4-308	0.195	3	3.96	1.19	0.77	0.23	0.31	0.09	3.00	0.90	10.97	3.29	1.02	0.31	2.90	0.87
FIS90-2266	04 45 21.6	-54 03 18	4-93	0.071	3	0.86	0.26	1.58	0.47	0.00	0.00	0.71	0.21	2.98	0.89	2.25	0.68	0.57	0.17
FIS90-1712	04 45 26.3	-53 48 09	4-88	0.108	3	1.06	0.32	0.81	0.24	1.88	0.56	4.23	1.27	1.08	0.32	0.02	0.01	0.06	0.02
FIS90-1011	04 45 28.8	-52 42 07	1-290	0.055	3	0.50	0.15	0.00	0.00	0.00	0.00	0.49	0.15	1.86	0.56	1.19	0.36	0.49	0.15
FIS90-118	04 45 29.7	-53 08 25	1-288	0.045	3	1.50	0.45	0.00	0.00	0.00	0.00	1.09	0.33	1.21	0.36	2.11	0.63	0.69	0.21
IRC24-148	04 45 30.3	-53 21 32	3-229	0.327	3	1.99	0.60	0.61	0.18	0.97	0.29	4.94	1.48	3.80	1.14	1.95	0.58	osr	
...	...	...	2-245	0.327	3	0.21	0.06	0.21	0.06	0.42	0.13	2.99	0.90	4.82	1.45	4.13	1.24	osr	
...	...	...	1-267	0.327	2	1.67	0.50	0.00	0.00	1.36	0.41	2.57	0.77	5.30	1.59	3.90	1.17	osr	
IRC24-74	04 45 31.1	-53 32 23	1-97	0.291	3	0.10	0.03	0.30	0.09	0.07	0.02	0.09	0.03	2.99	0.90	1.32	0.40	0.22	0.07

continued on next page

Table B.1: **(continued)** Sources with redshifts $z \leq 0.345$, page 5 of 7. For notes, see page 217.

ID	RA (J2000)	Dec (J2000)	AAO Fibre	z_{spec}	Q	[OII] 3727Å S μJy	[OII] 3727Å ΔS μJy	Hβ 4861Å S μJy	Hβ 4861Å ΔS μJy	[OIII] 4958Å S μJy	[OIII] 4958Å ΔS μJy	[OIII] 5007Å S μJy	[OIII] 5007Å ΔS μJy	Hα 6563Å S μJy	Hα 6563Å ΔS μJy	[NII] 6582Å S μJy	[NII] 6582Å ΔS μJy	[SII] 6716Å S μJy	[SII] 6716Å ΔS μJy
FIS90-1835	04 45 32.5	-54 02 11	1-122	0.121	3	7.32	2.20	1.18	0.35	8.11	2.43	43.89	13.17	6.10	1.83	5.84	1.75	2.44	0.73
FIS90-406	04 45 38.4	-52 30 37	5-307	0.123	3	0.97	0.29	1.65	0.50	0.00	0.00	0.00	0.00	9.44	2.83	5.48	1.65	1.20	0.36
FIS90-164	04 45 38.6	-53 47 28	1-117	0.290	3	0.26	0.08	0.52	0.16	0.00	0.00	0.10	0.03	5.45	1.64	3.25	0.98	0.61	0.18
IRC15-546	04 45 38.8	-53 34 41	4-67	0.315	3	1.50	0.45	0.66	0.20	0.31	0.09	1.21	0.36	2.67	0.80	0.23	0.07	1.24	0.37
IRC15-66	04 45 39.0	-53 19 32	3-325	0.169	3	0.56	0.17	0.25	0.07	0.00	0.00	0.00	0.00	2.01	0.60	1.08	0.32	1.18	0.35
...	...	...	2-333	0.169	3	0.00	0.00	0.00	0.00	0.00	0.00	0.00	0.00	1.86	0.56	1.56	0.47	0.39	0.12
FIS90-507	04 45 41.1	-53 52 47	1-119	0.237	3	1.11	0.33	1.34	0.40	1.02	0.31	4.56	1.37	16.83	5.05	10.23	3.07	2.19	0.66
FIS90-585	04 45 45.0	-53 56 53	1-116	0.056	3	4.13	1.24	2.86	0.86	0.00	0.00	0.46	0.14	12.96	3.89	5.13	1.54	2.02	0.61
IRC15-286	04 45 52.9	-53 27 41	2-254	0.117	1	0.00	0.00	0.12	0.04	0.00	0.00	0.00	0.00	0.95	0.28	0.00	0.00	0.00	0.00
FIS90-1103	04 45 55.7	-52 46 48	1-291	0.120	3	0.54	0.16	0.77	0.23	0.00	0.00	0.36	0.11	6.72	2.02	4.22	1.27	1.45	0.43
IRC15-265	04 45 58.5	-53 27 09	2-240	0.030	1	osr		0.42	0.13	0.00	0.00	0.00	0.00	1.57	0.47	0.00	0.00	0.00	0.00
FIS90-648	04 46 00.6	-54 09 04	4-86	0.166	3	6.59	1.98	1.66	0.50	0.00	0.00	0.40	0.12	2.48	0.74	2.16	0.65	0.66	0.20
IRC15-578	04 46 07.0	-53 35 23	2-72	0.289	3	0.49	0.15	0.10	0.03	0.00	0.00	0.00	0.00	1.62	0.49	0.96	0.29	0.46	0.14
IRC15-573	04 46 08.5	-53 35 18	3-72	0.290	3	1.87	0.56	0.98	0.30	0.17	0.05	0.69	0.21	4.87	1.46	1.67	0.50	1.40	0.42
IRC24-149	04 46 15.0	-53 21 18	1-235	0.284	1	0.00	0.00	0.05	0.02	0.19	0.06	0.60	0.18	0.40	0.12	0.00	0.00	0.02	0.00
FIS90-771	04 46 17.5	-53 11 56	1-275	0.181	3	5.15	1.54	1.22	0.37	0.49	0.15	1.90	0.57	14.57	4.37	2.49	0.75	3.71	1.11
IRC24-35	04 46 18.2	-53 37 48	1-85	0.223	3	0.45	0.14	2.02	0.61	0.00	0.00	0.58	0.17	13.36	4.01	7.19	2.16	2.48	0.74
IRC24-86	04 46 18.3	-53 30 23	1-73	0.223	3	0.47	0.14	0.04	0.02	0.00	0.00	0.00	0.00	1.54	0.46	2.03	0.61	0.24	0.07
IRC24-168	04 46 21.0	-53 18 29	2-278	0.073	3	0.00	0.00	0.00	0.00	0.00	0.00	0.00	0.00	0.75	0.23	0.00	0.00	0.00	0.00
IRC15-334	04 46 21.0	-53 28 57	3-54	0.187	3	0.70	0.21	0.28	0.08	0.00	0.00	0.15	0.04	1.87	0.56	0.20	0.06	0.47	0.14
FIS90-330	04 46 21.1	-52 37 51	1-297	0.109	3	0.00	0.00	0.36	0.11	0.00	0.00	0.00	0.00	5.38	1.61	2.32	0.70	3.83	1.15
IRC15-504	04 46 21.2	-53 33 35	3-42	0.229	3	1.64	0.49	1.19	0.36	0.00	0.00	0.21	0.06	6.07	1.82	4.38	1.31	0.55	0.16
IRC24-172	04 46 21.7	-53 17 07	1-298	0.201	3	0.87	0.26	0.45	0.14	0.00	0.00	1.53	0.46	7.86	2.36	3.56	1.07	1.61	0.48
FIS90-1590	04 46 21.9	-52 42 56	1-304	0.095	3	0.20	0.06	1.75	0.53	0.00	0.00	0.44	0.13	8.37	2.51	1.97	0.59	0.74	0.22
IRC15-376	04 46 23.8	-53 30 22	3-49	0.191	3	0.89	0.27	0.19	0.06	0.00	0.00	0.67	0.20	0.97	0.29	0.24	0.07	0.00	0.00
FIS90-330	04 46 24.1	-52 37 56	5-316	0.244	3	3.42	1.03	0.77	0.23	0.11	0.03	0.48	0.14	4.76	1.43	1.85	0.55	0.25	0.08
BLAST250-549	04 46 24.4	-53 07 57	5-335	0.305	1	0.00	0.00	0.00	0.00	0.00	0.00	0.00	0.00	1.40	0.42	0.00	0.00	0.05	0.02
BLAST500-422	04 46 27.9	-53 37 10	5-41	0.274	2	1.06	0.32	0.36	0.11	0.00	0.00	0.00	0.00	1.46	0.44	1.30	0.39	0.00	0.00
IRC24-121	04 46 29.4	-53 25 54	1-244	0.331	3	1.07	0.32	0.71	0.21	0.00	0.00	0.09	0.03	4.88	1.47	1.82	0.55	osr	
IRC24-107	04 46 30.5	-53 27 46	1-78	0.136	3	1.52	0.46	1.79	0.54	0.32	0.10	1.06	0.32	9.89	2.97	3.63	1.09	0.19	0.06
IRC24-152	04 46 32.4	-53 20 57	1-353	0.290	1	0.00	0.00	0.33	0.10	0.00	0.00	0.00	0.00	1.38	0.42	0.95	0.29	0.00	0.00
FIS90-1925	04 46 32.9	-53 03 25	5-326	0.045	3	0.61	0.18	2.29	0.69	1.37	0.41	2.14	0.64	8.02	2.41	3.36	1.01	3.11	0.93
IRC15-216	04 46 35.3	-53 25 23	3-280	0.211	3	0.97	0.29	0.52	0.16	0.00	0.00	0.16	0.05	1.80	0.54	1.52	0.46	0.41	0.12
...	...	...	2-277	0.211	2	0.14	0.04	0.00	0.00	0.00	0.00	0.00	0.00	3.70	1.11	1.73	0.52	0.66	0.20
IRC15-255	04 46 35.5	-53 26 33	3-376	0.206	3	0.75	0.22	0.81	0.24	0.00	0.00	0.00	0.00	2.26	0.68	1.56	0.47	0.43	0.13
IRC15-507	04 46 37.2	-53 33 37	5-24	0.201	1	0.00	0.00	0.00	0.00	0.00	0.00	0.00	0.00	1.32	0.40	0.00	0.00	0.32	0.09
IRC15-27	04 46 39.3	-53 17 20	4-357	0.055	3	0.00	0.00	0.30	0.09	0.00	0.00	0.18	0.05	2.30	0.69	0.77	0.23	0.49	0.15
IRC24-144	04 46 40.3	-53 22 13	2-274	0.113	1	0.00	0.00	0.00	0.00	0.00	0.00	0.00	0.00	1.26	0.38	0.00	0.00	0.00	0.00
FIS90-182	04 46 40.7	-52 54 56	1-302	0.120	3	0.00	0.00	0.00	0.00	0.00	0.00	0.00	0.00	3.32	1.00	4.56	1.37	0.34	0.10
FIS90-1122	04 46 44.3	-54 07 56	5-78	0.320	3	1.46	0.44	0.34	0.10	0.00	0.00	0.25	0.08	2.77	0.83	0.98	0.30	0.18	0.05
IRC24-80	04 46 45.8	-53 31 23	1-87	0.284	3	0.40	0.12	0.63	0.19	0.00	0.00	0.00	0.00	4.68	1.41	6.62	1.99	0.63	0.19
IRC15-280	04 46 48.0	-53 27 29	4-367	0.281	3	0.45	0.13	0.40	0.12	0.22	0.07	1.37	0.41	1.83	0.55	0.25	0.07	0.10	0.03
IRC15-39	04 46 49.9	-53 18 10	4-358	0.282	3	0.95	0.29	0.09	0.03	0.00	0.00	0.19	0.06	2.35	0.71	0.47	0.14	0.18	0.06
FIS90-970	04 46 54.6	-52 38 28	5-323	0.094	3	1.56	0.47	1.45	0.43	0.42	0.13	1.34	0.40	4.63	1.39	1.96	0.59	2.98	0.90
FIS90-2035	04 46 55.0	-52 46 07	5-325	0.136	3	0.07	0.02	0.00	0.00	0.00	0.00	0.00	0.00	3.01	0.90	1.74	0.52	0.06	0.02
FIS90-942	04 46 55.7	-53 24 13	1-328	0.125	3	1.90	0.57	0.95	0.29	0.00	0.00	0.13	0.04	5.44	1.63	1.32	0.40	2.49	0.75
FIS90-1354	04 46 57.9	-53 13 35	1-305	0.069	3	1.61	0.48	0.28	0.08	0.00	0.00	0.00	0.00	4.58	1.38	1.32	0.40	1.00	0.30
BLAST250-209	04 46 58.8	-52 42 48	4-324	0.071	3	0.44	0.13	1.24	0.37	0.00	0.00	0.47	0.14	6.36	1.91	1.26	0.38	2.50	0.75
FIS90-637	04 47 00.1	-53 00 40	5-343	0.225	3	4.81	1.44	0.59	0.18	0.00	0.00	0.41	0.12	5.99	1.80	2.32	0.70	0.00	0.00
FIS90-378	04 47 01.1	-53 50 21	1-90	0.227	3	0.43	0.13	1.36	0.41	0.00	0.00	1.01	0.30	10.10	3.03	5.78	1.74	1.79	0.54

continued on next page

Table B.1: **(continued)** Sources with redshifts $z \leq 0.345$, page 6 of 7. For notes, see page 217.

ID	RA (J2000)	Dec (J2000)	AAO Fibre	z_{spec}	Q	[OII] 3727Å S μJy	[OII] 3727Å ΔS μJy	Hβ 4861Å S μJy	Hβ 4861Å ΔS μJy	[OIII] 4958Å S μJy	[OIII] 4958Å ΔS μJy	[OIII] 5007Å S μJy	[OIII] 5007Å ΔS μJy	Hα 6563Å S μJy	Hα 6563Å ΔS μJy	[NII] 6582Å S μJy	[NII] 6582Å ΔS μJy	[SII] 6716Å S μJy	[SII] 6716Å ΔS μJy
IRC24-47	04 47 06.9	-53 35 40	1-81	0.276	1	0.89	0.27	0.13	0.04	0.00	0.00	0.14	0.04	0.74	0.22	0.39	0.12	0.00	0.00
FIS90-35	04 47 07.6	-52 40 33	1-307	0.048	2	0.00	0.00	0.00	0.00	0.00	0.00	0.00	0.00	3.04	0.91	2.59	0.78	1.76	0.53
BLAST500-359	04 47 11.3	-53 03 00	4-341	0.180	3	0.55	0.17	0.00	0.00	0.00	0.00	0.00	0.00	3.26	0.98	1.38	0.41	0.86	0.26
IRC15-63	04 47 12.0	-53 19 22	5-372	0.343	3	0.91	0.27	0.40	0.12	0.19	0.06	0.89	0.27	0.87	0.26	0.75	0.23	osr	
IRC15-558	04 47 12.6	-53 34 54	4-39	0.194	3	0.55	0.16	0.13	0.04	0.00	0.00	0.12	0.04	1.36	0.41	0.10	0.03	0.43	0.13
IRC24-77	04 47 13.5	-53 31 37	1-33	0.274	2	0.00	0.00	0.00	0.00	0.05	0.01	0.00	0.00	0.59	0.18	0.00	0.00	0.00	0.00
IRC24-128	04 47 15.3	-53 24 59	1-299	0.180	3	0.58	0.17	0.10	0.03	0.00	0.00	0.00	0.00	1.74	0.52	0.63	0.19	0.53	0.16
FIS90-324	04 47 15.9	-52 59 19	1-308	0.139	3	5.30	1.59	3.73	1.12	2.83	0.85	3.90	1.17	25.04	7.51	5.22	1.57	2.29	0.69
IRC15-157	04 47 18.3	-53 23 03	3-388	0.161	3	0.00	0.00	0.00	0.00	0.00	0.00	0.00	0.00	0.55	0.16	0.00	0.00	0.22	0.06
IRC15-156	04 47 19.0	-53 22 51	2-376	0.282	3	0.64	0.19	0.20	0.06	0.00	0.00	0.09	0.03	3.72	1.12	2.59	0.78	0.60	0.18
IRC24-129	04 47 22.5	-53 24 53	1-378	0.223	3	0.00	0.00	0.29	0.09	0.00	0.00	0.00	0.00	7.47	2.24	5.76	1.73	0.64	0.19
IRC15-467	04 47 22.5	-53 32 22	2-36	0.314	1	0.00	0.00	0.23	0.07	0.00	0.00	0.00	0.00	1.46	0.44	0.00	0.00	0.51	0.15
FIS90-408	04 47 23.0	-52 42 59	1-312	0.116	3	1.82	0.55	0.95	0.29	0.00	0.00	0.28	0.08	9.29	2.79	4.83	1.45	3.56	1.07
FIS90-349	04 47 25.3	-53 34 08	1-55	0.069	3	0.54	0.16	0.54	0.16	0.00	0.00	0.00	0.00	6.32	1.90	4.27	1.28	1.35	0.41
BLAST500-79	04 47 25.6	-53 25 03	4-385	0.282	3	0.98	0.30	0.35	0.10	0.00	0.00	0.28	0.08	1.89	0.57	0.55	0.17	0.20	0.06
IRC24-101	04 47 26.3	-53 28 39	1-17	0.223	3	0.00	0.00	0.00	0.00	0.00	0.00	0.54	0.16	9.73	2.92	5.03	1.51	2.10	0.63
FIS90-651	04 47 27.3	-53 26 27	1-389	0.223	3	0.76	0.23	0.87	0.26	0.00	0.00	0.32	0.10	7.15	2.14	5.39	1.62	2.66	0.80
IRC15-294	04 47 35.1	-53 27 48	3-365	0.284	3	0.47	0.14	0.28	0.08	0.01	0.00	0.01	0.00	2.51	0.75	1.69	0.51	0.41	0.12
IRC15-389	04 47 35.5	-53 30 31	5-16	0.207	3	0.84	0.25	0.29	0.09	0.00	0.00	0.00	0.00	2.10	0.63	0.62	0.19	0.26	0.08
IRC24-73	04 47 47.4	-53 32 13	1-35	0.190	3	0.84	0.25	0.54	0.16	0.26	0.08	0.38	0.11	4.38	1.31	1.45	0.44	0.99	0.30
IRC15-343	04 47 50.1	-53 29 09	3-375	0.162	3	0.64	0.19	0.33	0.10	0.00	0.00	0.17	0.05	2.19	0.66	0.17	0.05	0.50	0.15
FIS90-454	04 47 52.0	-53 22 26	1-376	0.047	3	0.69	0.21	1.34	0.40	0.00	0.00	0.33	0.10	4.55	1.37	6.18	1.85	0.97	0.29
FIS90-663	04 47 56.9	-53 13 34	1-306	0.181	3	1.32	0.40	1.08	0.32	0.19	0.06	0.53	0.16	11.70	3.51	3.63	1.09	2.76	0.83
IRC24-81	04 47 57.1	-53 30 47	1-2	0.276	3	1.58	0.47	1.33	0.40	0.00	0.00	0.00	0.00	10.51	3.15	5.22	1.57	2.45	0.73
FIS90-1219	04 47 59.3	-53 31 39	1-23	0.108	2	0.31	0.09	0.00	0.00	0.00	0.00	0.00	0.00	0.53	0.16	0.00	0.00	0.11	0.03
FIS90-190	04 48 00.9	-53 48 07	1-69	0.073	3	1.75	0.52	0.16	0.05	0.00	0.00	0.00	0.00	5.27	1.58	4.08	1.23	1.06	0.32
FIS90-267	04 48 01.4	-52 49 43	4-338	0.181	3	0.61	0.18	0.15	0.04	0.00	0.00	0.00	0.00	7.39	2.22	3.97	1.19	1.09	0.33
FIS90-6	04 48 02.6	-53 26 15	3-2	0.047	3	0.28	0.09	0.19	0.06	0.00	0.00	0.04	0.01	0.78	0.23	0.67	0.20	0.95	0.29
FIS90-2084	04 48 06.6	-52 47 32	4-337	0.058	3	0.18	0.05	1.90	0.57	0.00	0.00	1.63	0.49	7.59	2.28	1.63	0.49	2.29	0.69
FIS90-1624	04 48 08.4	-53 20 31	3-366	0.047	3	2.69	0.81	1.35	0.41	1.47	0.44	4.65	1.40	4.11	1.23	2.27	0.68	2.84	0.85
...	...	...	2-347	0.047	3	2.97	0.89	0.83	0.25	1.95	0.58	3.52	1.06	3.62	1.09	1.22	0.37	1.33	0.40
BLAST350-181	04 48 08.9	-54 10 54	5-62	0.036	3	osr		4.65	1.40	0.00	0.00	1.81	0.54	11.89	3.57	3.04	0.91	2.15	0.65
FIS90-343	04 48 09.0	-52 34 04	1-319	0.092	3	1.77	0.53	0.31	0.09	0.00	0.00	0.00	0.00	3.84	1.15	0.80	0.24	2.04	0.61
FIS90-1064	04 48 15.0	-53 41 54	3-18	0.054	3	1.53	0.46	1.55	0.47	0.23	0.07	1.62	0.48	6.94	2.08	2.56	0.77	2.31	0.69
...	...	...	2-23	0.055	3	2.10	0.63	0.85	0.25	0.00	0.00	0.61	0.18	4.75	1.43	1.45	0.44	1.69	0.51
FIS90-242	04 48 15.3	-52 39 04	3-320	0.325	3	0.42	0.13	0.25	0.08	0.00	0.00	0.26	0.08	1.31	0.39	0.34	0.10	osr	
...	...	...	2-320	0.324	3	2.11	0.63	0.66	0.20	0.00	0.00	0.52	0.16	3.21	0.96	1.76	0.53	osr	
FIS90-1384	04 48 24.8	-53 16 21	1-398	0.224	3	0.68	0.21	0.15	0.05	0.00	0.00	0.00	0.00	2.65	0.79	0.00	0.00	0.23	0.07
FIS90-84	04 48 30.6	-53 01 57	1-348	0.114	3	7.39	2.22	1.70	0.51	0.56	0.17	10.73	3.22	14.01	4.20	2.73	0.82	4.53	1.36
FIS90-1815	04 48 37.1	-53 35 16	1-8	0.340	3	0.51	0.15	1.33	0.40	1.23	0.37	3.97	1.19	8.04	2.41	6.16	1.85	osr	
FIS90-518	04 48 38.3	-53 26 38	1-5	0.136	1	0.42	0.13	0.00	0.00	0.00	0.00	0.00	0.00	3.39	1.02	11.60	3.48	abs	
FIS90-29	04 48 40.3	-53 54 44	1-62	0.039	3	2.18	0.66	1.03	0.31	0.00	0.00	0.00	0.00	18.80	5.64	17.59	5.28	2.82	0.85
FIS90-1455	04 48 47.7	-53 44 31	3-36	0.281	3	0.53	0.16	0.23	0.07	0.13	0.04	0.38	0.12	2.95	0.89	0.42	0.13	0.48	0.14
FIS90-410	04 48 48.5	-53 33 17	1-11	0.182	3	0.92	0.28	0.31	0.09	0.15	0.04	0.44	0.13	5.41	1.62	3.46	1.04	0.42	0.13
BLAST250-99	04 48 49.7	-52 45 33	4-343	0.182	3	2.30	0.69	0.31	0.09	0.00	0.00	0.04	0.01	9.15	2.75	4.62	1.39	1.59	0.48
FIS90-2233	04 48 52.8	-53 20 53	5-380	0.290	3	3.30	0.99	1.08	0.32	0.69	0.21	1.66	0.50	4.36	1.31	0.38	0.11	0.79	0.24
BLAST250-388	04 49 01.0	-53 46 01	5-28	0.188	1	0.00	0.00	0.11	0.03	0.00	0.00	0.00	0.00	9.31	2.79	0.29	0.09	0.80	0.24
FIS90-202	04 49 01.3	-53 41 11	5-22	0.053	3	0.60	0.18	0.00	0.00	0.00	0.00	3.46	1.04	1.03	0.31	4.58	1.38	1.84	0.55
...	...	...	1-58	0.053	3	0.00	0.00	0.28	0.08	0.00	0.00	0.00	0.00	1.62	0.49	0.90	0.27	0.20	0.06

continued on next page

Table B.1: **(continued)** Sources with redshifts $z \leq 0.345$, page 7 of 7. For notes, see page 217.

ID	RA (J2000)	Dec (J2000)	AAO Fibre	z_{spec}	Q	[OII] 3727Å S μJy	[OII] 3727Å ΔS μJy	Hβ 4861Å S μJy	Hβ 4861Å ΔS μJy	[OIII] 4958Å S μJy	[OIII] 4958Å ΔS μJy	[OIII] 5007Å S μJy	[OIII] 5007Å ΔS μJy	Hα 6563Å S μJy	Hα 6563Å ΔS μJy	[NII] 6582Å S μJy	[NII] 6582Å ΔS μJy	[SII] 6716Å S μJy	[SII] 6716Å ΔS μJy
FIS90-1661	04 49 02.3	-52 51 03	3-337	0.200	3	1.99	0.60	0.17	0.05	4.57	1.37	17.93	5.38	2.33	0.70	1.76	0.53	0.21	0.06
...	...	...	2-340	0.200	3	1.17	0.35	0.00	0.00	1.21	0.36	4.30	1.29	2.56	0.77	2.82	0.85	0.00	0.00
FIS90-109	04 49 03.2	-53 27 22	1-7	0.047	3	0.72	0.22	0.89	0.27	0.00	0.00	0.36	0.11	2.62	0.78	2.51	0.75	1.70	0.51
BLAST250-365	04 49 03.5	-54 06 43	5-53	0.057	3	0.00	0.00	1.53	0.46	0.00	0.00	0.00	0.00	4.12	1.24	0.61	0.18	1.26	0.38
BLAST250-574	04 49 03.7	-53 02 15	5-363	0.310	1	0.24	0.07	0.00	0.00	0.00	0.00	0.00	0.00	2.06	0.62	2.15	0.64	0.00	0.00
BLAST500-147	04 49 14.3	-52 52 24	4-349	0.055	3	0.45	0.13	1.06	0.32	0.00	0.00	1.49	0.45	3.72	1.12	0.43	0.13	0.58	0.17
FIS90-649	04 49 15.9	-53 38 02	1-38	0.181	3	1.64	0.49	1.41	0.42	0.00	0.00	0.51	0.15	9.28	2.78	2.60	0.78	1.57	0.47
FIS90-813	04 49 20.3	-53 52 08	1-47	0.055	3	2.24	0.67	1.34	0.40	0.30	0.09	0.85	0.26	4.97	1.49	1.59	0.48	1.78	0.54
FIS90-183	04 49 24.2	-53 11 27	1-360	0.192	3	3.18	0.95	2.10	0.63	0.00	0.00	1.66	0.50	19.57	5.87	4.67	1.40	2.65	0.80
FIS90-523	04 49 28.3	-53 26 01	1-399	0.143	3	1.26	0.38	1.58	0.47	0.00	0.00	0.51	0.15	11.84	3.55	2.09	0.63	1.18	0.35
FIS90-281	04 49 32.3	-52 59 35	1-343	0.069	3	16.56	4.97	6.21	1.86	1.08	0.32	12.00	3.60	30.91	9.28	12.50	3.75	10.75	3.23
FIS90-830	04 49 32.7	-53 48 23	1-45	0.073	3	0.81	0.24	0.44	0.13	0.00	0.00	0.00	0.00	4.98	1.49	1.74	0.52	0.51	0.15
FIS90-436	04 49 34.5	-52 56 48	1-344	0.144	3	0.11	0.03	0.64	0.19	0.00	0.00	0.00	0.00	9.09	2.73	3.97	1.19	0.65	0.20
FIS90-489	04 49 34.5	-52 46 34	5-348	0.077	3	1.26	0.38	3.69	1.11	1.47	0.44	2.72	0.82	13.11	3.93	9.45	2.84	3.42	1.03
FIS90-848	04 49 36.3	-53 32 12	1-29	0.058	3	2.87	0.86	1.82	0.55	0.30	0.09	0.48	0.14	11.32	3.40	1.85	0.56	2.71	0.81
FIS90-185	04 49 38.5	-53 00 58	3-354	0.114	3	1.54	0.46	1.19	0.36	0.00	0.00	0.33	0.10	11.55	3.47	3.61	1.08	1.68	0.50
...	...	...	2-364	0.114	3	0.57	0.17	0.13	0.04	0.00	0.00	0.00	0.00	8.36	2.51	4.01	1.20	1.51	0.45
FIS90-230	04 49 38.6	-53 45 15	1-48	0.107	3	0.00	0.00	0.00	0.00	0.00	0.00	0.00	0.00	0.00	0.00	1.51	0.45	4.16	1.25
FIS90-1359	04 49 40.6	-53 17 53	5-384	0.143	3	0.07	0.02	1.00	0.30	0.00	0.00	0.00	0.00	8.33	2.50	3.83	1.15	2.67	0.80
FIS90-814	04 49 45.9	-53 24 10	1-394	0.127	3	0.87	0.26	0.40	0.12	0.00	0.00	0.13	0.04	3.20	0.96	0.99	0.30	0.26	0.08
FIS90-226	04 49 46.1	-52 58 08	1-349	0.142	3	0.97	0.29	1.11	0.33	0.00	0.00	0.00	0.00	9.44	2.83	9.46	2.84	0.55	0.16
FIS90-175	04 49 47.7	-53 05 55	1-361	0.145	3	2.42	0.73	1.24	0.37	0.74	0.22	1.97	0.59	14.48	4.35	11.71	3.52	0.38	0.12
BLAST350-483	04 49 48.1	-52 57 47	4-361	0.118	3	1.00	0.30	0.29	0.09	0.17	0.05	0.35	0.11	4.26	1.28	4.01	1.20	0.53	0.16
FIS90-1405	04 49 48.7	-52 49 51	1-345	0.144	3	2.06	0.62	0.85	0.25	0.00	0.00	0.00	0.00	4.56	1.37	2.05	0.61	0.83	0.25
BLAST500-523	04 49 51.2	-52 59 36	4-363	0.019	3	osr		0.52	0.16	0.00	0.00	1.66	0.50	2.59	0.78	1.12	0.34	1.04	0.31
FIS90-980	04 49 52.6	-53 36 18	1-22	0.159	3	15.95	4.79	5.67	1.70	4.11	1.23	7.43	2.23	4.57	1.37	4.62	1.39	7.95	2.38
FIS90-2006	04 50 00.1	-52 50 48	5-356	0.166	1	1.17	0.35	0.44	0.13	0.00	0.00	0.00	0.00	1.07	0.32	1.26	0.38	0.64	0.19
FIS90-485	04 50 04.3	-52 56 34	1-346	0.055	3	3.20	0.96	1.91	0.57	0.33	0.10	1.63	0.49	15.66	4.70	3.94	1.18	9.22	2.77
FIS90-435	04 50 09.1	-52 50 22	3-347	0.047	3	0.25	0.07	0.00	0.00	0.00	0.00	0.00	0.00	1.06	0.32	1.01	0.30	0.40	0.12
FIS90-292	04 50 12.4	-53 40 24	1-31	0.182	3	0.71	0.21	0.64	0.19	0.00	0.00	0.28	0.08	9.54	2.86	5.49	1.65	1.79	0.54
BLAST250-270	04 50 18.1	-53 18 11	4-389	0.337	1	1.06	0.32	0.62	0.19	0.00	0.00	0.00	0.00	3.41	1.02	0.95	0.29	osr	
FIS90-168	04 50 19.8	-53 06 15	1-369	0.117	3	3.59	1.08	2.36	0.71	0.21	0.06	0.58	0.17	18.34	5.51	7.25	2.17	3.56	1.07
BLAST350-286	04 50 21.1	-53 05 52	4-372	0.115	3	0.79	0.24	0.45	0.14	0.00	0.00	0.19	0.06	4.16	1.25	1.04	0.31	1.90	0.57
FIS2008-1825	04 50 22.0	-52 53 51	5-360	0.168	3	0.26	0.08	0.20	0.06	0.00	0.00	0.00	0.00	2.24	0.67	1.11	0.33	0.00	0.00
FIS90-1410	04 50 32.1	-52 52 56	5-361	0.118	3	1.44	0.43	0.38	0.11	0.34	0.10	0.88	0.27	3.31	0.99	1.87	0.56	0.34	0.10
FIS90-514	04 50 38.1	-53 03 16	5-369	0.123	3	1.68	0.50	1.28	0.39	0.00	0.00	2.43	0.73	3.42	1.03	0.69	0.21	0.65	0.20
FIS90-38	04 50 46.8	-53 32 00	1-12	0.053	3	1.23	0.37	0.55	0.16	0.00	0.00	1.10	0.33	9.78	2.94	8.22	2.47	3.48	1.04
FIS90-21	04 50 55.5	-53 12 46	1-379	0.039	3	1.24	0.37	1.28	0.38	0.00	0.00	0.00	0.00	7.66	2.30	6.09	1.83	2.37	0.71
FIS90-842	04 50 56.0	-53 17 31	5-390	0.115	3	0.84	0.25	1.44	0.43	0.00	0.00	0.00	0.00	3.41	1.02	1.50	0.45	0.57	0.17
FIS90-764	04 51 01.9	-53 03 00	5-371	0.108	3	0.64	0.19	0.00	0.00	0.00	0.00	0.00	0.00	3.71	1.11	1.38	0.41	1.86	0.56
BLAST250-51	04 51 16.1	-53 02 20	5-374	0.039	3	osr		0.77	0.23	0.00	0.00	0.30	0.09	4.63	1.39	1.23	0.37	1.63	0.49
FIS90-48	04 51 19.0	-53 02 25	1-366	0.038	3	2.15	0.65	0.89	0.27	0.00	0.00	0.35	0.10	15.74	4.72	1.50	0.45	3.90	1.17
FIS90-300	04 51 24.1	-52 48 16	3-355	0.097	3	2.38	0.72	0.93	0.28	0.00	0.00	0.30	0.09	2.27	0.68	3.90	1.17	0.00	0.00
FIS90-1264	04 51 25.5	-53 47 32	1-30	0.178	3	9.72	2.92	6.58	1.97	9.04	2.71	15.38	4.61	34.97	10.49	3.11	0.93	4.91	1.47
FIS90-86	04 51 42.1	-53 45 11	3-25	0.021	3	1.45	0.43	0.00	0.00	0.00	0.00	0.56	0.17	1.37	0.41	1.72	0.52	0.51	0.15
...	...	...	1-27	0.021	3	0.00	0.00	0.13	0.04	0.00	0.00	0.00	0.00	1.38	0.41	1.81	0.54	0.00	0.00
...	...	...	2-25	0.022	2	0.00	0.00	0.00	0.00	0.00	0.00	0.00	0.00	2.76	0.83	2.20	0.66	1.22	0.37
FIS90-1884	04 51 42.9	-53 31 44	1-9	0.141	3	0.00	0.00	0.23	0.07	0.00	0.00	0.00	0.00	5.85	1.76	2.83	0.85	0.82	0.24
FIS90-239	04 52 20.4	-53 30 31	1-4	0.045	3	0.31	0.09	0.48	0.14	0.00	0.00	0.43	0.13	6.92	2.08	2.43	0.73	1.68	0.50
FIS90-2108	04 53 07.2	-53 29 17	1-6	0.316	1	0.00	0.00	0.00	0.00	0.00	0.00	0.00	0.00	0.68	0.20	0.00	0.00	0.00	0.00

Table B.2: Sources with redshifts $0.345 < z \leq 1.0$, page 1 of 2, in ADF-S. For notes, see page 217.

ID	RA (J2000)	Dec (J2000)	AAO Fibre	z_{spec}	Q	MgII 2798Å S μJy	MgII 2798Å ΔS μJy	[OII] 3727Å S μJy	[OII] 3727Å ΔS μJy	[NeIII] 3869Å S μJy	[NeIII] 3869Å ΔS μJy	Hγ 4340Å S μJy	Hγ 4340Å ΔS μJy	Hβ 4861Å S μJy	Hβ 4861Å ΔS μJy	[OIII] 4958Å S μJy	[OIII] 4958Å ΔS μJy	[OIII] 5007Å S μJy	[OIII] 5007Å ΔS μJy
FIS90-1735	04 42 52.3	-53 12 03	3-236	0.438	3	0.00	0.00	1.14	0.34	2.22	0.67	0.31	0.09	1.91	0.57	15.33	4.60	42.45	12.74
...	...	...	2-229	0.438	3	0.00	0.00	2.63	0.79	0.40	0.12	0.00	0.00	0.58	0.17	1.24	0.37	5.91	1.77
IRC24-56	04 43 11.8	-53 34 00	1-191	0.485	3	0.00	0.00	1.72	0.52	0.00	0.00	0.00	0.00	0.28	0.08	0.06	0.02	0.45	0.13
...	...	...	3-182	0.485	3	0.00	0.00	0.71	0.21	0.00	0.00	0.00	0.00	0.37	0.11	0.06	0.02	0.52	0.16
IRC15-491	04 43 15.1	-53 33 14	2-183	0.488	3	0.00	0.00	0.84	0.25	0.00	0.00	0.00	0.00	0.19	0.06	0.33	0.10	1.05	0.32
IRC24-48	04 43 45.4	-53 35 37	1-151	0.423	3	2.88	0.86	0.44	0.13	0.00	0.00	0.00	0.00	0.37	0.11	0.44	0.13	3.21	0.96
IRC15-606	04 43 46.8	-53 36 24	4-168	0.356	1	osr		1.47	0.44	0.00	0.00	0.00	0.00	0.67	0.20	0.00	0.00	0.24	0.07
IRC24-84	04 43 48.1	-53 30 30	1-202	0.591	1	0.00	0.00	0.51	0.15	0.00	0.00	0.00	0.00	0.09	0.03	0.13	0.04	0.59	0.18
IRC15-655	04 43 52.1	-53 39 03	2-181	0.537	3	0.00	0.00	0.00	0.00	0.00	0.00	0.00	0.00	1.23	0.37	0.00	0.00	0.33	0.10
AZTEC-5	04 43 54.5	-53 39 52	3-165	0.539	3	0.00	0.00	1.99	0.60	0.00	0.00	0.10	0.03	0.23	0.07	0.00	0.00	1.18	0.35
IRC24-83	04 43 59.7	-53 30 35	3-220	0.479	2	0.00	0.00	1.20	0.36	0.00	0.00	0.00	0.00	0.51	0.15	0.00	0.00	0.36	0.11
...	...	...	2-220	0.479	1	0.00	0.00	0.51	0.15	0.00	0.00	0.00	0.00	0.26	0.08	0.00	0.00	0.00	0.00
IRC15-707	04 44 00.3	-53 42 17	2-147	0.534	1	0.00	0.00	0.86	0.26	0.00	0.00	0.00	0.00	0.43	0.13	0.00	0.00	0.60	0.18
IRC24-23	04 44 06.2	-53 38 33	3-169	0.818	1	0.00	0.00	2.13	0.64	0.17	0.05	0.07	0.02	osr		osr		osr	
IRC24-104	04 44 09.2	-53 28 04	2-211	0.381	1	0.00	0.00	0.00	0.00	0.00	0.00	0.00	0.00	0.49	0.15	0.00	0.00	0.66	0.20
IRC24-63	04 44 21.7	-53 33 52	1-164	0.454	3	12.68	3.81	0.52	0.16	0.00	0.00	0.00	0.00	0.30	0.09	0.17	0.05	1.63	0.49
IRC24-12	04 44 21.9	-53 42 57	1-175	0.673	1	0.00	0.00	0.00	0.00	0.00	0.00	0.00	0.00	0.34	0.10	0.00	0.00	0.44	0.13
IRC24-66	04 44 23.0	-53 33 25	1-211	0.684	1	0.00	0.00	0.00	0.00	0.00	0.00	0.00	0.00	0.62	0.18	0.00	0.00	0.00	0.00
IRC24-33	04 44 24.4	-53 37 51	3-132	0.405	1	0.00	0.00	0.23	0.07	0.03	0.01	0.00	0.00	0.06	0.02	0.00	0.00	0.38	0.11
AZTEC-10	04 44 25.4	-53 48 07	3-129	0.575	3	0.00	0.00	1.96	0.59	0.00	0.00	0.32	0.10	0.41	0.12	0.00	0.00	0.20	0.06
IRC15-600	04 44 28.1	-53 36 07	2-174	0.405	3	0.00	0.00	0.34	0.10	0.00	0.00	0.00	0.00	0.59	0.18	0.00	0.00	0.81	0.24
IRC24-159	04 44 28.2	-53 20 19	3-244	0.376	1	0.00	0.00	1.24	0.37	0.00	0.00	0.00	0.00	0.36	0.11	0.00	0.00	0.00	0.00
IRC24-3	04 44 29.3	-53 46 32	1-133	0.642	3	2.94	0.88	0.00	0.00	0.21	0.06	0.82	0.25	0.00	0.00	0.72	0.22	5.61	1.68
BLAST250-230	04 44 32.9	-54 05 50	4-107	0.384	1	osr		2.40	0.72	0.00	0.00	0.00	0.00	0.34	0.10	0.00	0.00	0.00	0.00
IRC15-451	04 44 33.3	-53 32 04	3-191	0.405	3	0.18	0.05	0.97	0.29	0.00	0.00	0.08	0.03	0.58	0.17	0.00	0.00	0.28	0.08
IRC24-10	04 44 34.7	-53 43 47	3-146	0.825	1	0.00	0.00	1.54	0.46	0.10	0.03	0.15	0.05	osr		osr		osr	
IRC15-225	04 44 38.6	-53 25 33	3-247	0.564	3	0.00	0.00	2.70	0.81	0.32	0.10	0.18	0.06	0.00	0.00	1.00	0.30	4.96	1.49
IRC24-157	04 44 38.9	-53 20 17	1-225	0.488	1	0.00	0.00	0.00	0.00	0.00	0.00	0.51	0.15	0.16	0.05	0.00	0.00	0.00	0.00
IRC15-710	04 44 40.5	-53 42 52	3-127	0.549	3	abs		2.72	0.82	0.00	0.00	0.42	0.13	1.44	0.43	0.04	0.01	0.44	0.13
IRC24- 69	04 44 46.5	-53 33 14	1-144	0.732	3	0.00	0.00	0.00	0.00	0.00	0.00	0.00	0.00	0.00	0.00	0.25	0.08	1.98	0.59
IRC24-39	04 44 47.5	-53 37 13	1-155	0.602	1	0.00	0.00	0.00	0.00	0.00	0.00	0.00	0.00	0.14	0.04	0.00	0.00	0.00	0.00
IRC24-162	04 44 49.7	-53 19 22	3-233	0.583	3	0.00	0.00	1.40	0.42	0.00	0.00	0.00	0.00	0.75	0.22	0.48	0.14	0.85	0.25
...	...	...	1-245	0.583	3	0.00	0.00	2.24	0.67	0.00	0.00	0.00	0.00	0.62	0.19	0.00	0.00	0.99	0.30
IRC24-111	04 44 51.4	-53 27 14	1-224	0.472	3	32.51	9.76	3.29	0.99	1.51	0.45	7.05	2.12	8.87	2.66	3.75	1.13	18.62	5.59
IRC15-717	04 44 55.0	-53 43 40	4-104	0.448	1	0.00	0.00	2.24	0.67	0.45	0.13	0.00	0.00	0.13	0.04	0.01	0.00	0.21	0.06
IRC24-58	04 44 55.3	-53 34 06	3-144	0.732	3	0.00	0.00	0.71	0.21	0.00	0.00	0.09	0.03	0.52	0.16	0.70	0.21	1.80	0.54
...	...	...	1-154	0.732	2	0.00	0.00	0.53	0.16	0.00	0.00	0.00	0.00	1.29	0.39	0.49	0.15	1.54	0.46
IRC24-19	04 44 55.3	-53 41 01	1-180	0.444	3	0.00	0.00	0.39	0.12	0.00	0.00	0.00	0.00	0.62	0.19	0.64	0.19	3.58	1.08
FIS90-547	04 44 56.7	-53 15 30	3-264	0.393	3	0.00	0.00	1.26	0.38	0.00	0.00	0.00	0.00	0.63	0.19	0.00	0.00	0.23	0.07
IRC15-468	04 44 59.0	-53 32 32	3-87	0.403	3	0.00	0.00	2.47	0.74	0.00	0.00	0.33	0.10	0.76	0.23	0.14	0.04	1.10	0.33
...	...	...	2-216	0.403	3	0.00	0.00	1.71	0.51	0.00	0.00	0.26	0.08	0.89	0.27	0.00	0.00	1.40	0.42
FIS90-990	04 45 05.1	-54 07 41	1-118	0.403	1	0.00	0.00	0.16	0.05	0.00	0.00	0.00	0.00	0.23	0.07	0.00	0.00	0.23	0.07
IRC24-32	04 45 09.7	-53 37 52	1-114	0.577	3	0.00	0.00	0.17	0.05	0.00	0.00	0.00	0.00	0.00	0.00	0.00	0.00	1.48	0.44
IRC24-106	04 45 16.4	-53 28 06	3-267	0.474	3	0.00	0.00	0.64	0.19	0.00	0.00	0.01	0.00	0.54	0.16	0.24	0.07	0.55	0.16
...	...	...	2-279	0.475	1	0.00	0.00	0.63	0.19	0.00	0.00	0.00	0.00	0.80	0.24	0.00	0.00	0.00	0.00
IRC24-5	04 45 23.7	-53 45 00	1-127	0.548	1	0.00	0.00	0.22	0.07	0.00	0.00	0.00	0.00	0.20	0.06	0.01	0.00	0.01	0.00
IRC15-638	04 45 25.3	-53 38 12	3-67	0.498	1	0.00	0.00	0.00	0.00	0.00	0.00	0.00	0.00	0.12	0.04	0.00	0.00	0.00	0.00
IRC15-62	04 45 26.6	-53 19 22	2-227	0.521	3	0.00	0.00	1.04	0.31	0.13	0.04	0.00	0.00	0.34	0.10	0.20	0.06	0.75	0.23
IRC24-176	04 45 33.5	-53 16 39	3-286	0.380	3	0.00	0.00	1.59	0.48	0.00	0.00	0.24	0.07	1.29	0.39	0.14	0.04	0.66	0.20
...	...	...	1-264	0.380	3	0.00	0.00	0.82	0.24	0.00	0.00	0.00	0.00	2.43	0.73	0.10	0.03	0.96	0.29

continued on next page

Table B.2: **(continued)** Sources with redshifts $0.345 < z \leq 1.0$, page 2 of 2. For notes, see page 217.

ID	RA (J2000)	Dec (J2000)	AAO Fibre	z_{spec}	Q	MgII 2798Å S μJy	MgII 2798Å ΔS μJy	[OII] 3727Å S μJy	[OII] 3727Å ΔS μJy	[NeIII] 3869Å S μJy	[NeIII] 3869Å ΔS μJy	Hγ 4340Å S μJy	Hγ 4340Å ΔS μJy	Hβ 4861Å S μJy	Hβ 4861Å ΔS μJy	[OIII] 4958Å S μJy	[OIII] 4958Å ΔS μJy	[OIII] 5007Å S μJy	[OIII] 5007Å ΔS μJy
IRC24-177	04 45 38.2	-53 15 54	2-309	0.710	3	0.00	0.00	0.31	0.09	0.00	0.00	0.05	0.01	0.52	0.15	0.00	0.00	0.54	0.16
IRC15-618	04 45 48.4	-53 37 27	3-103	0.451	3	0.00	0.00	2.99	0.90	0.00	0.00	0.00	0.00	0.58	0.17	0.05	0.02	0.84	0.25
IRC24-68	04 45 54.4	-53 33 05	3-46	0.404	3	0.68	0.20	1.04	0.31	0.00	0.00	0.29	0.09	0.94	0.28	0.08	0.02	0.25	0.08
...	...	...	1-61	0.404	2	0.00	0.00	1.75	0.53	0.00	0.00	0.00	0.00	2.36	0.71	0.00	0.00	1.23	0.37
IRC24-14	04 45 55.2	-53 42 23	1-109	0.421	3	3.56	1.07	1.99	0.60	0.00	0.00	0.38	0.11	0.90	0.27	0.40	0.12	0.78	0.23
FIS90-633	04 45 56.0	-53 16 34	1-280	0.361	3	0.00	0.00	14.25	4.28	3.91	1.17	2.49	0.75	2.87	0.86	23.62	7.09	87.66	26.31
IRC24-97	04 45 56.5	-53 29 00	1-77	0.376	3	0.00	0.00	2.32	0.70	0.00	0.00	0.00	0.00	0.19	0.06	0.00	0.00	0.16	0.05
IRC24-53	04 45 59.6	-53 34 43	1-129	0.548	2	0.00	0.00	0.68	0.20	0.00	0.00	0.00	0.00	0.65	0.19	0.00	0.00	1.01	0.30
...	...	...	2-69	0.548	1	0.00	0.00	0.00	0.00	0.00	0.00	0.00	0.00	0.51	0.15	0.00	0.00	0.29	0.09
IRC24-95	04 46 03.6	-53 29 09	3-248	0.575	3	0.00	0.00	3.24	0.97	0.07	0.02	0.51	0.15	0.94	0.28	0.14	0.04	0.27	0.08
...	...	...	1-84	0.574	3	0.00	0.00	2.68	0.81	0.00	0.00	0.17	0.05	0.89	0.27	0.20	0.06	1.33	0.40
IRC15-398	04 46 05.6	-53 30 44	3- 85	0.454	3	0.00	0.00	0.37	0.11	0.00	0.00	0.00	0.00	0.31	0.09	0.05	0.02	0.19	0.06
IRC24-24	04 46 06.4	-53 38 28	4-51	0.402	3	0.00	0.00	5.49	1.65	0.00	0.00	0.20	0.06	0.74	0.22	0.91	0.27	4.49	1.35
...	...	...	1-60	0.402	3	0.00	0.00	2.66	0.80	0.00	0.00	0.00	0.00	0.59	0.18	0.97	0.29	2.15	0.65
IRC24-113	04 46 19.4	-53 26 53	3-234	0.404	3	0.00	0.00	1.58	0.47	0.00	0.00	0.00	0.00	0.34	0.10	0.09	0.03	0.31	0.09
IRC24-145	04 46 20.9	-53 22 03	1-283	0.455	3	0.00	0.00	2.85	0.86	0.18	0.05	1.34	0.40	3.78	1.13	0.24	0.07	1.08	0.32
IRC15-190	04 46 26.1	-53 24 03	3-289	0.405	3	0.00	0.00	1.12	0.34	0.06	0.02	0.24	0.07	1.12	0.34	0.23	0.07	1.03	0.31
...	...	...	2-281	0.405	3	0.00	0.00	0.60	0.18	0.00	0.00	0.00	0.00	0.36	0.11	0.32	0.10	1.31	0.39
IRC15-293	04 46 27.2	-53 27 53	3-76	0.572	3	0.00	0.00	1.74	0.52	0.00	0.00	0.20	0.06	0.47	0.14	0.18	0.05	1.14	0.34
IRC15-36	04 46 42.0	-53 17 56	3-273	0.347	3	ost		1.74	0.52	0.45	0.14	0.06	0.02	1.11	0.33	0.42	0.13	2.85	0.85
IRC15-76	04 46 54.9	-53 20 05	3-10	0.356	1	ost		0.22	0.07	0.00	0.00	0.35	0.10	0.37	0.11	0.00	0.00	0.14	0.04
IRC15-301	04 47 01.3	-53 28 10	3-371	0.393	3	0.00	0.00	1.02	0.31	0.08	0.02	0.10	0.03	0.59	0.18	0.16	0.05	0.66	0.20
IRC15-69	04 47 04.8	-53 19 31	3-346	0.717	1	0.00	0.00	1.19	0.36	0.00	0.00	0.07	0.02	0.71	0.21	0.23	0.07	0.57	0.17
IRC24-93	04 47 08.4	-53 29 34	1-36	0.449	3	0.00	0.00	1.17	0.35	0.00	0.00	0.00	0.00	0.57	0.17	0.00	0.00	1.31	0.39
IRC24-122	04 47 08.3	-53 25 51	1-311	0.355	3	7.03	2.11	0.00	0.00	0.00	0.00	0.56	0.17	0.00	0.00	0.33	0.10	4.32	1.30
IRC15-500	04 47 13.5	-53 33 28	3-84	0.530	1	0.00	0.00	0.43	0.13	0.00	0.00	0.01	0.00	0.33	0.10	0.16	0.05	0.34	0.10
BLAST250-596	04 47 14.1	-52 53 32	4-333	0.393	3	ost		3.27	0.98	0.00	0.00	0.00	0.00	1.14	0.34	0.00	0.00	1.64	0.49
IRC24-136	04 47 20.3	-53 23 48	1-377	0.473	3	0.00	0.00	2.90	0.87	0.00	0.00	0.92	0.28	1.41	0.42	0.51	0.15	1.04	0.31
IRC15-497	04 47 21.7	-53 33 26	3-16	0.356	3	0.00	0.00	0.87	0.26	0.00	0.00	0.00	0.00	0.56	0.17	0.02	0.01	0.36	0.11
IRC24-62	04 47 22.3	-53 33 52	2-34	0.356	1	0.00	0.00	0.18	0.05	0.24	0.07	1.24	0.37	0.69	0.21	0.00	0.00	0.38	0.11
IRC15-315	04 47 25.0	-53 28 34	3-37	0.436	3	0.00	0.00	0.03	0.01	0.00	0.00	0.00	0.00	0.32	0.10	0.01	0.00	0.24	0.07
IRC24-90	04 47 28.4	-53 29 56	1-34	0.760	3	0.00	0.00	0.81	0.24	0.00	0.00	0.00	0.00	0.28	0.08	0.37	0.11	4.27	1.28
IRC15-253	04 47 28.8	-53 26 25	5-379	0.692	1	0.00	0.00	0.32	0.10	0.00	0.00	0.44	0.13	0.27	0.08	0.00	0.00	1.35	0.41
FIS90-997	04 48 37.5	-53 48 19	1-70	0.682	1	0.00	0.00	0.00	0.00	0.00	0.00	0.00	0.00	0.20	0.06	0.00	0.00	0.70	0.21
FIS90-287	04 49 39.2	53 34 20	2-10	0.347	3	0.00	0.00	0.98	0.29	0.00	0.00	0.00	0.00	0.76	0.23	q.06	0.32	0.99	0.30
...	...	...	3-19	0.347	2	0.00	0.00	1.34	0.40	0.00	0.00	0.00	0.00	0.00	0.00	0.24	0.07	0.31	0.09
FIS90-219	04 51 55.2	-53 03 11	1-372	0.395	3	0.00	0.00	3.97	1.19	0.00	0.00	0.00	0.00	4.69	1.41	0.50	0.15	3.64	1.09

Table B.3: High-redshift ($1 < z$) detections by AAOmega in ADF-S, showing the main emission lines identified. For notes, see page 217.

ID	RA (J2000)	Dec (J2000)	AAO Fibre	z_{spec}	Q	Lyα 1216Å S μJy	Lyα 1216Å ΔS μJy	CIV 1549Å S μJy	CIV 1549Å ΔS μJy	CIII] 1909Å S μJy	CIII] 1909Å ΔS μJy	MgII 2798Å S μJy	MgII 2798Å ΔS μJy	[NeV] 3426Å S μJy	[NeV] 3426Å ΔS μJy	[OII] 3727Å S μJy	[OII] 3727Å ΔS μJy
FIS90-1700	04 38 45.4	-53 32 46	5-196	1.486	3	osr		osr		32.03	9.61	6.27	1.88	0.00	0.00	osr	
FIS90-1845	04 43 01.3	-53 04 10	4-248	1.833	1	osr		0.00	10.08	3.02	28.24	8.47	0.00	osr		osr	
IRC15-463	04 44 32.6	-53 32 24	4-251	1.856	1	osr		13.11	3.94	31.31	9.40	0.00	0.00	osr		osr	
IRC24-155	04 45 00.0	-53 20 46	2-246	1.454	3	osr		15.67	4.70	10.59	3.18	4.87	1.46	0.00	0.00	osr	
...	...	...	1-232	1.454	3	osr		diff		5.40	1.62	506	1.52	0.00	0.00	osr	
IRC24-6	04 45 01.0	-53 44 55	3-122	1.595	3	osr		26.01	7.80	10.18	3.05	14.84	4.45	osr		osr	
IRC15-257	04 45 24.5	-53 26 44	3-265	2.858	3	34.67	10.41	8.32	2.50	9.94	2.98	0.00	0.00	osr		osr	
IRC24-167	04 45 52.0	-53 18 27	1-265	1.541	3	osr		0.00	0.00	5.54	1.66	0.39	0.12	0.62	0.19	osr	
IRC15-92	04 45 55.4	-53 20 16	4-342	1.810	1	osr		0.00	0.00	2.52	0.75	8.56	2.57	osr		osr	
IRC24-163	04 45 58.5	-53 19 27	1-330	1.437	3	osr		23.45	7.04	19.77	5.93	9.06	2.72	0.64	0.19	osr	
IRC24-115	04 46 04.1	-53 26 31	1-257	1.321	3	osr		osr		6.09	1.83	4.42	1.33	0.00	0.00	0.00	0.00
IRC24-22	04 46 06.8	-53 39 27	1-59	2.357	3	35.70	10.71	14.18	4.26	8.26	2.48	0.00	0.00	osr		osr	
IRC24-160	04 46 14.2	-53 20 26	1-284	1.376	3	osr		osr		36.88	11.07	7.38	2.22	0.00	0.00	osr	
IRC24-52	04 46 23.5	-53 35 41	1-80	1.307	3	osr		osr		19.20	5.76	2.79	0.84	1.28	0.38	6.28	1.88
IRC24-138	04 46 38.4	-53 24 00	1-336	1.103	3	osr		osr		28.16	8.45	18.76	5.63	0.00	0.00	0.31	0.09
IRC24-89	04 47 22.6	-53 30 07	1-39	1.051	3	osr		osr		26.60	7.98	25.44	7.63	0.13	0.04	0.20	0.06
...	...	...	3-27	1.050	3	osr		osr		10.75	3.22	9.84	2.95	0.00	0.00	0.00	0.00

Appendix C: Publications in peer-reviewed journals

Far Infrared Luminosity Function of Local Star-forming Galaxies in the AKARI Deep Field South
Chris Sedgwick, Stephen Serjeant, Chris Pearson, Shuji Matsuura, Mai Shirahata, Shinki Oyabu, Tomotsugu Goto, Hideo Matsuhara, D. L. Clements, Mattia Negrello, and Glenn J. White
MNRAS, 416, 1862 (2011)

Detection of Hα Emission from $z > 3.5$ Galaxies with AKARI-FUHYU NIR Spectroscopy
Chris Sedgwick, Stephen Serjeant, Chris Pearson, Toshinobu Takagi, Hideo Matsuhara, Takehiko Wada, Hyung Mok Lee, Myungshin Im, Woong-Seob Jeong, Shinki Oyabu and Glenn J. White
PKAS, 27, 357 (2012)

Detection of Hα emission from $z > 3.5$ submillimetre luminous galaxies with AKARI-FUHYU spectroscopy
Chris Sedgwick, Stephen Serjeant, Chris Pearson, Ian Smail, Myungshin Im, Shinki Oyabu, Toshinobu Takagi, Hideo Matsuhara, Takehiko Wada, Hyung Mok Lee, Woong-Seob Jeong and Glenn J. White
MNRAS, 436, 395 (2013)

Luminosity functions of local infrared galaxies with AKARI: implications for the cosmic star formation history and AGN evolution
Tomotsugu Goto, Stephane Arnouts, Hanae Inami, Hideo Matsuhara, Chris Pearson, Tsutomu T. Takeuchi, Emeric Le Floc'h, Toshinobu Takagi, Takehiko Wada, Takao Nakagawa, Shinki Oyabu, Daisuke Ishihara, Hyung Mok Lee, Woong-Seob Jeong, Chisato Yamauchi, Stephen Serjeant, **Chris Sedgwick**, Ezequiel Treister
MNRAS, 410, 573 (2011)

Infrared luminosity functions of AKARI Sloan Digital Sky Survey galaxies
Tomotsugu Goto, Stephane Arnouts, Matthew Malkan, Toshinobu Takagi, Hanae Inami, Chris Pearson, Takehiko Wada, Hideo Matsuhara, Chisato Yamauchi, Tsutomu T. Takeuchi, Takao Nakagawa, Shinki Oyabu, Daisuke Ishihara, David B. Sanders, Emeric

Le Floc'h, Hyung Mok Lee, Woong-Seob Jeong, Stephen Serjeant, **Chris Sedgwick**
MNRAS, 414, 1903 (2011)

A deep ATCA 20 cm radio survey of the AKARI Deep Field South near the South Ecliptic Pole
Glenn J. White, Bunyo Hatsukade, Chris Pearson, Toshinobu Takagi, **Chris Sedgwick**, Shuji Matsuura, Hideo Matsuhara, Stephen Serjeant, Takao Nakagawa, Hyung Mok Lee, Shinki Oyabu, Woong-Seob Jeong, Mai Shirahata, Kotaro Kohno, Issei Yamamura, Hitoshi Hanami, Tomotsugu Goto, Sin'itirou Makiuti, David L. Clements, K. Malek, Sophia A. Khan
MNRAS, 427, 1830 (2012)

The Synergy of Large Area Surveys with AKARI and Herschel
Chris Pearson, Stephen Serjeant, **Chris Sedgwick**, Glenn J. White, Hideo Matsuhara, Toshinobu Takagi, Oi Nagisa, Kazumi Murata, Takao Nakagawa, Issei Yamamura
PKAS, 27, 375 (2012)

Evolution of mid-infrared galaxy luminosity functions from the entire *AKARI* NEP deep field with new CFHT photometry
Tomotsugu Goto, Nagisa Oi, Youichi Ohyama, Matthew Malkan, Hideo Matsuhara, Takehiko Wada, Marios Karouzos, Myungshin Im, Takao Nakagawa, Veronique Buat, Denis Burgarella, **Chris Sedgwick**, Yoshiki Toba, Woong-Seob Jeong, Lucia Marchetti, Katarzyna Małek, Ekaterina Koptelova, Dani Chao, Yi-Han Wu, Chris Pearson, Toshinobu Takagi, Hyung Mok Lee, Stephen Serjeant, Tsutomu T. Takeuchi and Seong Jin Kim
MNRAS, 452, 1684 (2015)

The *Spitzer*-IRAC/MIPS Extragalactic Survey (SIMES) in the South Ecliptic Pole Field
I. Baronchelli, C. Scarlata, G. Rodighiero, A. Franceschini, P. L. Capak, S. Mei, M. Vaccari, L. Marchetti, P. Hibon, **C. Sedgwick**, C. Pearson, S. Serjeant, K. Menéndez-Delmestre, M. Salvato, M. Malkan, H. I. Teplitz, M. Hayes, J. Colbert, C. Papovich, M. Devlin, A. Kovacs, K. S. Scott, J. Surace, J. D. Kirkpatrick, H. Atek, T. Urrutia, N. Z. Scoville and T. T. Takeuchi
ApJS, 223, 1 (2016)

Acknowledgements

Firstly, I would like to acknowledge my supervisors, Dr Stephen Serjeant, for his enthusiasm, encouragement and continuous stream of ideas, and Professor Glenn J. White and Dr Chris Pearson. Together, they have provided excellent guidance, advice and help during my years as a research student.

All the research in this thesis was based on observations with *AKARI*, a JAXA project with the participation of ESA. The research was funded in part by the Sasakawa Foundation (3108). Thanks to Carlotta Gruppioni for the model data used in Chapter 4. Thanks to Ivano Baronchelli for the CTIO, WFI, VST and *Spitzer*-IRAC data and to Bunyo Hatsukade for the *Herschel*-PACS data used in Chapter 5. Thanks to Mark Swinbank for the SMMJ2135-0102 SED in Chapter 7.

I should also like to thank the co-authors of the papers on which Chapters 4 and 7 are based; they are listed in Appendix C.

Much of the work in this thesis has been done with IDL, and I would like to acknowledge the many astronomical and statistical routines and functions which are available. In particular, I made use of routines written by my supervisor Stephen Serjeant, routines on AstroLib, and routines by David Fanning (Coyote), Liam Gumley, Craig Markwardt, and those written at the Imperial College astronomy group some years ago.

Thanks to my examiners, Dr Kate Isaak and Dr Simon Clark for many helpful suggestions which significantly improved the clarity of the thesis.

Also, thanks to everyone who has come to Cosmology Coffee Club on Thursdays at The Open University for helpful suggestions on many topics over the past six years.

This thesis has been typeset from TEX/ LATEX files prepared by the author, using a template designed by Harish Bhanderi of the University of Cambridge.

References

Abraham, S., Philip, N.S., Kembhavi, A. et al. (2012). MNRAS, 419, 80. 188, 189

Adelman-McCarthy, J.K., Aqueros, M.A., Allam, S.S. et al. (2008). ApJS, 175, 297. 189

Alam, S., Albareti, F.D., Allende Prieto, C. et al. (2015). ApJS, 219, 12. 187

Alberts, S., Pope, A., Brodwin, M. et al. (2014). MNRAS, 437, 437. 46

Alexander, D.M., Smail, I., Bauer, F.E. et al. (2005). Nature, 434, 740. 45

Allamandola, L.J., Tielens, A.G.G.M. and Baker, J.R. (1985). ApJ, 290, L25. 20

Antonucci, R. (1993). ARA&A, 31, 473. 41

Aretxaga, I., Hughes, D.H., Coppin, K. et al. (2007). MNRAS, 379, 1571. 158, 159, 162

Armus, L., Mazzarella, J.M., Evans, A.S. et al. (2009). PASP, 121, 559. 44, 71

Arnouts, S., Cristiani, S., Moscardini, L. et al. (1999). MNRAS, 310, 540. 127, 137

Atek, H., Kneib, J.P., Pacifici, C. et al. (2014). ApJ, 789, 96. 49

Atek, H., Richard, J., Kneib, J.P. et al. (2015). ApJ, 800, 18. 104

Avni, Y. and Bahcall, J.N. (1980). ApJ, 235, 694. 97

Babbedge, T.S.R., Rowan-Robinson, M., Vaccari, M. et al. (2006). MNRAS, 370, 1159. 99, 101, 103, 106

Bai, L., Rieke, G.H., Rieke, M.J. et al. (2009). ApJ, 693, 1840. 110

Baldry, I.K., Alpasian, M., Bauer, A.E. et al. (2014). MNRAS, 441, 2440. 63

Baldwin, J.A., Phillips, M.M. and Terlevich, R. (1981). PASP, 93, 5. 68, 86

Barger, A.J., Cowie, L.L., Chen, C.C. et al. (2014). ApJ, 784, 9. 29, 176

Barger, A.J., Cowie, L.L., Saunders, D.B. et al. (1998). Nature, 394, 248. 22

Baronchelli, I., Scarlata, C., Rodighiero, G. et al. (2016). ApJS, 223, 1. 83, 94, 132

REFERENCES

Barvainis, R., Antonucci, R., Hurt, T. et al. (1995). ApJ, 451, L9. 191

Bastian, N., Covey, K.R. and Mayer, M.R. (2010). ARA&A, 48, 339. 130

Bauer, A.E., Hopkins, A.M., Gunawardhana, M. et al. (2013). MNRAS, 434, 209. 49

Baum, W.A. (1962). IAUS, 15, 390. 127

Bavouzet, N., Dole, H., Le Floc'h, E. et al. (2008). A&A, 479, 83. 51, 52

Beckwith, S.V.W., Stiavelli, M., Koekemoer, A.M. et al. (2006). AJ, 132, 1729. 33

Bell, E.F. (2003). ApJ, 586, 794. 53

Bennett, C.L., Fixsen, D.J., Hinshaw, G. et al. (1994). ApJ, 434, 587. 5

Bennett, C.L., Larson, D., Wieland, J.L. et al. (2014). ApJ, 794, 135. 57

Bernard-Salas, J., Cami, J., Jones, A. et al. (2013). PoS, LCDU, 032. 21

Berta, S., Magnelli, B., Nordon, R. et al. (2011). A&A, 532, A49. 55

Bertoldi, F., Carilli, C.I., Menten, K.M. et al. (2000). A&A, 360, 92. 158

Bilicki, M., Jarrett, T.H., Peacock, J.A. et al. (2014). ApJS, 210, 9. 127

Blain, A.W. (1996). MNRAS, 283, 1340. 192, 193

Blain, A.W. (1999). MNRAS, 304, 669. 185

Blain, A.W. and Longair, M.S. (1993). MNRAS, 264, 509. 23

Bluck, A.F.L., Ellison, S.L., Patton, D.R. et al. (2014). arXiv, 1412, 3862. 45

Boggess, N.W., Mather, J.C., Weiss, R. et al. (1992). ApJ, 397, 420. 4, 10

Bolton, A.S., Burles, S., Koopmans, L.V.E. et al. (2006). ApJ, 638, 703. 185

Bonfield, D.G., Jarvis, M.J., Hardcastle, M.J. et al. (2011). MNRAS, 416, 13. 184

Bongiorno, A., Merloni, A., Brusa, M. et al. (2012). MNRAS, 427, 3103. 45

Boquien, M., Bendo, G., Calzetti, D. et al. (2010). ApJ, 713, 626. 51

Bouché, N., Murphy, M.T., Kacprzak, G.G. et al. (2013). Science, 341, 50. 39

Bouwens, R.J., Illingworth, G.D., Labbe, I. et al. (2011). Nature, 469, 504. 36, 37

Bower, R.G., Benson, A.J., Malbon, R. et al. (2006). MNRAS, 370, 645. 44

Boyle, B.J. and Terlevich, R.J. (1998). MNRAS, 293, L49. 42

Brand, K., Weedman, D.W., Desai, V. et al. (2008). ApJ, 673, 119. 163

Brescia, M., Cavuoti, S. and Longo, G. (2015). MNRAS, 450, 3893. 188, 190

Brinchmann, J., Charlot, S., White, S.D.M. et al. (2004). MNRAS, 351, 1151. 48

Brinchmann, J. and Ellis, R.S. (2000). ApJ, 535, L77. 36

Bruzual, G. and Charlot, S. (2003). MNRAS, 344, 1000. 125, 128

Burgarella, D., Buat, V. and Iglesias-Páramo, J. (2005). MNRAS, 360, 1413. 127

Calzetti, D., Armus, L., Bohlin, R.C. et al. (2000). ApJ, 533, 682. 125, 179

Calzetti, D., Kinney, A.L. and Storchi-Bergmann, T. (1994). ApJ, 429, 582. 67, 125

Caputi, K.I., Lagache, G., Yan, L. et al. (2007). ApJ, 660, 97. 19, 99, 102, 104, 106, 112

Carilli, C.L., Bertoldi, F., Rupen, M.P. et al. (2001). ApJ, 555, 625. 184

Carilli, C.L. and Yun, M.S. (1999). ApJ, 513, L13. 54

Casey, C.M., Narayanan, D. and Cooray, A. (2014). PhR, 541, 45. 19, 126

Chabrier, G. (2003). PASP, 115, 763. 129, 130

Chapman, S.C., Blain, A.W., Smail, I. et al. (2005). ApJ, 622, 772. 23, 42, 157, 158, 162, 170

Chapman, S.C., Smail, I., Windhorst, R. et al. (2004). ApJ, 611, 732. 158, 159

Charlot, S. and Fall, S.M. (2000). ApJ, 539, 718. 128

Charmandaris, V., Uchida, K.I., Weedman, D. et al. (2004). ApJS, 154, 142. 158

REFERENCES

Chary, R. and Elbaz, D. (2001). ApJ, 556, 562. 125

Chen, C., Smail, I., Swinbank, A.M. et al. (2015). ApJ, 799, 194. 24

Chen, C.T.J., Hickox, R.C., Alberts, S. et al. (2013). ApJ, 773, 3. 42, 45

Cirasuolo, M., McLure, R.J., Dunlop, J.S. et al. (2010). MNRAS, 401, 1166. 100, 104, 106

Clements, D., Bendo, G., Pearson, C. et al. (2011). MNRAS, 411, 373. 132

Coe, D., Benitez, N., Sanchez, F. et al. (2006). AJ, 132, 926. 158

Coe, D., Bradley, L. and Zitrin, A. (2015). ApJ, 800, 84. 35

Coil, A.L., Aird, J., Reddy, N. et al. (2015). ApJ, 801, 35. 69

Cole, S., Aragón-Salamanca, A., Frenk, C.S. et al. (1994). MNRAS, 271, 781. 55

Condon, J.J. (1974). ApJ, 188, 279. 33

Condon, J.J. (1992). ARAA, 30, 575. 53, 130

Coppin, K., Pope, A., Menendez-Delmestre, K. et al. (2010). ApJ, 713, 503. 162

Coppin, K.E.K., Geach, J.E., Almaini, O. et al. (2015). MNRAS, 446, 1293. 38

Coppin, K.E.K., Geach, J.E., Smail, I. et al. (2011). MNRAS, 416, 680. 23, 109

Cowie, L.L., Songaila, A., Hu, E.M. et al. (1996). AJ, 112, 839. 36

Croom, S.M., Richards, G.T., Shanks, T. et al. (2009). MNRAS, 392, 19. 187

Croom, S.M., Smith, R., Boyle, B.J. et al. (2004). MNRAS, 349, 1397. 193

Croom, S.M., Smith, R.J., Boyle, B.J. et al. (2001). MNRAS, 322, L29. 189

Croton, D.J., Springel, V., White, S.D.M. et al. (2006). MNRAS, 365, 11. 44

da Cunha, E., Charlot, S. and Elbaz, D. (2008). MNRAS, 388, 1595. 127

Daddi, E., Dickinson, M., Morrison, G. et al. (2007). ApJ, 670, 156. 47, 48

Dale, D.A. and Helou, G. (2002). ApJ, 576, 159. 125, 127

Davies, R.L., Kewley, L.J., Ho, I.T. et al. (2014). MNRAS, 444, 3961. 69

de Breuck, C., van Breugel, W., Roettgering, H. et al. (2001). AJ, 121, 1241. 162, 170, 175

Delvecchio, I., Gruppioni, C., Pozzi, F. et al. (2014). MNRAS, 439, 2736. 43, 104, 106

Devlin, M.J., Ade, P.A.R., Aretxaga, I. et al. (2009). Nature, 458, 737. 105

Dey, A., Soifer, B., Desai, V. et al. (2008). ApJ, 677, 943. 7, 19

di Matteo, P., Bournaud, F., Martig, M. et al. (2008). A&A, 492, 31. 32

di Matteo, T., Springel, V. and Hernquist, L. (2005). Nature, 433, 604. 44

DiPompeo, M.A., Bovy, J., Myers, A.D. et al. (2015). MNRAS, 452, 3124. 188, 190

DiPompeo, M.A., Myers, A.D., Brotherton, M.S. et al. (2014). ApJ, 787, 73. 192

Djorgovski, S. (1991). ASPC, 21, 349. 179

Dole, H., Lagache, G., Puget, J.L. et al. (2006). A&A, 451, 417. 17, 18

Domínguez, A., Siana, B., Henry, A.L. et al. (2013). ApJ, 763, 145. 90

Domínguez Sanchez, H., Mignoli, M., Pozzi, F. et al. (2012). MNRAS, 426, 330. 179

Donley, J.L., M.Koekemoer, A., Brusa, M. et al. (2012). ApJ, 748, 142. 70, 73

Dowell, C.D., Allen, C.A., Sachidananda Babu, R. et al. (2003). SPIE, 4855, 73. 16

Dowell, C.D., Conley, A., Glenn, J. et al. (2014). ApJ, 780, 75. 38

Dressler, A. (1980). ApJS, 42, 565. 60, 91

Duc, P.A., Mirabel, I.F. and Maza, J. (1997). A&AS, 124, 533. 178

Duley, W.W. and Williams, D.A. (1981). MNRAS, 196, 269. 20

Duncan, W.D., Robson, E.I., Ade, P.A.R. et al. (1990). MNRAS, 243, 126. 16

Dunne, L., Eales, S., Edmunds, M. et al. (2000). MNRAS, 315, 115. 14, 103, 106

Dwek, E., Arendt, R.G., Hauser, M.G. et al. (1998). ApJ, 508, 106. 5

REFERENCES

Dye, S., Dunne, L., Eales, S. et al. (2010). A&A, 518, 10. 36, 103, 106

Dye, S., Eales, S.A., Aretxaga, I. et al. (2008). MNRAS, 386, 1107. 157, 158, 159, 162

Eales, S., Bertoldi, F., Ivison, R.J. et al. (2003). MNRAS, 344, 169. 158

Eales, S., Chapin, E.L., Devlin, M.J. et al. (2009). ApJ, 707, 1779. 11, 103, 106

Eales, S.A., Raymond, G., Roseboom, I.G. et al. (2010). A&A, 518, 23. 103, 106, 180

Eddington, A.S. (1913). MNRAS, 73, 359. 97

Efstathiou, A., Oliver, S., Rowan-Robinson, M. et al. (2000a). MNRAS, 319, 1169. 6

Efstathiou, A., Pearson, C., Farrah, D. et al. (2014). MNRAS, 437, L16. 19

Efstathiou, A. and Rowan-Robinson, M. (1995). MNRAS, 273, 649. 41, 125

Efstathiou, A., Rowan-Robinson, M. and Siebenmorgen, R. (2000b). MNRAS, 313, 734. 125

Elbaz, D., Daddi, E., Borgne, D.L. et al. (2007). A&A, 468, 33. 47

Elbaz, D., Dickinson, M., Hwang, H.S. et al. (2011). A&A, 533, A119. 11, 19, 51

Elbaz, D., Hwang, H.S., Magnelli, B. et al. (2010). A&A, 518, L29. 52

Farrah, D., Bernard-Salas, J., Spoon, H.W.W. et al. (2007). ApJ, 667, 149. 70, 71

Farrah, D., Lebouteiller, V., Spoon, H.W.W. et al. (2013). ApJ, 776, 38. 19, 72

Fazio, G.G., Hora, J.L., Allen, L.E. et al. (2004). ApJS, 154, 10. 6

Ferrarese, L. and Merritt, D. (2000). ApJ, 539, L9. 41

Finkelstein, S.L., Papovich, C., Dickinson, M. et al. (2013). Nature, 502, 524. 38

Fixsen, D.J., Bennett, C.L. and Mather, J.C. (1999). ApJ, 526, 207. 5

Fixsen, D.J., Cheng, E.S., Cottingham, D.A. et al. (1994). ApJ, 420, 457. 5

Flesch, E.W. (2015). PASA, 32, 10. 190

Flores, H., Hammer, F., Elbaz, D. et al. (2004). A&A, 415, 885. 178

Franceschini, A., Hasinger, G., Miyaji, T. et al. (1999). MNRAS, 310, L5. 43

Francis, P.J., Hewett, P.C., Foltz, C.B. et al. (1991). ApJ, 373, 465. 66, 82

Frayer, D.T., Huynh, M.T., Chary, R. et al. (2006). ApJ, 647, L9. 110, 164

Frayer, D.T., Sanders, D.B., Surace, J.A. et al. (2009). AJ, 138, 1261. 111

Fruchter, A.S. and Hook, R.N. (2002). PASP, 114, 144. 155

Fu, H., Yan, L., Scoville, N.Z. et al. (2010). ApJ, 722, 653. 99, 103, 106

Gardner, J.P., Mather, J.C., Clampin, M. et al. (2006). SSR, 123.4, 485. 10, 13

Geach, J.E., Matsuda, Y., Smail, I. et al. (2005). MNRAS, 363, 1398. 160, 162

Gebhardt, K., Bender, R., Bower, G. et al. (2000). ApJ, 539, L13. 41

Geller, M.J., Hwang, H.S., Fabricant, D.G. et al. (2014). ApJS, 213, 35. 67, 90

Genzel, R. and Cesarsky, C.J. (2000). ARA&A, 38, 761. 6, 20, 117

Genzel, R., Lutz, D., Sturm, E. et al. (1998). ApJ, 498, 579. 44, 71, 117

Gillett, F.C., Forrest, W.J. and Merrill, K.M. (1973). ApJ, 183, 87. 20

Gonzalez-Nuevo, J., Lapi, A., Fleuren, S. et al. (2012). ApJ, 749, 65. 11, 27, 185

Goto, T., Arnouts, S., Inami, H. et al. (2011a). MNRAS, 410, 573. 51, 103, 104, 106

Goto, T., Arnouts, S., Malkan, M. et al. (2011b). MNRAS, 414, 1903. 103, 106

Goto, T., Takagi, T., Matsuhara, H. et al. (2010). A&A, 514, A6. 8, 103, 105, 106

Greve, T.R., Bertoldi, F., Smail, I. et al. (2005). MNRAS, 359, 1165. 162

Greve, T.R., Ivison, R.J., Papadopoulos, P.P. et al. (2004). A&A, 419, 99. 171

Greve, T.R., Ivison, R.J., Stevens, J.A. et al. (2006). AN, 327, 208. 171

Greve, T.R., Stern, D., Ivison, R.J. et al. (2007). MNRAS, 382, 48. 162

Griffin, M.J., Abergel, A., Abreu, A. et al. (2010). A&A, 518, L3. 9

Gruppioni, C., Pozzi, F., Andreani, P. et al. (2010). A&A, 518, L27. 102, 106, 119

Gruppioni, C., Pozzi, F., Polletta, M. et al. (2008). ApJ, 684, 136. 117

Gruppioni, C., Pozzi, F., Rodighiero, G. et al. (2013). MNRAS, 432, 23. 102, 104, 106, 108, 117, 119, 120

Gruppioni, C., Pozzi, F., Zamorani, G. et al. (2011). MNRAS, 416, 70. 26, 56, 100, 117, 118

Haas, M., Klaas, U., Muller, S.A.H. et al. (2003). A&A, 402, 87. 191

Haines, C.P., Busarello, G., Merluzzi, P. et al. (2011). MNRAS, 412, 145. 110

Haines, C.P., Pereira, M.J., Smith, G.P. et al. (2013). ApJ, 775, 126. 46

Hainline, L.J., Blain, A.W., Greve, T.R. et al. (2006). ApJ, 650, 614. 162

Häring, N. and Rix, H.W. (2004). ApJ, 604, L89. 41

Harrison, C.M., Alexander, D.M., Mullaney, J.R. et al. (2012). ApJ, 760, L15. 45

Hasinger, G., Miyaji, T. and Schmidt, M. (2005). A&A, 441, 417. 43

Hatsukade, B., Kohno, K., Aretxaga, I. et al. (2011). MNRAS, 411, 102. 74, 132

Hauser, M.G., Arendt, R.G., Kelsall, T. et al. (1998). ApJ, 508, 25. 5, 16

Hauser, M.G. and Dwek, E. (2001). AR&A, 39, 249. 5, 16

Helou, G. (1986). ApJ, 311, L33. 18, 73

Helou, G., Soifer, B.T. and Rowan-Robinson, M. (1985). ApJ, 298, L7. 53

Hennawi, J.F., Myers, A.D., Shen, Y. et al. (2010). ApJ, 719, 1672. 179

Héraudeau, P., Oliver, S., del Burgo, C. et al. (2004). MNRAS, 354, 924. 55, 107

Hezaveh, Y.D., Marrone, D.P. and Holder, G.P. (2012). ApJ, 761, 20. 185

Hickox, R.C., Mullaney, J.R., Alexander, D.M. et al. (2014). ApJ, 782, 9. 45

Hickox, R.C., Wardlow, J.L., Smail, I. et al. (2012). MNRAS, 421, 284. 42

Hildebrandt, H., Bomans, D.J., Erban, T. et al. (2005). A&A, 441, 905. 162

Hinshaw, G.F., Larson, D., Komatsu, E. et al. (2013). ApJS, 208, 19. 5

Ho, S., Agarwal, N., Myers, A.D. et al. (2015). JCAP, 05, 040. 188, 190

Hodge, J.A., Karim, A., Smail, I. et al. (2013). ApJ, 768, 91. 24

Holland, W.S., Bintley, D., Chapin, E.L. et al. (2013). MNRAS, 430, 2513. 15, 16

Holland, W.S., Cunningham, C.R., Gear, W.K. et al. (1998). SPIE, 3357, 305. 14, 16

Hopkins, P.F. and Hernquist, L. (2009). ApJ, 698, 1550. 42

Huang, J.S., Ashby, M.L.N., Barmby, P. et al. (2007). ApJ, 664, 840. 73, 103, 104, 106

Hughes, D.H., Serjeant, S., Dunlop, J. et al. (1998). Nature, 394, 241. 22

Hung, C.L., Sanders, D.B., Casey, C.M. et al. (2013). ApJ, 778, 129. 50

Huynh, M.T., Frayer, D.T., Mobasher, B. et al. (2007). ApJ, 667, L9. 102, 103, 106, 107

Ikarashi, S., Ivison, R.J., Caputi, K.I. et al. (2015). ApJ, 810, 133. 24

Ilbert, O., Arnouts, S., McCracken, H.J. et al. (2006). A&A, 457, 841. 127, 138

Illingworth, G.D., Magee, D., Oesch, P.A. et al. (2013). ApJS, 209, 6. 38

Inami, H., Armus, L., Charmandaris, V. et al. (2013). ApJ, 777, 156. 44, 72

Isaak, K.G., McMahon, R.G., Hills, R.E. et al. (1994). MNRAS, 269, L28. 183, 184

Isaak, K.G., Priddey, R.S., McMahon, R.G. et al. (2002). MNRAS, 329, 149. 184

Ishigaki, M., Kawamata, R., Ouchi, M. et al. (2015). ApJ, 799, 12. 27, 35

Ivezic, Z., Brandt, W.N., Fan, X. et al. (2014). IAUS, 304, 11. 42, 187, 188, 190, 201

Ivison, R.J., Dunlop, J.S., Smail, I. et al. (2000a). ApJ, 542, 271. 162

Ivison, R.J., Greve, T.R., Dunlop, J.S. et al. (2007). MNRAS, 380, 199. 158, 162

Ivison, R.J., Magnelli, B., Ibar, E. et al. (2010). A&A, 518, L31. 53

Ivison, R.J., Morrison, G.E., Biggs, A.D. et al. (2008). MNRAS, 390, 1117. 162, 171, 173, 174, 177

Ivison, R.J., Smail, I., Amblard, A. et al. (2012). MNRAS, 425, 1320. 171

Ivison, R.J., Smail, I., Barger, A.J. et al. (2000b). MNRAS, 315, 209. 160, 162

Jun, H.D., Im, M., Lee, H.M. et al. (2015). ApJ, 806, 109. 190

Juneau, S., Bournaud, F., Charlot, S. et al. (2014). ApJ, 788, 88. 69

Juneau, S., Dickinson, M., Alexander, D.M. et al. (2011). ApJ, 726, 104. 73

Juneau, S., Glazebrook, K., Crampton, D. et al. (2005). ApJ, 619, L135. 36

Kang, W.R., Woo, J.H., Schultze, A. et al. (2013). ApJ, 767, 26. 41

Karman, W., Caputi, K.I., Trager, S.C. et al. (2014). A&A, 565, A5. 45

Karouzos, M., Im, M., Trichas, M. et al. (2014). ApJ, 784, 137. 46

Kartaltepe, J.S., Sanders, D.B., Le Floc'h, E. et al. (2010). ApJ, 709, 572. 128

Kauffmann, G., Heckman, T.M., Tremonti, C. et al. (2003). MNRAS, 346, 1055. 68, 86, 87

Kauffmann, G., White, S.D.M. and Guiderdoni, B. (1993). MNRAS, 264, 201. 55

Kaviraj, S., Cohen, S., Windhorst, R.A. et al. (2013). MNRAS, 429, L40. 39

Kawada, M., Baba, H., Barthel, P.D. et al. (2007). PASJ, 59, S389. 7, 74, 107

Kayo, I. and Oguri, M. (2012). MNRAS, 424, 1363. 27, 179

Keel, W.C., Chojnowski, S.D., Bennert, V.N. et al. (2012). MNRAS, 420, 878. 42

Kennicutt, R.C. (1998a). ApJ, 498, 541. 48, 51

Kennicutt, R.C. (1998b). ARA&A, 36, 189. 50, 87, 89, 130, 176

Kessler, M.F., Steinz, J.A., Anderegg, M.E. et al. (1996). A&A, 315, L27. 6, 10

Kewley, L.J., Dopita, M.A., Sutherland, R.S. et al. (2001a). ApJ, 556, 121. 68

Kewley, L.J., Groves, B., Kauffmann, G. et al. (2006). MNRAS, 372, 961. 69, 86, 87, 109

Kewley, L.J., Heisler, C.A. and Dopita, M.A. (2001b). ApJS, 132, 37. 68, 69

Kewley, L.J., Maier, C., Yabe, K. et al. (2013). ApJ, 774, L10. 69

Khan, S.A., Chanial, P.F., Willner, S.P. et al. (2009). ApJ, 706, 319. 157, 158

Kim, D.C. and Sanders, D. (1998). ApJS, 119, 41. 102, 103, 106, 107

King, L.J., Jackson, L., Blandford, R.D. et al. (1998). MNRAS, 295, L41. 185

Kinney, A.L., Calzetti, D., Bohlin, R.C. et al. (1996). ApJ, 467, 38. 67

Kirkpatrick, A., Pope, A., Charmandaris, V. et al. (2013). ApJ, 763, 123. 69, 73

Kleinmann, D.E. and Low, F.J. (1970). ApJ, 159, L165. 17

Kneib, J.P. and Natarajan, P. (2011). A&ARv, 19, 47. 185

Kobulnicky, H.A. and Kewley, L.J. (2004). ApJ, 617, 240. 67, 90

Kormendy, J. and Ho, L.C. (2013). ARA&A, 51, 511. 42

Kozłowski, S., Kochanek, C.S., Udalski, A. et al. (2010). ApJ, 708, 927. 190

Kreysa, E., Gemund, H.P., Gromke, J. et al. (1999). InPhT, 40, 191. 16

Kroupa, P. (2001). MNRAS, 322, 231. 129, 130

la Franca, F., Gruppioni, C., Matute, I. et al. (2004). AJ, 127, 3075. 117

Lagache, G., Dole, H., Puget, J.L. et al. (2004). ApJS, 154, 112. 56, 110, 111

Lapi, A., González-Nuevo, J., Fan, L. et al. (2011). ApJ, 742, 24. 105, 106

Larkin, J.E., McLean, I.S., Graham, J.R. et al. (2000). ApJ, 533, L61. 177

Läsker, R., van den Bosch, R.C.E., van de Ven, G. et al. (2013). MNRAS, 434, L31. 130

Laureijs, R., Amiaux, J., Arduini, S. et al. (2011). arXiv, 1110, 3193. 10, 13, 185

Laurent, G.T., Aguirre, J.E., Glenn, J. et al. (2005). ApJ, 623, 742. 16

Laurent, O., Mirabel, I.F., Charmandaris, V. et al. (2000). A&A, 359, 887. 73

Lawrence, A., Warren, S.J., Anmaini, O. et al. (2007). MNRAS, 379, 1599. 14

Le Fevre, O., Vettolani, G., Paltani, S. et al. (2004). A&A, 428, 1043. 158

Le Floc'h, E., Papovich, C., Dole, H. et al. (2005). ApJ, 632, 169. 99, 101, 104, 105, 106, 112

Lee, N., Sanders, D.B., Casey, C.M. et al. (2015). ApJ, 801, 80. 50

Leger, A. and Puget, J.L. (1984). A&A, 135, L5. 20

Leja, J., van Dokkum, P., Franx, M. et al. (2015). ApJ, 798, 115. 49

Lilly, S.J., Le Fevre, O., Hammer, F. et al. (1996). ApJ, 460, L1. 36

Lonsdale, C. (1996). AIPC, 348, 147. 56

Lonsdale, C.J., Smith, H.E., Rowan-Robinson, M. et al. (2003). PASP, 115, 897. 7

Lutz, D., Poglitsch, A., Altieri, B. et al. (2011). A&A, 532, A90. 11

Lutz, D., Spoon, H.W.W., Rigopoulou, D. et al. (1998). ApJ, 505, L103. 44, 71

Madau, P. and Dickenson, M. (2014). ARA&A, 52, 415. 36, 43

Madau, P., Ferguson, H., Dickenson, M.E. et al. (1996). MNRAS, 283, 1388. 36

Madau, P., Pozzetti, L. and Dickinson, M. (1998). ApJ, 498, 106. 36, 37

Madden, S.C., Galliano, F., Jones, A.P. et al. (2006). A&A, 446, 877. 71

Maddox, S.J., Sutherland, W.J., Efstathiou, G. et al. (1990). MNRAS, 243, 692. 74

Magdis, G.E., Rigopoulou, D., Helou, G. et al. (2013). A&A, 558, A136. 70, 71, 73

Magnelli, B., Elbaz, D., Charyi, R.R. et al. (2009). A&A, 496, 57. 99, 102, 103, 106

Magnelli, B., Ivison, R.J., Lutz, D. et al. (2015). A&A, 573A, 45. 54

Magnelli, B., Popesso, P., Berta, S. et al. (2013). A&A, 553, A132. 103, 106, 108

Magorrian, J., Tremaine, S., Richstone, D. et al. (1998). AJ, 115, 2285. 41

Maiolino, R., Carniani, S., Fontana, A. et al. (2015). MNRAS, 452, 54. 176

Maiolino, R., Gallerani, S., Neri, R. et al. (2012). MNRAS, 425, L66. 45

Małek, K., Pollo, A., Takeuchi, T.T. et al. (2010). A&A, 514, A11. 76, 133

Małek, K., Pollo, A., Takeuchi, T.T. et al. (2013). EP&S, 65, 1101. 94

Małek, K., Pollo, A., Takeuchi, T.T. et al. (2014). A&A, 562, 15. 76, 94, 133

Man, A.W.S., Greve, T.R., Toft, S. et al. (2014). arXiv, 1411, 2870. 38, 47

Manners, J.C., Serjeant, S., Bottinelli, S. et al. (2004). MNRAS, 355, 97. 117

Maraston, C. (2005). MNRAS, 362, 799. 125, 127

Marconi, A. and Hunt, L.K. (2003). ApJ, 589, L21. 42

Matsuhara, H., Wada, T., Matsuura, S. et al. (2006). PASJ, 58, 673. 7, 35, 61, 142

Matsuura, S., Shirahata, M., Kawada, M. et al. (2011). ApJ, 737, 2. 61

Matute, I., la Franca, F., Pozzi, F. et al. (2006). A&A, 451, 443. 117

Mauch, T. and Sadler, E.M. (2007). MNRAS, 375, 931. 54

Mayya, Y.D., Bressan, A., Carrasco, L. et al. (2006). ApJ, 649, 172. 32

McMahon, R.G., Banerji, M., Gonzalez, E. et al. (2013). Msngr, 154, 35. 133

McMahon, R.G., Omont, A., Bergeron, J. et al. (1994). MNRAS, 267, L9. 183, 184

Mortier, A.M.J., Serjeant, S., Dunlop, J.S. et al. (2005). MNRAS, 363, 563. 14

Moshir, M., Kopman, G. and Conrow, T.A.O. (1992). Pasadena: Infrared Processing and Analysis Centre, Caltech 3

Murakami, H., Baba, H., Barthel, P. et al. (2007). PASJ, 59S, 369. 7, 10, 75

Murata, K., Matsuhara, H., Inami, H. et al. (2014). A&A, 566, A136. 20

Negrello, M., Clemens, M., Gonzalez-Nuevo, J. et al. (2013). MNRAS, 429, 1309. 103, 106

Negrello, M., Hopwood, R., Dye, S. et al. (2014). MNRAS, 440, 1999. 185

Negrello, M., Hopwood, R., Zotti, G.D. et al. (2010). Science, 330, 800. 11, 27, 185, 187, 202

Negrello, M., Serjeant, S., Pearson, C. et al. (2009). MNRAS, 394, 375. 148

Nesvadba, N.P.H., Boulanger, F., Salomé, P. et al. (2010). A&A, 521, A65. 46

Nesvadba, N.P.H., de Breuck, C., Lehnert, M.O. et al. (2011). A&A, 525, A43. 177, 179

Neugebauer, G., Becklin, E.E., Oke, J.B. et al. (1976). ApJ, 205, 29. 18

Neugebauer, G., Habing, H.J., van Duinen, R. et al. (1984). ApJ, 278, L1. 2, 10

Neugebauer, G., Miley, G.K., Soifer, B.T. et al. (1986). ApJ, 308, 815. 183, 190

Noeske, K.G., Weiner, B.J., Faber, S.M. et al. (2007). ApJ, 660, L43. 47

Noll, S., Burgarella, D., Giovannoli, E. et al. (2009). A&A, 507, 1793. 127

Oesch, P.A., Bouwens, R.J., Illingworth, G.D. et al. (2014). ApJ, 786, 108. 37

Ohta, K., Yamada, T., Nakanishi, K. et al. (1996). Nature, 382, 426. 183

Ohyama, Y., Onaka, T., Matsuhara, H. et al. (2007). PASJ, 59S, 411. 150

Oliver, S., Rowan-Robinson, M., Alexander, D.M. et al. (2000). MNRAS, 316, 749. 6, 115

Oliver, S.J., Bock, J., Altieri, B. et al. (2012). MNRAS, 424, 1614. 11, 74

Omont, A., Beelen, A., Bertoldi, F. et al. (2003). A&A, 398, 857. 184

Omont, A., Cox, P., Bertoldi, F. et al. (2001). A&A, 374, 371. 184

Omont, A., McMahon, R.G., Cox, P. et al. (1996). A&A, 315, 1. 183, 184

Onaka, T., Lorente, R., Ita, Y. et al. (2009). AKARI IRC data user manual for post-helium (phase 3) mission, v. 1.1 150, 151, 152, 210, 211

Onaka, T., Matsuhara, H., Wada, T. et al. (2007). PASJ, 59S, 401. 7, 74, 148

Osterbrock, D.E. and Ferland, G.J. (2006). Astrophysics of gaseous nebulae and active galactic nuclei. University Science Books, California 90

Oyabu, S., Yun, M.S., Murayama, T. et al. (2005). AJ, 130, 2019. 106

Page, M.J., Symeonidis, M., Vieira, J.D. et al. (2012). Nature, 485, 213. 44

Pagel, B.E.J., Edmunds, M.G., Blackwell, D.E. et al. (1979). MNRAS, 189, 95. 67, 90

Pannella, M., Elbaz, D., Daddi, E. et al. (2015). ApJ, 807, 141. 49, 53, 138

Papadopoulos, P.P., Padeli, P., Roettgering, H.J.A. et al. (2000). ApJ, 528, 626. 171

Papovich, C., Dole, H., Egami, E. et al. (2004). ApJS, 154, 70. 55

Pascale, E., Ade, P.A.R., Bock, J.J. et al. (2008). ApJ, 681, 400. 9, 74

Pascale, E., Ade, P.A.R., Bock, J.J. et al. (2009). ApJ, 707, 1740. 17

Patel, H., Clements, D.L., Vaccari, M. et al. (2013). MNRAS, 428, 291. 102, 104, 105, 106, 107, 117

Pearson, C., Takagi, T., Serjeant, S. et al. (2008). *AKARI* Mission Program Proposal: FUHYU 163

Pearson, C.P. (2001). MNRAS, 325, 1511. 55, 110, 111

Pearson, C.P. and Rowan-Robinson, M. (1996). MNRAS, 283, 174. 56

Pearson, C.P., Serjeant, S., Negrello, M. et al. (2010). A&A, 514, A9. 148

Pearson, C.P., Serjeant, S., Oyabu, S. et al. (2014). MNRAS, 444, 846. 8

Peeters, E., Spoon, H.W.W. and Tielens, A.G.G.M. (2004). ApJ, 613, 986. 73

Pérez-González, P., Rieke, G.H., Egami, E. et al. (2005). ApJ, 630, 82. 101, 106

Perrotta, F., Baccigalupi, C., Bartelmann, M. et al. (2002). MNRAS, 329, 445. 192, 193, 201

Perrotta, F., Magliocchetti, M., Baccigalupi, C. et al. (2003). MNRAS, 338, 623. 192, 193

Peterson, B.M., Barth, A.J., Berlind, P. et al. (1999). ApJ, 510, 659. 42

Petric, A.O., Armus, L., Howell, J. et al. (2011). ApJ, 730, 28. 44, 72

Pilbratt, G.L. (2003). ESASP, 511, 31. 9, 10

Pilbratt, G.L., Riedinger, J.R., Passvogel, T. et al. (2010). A&A, 518, L1. 9, 10

Planck-Collaboration (2011). A&A, 536, A1. 13

Planck-Collaboration (2014). A&A, 571, A1. 5

Planck-Collaboration (2015). arXiv, 1502, 01589. 13, 57

Poglitsch, A., Waelkens, C., Geis, N. et al. (2010). A&A, 518, L2. 9

Popescu, C.C., Misiriotis, A., Kylafis, N.D. et al. (2000). A&A, 362, 138. 126

Pozzi, F., Gruppioni, C., Oliver, S. et al. (2004). ApJ, 609, 122. 101, 104, 106

Press, W.H. and Schechter, P. (1974). ApJ, 187, 425. 98

Priddey, R.S. and McMahon, R.G. (2001). MNRAS, 324, L17. 183, 184

Puget, J.L., Abergel, A., Bernard, J.P. et al. (1996). A&A, 308, L5. 16

Rawlings, S., Lacy, M., Sivia, D.S. et al. (1995). MNRAS, 274, 428. 177

Richard, J., Jauzac, M., Limousin, M. et al. (2014). MNRAS, 444, 268. 35

Richards, G.T., Fan, X., Newberg, H.J. et al. (2002). AJ, 123, 2945. 187

Richards, G.T., Myers, A.D., Gray, A.G. et al. (2009). ApJS, 180, 67. 127, 186, 188, 189, 190, 194

Riechers, D.A., Pope, A., Daddi, E. et al. (2014). ApJ, 786, 31. 24

Rieke, G.H., Alonso-Herrero, A., Wiener, B.J. et al. (2009). ApJ, 692, 556. 51

Rieke, G.H., Lebofsky, M.J., Thompson, R.I. et al. (1980). ApJ, 238, 24. 30

Rieke, G.H., Loken, K., Rieke, M.J. et al. (1993). ApJ, 412, 99. 32

Rieke, G.H. and Low, F.J. (1972). ApJ, 176, L100. 17

Rieke, G.H., Young, E.T., Engelbracht, C.W. et al. (2004). ApJS, 154, 25. 6

Rigopoulou, D., Hopwood, R., Magdis, G.E. et al. (2014). ApJ, 781, L15. 19, 72

Rigopoulou, D., Pearson, C., Ellison, B. et al. (2015). arXiv, 1507, 06458. 10, 13

Rodighiero, G., Brusa, M., Daddi, E. et al. (2015). ApJ, 800, L10. 46

Rodighiero, G., Daddi, E., Baronchelli, I. et al. (2011). ApJ, 739, L40. 39, 48

Rodighiero, G., Renzini, A., Daddi, E. et al. (2014). MNRAS, 443, 19. 49

Rodighiero, G., Vaccari, M., Franceschini, A. et al. (2010). A&A, 515A, 8. 102, 104, 106

Roettgering, H.J.A., van Ojik, R., Miley, G.K. et al. (1997). A&A, 326, 505. 162, 171

Roos, O., Juneau, S., Bournaud, F. et al. (2015). ApJ, 800, 19. 44, 45

Rosario, D.J. and Lutz, D. (2013). arXiv, 1309, 3569. 47, 192

Rosario, D.J., Trakhtenbrot, B., Lutz, D. et al. (2013). A&A, 560, A72. 45, 192

Rosenberg, M.J.F., Berné, O. and Boersma, C. (2014). A&A, 566, 4. 21

Rowan-Robinson, M. (1992). MNRAS, 258, 787. 125

Rowan-Robinson, M. (2000). MNRAS, 316, 885. 18, 191, 201

Rowan-Robinson, M. and Wang, L. (2010). MNRAS, 406, 720. 4, 191

Rujopakarn, W., Eisenstein, D.J., Rieke, G.H. et al. (2010). ApJ, 718, 1171. 102, 103, 106

Rush, B., Malkan, M.A. and Spinoglio, L. (1993). ApJS, 89, 1. 103, 106

Russell, R.W., Soifer, B.T. and Forrest, W.J. (1975). ApJ, 198, L41. 20

Salpeter, E.E. (1955). ApJ, 121, 161. 129, 130

Sandage, A., Tammann, G.A. and Yahil, A. (1979). ApJ, 232, 352. 97

Sanders, D.B., Mazzarella, J.M., Kim, D.C. et al. (2003). AJ, 126, 1607. 19, 99, 102, 106, 107

Sanders, D.B. and Mirabel, L.F. (1996). ARA&A, 34, 749. 18, 112

Sanders, D.B., Phinney, E.S., Neugebauer, G. et al. (1989). ApJ, 347, 29. 183

Saunders, W., Bridges, T., Gillingham, P. et al. (2004). SPIE, 5492, 389. 75

Saunders, W., Rowan-Robinson, M., Lawrence, A. et al. (1990). MNRAS, 242, 318. 99, 100, 102, 104, 106, 107, 115

Saunders, W., Sutherland, W.J., Maddox, S.J. et al. (2000). MNRAS, 317, 55. 3, 112

Schechter, P. (1976). ApJ, 203, 297. 98

Schlegel, D.J., Finkbeiner, D.P. and Davis, M. (1998). ApJ, 500, 525. 60, 142

Schmidt, K.B., Treu, T., Trenti, M. et al. (2014). ApJ, 786, 57. 103, 106

Schmidt, M. (1959). ApJ, 129, 243. 48, 51

Schmidt, M. (1968). ApJ, 151, 393. 97, 112

Schmidt, M. and Green, R.F. (1983). ApJ, 269, 352. 188

Schmidt, S.J., Ménard, B., Scranton, R. et al. (2015). MNRAS, 446, 2696. 17

Schneider, D.P., Hall, P.B., Richards, G.T. et al. (2007). AJ, 134, 102. 187

Schneider, D.P., Richards, G.T., Hall, P.B. et al. (2010). AJ, 139, 2360. 186

Schreiber, C., Pannella, M., Elbaz, D. et al. (2015). A&A, 575A, 74. 39

Scott, K.S., Stabenau, H.F., Braglia, F.G. et al. (2010). ApJS, 191, 212. 132

Scott, K.S., Wilson, G.W., Aretxaga, I. et al. (2012). MNRAS, 423, 575. 55

Scott, S.E., Fox, M.J., Dunlop, J.S. et al. (2002). MNRAS, 331, 817. 155

Scoville, N.Z., Evans, A.S., Dinshaw, N. et al. (1998). ApJ, 492, L107. 32

Sedgwick, C., Serjeant, S., Pearson, C. et al. (2011). MNRAS, 416, 1862. 95, 103, 106, 119

Sedgwick, C., Serjeant, S., Pearson, C. et al. (2013). MNRAS, 436, 395. 162, 169

Sell, P.H., Tremonti, C.A., Hickox, R.C. et al. (2014). MNRAS, 441, 3417. 46

Serjeant, S. (2012). MNRAS, 424, 2429. 185

Serjeant, S. (2014). ApJ, 793, L10. 202

Serjeant, S., Bertoli, F., Blain, A.W. et al. (2010a). A&A, 518, L7. 184, 191, 193, 196

Serjeant, S., Carraminana, A., Gonzáles-Solaris, E. et al. (2004). MNRAS, 355, 813. 6, 103, 106, 107, 108, 112, 115, 119

Serjeant, S., Dunlop, J.S., Mann, R.G. et al. (2003). MNRAS, 344, 887. 155, 173, 212

Serjeant, S., Dye, S., Mortier, A. et al. (2008). MNRAS, 386, 1907. 152, 212

Serjeant, S., Efstathiou, A., Oliver, S. et al. (2001). MNRAS, 322, 262. 111, 115

Serjeant, S., Gruppioni, C. and Oliver, S. (2002). MNRAS, 330, 621. 89

Serjeant, S. and Harrison, D. (2005). MNRAS, 356, 192. 3, 99, 103, 104, 106, 107, 112, 113, 114, 115, 116, 117, 120

Serjeant, S. and Hatziminaoglou, E. (2009). MNRAS, 397, 265. 184, 188, 191

Serjeant, S. and Marchetti, L. (2014). MNRAS, 443, 3118. 24

Serjeant, S., Negrello, M., Pearson, C. et al. (2010b). A&A, 514, A10. 148, 158

Serjeant, S., Oliver, S., Rowan-Robinson, M. et al. (2000). MNRAS, 316, 768. 6

Shirahata, M., Matsuura, S., Hasegawa, S. et al. (2009). PASJ, 61, 737. 74, 108

Siebenmorgen, R. and Kreugel, E. (2007). A&A, 461, 445. 125, 126, 137

Simpson, J.M., Smail, I., Swinbank, A.M. et al. (2015). ApJ, 799, 81. 24

Siringo, G., Kreysa, E., Kovács, A. et al. (2009). A&A, 497, 945. 15, 16

Sklias, P., Zamojski, M., Schaerer, D. et al. (2014). A&A, 561, A149. 125

Skrutskie, M.F., Cutri, R.M., Stiening, R. et al. (2006). AJ, 131, 1163. 14, 133

Smail, I., Chapman, S.C., Blain, A.W. et al. (2004). ApJ, 616, 71. 158, 162

Smail, I., Ivison, R.J., Blain, A.W. et al. (1997). ApJ, 490, L5. 22, 185

Smit, R., Bouwens, R.J., Franx, M. et al. (2012). ApJ, 756, 14. 36

Smith, D.J.B., Jarvis, M.J., Hardcastle, M.J. et al. (2014). MNRAS, 445, 2232. 53

Sobral, D., Best, P.N., Smail, I. et al. (2014). MNRAS, 437, 3516. 36

Soifer, B.T., Helou, G., Lonsdale, C.J. et al. (1984). ApJ, 283, L1. 32

Soifer, B.T., Houck, J.R. and Neugebauer, G. (1987a). ARA&A, 25, 187. 3, 53, 73

Soifer, B.T. and Neugebauer, G. (1991). AJ, 101, 354. 17, 102, 106, 107

Soifer, B.T., Sanders, D.B., Madore, B.F. et al. (1987b). ApJ, 320, 238. 103, 104, 106, 107

Solomon, P.M., Radford, S.J.E. and Downes, D. (1990). ApJ, 348, L53. 32

Sopp, H.M. and Alexander, P. (1991). MNRAS, 251, P14. 53

Speagle, J.S., Steinhardt, C.L., Capak, P.L. et al. (2014). ApJS, 214, 15. 49

Spinrad, H., Dey, A. and Graham, J.R. (1995). ApJ, 438, 51. 162

Spitler, L.R., Straatman, C.M.S., Labbé, I. et al. (2014). ApJ, 787, L36. 39

Spoon, H.W.W., Marshall, J.A., Houck, J.R. et al. (2007). ApJ, 654, L49. 44, 71

Spoon, H.W.W., Moorwood, A.F.M., Lutz, D. et al. (2004). A&A, 414, 873. 32

Springel, V., di Matteo, T., Hernquist, L. et al. (2005). MNRAS, 361, 776. 44, 55, 126

Steidel, C.C., Adelberger, K.L., Shapley, A.E. et al. (2000). ApJ, 532, 170. 38

Steinhardt, C.L., Speagle, J.S., Capak, P. et al. (2014). ApJ, 791, L25. 49

Stevens, J.A., Ivison, R.J., Dunlop, J.S. et al. (2003). Nature, 425, 264. 162, 170, 171, 172, 174, 179

Straatman, C.M.S., Labbé, I., Spitler, L.R. et al. (2014). ApJ, 783, L14. 39

Sturm, E., Lutz, D., Tran, D. et al. (2000). A&A, 358, 481. 71

Swinbank, A.M., Simpson, J.M., Smail, I. et al. (2014). MNRAS, 438, 1267. 24

Swinbank, A.M., Smail, I., Chapman, S.C. et al. (2004). ApJ, 617, 64. 170, 176, 180

Swinbank, A.M., Smail, I., Longmore, S. et al. (2010). Nature, 464, 733. 31, 32

Swinyard, B., Nakagawa, T., Merken, P. et al. (2009). ExA, 23, 193. 10, 13

Symeonidis, M., Rosario, D., Georgakakis, A. et al. (2010). MNRAS, 403, 1474. 70

Symeonidis, M., Vaccari, M., Berta, S. et al. (2013). MNRAS, 431, 2317. 126

Szokoly, G.P., Bergeron, J., Hasinger, G. et al. (2004). ApJS, 155, 271. 162

Takata, T., Sekiguchi, K., Smail, I. et al. (2006). ApJ, 651, 713. 176, 178

Takeuchi, T.T., Ishii, T.T., Dole, H. et al. (2006). A&A, 448, 525. 104, 106

Takeuchi, T.T., Yoshikawa, K. and Ishii, T.T. (2003). ApJ, 587, 89. 102

Toba, Y., Oyabu, S., Matsuhara, H. et al. (2013). PASJ, 65, 113. 70, 103, 106

Torres, D.F. and Anchordoqui, L.A. (2004). Rep Prog Phys, 67, 1663. 40

Torres-Papaqui, P., Coziol, R., Plauchu-Frayn, I. et al. (2013). RMxAA, 49, 311. 45

Trenti, M., Bradley, L.D., Stiavelli, M. et al. (2011). ApJ, 727, L39. 38

Tuffs, R.J., Popescu, C.C., Völk, H.J. et al. (2004). A&A, 419, 821. 126

Urry, C.M. and Padovani, P. (1995). PASP, 107, 803. 41

Vaccari, M., Marchetti, L., Franceschini, A. et al. (2010). A&A, 518, L20. 104, 106

Valiante, E., Ade, P., Bock, J. et al. (2010). ApJS, 191, 222. 74, 133

Valiante, E., Lutz, D., Sturm, E. et al. (2007). ApJ, 660, 1060. 158

Valtchanov, I., Virdee, J., Ivison, R.J. et al. (2011). MNRAS, 415, 3473. 180

van der Kruit, P.C. (1971). A&A, 15, 110. 53

vanden Berk, D.E., Richards, G.T., Bauer, A. et al. (2001). AJ, 122, 549. 66

Veilleux, S., Kim, D.C. and Sanders, D.B. (1999). ApJ, 522, 113. 178

Veron-Cetty, M.P. and Veron, P. (2010). A&A, 518, A10. 190

Vieira, J.D., Marrone, D.P., Chapman, S.C. et al. (2013). Nature, 495, 344. 15, 185

Viero, M.P., Moncelsi, L., Quadri, R.F. et al. (2013). ApJ, 779, 32. 17

Vogt, F.P.A., Dopita, M.A., Kewley, L.J. et al. (2014). ApJ, 793, 127. 69

Walcher, J., Groves, B., Budavári, T. et al. (2011). Ap&SS, 331, 1. 126

Walter, F., Declari, R., Carilli, C. et al. (2012). Nature, 486, 233. 24

Wang, L. and Rowan-Robinson, M. (2010). MNRAS, 401, 35. 102, 104, 106, 107

Wang, L., Rowan-Robinson, M., Norberg, P. et al. (2014a). MNRAS, 442, 2739. 3

Wang, L., Viero, M., Clarke, C. et al. (2014b). MNRAS, 444, 2870. 11, 132

Watabe, Y., Risaliti, G., Salvati, M. et al. (2009). MNRAS, 396, 1. 158

Watson, D., Christensen, L., Knudsen, K.K. et al. (2015). Nature, 519, 327. 176

Weedman, D.W. and Houck, J.R. (2008). ApJ, 686, 127. 163

Weiss, A., Ivison, R.J., Downes, D. et al. (2009a). ApJ, 705, 45. 158, 160, 162

Weiss, A., Kovács, A., Coppin, K. et al. (2009b). ApJ, 707, 1201. 162

Werner, M.W., Roellig, T.L., Low, F.J. et al. (2004). ApJS, 154, 1. 6, 10

Whitaker, K.E., Franx, M., Leja, J. et al. (2014). ApJ, 795, 104. 49

Whitaker, K.E., van Dokkum, P.G., Brammer, G. et al. (2012). ApJ, 754, L29. 49

White, G.J., Hatsukade, B., Pearson, C. et al. (2012). MNRAS, 427, 1830. 61, 74, 132

White, S.D.M. and Frenk, C.S. (1991). ApJ, 379, 52. 55

Wiklind, T., Conselice, C.J., Dahlen, T. et al. (2014). ApJ, 785, 111. 24

Williams, R.E., Blacker, B., Dickinson, M. et al. (1996). AJ, 112, 1335. 33

Wilson, C.D., Harris, W.E., Longden, R. et al. (2006). ApJ, 641, 763. 32

Wilson, G.W., Austermann, E., Perera, T.A. et al. (2008). MNRAS, 386, 807. 15, 16

Wisotzki, L., Christlieb, N., Bade, N. et al. (2000). A&A, 358, 77. 188

Wong, T. (2009). ApJ, 705, 650. 42

Woo, J.H., Schultze, A., Park, D. et al. (2013). ApJ, 772, 49. 41

Wright, E.L., Eisenhardt, P.R.M., Mainzer, A.K. et al. (2010). AJ, 140, 1868. 8, 10

Wright, E.L., Mather, J.C., Bennett, C.L. et al. (1991). ApJ, 381, 200. 5

Yamamura, I., Makiuti, S., Ikeda, N. et al. (2010). AIPC, 1158, 169. 182

Yan, R., Ho, L.C., Newman, J.A. et al. (2011). ApJ, 728, 38. 73

Yesuf, H.M., Faber, S.M., Trump, J.R. et al. (2014). ApJ, 792, 84. 45

York, D.G., Adelman, J., Anderson Jr, J.E. et al. (2000). AJ, 120, 1579. 186

Young, E.T., Becklin, E.E., Marcum, P.M. et al. (2012). ApJ, 749, L17. 15

Young, J.S. and Scoville, N.Z. (1991). ARA&A, 29, 581. 32

Zahn, O., Reichardt, C.L., Shaw, L. et al. (2012). ApJ, 756, 65. 37

Zinn, P.C., Middleberg, E., Norris, R.P. et al. (2013). ApJ, 774, 66. 46